

RE-219

PHOTOMETRIC MEASUREMENTS OF
SIMULATED LUNAR SURFACES

July 1965

GPO PRICE \$ _____

CFSTI PRICE(S) \$ _____

Hard copy (HC) _____

Microfiche (MF) _____

ff 653 July 65

Graham

RESEARCH DEPARTMENT

N 66 11876

FACILITY FORM 602

(ACCESSION NUMBER)

(FRRU)

150

1

(PAGES)

(CODE)

CR65169

30

(NASA CR OR TMX OR AD NUMBER)

(CATEGORY)

GRUMMAN ENGINEERING CORPORATION
BETHPAGE NEW YORK

Grumman Research Department Report RE-219

PHOTOMETRIC MEASUREMENTS OF
SIMULATED LUNAR SURFACES

by

J. D. Halajian

Geo-Astrophysics Section

July 1965

Interim Report on NASA Contract No. NAS9-3182

Approved by: *Charles E. Mack, Jr.*
Charles E. Mack, Jr.
Director of Research

FOREWORD

This work represents the Interim Report on the "Photometric Measurements of Simulated Lunar Surfaces" for the National Aeronautics and Space Administration, Manned Spacecraft Center, Houston, Texas, under Contract NAS9-3182 to the Grumman Aircraft Engineering Corporation, Bethpage, N.Y.

The contract authorized a ten-month study commencing July 28, 1964, and delineated work in experimental investigations and interpretations of the lunar photometric data. The study was conducted under the cognizance of the Advanced Spacecraft Technology Division, with Mr. Robert L. Jones of the Lunar Surface Technology Branch serving as Technical Representative.

ABSTRACT

11876

The primary purpose of these investigations is to infer certain physical properties of the lunar surface from terrestrial specimens that reproduce the lunation curves of the moon at representative longitudes. An improved photometer capable of examining 3-inch diameter areas at all phase angles, including 0° , has been developed and used to measure the brightness versus phase relationship of "natural," "artificial," and "controlled" models.

Good photometric agreement with the moon at 0° , 30° and 60° longitudes is obtained with "natural" specimens including fine dust, coarse volcanic cinders, furnace slags, sea corals, metallic meteorites, etc. A low albedo and a high porosity are properties that are most common to these specimens which, otherwise, differ widely from one another in composition, strength, consistency, depth, grain size or actual roughness, etc. Conflicting statements made in the past regarding the nature of the lunar surface on the basis of similar experiments can be avoided if test results are interpreted in terms of photometrically relevant properties rather than in terms of natural specimens that are photometrically analogous to the moon.

Contrived models developed and investigated for the purpose of identifying "relevant" properties confirm the importance of low albedo and high porosity (rather than grain size or composition) as key photometric properties and suggest that the surface of the moon is nearly uniformly covered with an "underdense" microporous material having innumerable, random, sharp edges and overhanging members. The models promise further insight and quantitative data on the photometric and geometric relationship of backscattering surfaces and also account for some recently observed photometric peculiarities of the moon.

Preliminary quantitative estimates of some physical properties of the lunar surface that can be directly inferred from its photometry are given and a number of useful areas of further inquiry are recommended in order to confirm or refine these estimates and utilize the information in interpreting the less explored regions of the lunar data.

Author

TABLE OF CONTENTS

<u>Item</u>	<u>Page</u>
Introduction	1
A Brief Review of Lunar Photometry	3
Lunar Observations	3
Theoretical Investigations	5
Experimental Investigations	7
Test Equipment	11
Test Procedure	14
Standard Lunation Curves and Data Presentation	15
Phase I — Photometry of Natural Specimens	17
Purpose	17
Test Specimens and Experiments	17
Discussion of Test Results	19
Lunar Implications	23
Phase II — Photometry of Artificial Models	92
Purpose	92
Test Specimens	92
Experiments	93
Discussion of Test Results of "Composite" Models	94
An Analysis of the Basic Geometry of Backscattering Surfaces	98
Discussion of Test Results of "Simple" Models	101
Significance of the "Thumb Tacks" Model	103
Phase III — Photometry of "Controlled" Particulate Specimens	127
Purpose	127
Test Specimens	127
Experiments	129
Discussion of Test Results	132
Reevaluation of Former Lunar Photometric Models	135
Conclusions	157
Recommendations	161
Acknowledgments	163
References	164
Appendix	167

LIST OF ILLUSTRATIONS

<u>Figure</u>		<u>Page</u>
1	Standard Lunar Photometric Curves	26
2	Lunation Curves of Four Ray Craters Near the Standard Points, Copernicus, Tycho, Kepler and Aristarchus ..	29
3	Gehrels' Observed Brightness as a Function of Phase for Various Lunar Regions	30
4	Reflection Laws of Lambert, Öpik, and Lommel-Seeliger Compared with the Tschunko Triangles in the Four Van Diggelen Standard Points	31
5	Hapke's Photometric Function	32
6	Lunation Curves of the Moon and Volcanic Cinder ...	33
	Lunation Curves for Different Volcanic Cinder	34
8	Lunation Curves of the Lichen Cladonia Rangiferina..	35
9	van Diggelen's Mean Lunation Curves of Crater Floors for Four Different Crescents of Illumination	36
10	Photograph of Grumman Photometric Analyzer	37
11	Sketch of Grumman Photometric Analyzer	38
12	Viewing and Illumination Geometry at the Lunar Intensity Equator	39
13	Laboratory Simulation of Sun-Moon-Earth Optical Relationship	39
14	Aged Silver Chloride Powder	40
15	Copper Oxide Powder	42
16	Carborundum Powder	44

LIST OF ILLUSTRATIONS (Cont)

<u>Figure</u>	<u>Page</u>
17 Volcanic Cinder #1	46
18 Volcanic Cinder #2	48
19 Volcanic Cinder #3	50
20 Furnace Slag #1	52
21 Furnace Slag #1	54
22 CuO Powder on Furnace Slag #1	56
23 Scoria #1	58
24 Scoria #2	60
25 CuO Powder on Scoria #2	62
26 Meteorite #307	64
27 Meteorite #896	66
28 Meteorite #897	68
29 Foam	70
30 AgCl Powder on Foam	72
31 Coral #1	74
32 Coral #2	76
33 Coral #3	78
34 Coral #4	80
35 Coral #1 at Various Albedos	82
36 Grain Size Distribution of Hawaiian Volcanic Cinders	83

LIST OF ILLUSTRATIONS (Cont)

<u>Figure</u>	<u>Page</u>
37 Furnace Slag #1	84
38 CuO Powder on Scoria #2	86
39 Volcanic Cinder #1	88
40 Meteorite #896	90
41 CuO Powder on Pyramids	106
42 CuO Powder on Surface as Shown	108
43 Cross Section of Prismatic Ridges	110
44 CuO Powder on Prisms and Flat Tilted Surface	111
45 CuO Powder on Prisms	114
46 Lunation Curves of 0° to 10° Longitude Crescent	117
47 CuO Powder on Fine Prisms, Intensity Equator Parallel to Ridges	118
48 CuO Powder on Fine Prisms, Intensity Equator Perpendicular to Ridges	118
49 Albedo vs. Viewing Angle of CuO and/or SiC Powders .	119
50 Mixed Powders on Flat Surface	120
51 Mixed Powders on Prisms	120
52 Intensity Equator and Model Orientation	121
53 "Simple" Models and Their Photometric Function	122
54 Thumb Tacks Model	123
55 Cross Sections of and Shadowing Sequence in Thumb Tack Model	125
56 Grain Size Distribution of Hawaiian Volcanic Cinder #4	137

LIST OF ILLUSTRATIONS (Cont)

<u>Figure</u>		<u>Page</u>
57	Photometry of Coarse-Grained Volcanic Cinder Specimens	138
58	Photometry of Volcanic Cinder #4 as Function of Grain Size, Porosity, and Albedo	143
59	Photometry of Massive Furnace Slag Specimens	148
60	Photometry of Furnace Slag as Function of Grain Size, Porosity, and Albedo	151
61	Albedo and Porosity of Volcanic Cinder Powders vs. Grain Size	153
62	Photometric Match Index vs. Grain Size of Volcanic Cinder #4	154
63	Albedo and Porosity of Furnace Slag #4 Powders vs. Grain Size	155
64	Photometric Match Index vs. Grain Size of Furnace Slag #4	156

INTRODUCTION

This report gives a detailed account of all work performed under NASA Contract No. NAS9-3182 to date. It includes most of the material submitted in two previous progress reports (Refs. 13 and 14)* and represents the final report on the "Photometric Measurements of Simulated Lunar Surface" performed to date.

Recent interest in lunar landing and exploration has stimulated a great deal of earth-based research aimed at interpreting lunar observational data in terms of the engineering properties of the lunar surface and environment. Currently, the lunar photometric data are being utilized in studies of lighting and visibility conditions on the moon as well as in investigating the nature of its surface. This investigation is oriented more toward the latter inquiry. The facilities, techniques, models, and knowledge developed in this connection may be equally useful to those interested in simulating lunar visibility conditions.

This work was largely motivated by the notion that the scarcity of physical and theoretical models that obey the reflection laws of the moon could be due in part to the limitations of instruments used in "model-matching" experiments of this nature, and that improvements or modifications in test equipment, testing techniques, specimen preparation, and methods of analysis, could render photometric test results more meaningful. It should be noted that the purpose of this study is not merely to proliferate the number of lunar photometric models for their own sake, but to understand the physics of the photometric phenomena as it applies to the moon and to improve our knowledge of the lunar surface insofar as such knowledge can be obtained from the lunar photometric data. Additional inferences, beyond the scope of this study, can be made from other portions of the lunar sensor data, either to confirm or to complement the photometric findings.

*References are listed at the end of this report in alphabetical order of author's name and are numbered accordingly.

The experiments are divided into three parts, designated Phase I, Phase II, and Phase III.

Phase I consists of brightness vs. phase angle measurements at 0° , 30° , and 60° viewing angles of 21 "natural" specimens; these specimens were selected on the basis of their promising photometric properties at 0° viewing angle determined during preliminary Grumman-funded experiments (Ref. 11). The purpose of this phase is to establish as broad a match as possible with the known photometric properties of the moon.

The purpose of the succeeding phases is to evaluate the effect of albedo, relative surface roughness, porosity, and grain size on the photometric function by varying each variable more or less independently of the others, and, possibly, to formulate quantitative relationships between the physical and photometric properties of the surfaces. Although Phases II and III pursue similar objectives, they differ from one another by the techniques used in preparing the test models and the methods of analysis.

The three phases are essentially interrelated, but they are treated as complete entities so that each section may be read independently. Each contains a statement of purpose, detailed descriptions of test specimens and experiments, and discussions of test results and their significances. They are preceded by a general review of past efforts in the field of lunar photometry and a detailed description of the Grumman Photometric Analyzer used in our experiments. They are followed by tentative conclusions regarding the nature of the lunar surface, as suggested by the lunar photometric data, and a number of recommendations for further earth-based research in this and other related fields.

The primary purpose of these investigations is to contribute to the definition of an "engineering" lunar surface model that is consistent with the available lunar observational data and the known environmental characteristics of the moon. The search for such a model may be conveniently started by establishing a large variety of photometric models and then narrowing these down in terms of the polarimetric, radiothermal, dielectric, and other known properties of the lunar surface. The validity of these models may also be assessed independently under simulated lunar environmental conditions. Earth-based investigation of this nature could assist or complement, in a number of ways, the mission of unmanned lunar probes paving the way for manned landing and in identifying problem areas in engineering operations on the moon.

A BRIEF REVIEW OF LUNAR PHOTOMETRY

The term "photometry" as used in the study of nonincandescent bodies, such as the moon and the planets, deals with the reflecting properties of the surface of these bodies (mostly in the visible part of the electromagnetic spectrum) as a function of "phase angle," the angle between sunlight incident on the moon and the emergent ray as seen by an observer on earth. By measuring the variation of brightness of the moon under varying conditions of illumination, or phase angle, one is able to obtain information about the detailed structure of its surface that cannot be obtained by visual telescopic means.

Lunar Photometric studies may be conveniently divided into the following three main areas: 1) direct measurements of the albedo and the change in brightness of various areas of the moon throughout a lunation, 2) theoretical formulations of the reflection laws of the moon, and 3) experimental investigations of terrestrial specimens in an attempt to match the measured lunar data and to infer certain physical properties of the lunar surface. These areas will be reviewed critically as a background to and justification for the present work. More detailed reviews of these areas may be found in the literature; in this respect the works of van Diggelen and of Pearse are the most extensive and up-to-date.

Lunar Observations

The earliest photometric measurements of the moon date back to 1847 when Herschel studied the variation of the integrated brightness of the moon over the lunar cycle. The first studies of the change in brightness of selected features on the moon were made by Wislezinus in 1893-95 by means of a stellar photometer. This work was refined later by Wirtz in 1915 and by Barabashev in 1918. These workers demonstrated that the maximum brightness of any region on the moon occurred approximately at full moon. Barabashev explained this result as evidence that the lunar surface is extremely rough and porous, thus confirming an earlier prediction made by Galileo who in the 17th Century (without the benefit of actual measurements) had correctly attributed the absence of limb darkening to the roughness of the lunar surface. The essential validity of Barabashev's conclusions for the entire visible surface of the moon was demonstrated by Markov in 1923 and subsequently by Fedoretz and van Diggelen.

More recently, lunar photometric measurements have been made by Minnaert and Fedoretz using the photographic technique. This technique consists of measuring (by means of a microphotometer) the density of lunar photographic plates taken at various phase angles. From the analysis of 172 regions distributed almost uniformly over the entire surface of the moon, Fedoretz constructed tables in which the angle of incidence, the angle of emergence and the relative brightness were given for each feature and for each lunar phase angle. Orlova constructed similar tables for two groups of lunar areas, the maria and the continents. These tables were based on the photographic studies of Fedoretz and on the visual studies of Sharanov. Typical brightness versus phase curves taken from the Orlova tables, representing averages for lunar maria and continents at 0° , 30° , and 60° longitudes, are shown in Figs. 1a, b, and c respectively.

A careful investigation of the photometric properties of 38 crater floors on the moon was made by van Diggelen who analyzed photographs that were exposed in 1946 by Minnaert. As can be seen in Fig. 1a, b, and c, van Diggelen's results agree reasonably well with those of Orlova, which as we have noted were based on lunar data originally measured by Fedoretz and Sharanov. The results of van Diggelen also confirmed Barabashev's conclusion regarding the maximum brightness occurring at full moon, irrespective of the location of the crater on the lunar disc. However, several rayed craters were found with maximum brightness occurring slightly after zero phase as shown in Fig. 2. No reasonable explanation has yet been offered for this anomaly.

Photometrically, the moon appears to be remarkably uniform. The brightness of different parts of the lunar surface, maria, mountains, and crater floors, approximately changes according to the same relation — namely that the brightness increases rapidly near full moon and decreases rapidly after full moon, regardless of location on the lunar disk. The physical homogeneity of the lunar surface suggested by the photometric data seems to be confirmed by radiothermal data as well as by Ranger VII and VIII photographs, which reveal maria surfaces essentially similar in appearance although some 800 miles apart. After albedo differences of individual objects have been taken into account by normalizing the lunation curves, it is found that the photometric function is almost independent of latitude and dependent only upon longitude. Hence, in attempting to match the lunation curves of the moon with those of laboratory specimens, it is important to examine these specimens under a wide range of viewing positions in the plane of vision.

The moon exhibits also minor variations in albedo or brightness. The term albedo as used in this work implies "directional" albedo, and is defined as the ratio of the brightness of an object to that of an "ideal white diffused reflector" under the same conditions of illumination. Local variations in lunar albedos seem to be due to differences in material rather than changes in viewing geometry. According to data reported by Sytinskaya, the albedo for maria and continents, is almost constant across the lunar disk ranging from .064 to .069 for the maria and from .096 to .115 for the continents. Locally, a minimum of .04 has been found for the bottom of certain craters, and a maximum of .18 for rayed craters.

Gehrels et al. have reported very recently new lunar photometric and albedo measurements for various lunar regions, including some rayed craters. The observations were made before an eclipse (period of 1956-59) in order to determine albedo and the change in brightness at rarely observed small phase angles. Measurements down to 0.8° phase were made. The results, some of which are shown in Fig. 3, differ from previous observations in three major respects. First, the lunation curves are characterized by a more pronounced surge of brightness close to zero phase angle than the van Diggelen and Orlova curves, Fig. 1. Second, the albedo measurements indicate an increasing trend with wavelength ranging from 0.36 to 0.94μ , as expected, but these measurements are generally higher than previously reported. The estimated average albedo at zero phase (extrapolated from measurements at 5° to 0.8° phase angles) gives 0.2 for the normal albedo at 0.55μ wavelength. This average includes high and low albedo measurements taken in the 1955-59 and 1963-64 periods respectively. Third, the rayed craters, Tycho and Copernicus in Fig. 3, unlike those of van Diggelen in Fig. 2, do not show any anomalous phase shift of maximum brightness at opposition.

Available observational data in lunar photometry are taken in the full width of the visible spectrum. No complete brightness vs. phase data at discrete wavelength in the visible or near infrared part of the spectrum are known to exist.

Theoretical Investigations

Various analytical relationships of increasing complexity have been derived during the last few decades in an attempt to formulate a reflection law of the moon as a function of illumination geometry (i.e., angle of incidence i , angle of emergence or viewing angle E , phase angle α), albedo a , and geometry p ,

of the reflecting surface. These formulas have evolved with the successive introduction by various investigators of the parameters i , E , α , and p into the photometric equation. The early attempts were not very successful in accounting for the photometric properties of the moon, largely because they ignored the important surface geometry factor p , which has been recently introduced by Hapke and which will be discussed later.

The simplest and oldest reflection law is that of Lambert stating that the brightness of a surface is a function of its albedo and $\cos i$. This law does not account for the reflecting properties of the moon, because a spherical surface obeying it would have its brightest region at the normal to the incident light and, unlike the moon, would be limb-dark.

The Lommel-Seeliger law takes into account the angle of emergence or viewing angle E of the surface and expresses the brightness as

$$\phi = \frac{a \cos i}{\cos i + \cos E} .$$

This law has the advantage of giving a uniformly bright surface on a sphere at zero phase angle when $i = E$ (assuming a collimated light source) and correctly represents the appearance of a full moon. However, at phase angles other than zero, when i is not equal to E , it agrees very poorly with the lunar data. Neither the Lambert nor the Lommel-Seeliger law satisfies the condition that the brightness of all lunar areas reaches a maximum at full moon.

A number of empirical brightness-phase relationships for the moon have been derived by Schoenberg (Van de Hulst, 1957), Fesenkov, and Öpik. These investigators have improved upon the Lambert and Lommel-Seeliger laws by introducing a function of the phase angle. These formulas are discussed in detail by van Diggelen and Pearse. Tschunko has compared them with the lunar data. The results, shown in Fig. 4, do not satisfactorily conform to the lunar curves, especially at larger longitudes.

Van Diggelen tried to apply the calculations of Chandrasekhar for the scattering of sunlight by a planet and found that this method also fails to describe the lunar observations.

More recently Hapke utilized the Schoenberg Lommel-Seeliger formula as a starting point and multiplied it by a factor which he called the "retro-directive" function in order to account for the "preferred direction" effect. This relationship may be represented conceptually as follows:

$$\phi = \underbrace{f(a, i, E)}_{\text{Lommel-Seeliger}} \cdot \underbrace{f(\alpha)}_{\text{Schoenberg}} \cdot f(\alpha, p)$$

Hapke

The retro-directive function, $f(\alpha, p)$, as introduced by Hapke, is a function only of the phase angle α and a factor p . The latter essentially depends upon the porosity of the material. Curves that fit the lunar data best are characterized, according to Hapke, by $p = 0.6$, corresponding to a porosity of 85%, indicating a model in which 15% of the volume is occupied by solid, shadow-casting elements.

Byrne has compared the curve of the Hapke function for $\alpha = -40^\circ$ with individual data points across the lunar disk obtained by Fedoretz and Orlova. He found that the theoretical curve shows good agreement with the moon between $+50^\circ$ longitude (near the terminator) and -30° longitude, but deviates considerably between -30° longitude and the sunlit limb at -90° longitude, as shown in Fig. 5. Generally, however, Hapke's formula matches the lunar brightness-phase curves better than other theoretical and empirical relationships that have been proposed to date.

Experimental Investigations

Several attempts have been made to match the lunation curves of the moon with those of terrestrial specimens commonly found in nature and with artificial models consisting of controlled, geometric shapes.

Barabashev in 1924 and Bennett in 1938 proposed that much of the moon's surface is covered by random hemispheric pits. The attempts failed to fit the observed lunation curves in the steep portion near maximum brightness. Bennett then postulated deeper pits in the form of half ellipsoids and found a better though still

imperfect fit. Van Diggelen further improved upon this model by interspersing the pits with ash covered level areas, but the agreement with the lunar data was still unsatisfactory.

Lack of success with contrived models led to the search for terrestrial materials that could duplicate the observed lunation curves. A material that has received particular attention in this respect is volcanic cinder, in view of the success that Lyot had in matching it with the polarimetric curves of the moon. Unfortunately, contradictory statements have been made by Barabashev and van Diggelen regarding the photometric properties of this material.

After comparing the reflecting properties of numerous terrestrial rocks, both in their natural and pulverized states, with the observed values for the moon, Barabashev and Chekirda (1959) concluded that the material forming the lunar surface does not resemble a fused or primeval surface, but comes closest to a light (i.e., underdense) disrupted tuffaceous rock in a crushed condition, such as "coarse-grained volcanic ash." More recently, Barabashev and Garazha (1962) investigated the effect of grain size on the photometric signature and found that volcanic cinder with grain diameter ranging from 2 to several millimeters fits the lunar data best, as shown in Fig. 6. They concluded that the lunar surface is covered with volcanic "ash" whose average diameter is unlikely to be less than 1 mm.

Almost simultaneously with Barabashev, van Diggelen also investigated volcanic powders (mean particle diameter 0.1 mm) which he described as "Vesuvius sand 1830" and "Vesuvius ash 1906." Even though these powders had albedos within range of lunar values, the results, shown in Fig. 7, failed to match the brightness-phase curves of the moon. However, van Diggelen, without investigating the effects and interrelationship of grain size and porosity, was led to conclude that "from a photometric point of view, the lunar surface is in no case to be described as a plane layer covered by volcanic ashes" (Ref. 28).

Further investigations by van Diggelen of glass beads, loosely packed stones, seeds, black carbon powder, etc. as possible lunar photometric models were equally unsatisfactory. His numerous attempts finally met with success when he tried a spongy form of lichen, known as "Cladonia rangiferina," having a great number of irregular cups, pits or clefts. The results, shown in Fig. 8, compare very favorably with the curves of observed crater floors, Fig. 9, except for minor deviations at large phase and viewing angles.

It has now become clear, largely due to subsequent work by Hapke, that the unusual backscattering qualities of lichen are mostly due to its high porosity, complex microstructure, and interconnected cavities. Porosity, rather than grain size, may well be the key to reconcile Barabashev's and van Diggelen's opposing views on volcanic cinder as a lunar photometric model. Neither one of these investigators seems to have appreciated the importance of porosity on the lunar photometric functions. This point will be discussed later in this work when an experimental attempt is made to resolve the apparent contradiction in terms of porosity rather than grain size.

In view of the artificiality of the lichen as a lunar model, Hapke built and studied a dust model which Gold had originally proposed as being more realistic in terms of lunar history and environment. Hapke duplicated the lunation curves of the moon at all viewing angles by a surface on which he loosely sprinkled micron-size particles of low reflectivity. The results that he obtained with silver chloride and copper oxide powders have been duplicated by us and are shown in Figs. 14 and 15. Dust particles, when sufficiently small, form, on a microscopic scale, complex labyrinthine structures that have been appropriately described by Hapke as "fairy castles." He explained that such a structure traps most of the light reflected in all directions except in the direction of incidence and accounts for the "backscattering" and "opposition" effects exhibited by the moon regardless of the location or geologic history of the observed area.

Hapke's "fairy castle" model is a marked improvement on the Bennett-van Diggelen "pitted" model or Barabashev's "fragmented tuff," insofar as it postulates an "underdense" porous structure necessary to trap the incoming light and to reflect it preferentially in the direction of incidence. Such a structure also is independently suggested by the rapid cooling curves of the moon. Unfortunately, the photometric significance of this model has been obscured by conclusions regarding the dusty nature of the lunar surface. Such inferences could be premature, since the photometric function of a surface is primarily dependent upon the geometry of its elements and not uniquely dependent upon the actual size of and cohesion between those elements.

The contention that the "fairy castle" structure needed to backscatter light, as is done on the moon, may not be peculiar to dust alone, has in part motivated the photometric investigations at Grumman. It was suspected that such structures could be possessed (although on a larger scale) by hard, highly porous, "macro-rough" volcanic cinders, scoriae, and slags, which are just as likely to exist on the moon as fine dust.

The discovery of lunar photometric models, other than fine dust, which meet Hapke's specifications, has been hampered largely by instrumental limitations. The photometer used by Hapke and his predecessors was not capable of examining spots larger than about a half inch in diameter. It is doubtful that the photometric function of such a small area could do justice to the complexity of a rough surface other than fine dust or lichen. It is clear that the values obtained from lunar observations are averaged over surfaces several orders of magnitude larger than those examined in the laboratory. The actual size of lunar reliefs contributing to its sharp backscatter may well exceed a few microns or even millimeters, and a laboratory specimen having large scale irregularities may be equally valid if it reproduces the lunar data. A large photometric analyzer capable of "seeing" a representative number of protrusions and cavities is necessary to assure a meaningful match. Such a photometer, described in the next section, has been developed at Grumman.

TEST EQUIPMENT

The photometric analyzer built at Grumman for the purpose of viewing large areas is shown in Figs. 10 and 11. The manner in which this device simulates the sun-moon-earth optical relationship is illustrated in Figs. 12 and 13. The sun is simulated by a collimated light source mounted on a counterbalanced rotating arm, approximately 8 feet from the sample. At the center of rotation, the sample simulates a portion of the lunar surface; the table on which it rests can be tilted to change the viewing angle. The table can be adjusted vertically to assure that the light is always beamed to the same part of the sample. The electronic photometer, mounted on the ceiling, views the sample as a similar instrument would view the moon from the earth. The phase angle of the sun-moon-earth geometry can be set by rotating the sun source. Two additional photometers at 30° and 60° viewing angles have been mounted on the ceiling, not only for convenience, but also to obviate the necessity of tilting the sample table and disturbing particulate specimens.

Some of the unique capabilities of this photometric analyzer are as follows:

1. The ability to read at zero and near-zero phase angles. This is accomplished by means of a "beam splitter" which, at phase angles other than zero (or near zero), is replaced by a first-surface mirror to assure a source of unpolarized light to and from the sample. At small phase angles, the polarization produced by the beam splitter is negligible for photometric purposes.
2. To plot the photometric curve automatically as the light source swings over the sample.
3. To take polarimetric readings. This is accomplished by means of a rotating polarizing filter (polaroid) mounted in front of the photometer.*

*The polarimetric part of the photometer is described in greater detail in Ref. 6.

4. To sample large areas. This capability assures meaningful data from surfaces having large-scale irregularities, i.e., mm to cm. Presently, 3-inch diameter areas can be measured. This capability could be expanded to 12 inches or more; the limit is established by the physical dimensions of the facility. Focused light may be used in place of collimated light for very large, less precise work.

The objective lenses for the photometers and sun source are 12-inch $f/2.5$ units.

The sun source and polarizer are motor driven and controlled at a single panel, from which the selection of one of the three photometers can also be made. The three photometers may be seen in Fig. 10. Only the photometers with 0° and 60° viewing angles are equipped with the polarimetric analyzer.

Crossed axes front surface mirrors are used with the sun source to eliminate polarization bias in the light received by the specimen. At a zero degree phase angle, a beam splitter is substituted for the second mirror.

The following features of the Grumman Photometric Analyzer assure accurate and repeatable photometric measurements:

1. The light is well collimated, allowing the formation of sharp shadows. The angular size of the sun (30 minutes of arc) is duplicated in the collimated source, so that the shadowing is realistic. The sun source is made uniform by the use of diffuser disks.
2. Considerable care is taken to minimize extraneous scattered light that could seriously prejudice the results. The equipment is operated in a darkened room. Were the source modulated, some low level illumination would be permissible, but the scatter of modulated light from the source itself would require close attention. In a darkened room, undesirable scatter can be observed and eliminated..

3. The illuminated portion of the sample is slightly less than 4 inches in diameter. This is sufficiently large to assure an integration of the macrostructure of the coarsest specimens used, such as slag, volcanic cinder, meteorites, etc.
4. Each of the three photometers is equipped with a field stop carefully and definitely limiting the viewed area to a disk within the perimeter of the illuminated area. Viewing of the natural boundaries or edges of the specimen is avoided. The viewed area is carefully centered on the axis of rotation of the sun source so that the center of the illuminated disk does not shift appreciably as the arm supporting the sun source is rotated. Keeping the photometers static while rotating the sun source permits the examination of particulate materials that remain undisturbed throughout the test.
5. With the use of large receiver optics, the light collection efficiency is high, and the signal-to-noise ratio in the phototube output is high. The use of a tungsten-iodine lamp with a high intensity, behind the diffuser disk, also favors an excellent signal-to-noise ratio. The recorder is operated at a high gain to minimize the servo error. Some slight servo "jitter" of the recorder is evident, but insufficient to impair its accuracy. The multiplier phototube (931A) increases the system gain.
6. The combination of the tungsten-iodine source (operating in excess of 3000°K) and a blue-sensitive S-4 phototube approximates the spectral response of lunar photographic photometry.
7. The alignment of the sun source and the receivers (photometers) relative to the specimen is carefully adjusted and periodically checked by optical techniques. The performance of the entire system is calibrated regularly by using standard samples with stable, known characteristics. The error of the data can be shown to be less than two per cent for low albedo materials.

TEST PROCEDURE

The initial step with all of the photometric tests, following sample preparation, is to position the specimen properly on its stand. It is aligned in a manner that permits all of the photometers to view the same illuminated disk, never an edge of the specimen or the stand itself. The sample, whether it is a thin veneer of powder or a thick rock specimen, is accommodated by raising or lowering the stand so as always to position the upper surface of the specimen at the same level.

With the sun source extinguished, the arm is rotated in a totally dark room, thereby producing a horizontal trace on the two-axis recorder, representing the dark current level. The operation is repeated with the sun source turned on, with the gain of the photometer adjusted so that the output above the dark current level is normalized to a standard reference point in the lunation curve. The photometric curve is then taken with the front surface metal mirrors through a complete rotation of the sun source. The second mirror is then replaced by the beam splitter. The curve then is completed through the previously eclipsed nine degrees of arc.

In succession, the 30° and 60° photometers are used to plot the reflectivity of the undisturbed specimen. The mirrors and the beam splitter are carefully cleaned at each removal or replacement. Light reflected by the beam splitter to the wall is absorbed by a drape of black flock cloth* to prevent a secondary reflection from this source.

The test curves are automatically plotted by the recorder as the sun source is rotated throughout a full lunation. The sheet on which the test curve is recorded contains a standard lunation curve (of the moon) as described in the next section.

Albedo measurements at all viewing angles are made for all specimens at 0° phase angle through the beam splitter. Since albedo is the ratio of the brightness of the specimen and a standard white diffuser, both measured through the beam splitter under the same illumination, no correction has to be made for passage of light through the beam splitter.

*Synthon, Inc., Cambridge, Mass.

STANDARD LUNATION CURVES AND DATA PRESENTATION

The best known lunar photometric curves that are used today in lunar visibility and model-matching studies are mostly based on the extensive observations made in the late forties by Fedoretz at the Kharkov Observatory and by Minnaert at the Yerkes Observatory. Although these observations do not come as close to zero phase as the more recent ones made by Gehrels, unlike the Gehrels measurements, they contain a great number of points that allow confident construction of brightness-phase curves for large areas of the moon down to about 4° phase (roughly the time of full moon).

Averages for a representative number of crater floors, maria, and continents distributed widely over the lunar disk, have been derived by Orlova and van Diggelen. These averages are shown as brightness vs. phase curves in Figs. 1a, b, and c for 0° , 30° , and 60° longitudes (or viewing angles). The Orlova and van Diggelen curves, based on data by Fedoretz and Minnaert respectively, are in fair agreement with one another and support the view expressed by many authors that the moon is nearly, photometrically homogeneous. The gray band enclosed by these curves may be considered as the data scatter for the entire lunar disk; it is adopted as the lunar standard and is used as a basis for comparison with all our test curves. For the sake of clarity, the lines delimiting the band are omitted in the figures containing the test curves. Comparisons of the actual lunar curves for maria or continents with some of the natural specimens showing the best fit with the lunar data, are presented at the end of Phase I.

In plotting the curves in Fig. 1, the individual albedo differences of the crater floors, maria, and continents have been eliminated by normalizing the brightness of each area to a value of 1.00 at about 4° phase angle. This point represents approximately the smallest phase angle at full moon in the Fedoretz-Minnaert observations. The brightness values of the moon at smaller phase angles are extrapolated beyond this point, and hence are unreliable. It was decided, therefore, to normalize the test curves at this point, rather than at 0° phase angle. In our photometric set-up, this point corresponds to the position of the sun-source when the frame of the beam splitter obscures the sample. Beyond this position the beam splitter is used (between $+4^\circ$ and -4° phases), and the actual plot is shown by the solid, "dipped" curve which peaks between 0.5 and 0.75 units. This peak represents the brightness of the sample as seen through the beam splitter. The actual

brightness of the sample near 0° phase (shown in dotted line) is obtained by multiplying the "dipped" peak value by a factor of 1.66 which represents the correction for the attenuation of light coming through the beam splitter.

Of course, the brightness of the moon at 0° phase, unlike that of our test specimens, is not known, since this position of the moon corresponds to total eclipse, but Gehrels' recent measurements (Fig. 3) taken before an actual eclipse come as close as 0.8° to totality, and reveal a much sharper rise in brightness in this previously unexplored region than indicated by the extrapolations on the lunar standards in Fig. 1. This fact, which Gehrels calls the "opposition effect," may be quite significant and will be considered when evaluating the test results in Phases I and II.

PHASE I — PHOTOMETRY OF NATURAL SPECIMENS

Purpose:

In this phase the albedo and photometry of granular, vesicular, and dendritic specimens are measured at 0°, 30°, and 60° viewing angles by the large Grumman photometers, and the curves are compared with the corresponding lunation curves of the moon. An attempt is made to infer certain properties of the lunar surface from the material and geometrical properties of the specimens. It is also the purpose of this phase to identify and assess, qualitatively, which of these numerous properties have a significant bearing on the photometry of a surface.

Test Specimens and Experiments

The selection of the test specimens was based largely upon existing knowledge and experience in lunar photometry. For instance, it was known that smooth surfaces composed of ordinary terrestrial rocks and common granular materials such as sand, gravel, etc., were not compatible with the lunar photometric data. Therefore, no attempt was made to investigate such specimens. On the other hand, it was widely accepted, even among proponents of conflicting lunar models (such as meteor slag or fine dust), that the surface of the moon was very dark, porous, and rough at some scale coarser than the wavelength of visible light. These properties were used as guidelines in selecting the 21 samples listed and described next.

<u>Specimen No.</u>	<u>Description</u>	<u>Albedo</u>	<u>Figure No.</u>
1	Silver Chloride Powder (Aged)	.13	14
2	Copper Oxide Powder	.07	15
3	Carborundum Powder (SiC)	.14	16
4	Volcanic Cinder No. 1 (cm-size particles)	.11	17
5	Volcanic Cinder No. 2 (cm-size particles)	.12	18
6	Volcanic Cinder No. 3 (cm-size particles)	.05	19
7	Furnace Slag No. 1 (Smooth side)	.10	20
8	Furnace Slag No. 1 (Rough side)	.09	21
9	CuO on Furnace Slag No. 1 (Rough side)	.06	22

<u>Specimen No.</u>	<u>Description</u>	<u>Albedo</u>	<u>Figure No.</u>
10	Volcanic Scoria No. 1	.13	23
11	Volcanic Scoria No. 2	.07	24
12	CuO on Volcanic Scoria No. 2	.05	25
13	Meteorite (Imilac)	.08	26
14	Meteorite (Krasnojarsk 896)	.05	27
15	Meteorite (Krasnojarsk 897)	.08	28
16	Foam	.06	29
17	Silver Chloride on Foam	.11	30
18	Coral No. 1	.16	31
19	Coral No. 2	.32	32
20	Coral No. 3	.25	33
21	Coral No. 4	.35	34

The silver chloride, copper oxide, and carborundum are fine powders (less than .037 mm diameter). They were lightly sifted, from a height of a few inches, through a 400 mesh screen on to a flat, smooth board for a minimum thickness of 2 mm. The silver chloride was then darkened by exposure to sunlight, thus modifying the surface to an oxide and possibly to some free silver.

The three volcanic cinder specimens are from the Haleakala Volcano in Hawaii. They consist of dark, porous particles, predominantly of centimeter size, as can be seen from the photographs in Figs. 17 through 19. The grain size distributions of these specimens are shown in Fig. 36.

The furnace slag, shown in Fig. 20, was supplied by NASA, Manned Spacecraft Center. Its composition is not known, but its structure (which is of greater interest here) consists of a complex agglomeration of dark, coarse, sintered particles overhanging deep recesses that interconnect and extend into the bulk of the specimen. Its surface roughness, unlike that of the powder specimens Nos. 1 through 3, is visible to the naked eye. One side of the slab is fairly flat and is referred to as "smooth"; the other side is more irregular and knobby and is termed "rough." Both sides are equally rough in a $1/8$ to $1/4$ inch scale, which is

the size of the grains and cavities. This particular specimen has a porosity of 68%, as determined by the method described in Phase III. Its bearing or crushing strength has not been measured, but appears to be in the range of a few tons per square inch. Specimen No. 9, a composite model, was created by sifting copper oxide powder onto the furnace slag.

The scoria specimens are volcanic in origin. They are almost identical slabs having closed vesicles with a depth-to-diameter ratio of two to one. Scoria No. 1 is slightly darker than No. 2.

The meteorites have a metallic composition and a pitted surface of deep vesicles and sharp vertical edges, due mostly to terrestrial weathering. They were loaned by the American Museum of Natural History in New York City.

The foam (Specimen No. 16) is a dark, flexible, polyurethane material, plucked to give it an irregular surface. A composite model was created by sifting silver chloride (Specimen No. 1) upon it, and aging it in sunlight. An 8-ft-wide belt of this material is currently being used at Grumman as a movable roadbed to simulate lunar visibility in roving vehicle operations.

The sea corals, Specimen Nos. 1 through 4, were chosen because they appeared to be very promising in view of the very intricate structure they possessed both on a microscopic and a macroscopic scale. Their albedo is high compared to that of the moon. Coral No. 1 was darkened with a spray of paint, and its albedo was lowered from 0.22 to 0.16. The other three coral specimens were examined in their natural condition.

The brightness-phase relationships of all 21 specimens described above were measured at 0°, 30°, and 60° viewing angles over an area 3 inches in diameter. The area was illuminated by integrated visible light. The results of the measurements are discussed in the next section.

Discussion of Test Results

The results of the photometric measurements of the 21 specimens listed above are shown in Figs. 14 through 35. The standard lunation "bands" used for comparison with the test curves are those delimited by the Fedoretz-Orlova, and Minnaert-van Diggelen curves shown in Fig. 1. Albedo values accompany the test curves.

A study of the test results suggests a number of conclusions, some of which have been found by other investigators. Briefly, the following remarks could be made at this time:

1. Most of the specimens show a maximum brightness at zero phase angle (corresponding nearly to full moon), this brightness being independent of the viewing angle. This photometric peculiarity of the moon, first discovered by Barabashev, is obeyed by nearly all the specimens we have selected. In no case was a shift in phase noticed, that is to say, a lag between zero phase (full moon) and maximum radiance, as reported by van Diggelen for the rayed craters shown in Fig. 2. It may be pertinent to note that Gehrels' recent observations of certain lunar craters, like our own measurements of laboratory specimens, do not reproduce or confirm this photometric anomaly.
2. The zero phase brightness peak of most of our specimens (measured by means of the beam splitter) exceeds the extrapolated peak of the standard lunar curve, within the $+4.5^\circ$ phase region near eclipse. The "standard" lunar data in this region appears to be suspect in view of Gehrels' recent measurements showing a "non-linear surge of brightness" near zero phase angle, similar to that shown by our test specimens, particularly the furnace slag.
3. The match between the test and lunar curves at larger phase angles is good for the 0° as well as for the 30° and 60° viewing positions for a number of the specimens, particularly for the furnace slag. The photometric properties of the "cohesive-macrorough" specimens at large viewing angles, unlike those of the AgCl and CuO fine powders, were unknown before these investigations, but appear to be equally good. The hard furnace slag and the coarse-grained volcanic cinder reproduce the lunar curves as well as or better than the fine powders, at all viewing angles.

The photometric curves and the microphotos of the AgCl, CuO, and SiC fine powders are shown in Figs. 14, 15, and 16 respectively. Of course, the microphotos do not do justice to the tridimensional complexity of the "fairy castles" built by the AgCl and CuO particles. They do however, suggest the degree of and difference in fluffing or "fairy castling" when one compares the relative size of the agglomerated particles; this size is largest in the AgCl, it is less pronounced in the CuO and almost negligible in the SiC. This observation partly accounts for their photometric signatures which exhibit back-scattering characteristics consistent with their degree of agglomeration or complexity.

The backscatter from the furnace slag is stronger on the rough side than on the smooth side, as expected, and is strongest (surpassing the lunar backscatter) when the smooth side is covered with CuO powder. This indicates that the superposition of fine dust or a "fairy castle" microstructure on top of a sufficiently macrorough structure unnecessarily steepens the backscatter curve beyond that of the moon, and that macro-rough structures could reproduce the normalized lunar curve equally well, provided they have the proper geometry. What this geometry consists of in terms of actual size, shape, and porosity is not yet very clear; all that can be said about it at this time is that the solid, shadow casting elements are arranged in an "underdense" pattern separated by a complex array of cavities appearing in many cases to be interconnected.

The Hawaiian volcanic cinder No. 2, Fig. 18, does not follow the lunar standard curves as closely as the volcanic cinder No. 1, Fig. 17, particularly at large phase and viewing angles. There is a slight "bulge" or increase in brightness at these angles, having a curious similarity to the photometric properties of individual lunar craters (Albategnius, Plato, Grimaldi and Schikhard) as shown in Fig. 9. Generally, the elongation of the diagram of light scattering in the direction of the light source (at zero phase angle) denotes roughness of the surface, but the elongation or "bulge" at large phase and viewing angles (i.e., in the direction of mirror-reflected rays) could denote smoothness and gloss of surface. (It could also denote other properties which will be discussed in Phase II in connection with the "Thumb Tacks model"). Thus, the existences of two brightness maxima, one toward the light source and the other in the mirror-reflected direction, generally denote a combination of gloss with roughness. This phenomenon becomes most conspicuous at large viewing angles, as illustrated

by one of the meteorite specimens (Krasnojarsk 897) in Fig. 28, and by the synthetic foam in Fig. 29. In the case of the foam, the elongation in the mirror-reflected direction was considerably reduced by covering it with silver chloride powder. The results are shown in Fig. 30.

Except for the sea corals, the albedo of all specimens showing a good fit with the lunar curves is of the same order as that of the lunar surface. Also, like the surface of the moon, these specimens have a nearly constant albedo at all viewing angles.

The sea corals, particularly Nos. 1, 3, and 4, are interesting insofar as they all exhibit a stronger backscatter than the moon despite their relatively high albedo. This behavior is due most probably to their extreme macroroughness, dendritic structure, and an equally complex microstructure. The anomalous, rough outline of the coral No. 4 curves, Fig. 34, is consistent with the exceedingly large scale roughness of the specimen relative to the area viewed, and is indicative of poor integration by the photometer of the changing shadow and light within the viewed area. The 3-inch area seen by the photometer is not large enough to encompass a sufficient number of shadow-casting irregularities which, in this case, are of the order of inches. In addition, the plane of the viewed area is poorly defined.

Coral No. 1 was progressively darkened by a paint spray in order to investigate its photometry under varying albedos. Specifically, the experiment was made to verify the notion that the light scattering function of a given geometrical structure can vary with its absolute reflecting capacity because of the influence of higher-order scattering, that is, the light exchange between the uneven surfaces themselves. The photometric properties of coral No. 1 were measured at 0.22, 0.16, and 0.14 albedo respectively. The results, at normal viewing positions only, are shown in Fig. 35 and indicate, as expected, that the backscatter of the specimen does increase as its albedo is reduced, while its geometry remains unchanged. One may state, therefore, that the backscattering function of a surface, particularly a complex one like the coral, is approximately proportional to its roughness and inversely proportional to its albedo. Since most of the coral specimens exhibit a stronger backscatter than the moon despite their high albedo (no such specimens have been reported before), one may reasonably conclude that, on a relative scale, the sea corals examined here may be rougher and more complex than the surface of the moon. However, one cannot determine on the basis of these experiments the absolute scale of the lunar surface reliefs responsible for the observed backscatter, or the distribution of its micro or macro-roughness.

In evaluating the test results, it would be useful to recall that what is being compared is the "detailed" photometry of small laboratory specimens with the "integrated" photometry of the moon, the latter representing an area orders of magnitude larger. The standard lunation curves of van Diggelen represent averages for lunar crescents encompassing some 10° to 40° longitudes; as to the Fedoretz-Orlova standards, they represent averages for the highlands or the maria. The lunation curves of individual areas on the moon reveal a noticeable scatter when shown with the average curves, as can be seen in Fig. 9. What is significant in the lunar standards, in addition to the scatter, is the fact that in all cases they peak at or near zero phase and follow a consistently uniform trend at larger phase angles, regardless of location on the moon or the geologic history of the area. Hence, the test curves should be assessed in the light of the scatter within the existing lunar data and in the light of the significant properties that are common to the lunation curves of individual lunar areas or standard averages. In this perspective most of the specimens that were proposed for this work on the basis of their good match at normal viewing angle (Ref. 11) reproduce the lunar data at the larger viewing angles reasonably well.

The best matches with the lunar photometric data have been with the following four specimens: Furnace Slag No. 1, CuO-covered Volcanic Slag No. 2, Hawaiian Volcanic Cinder No. 1, and metallic Meteorite Krasnojarsk No. 896. The photometric curves of these specimens have been redrawn in order to be compared with the actual Fedoretz-Orlova lunar photometric curves that represent the averages for the continents and maria. Figures 37 through 40, in which these comparisons are shown, speak for themselves.

Lunar Implications

A great deal of caution must be exercised in reaching conclusions about the moon based on the properties of laboratory specimens that reproduce or fail to reproduce the lunar photometric data. In order to avoid the pitfalls which in the past have led to premature, irrelevant or contradictory conclusions, it is essential to understand the physics of the phenomenon that is responsible for the observed results so that one may limit his inferences to those properties of the lunar surface that could influence these observed results excluding those physical properties that have little or no bearing on these observations.

The photometry of nonincandescent bodies such as the moon or laboratory specimens is largely a function of the geometry or spatial distribution and orientation of the surface elements of the body capable of casting shadows and, of course, a function of the change in the relative position of the light source, viewer, and object. Hence, the possibilities of photometric investigations are limited by the fact that the internal consistency, material composition,* and absolute scale of roughness of the shadow-casting elements have little or no effect on the photometry of a surface. Roughnesses similar in shape and location, but different in size, will produce the same variation of light scattering, provided their dimensions are not below a certain limit; this limit is the point at which the shadow-casting elements become partly transparent (as in the case of sand) or cause diffraction, and consequently lose their characteristic reflection. Moreover, for each type of photometric relief there is an infinite variety of corresponding geometrical reliefs. Hence, the photometric similarity of a given model to the lunar data cannot be looked upon as proof that the real structure of the lunar surface corresponds to an investigated scheme. The latter is only a conditional representative of a whole variety of photometrically similar reliefs. The differences in material composition, bearing strength, consistency, depth, and actual scale of roughness that exist between the good photometric specimens revealed by these investigations, indicate that these properties are not very relevant photometrically, as one would have expected from theoretical considerations; hence, they should not be inferred from the lunar photometric data.

On the other hand, the low albedo and high porosity that is common to nearly all the good photometric models (whether fine dust, coarse volcanic ash, hard scoria, etc.) confirm previous findings by others (notably by van Diggelen and Hapke), and indicate that the outermost layer of the moon, whatever its origin, is nearly uniformly covered by a dark, disrupted, and intricately vesicular, granular or dendritic material. The albedo and porosity of the contending lunar models (of the order of 10% and 80% respectively) deviate considerably from those of common terrestrial soils and rocks. These peculiarities of the lunar surface could be reasonably accounted for by the action of micrometeorites and radiation in an environment of high vacuum and low gravity, as discussed in Ref. 12.

* Assuming the material is effectively not transparent.

The major significance of our experimental findings is that it is no longer necessary to postulate the existence of a layer or veneer of fine dust on the moon as the only way to account for the lunar photometric data, since "macrorough-cohesive" specimens such as the furnace slag and volcanic scoria appear to satisfy this data equally well when viewed by a "large" photometer. These materials could exist on the moon as well as fine dust.

It does not appear possible to favor any one model or to narrow the considerable divergence in bearing strength that exists between these models, by using the lunar photometric data alone. However, the high porosity that is common to nearly all these models could provide the independent clue necessary to interpret the lunar radio-thermal data, this, in turn, could lead to an estimate of the internal consistency and bearing strength of the lunar surface as discussed in Ref. 12. Phase II of this investigation was largely conceived as an attempt to provide a quantitative estimate of the range of porosities compatible with the lunar photometric data.

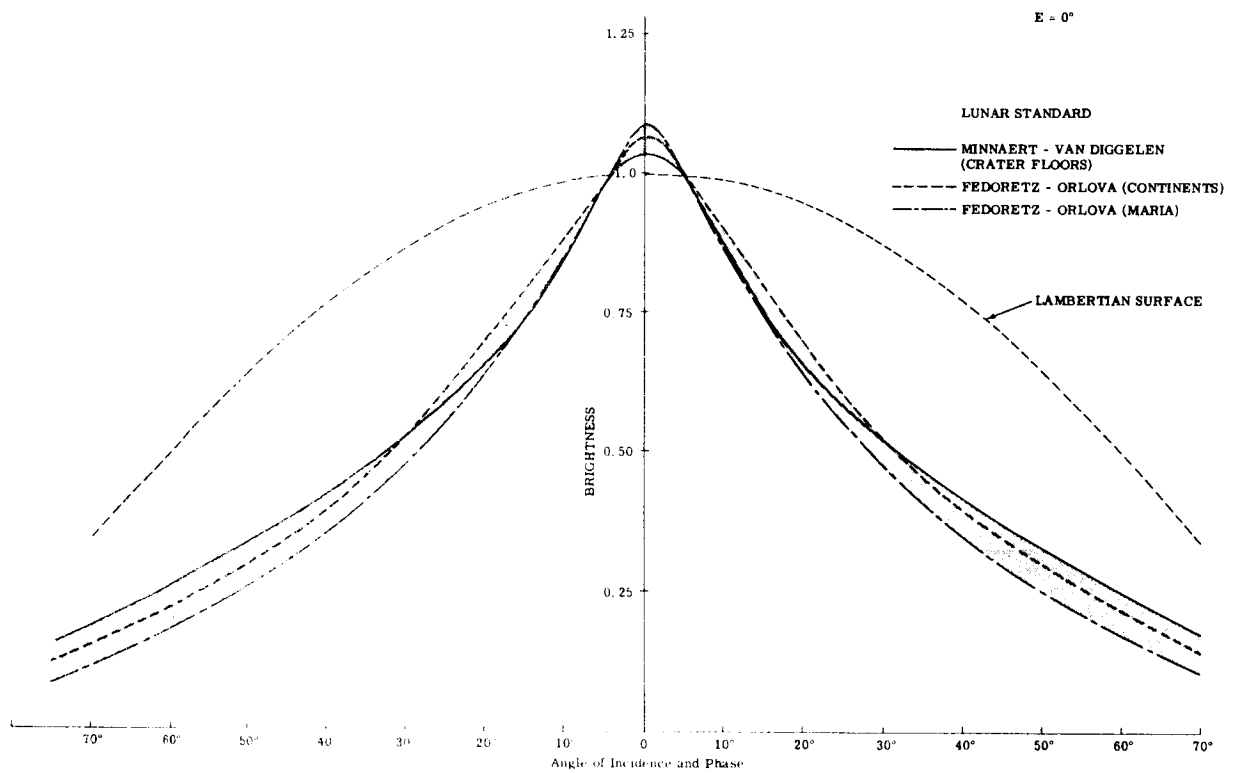


Figure 1a. Standard Lunar Photometric Curve

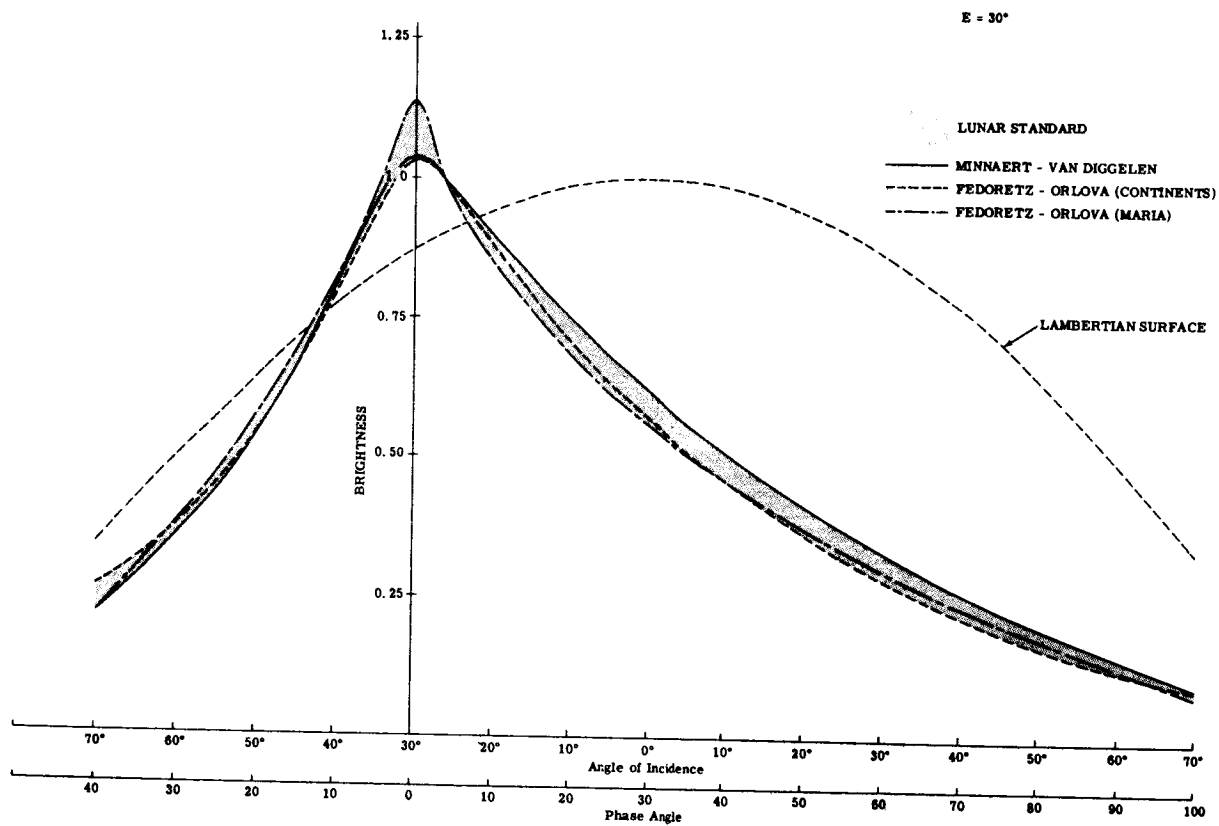


Figure 1b. Standard Lunar Photometric Curve

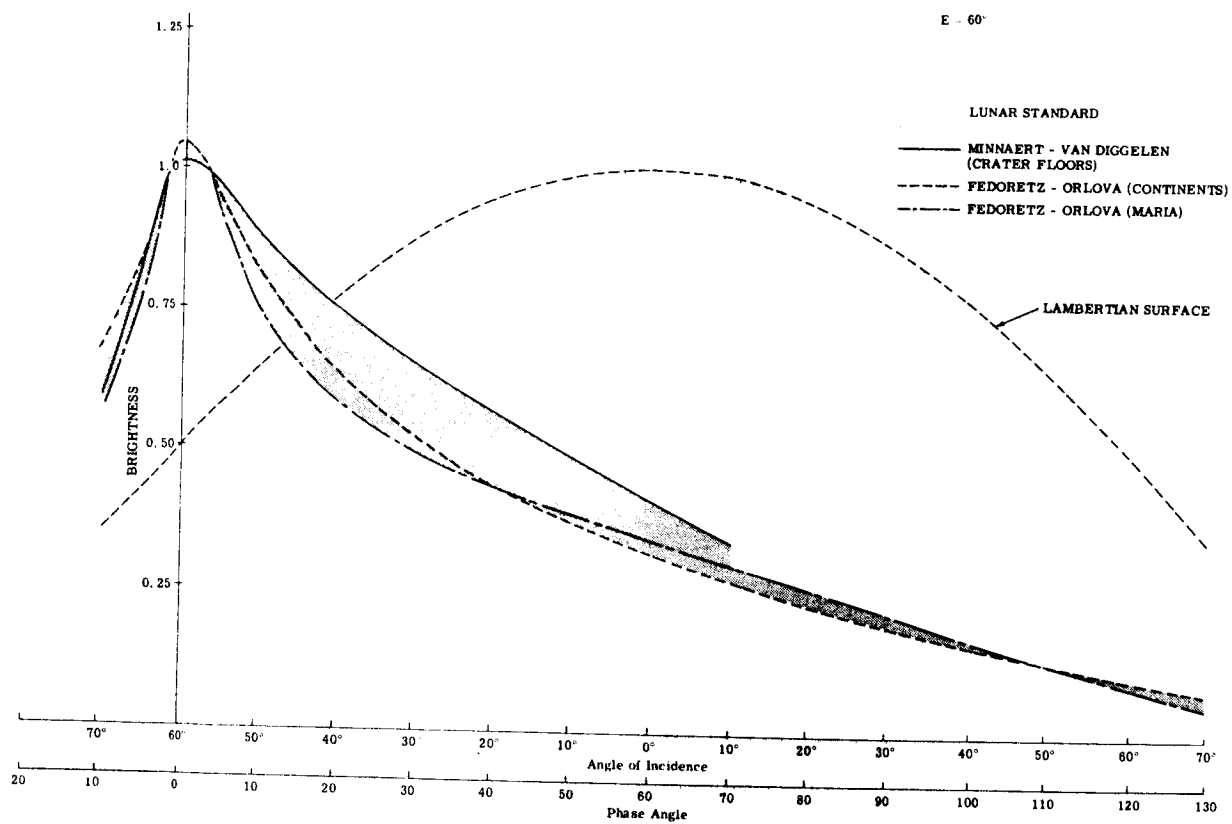


Figure 1c. Standard Lunar Photometric Curve

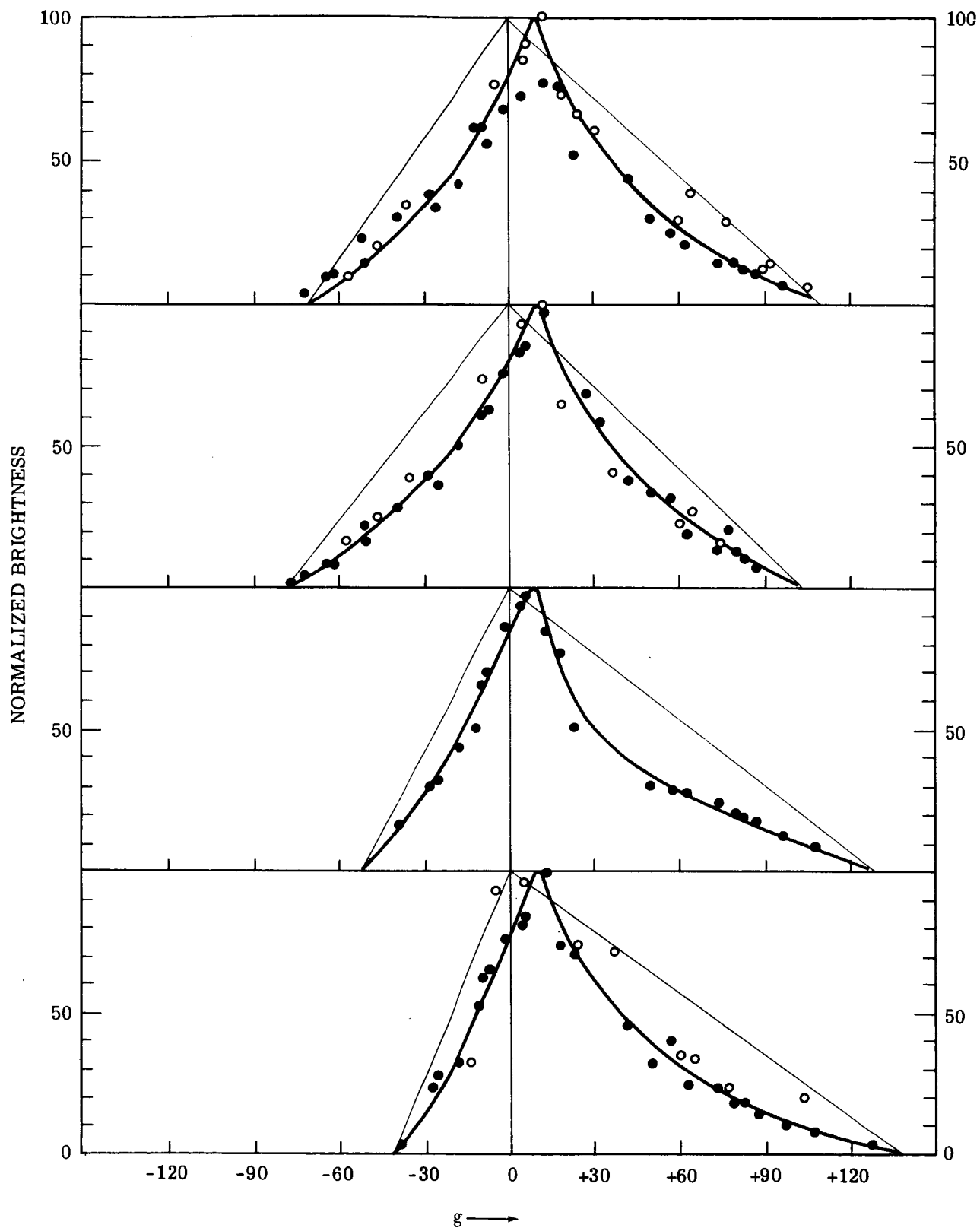


Figure 2. Lunation Curves of Four Ray Craters Near the Standard Points, Copernicus, Tycho, Kepler and Aristarchus. The Observers and the Meaning of the Marks are Given in Ref (28).

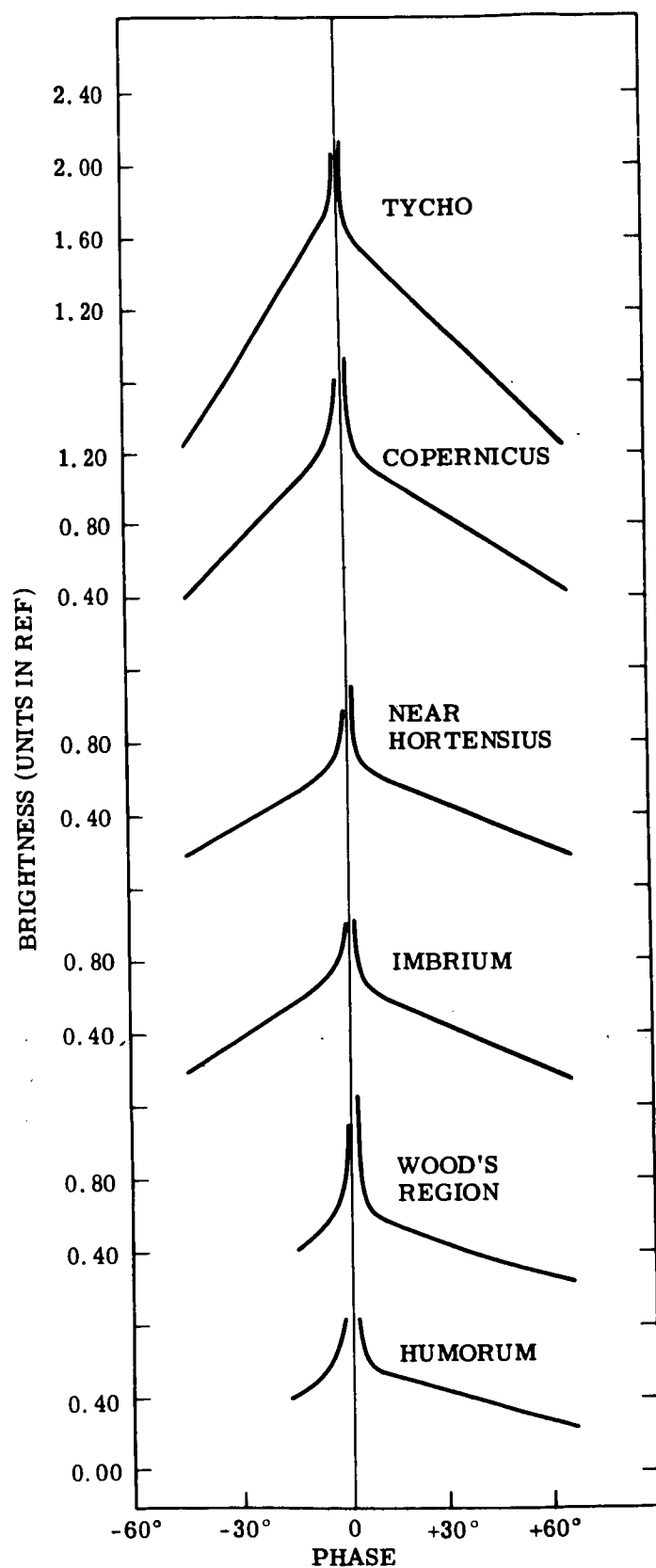


Figure 3. Gehrels' Observed Brightness as a Function of Phase for Various Lunar Regions. Ref (9)

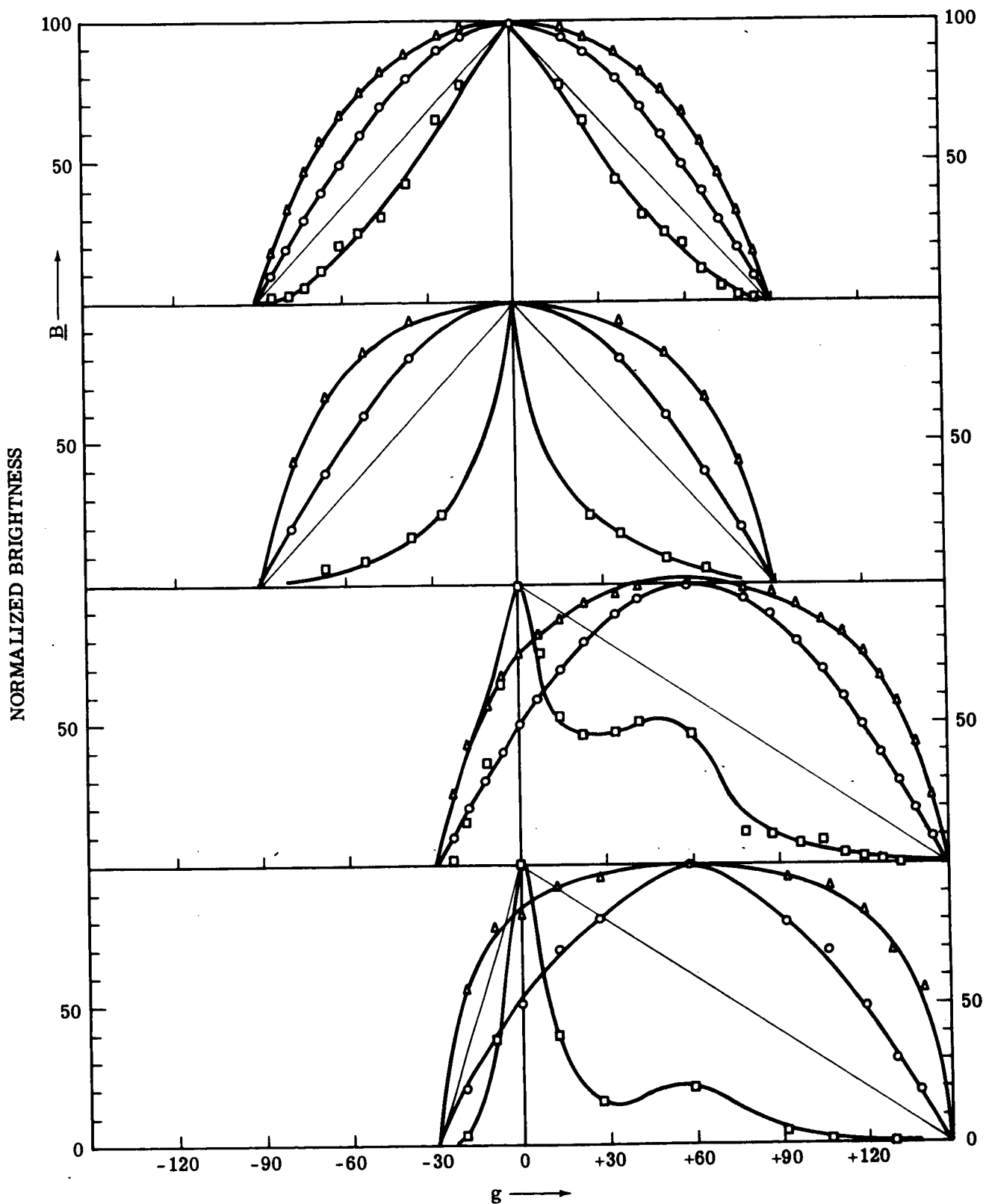


Figure 4. Reflection Laws of Lambert (\circ), Öpik (\square), and Lommel - Seeliger (\triangle), compared with the Tschunko Triangles in the Four Van Diggelen Standard Points as Shown in Figure 9. Ref (28).

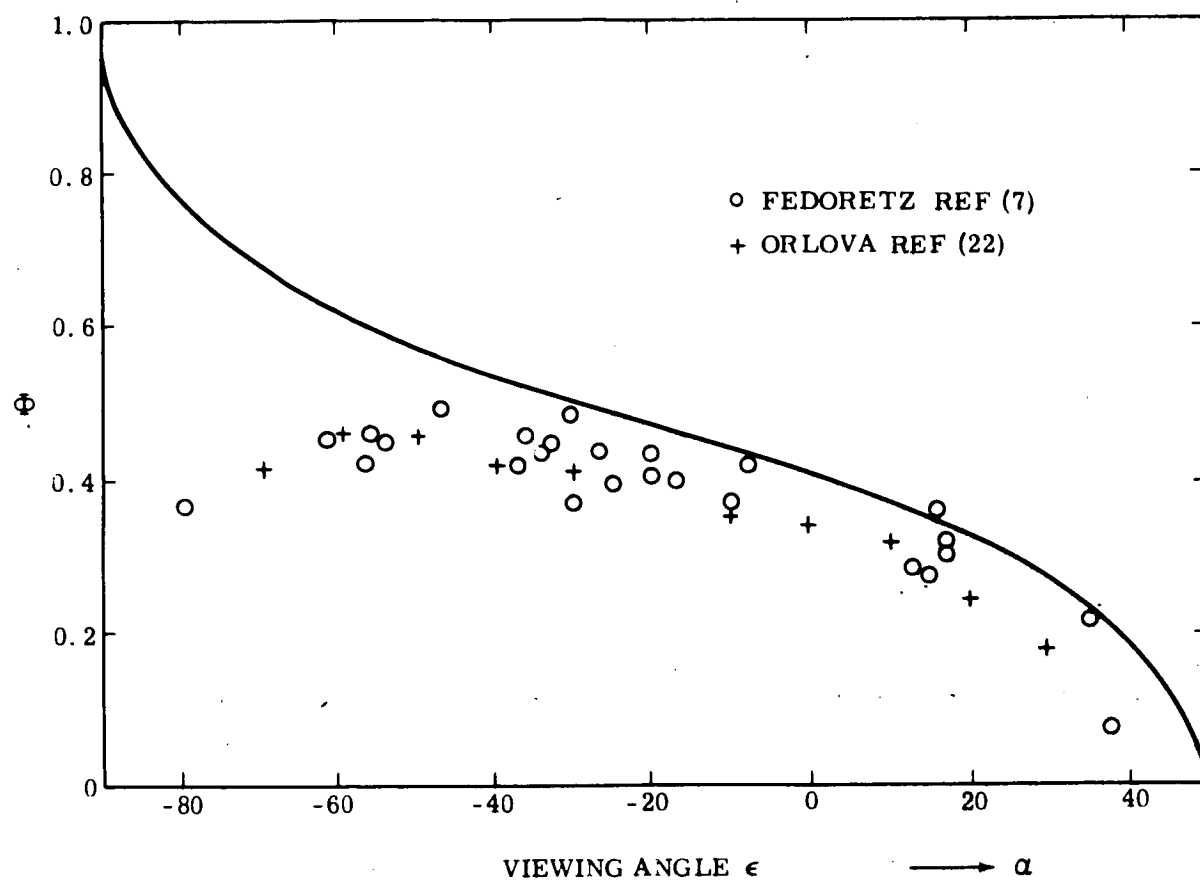
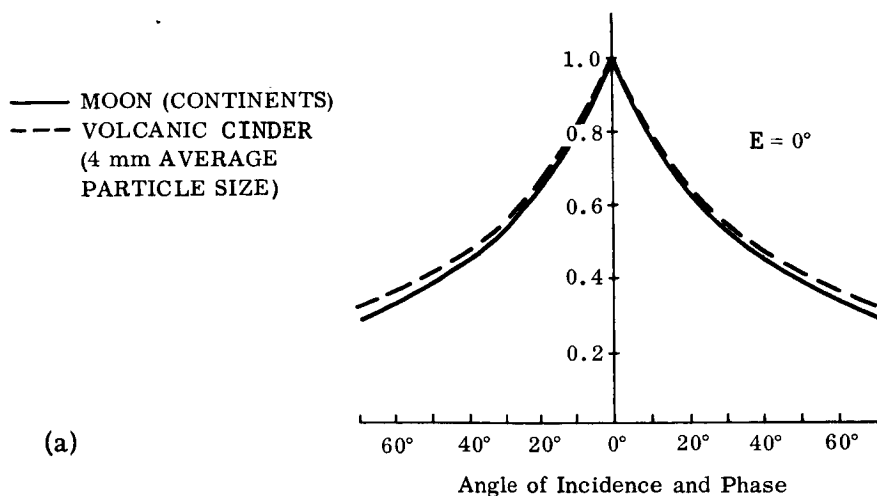
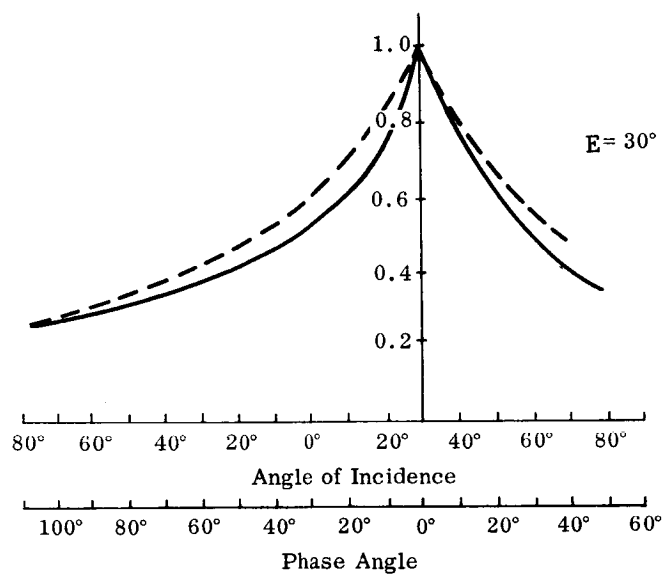


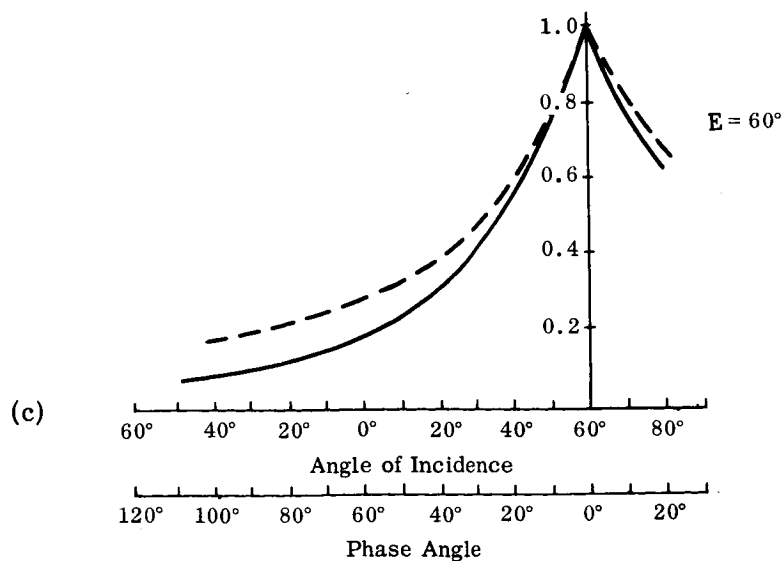
Figure 5. Hapke's Photometric Function ($p \approx 0.8$, $g \approx -40^\circ$). Ref (5).



(a)



(b)



(c)

Figure 6. Lutation Curves of the Moon and Volcanic Cinder. Ref (3).

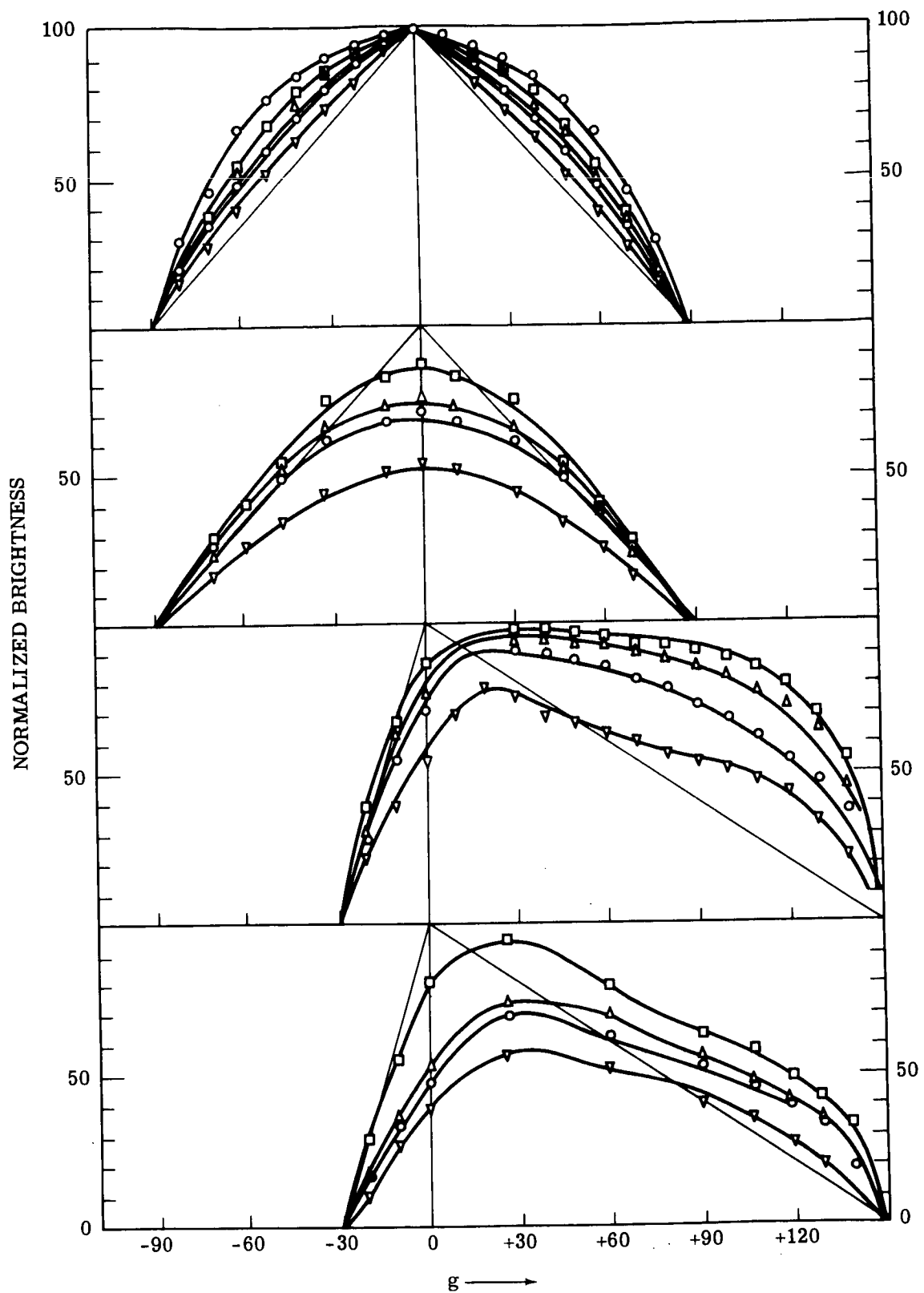


Figure 7. The Lunation Curves for Different Volcanic Cinders Ref (28).
(0.1 mm Average Particle Size)

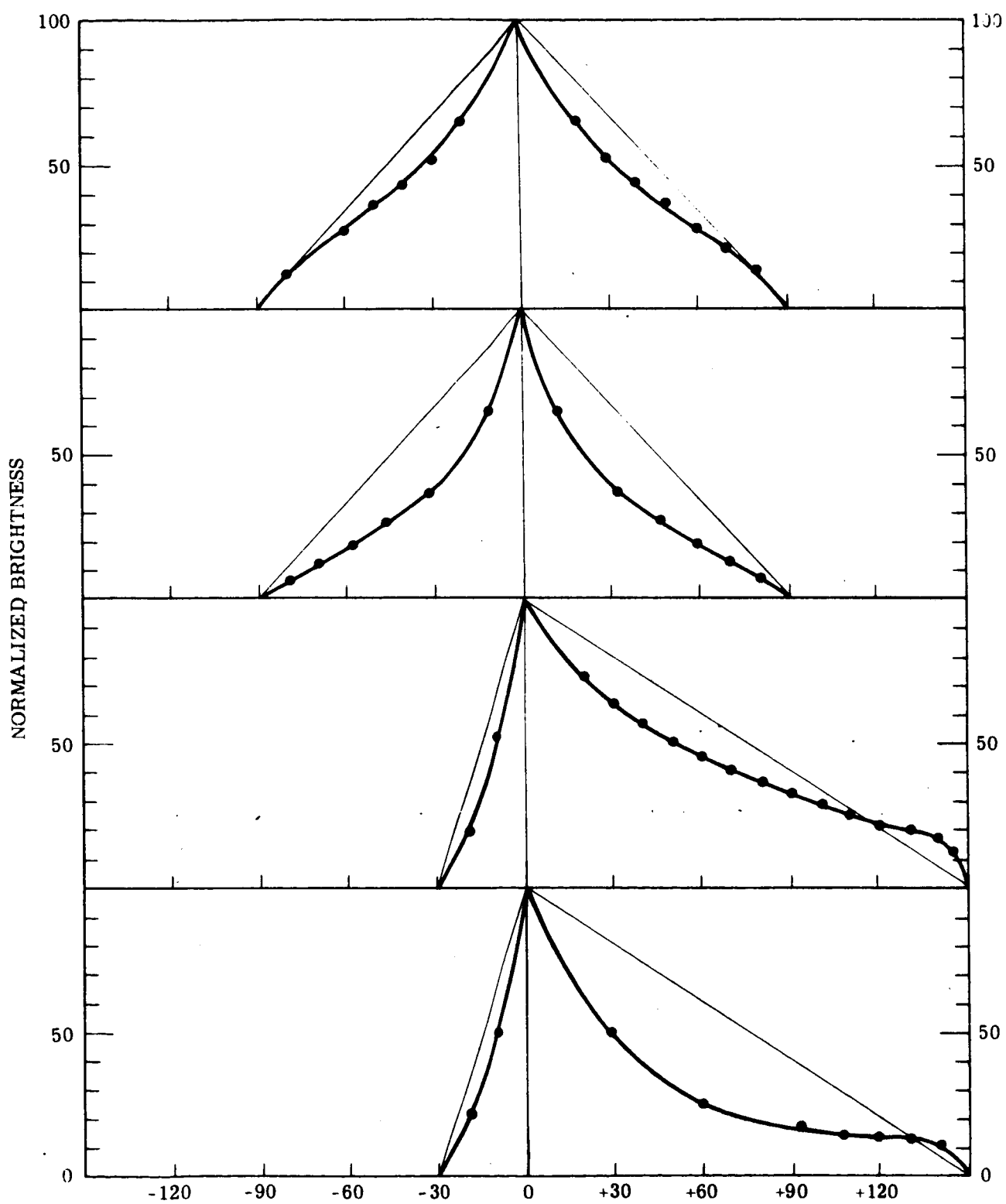


Figure 8. Lutation Curves of the Lichen *Cladonia Rangiferina*. Ref (28).

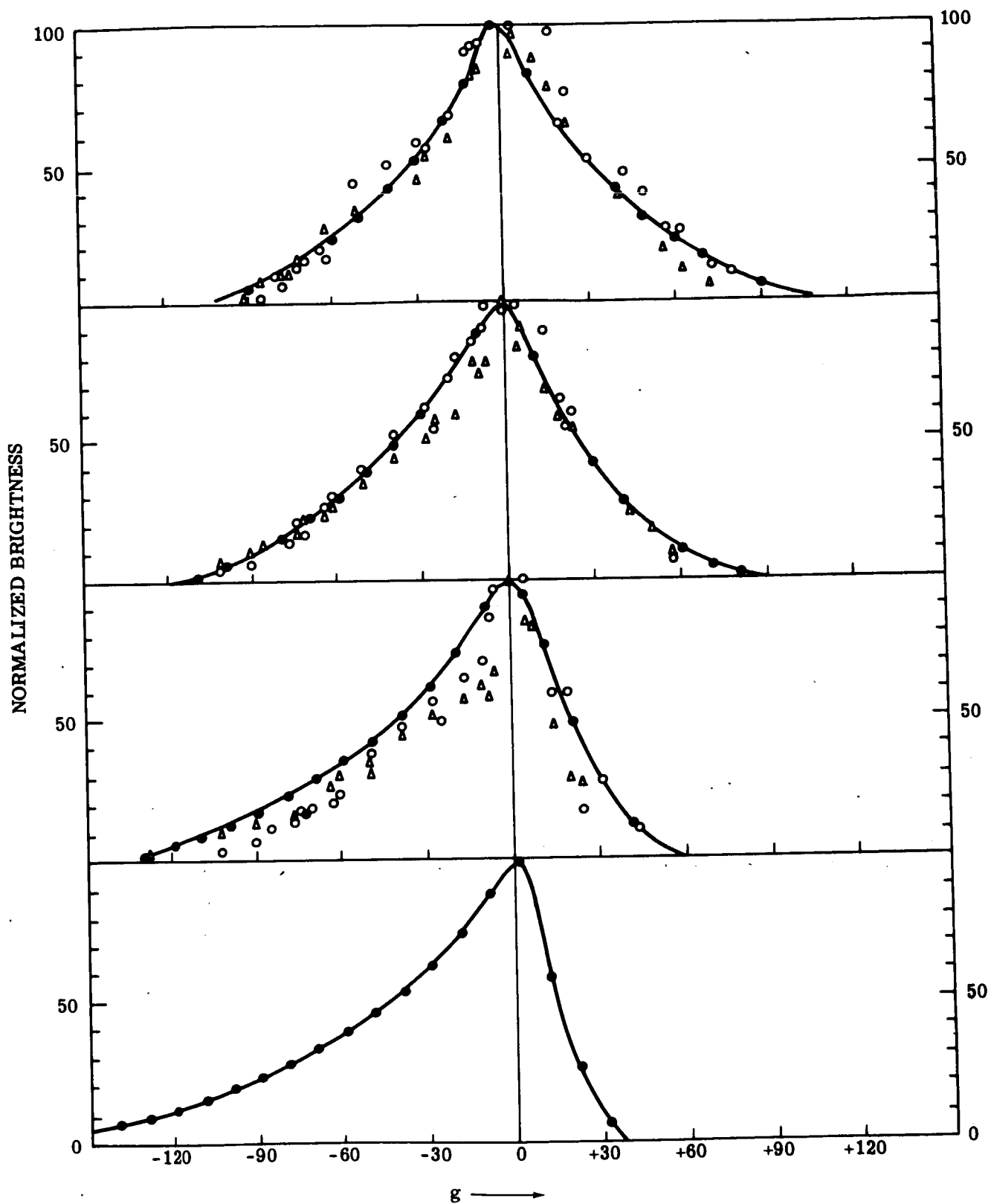


Figure 9. Van Diggelen's Mean Lutation Curves of Crater Floors for Four Different Crescents of Selenographic Longitude. Individual Plains (Δ) and Highlands (\circ) in the Same Crescent Are Measurements by Fedoretz. The Four Figures Are Related with:

- 1) Crescent λ 0 - 10, β 0 - 90
- 2) Crescent λ 10 - 30, β 0 - 90
- 3) Crescent λ 30 - 50, β 0 - 90
- 4) Crescent λ 50 - 90, β 0 - 90. Ref (28).

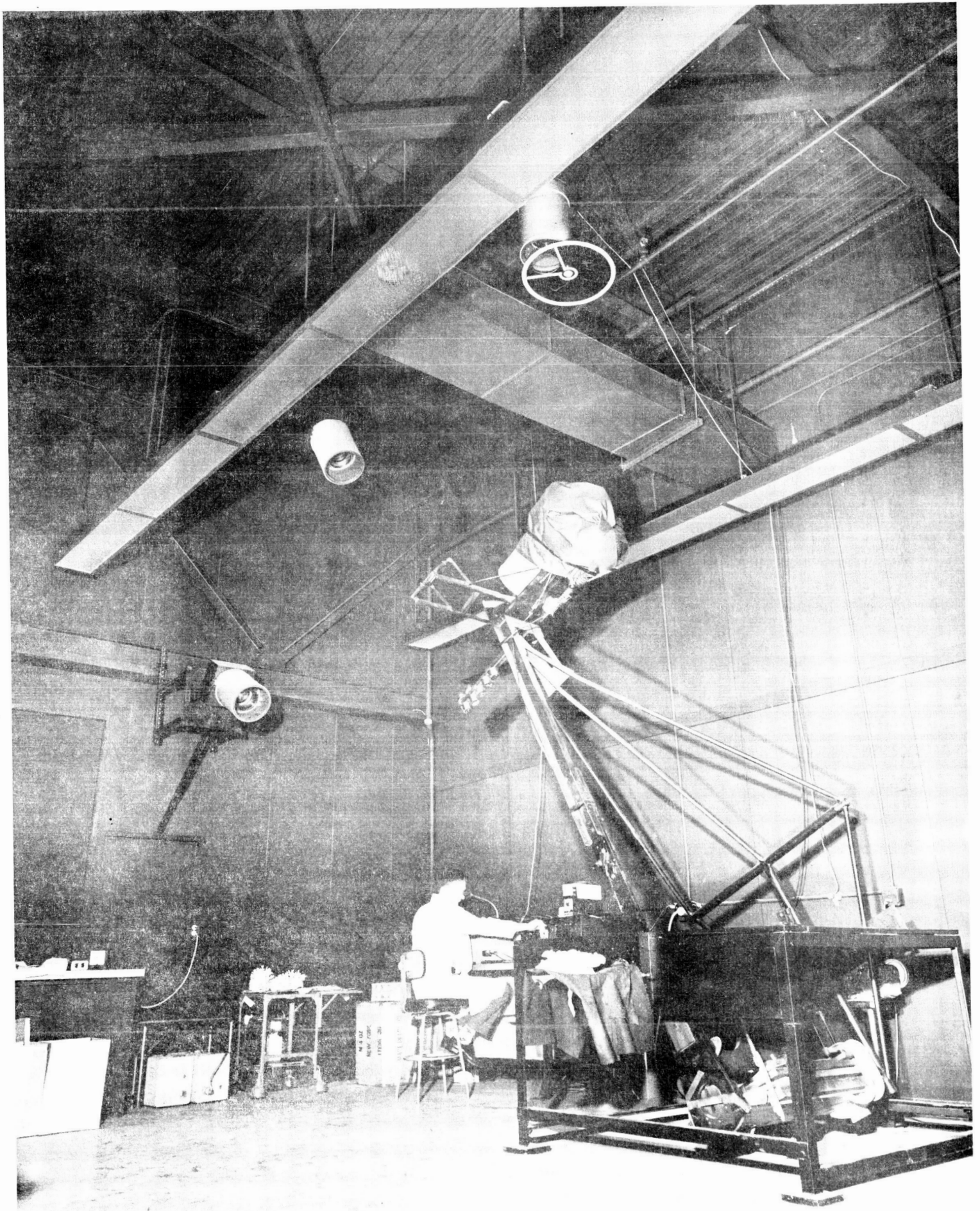


Fig. 10. Photograph of Grumman Photometric Analyzer

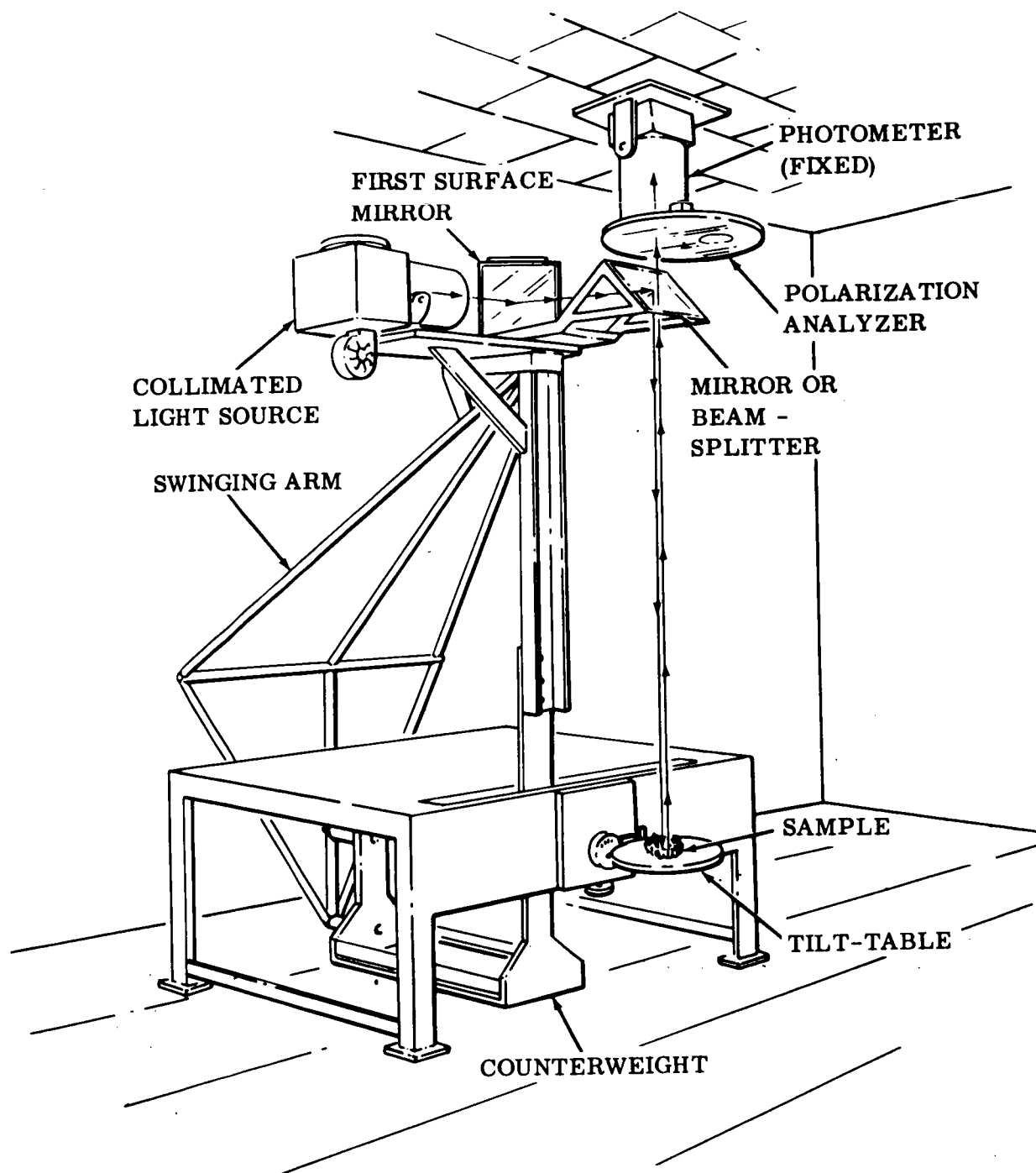


Figure 11. Sketch of Grumman Photometric Analyzer
(30° & 60° Photometers Not Shown)

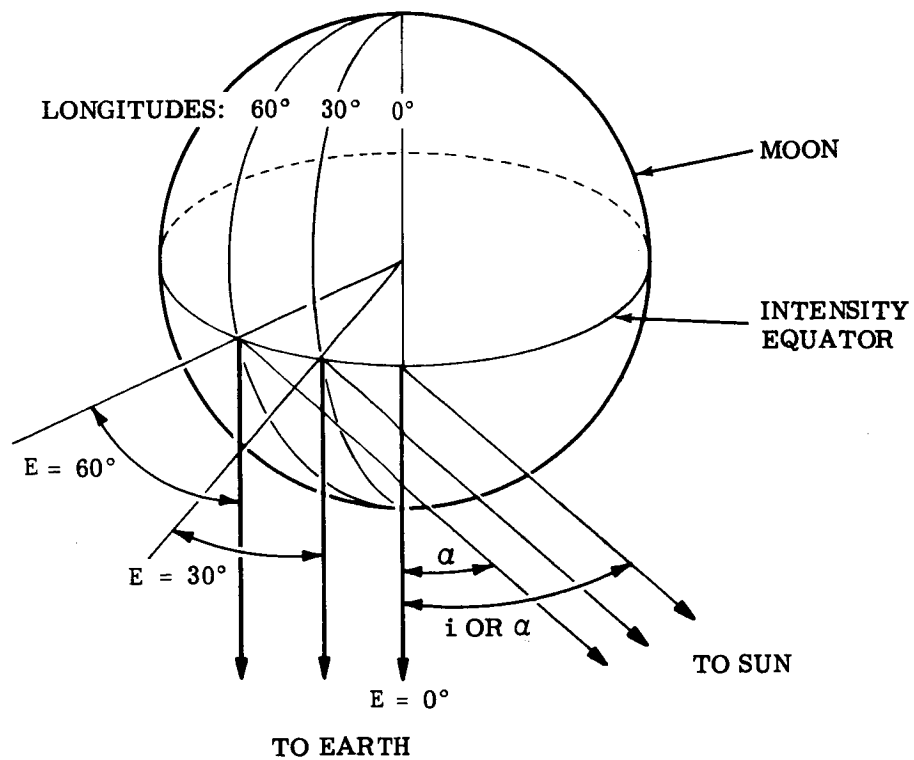


Figure 12. Viewing and Illumination Geometry at the Lunar Intensity Equator

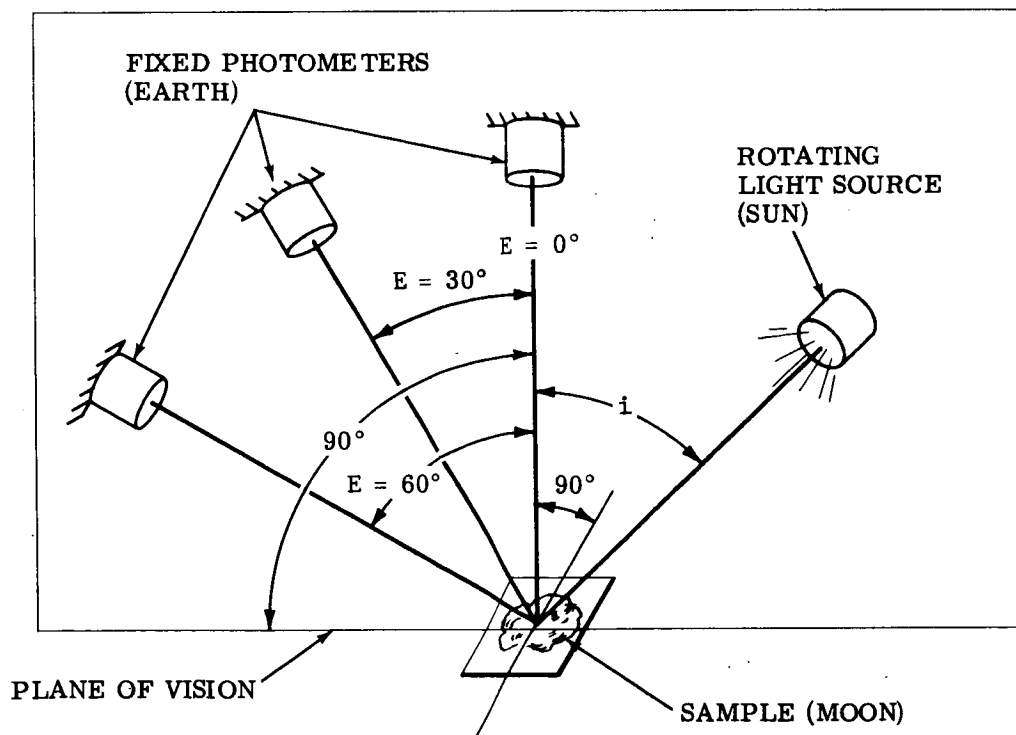
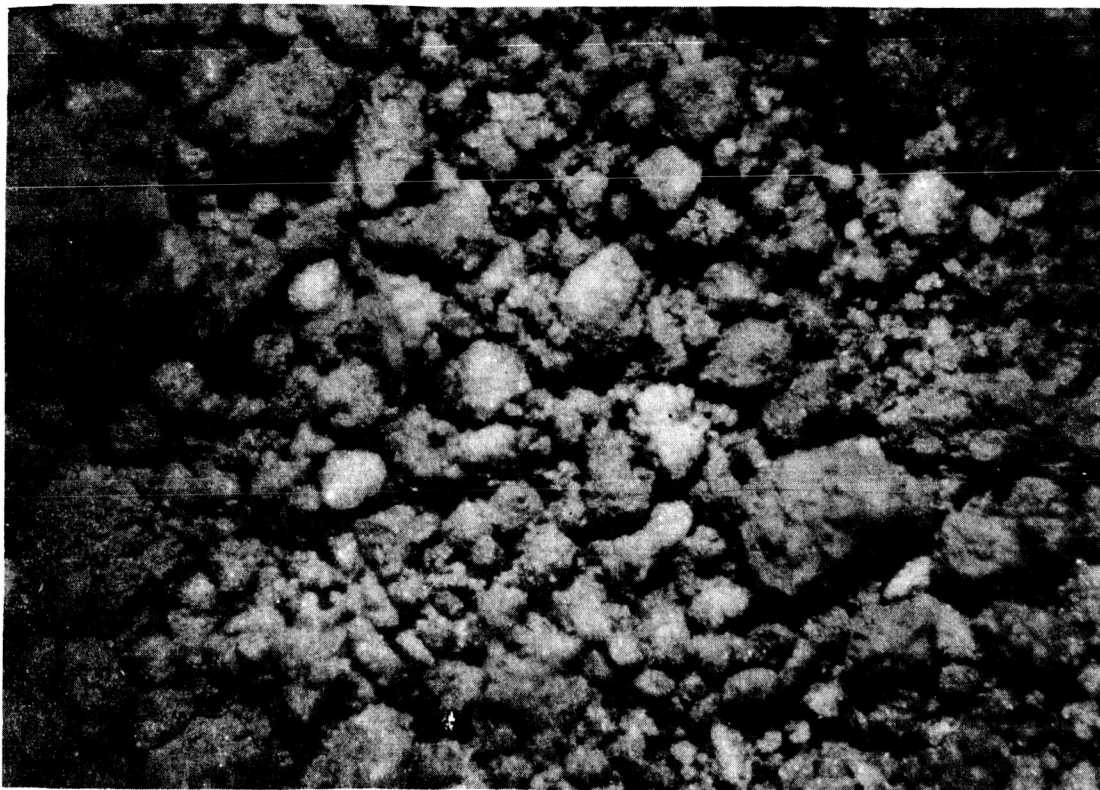
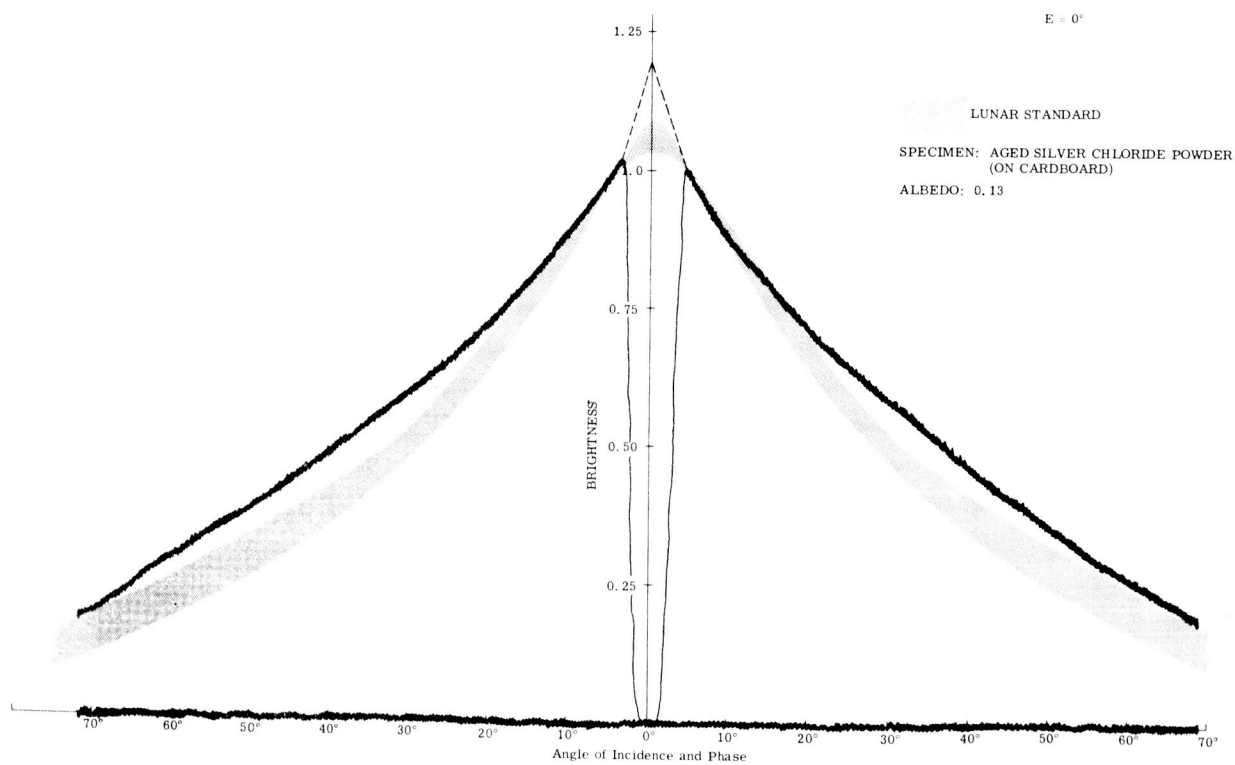


Figure 13. Laboratory Simulation of Sun-Moon-Earth Optical Relationship (Intensity Equator and Phase Angle are in Plane of Vision)

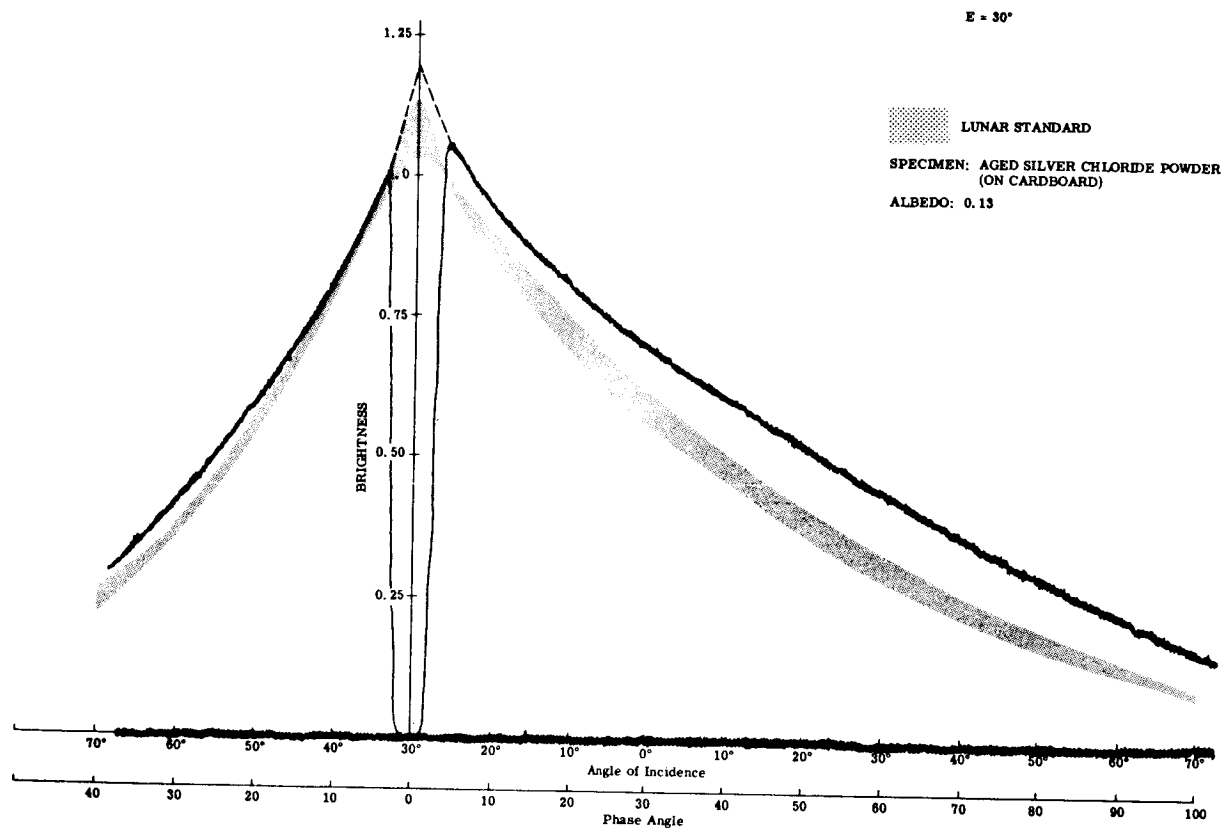


(a) Magnified 25X

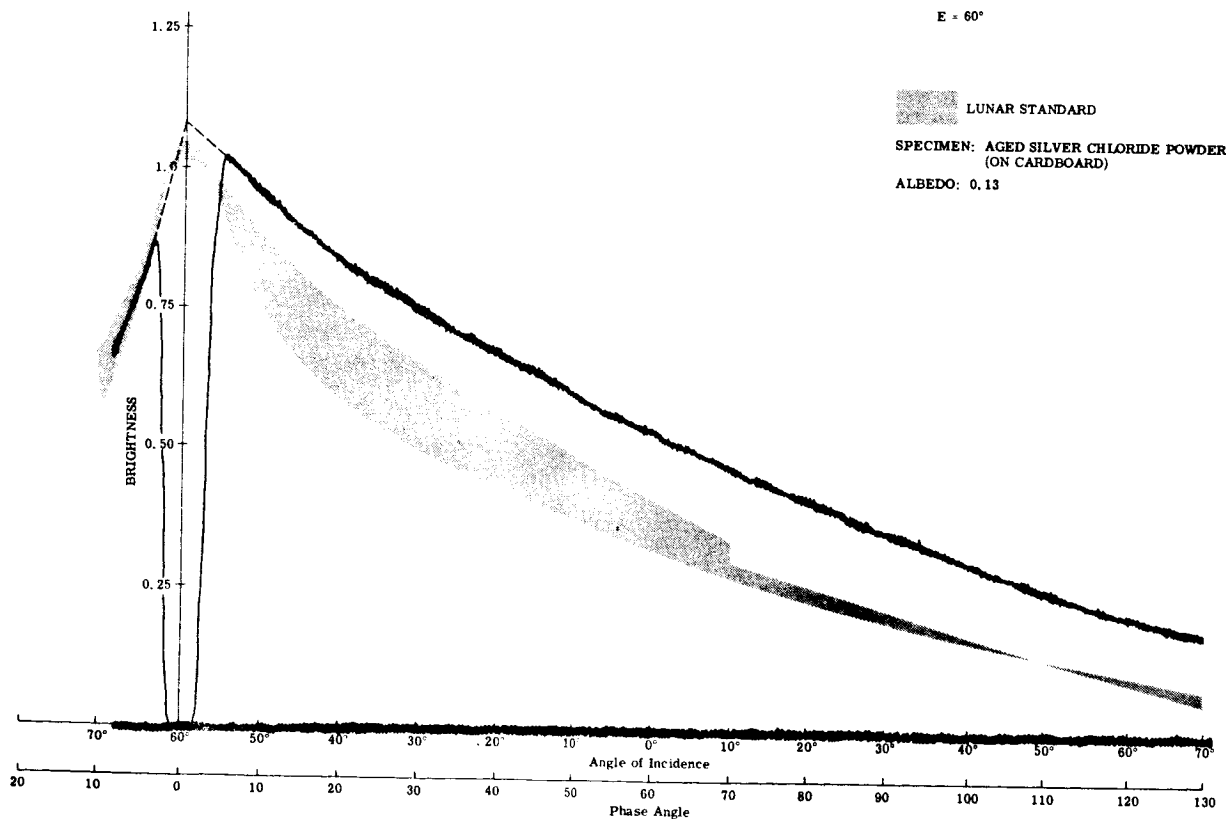


(b)

Figure 14. Aged Silver Chloride Powder (Sheet 1 of 2)

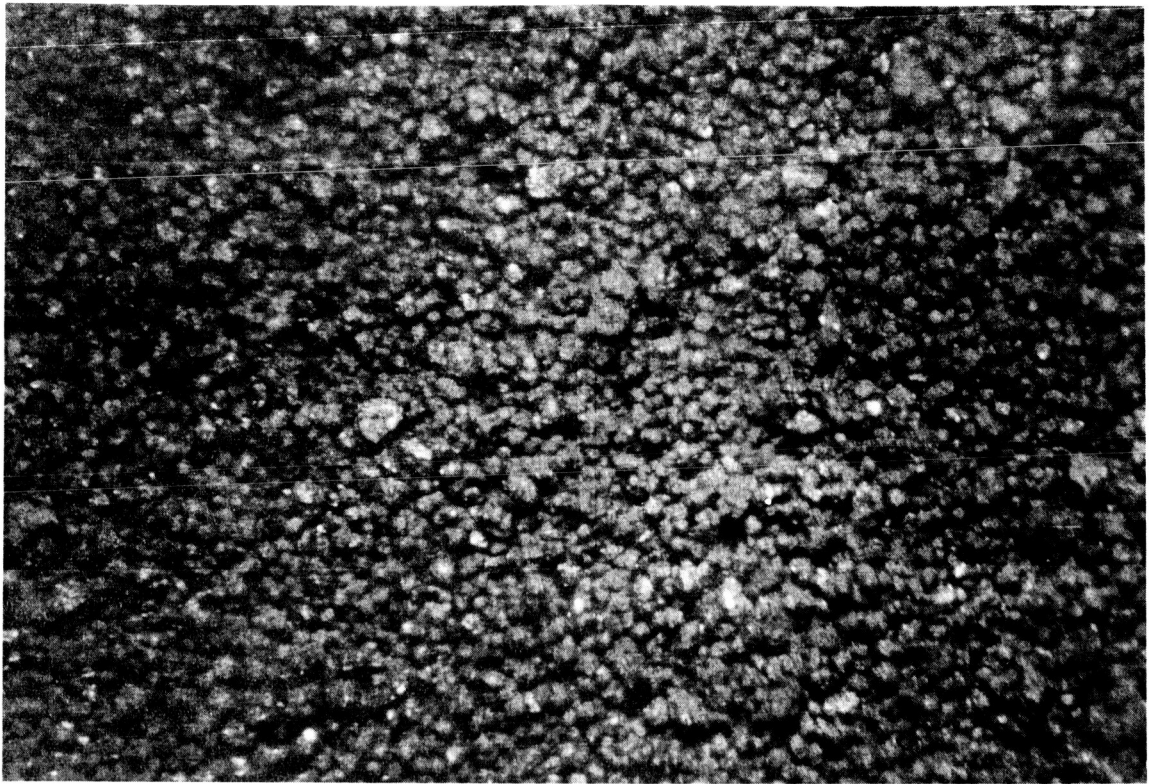


(c)



(d)

Figure 14. Aged Silver Chloride Powder (Sheet 2 of 2)



(a) Magnified 25X

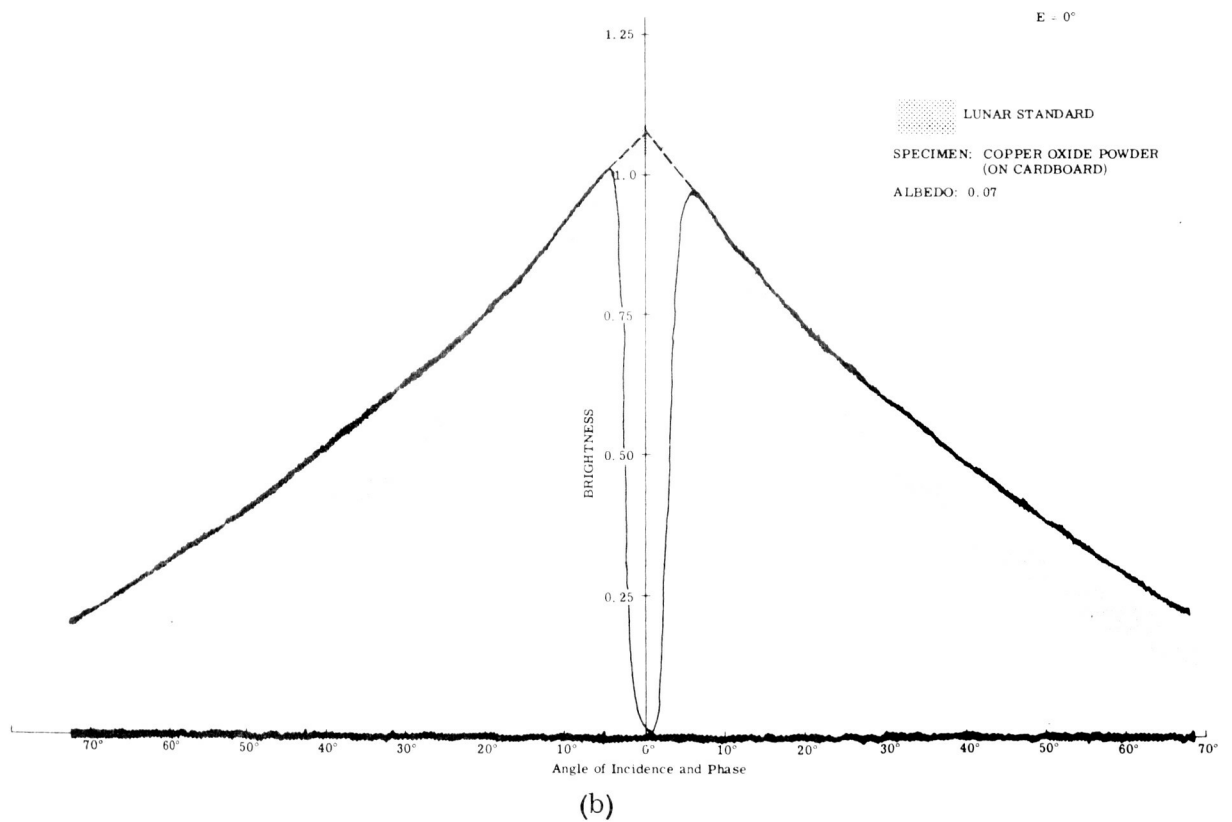


Figure 15. Copper Oxide Powder (Sheet 1 of 2)

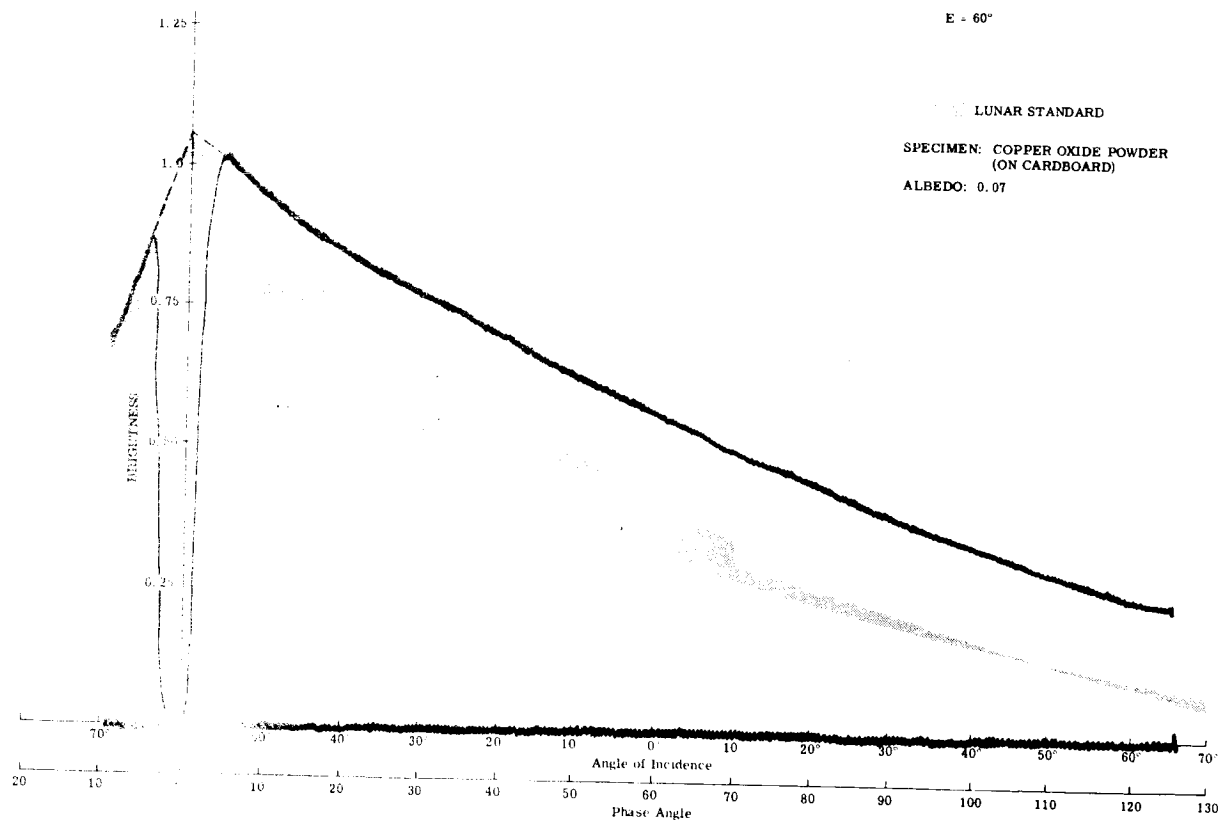
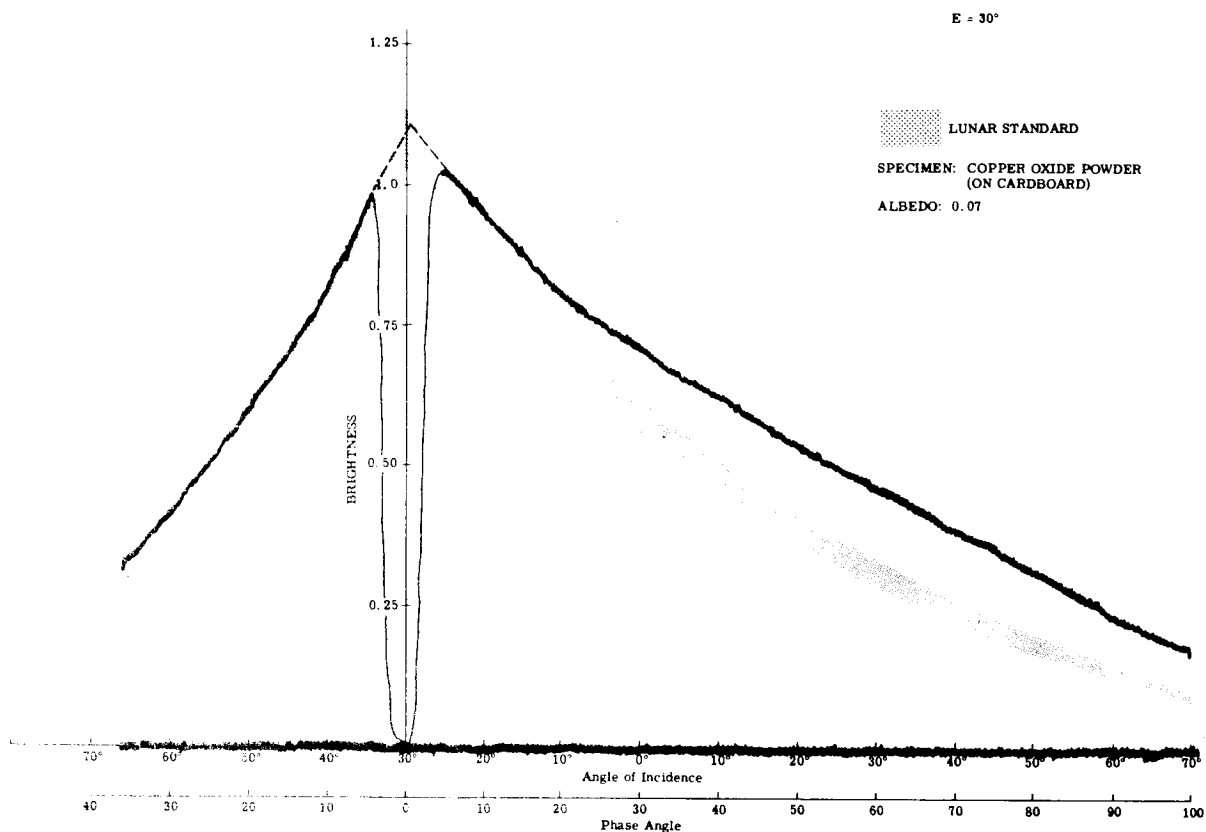
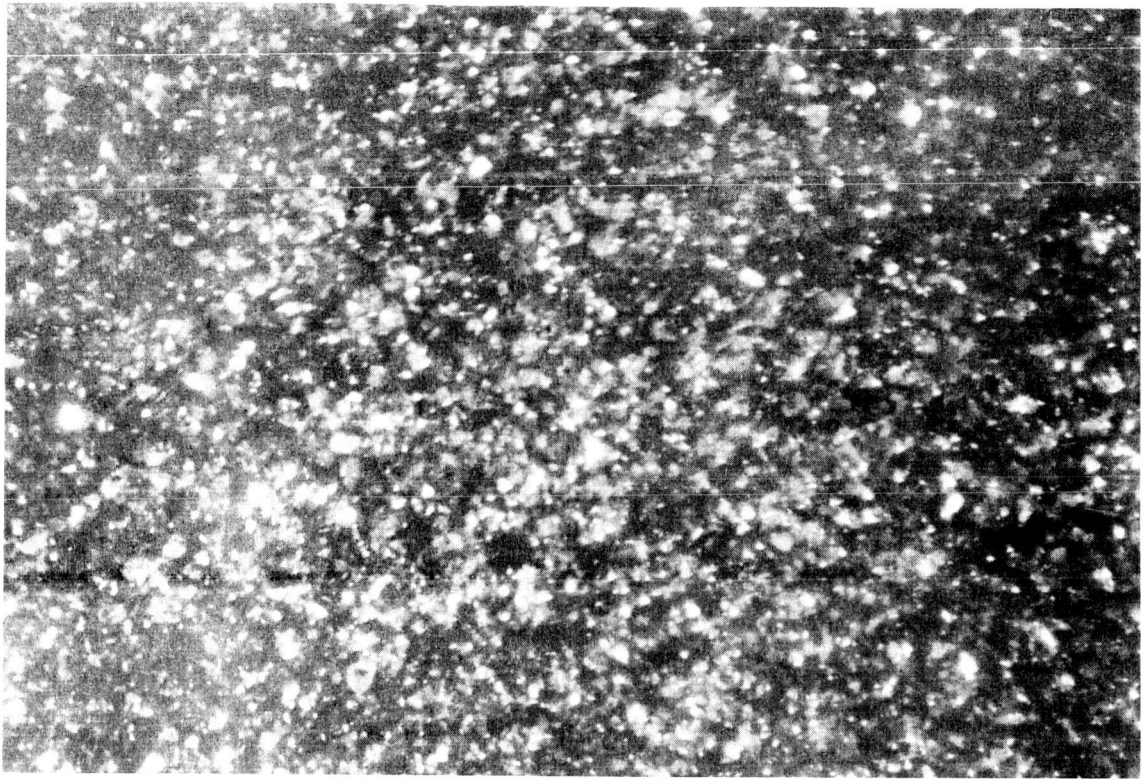
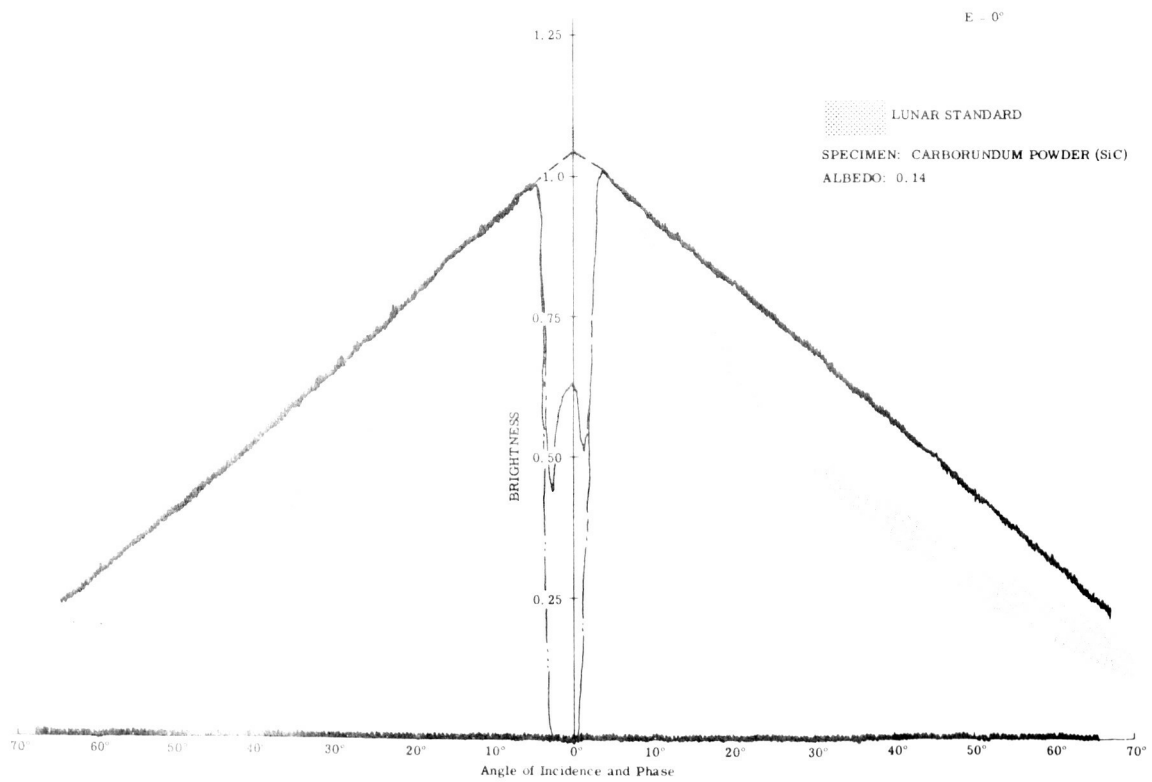


Figure 15. Copper Oxide Powder (Sheet 2 of 2)



(a) Magnified 25X



(b)

Figure 16. Carborundum Powder (Sheet 1 of 2)

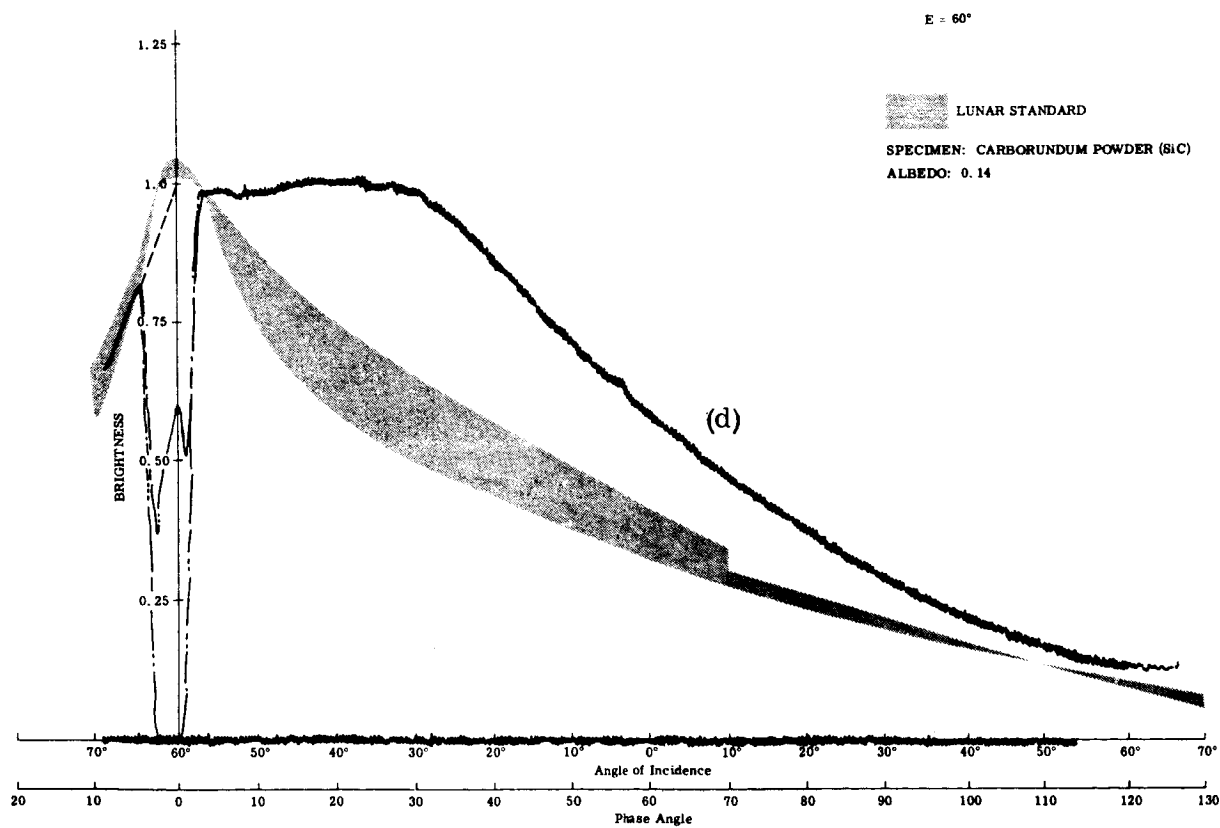
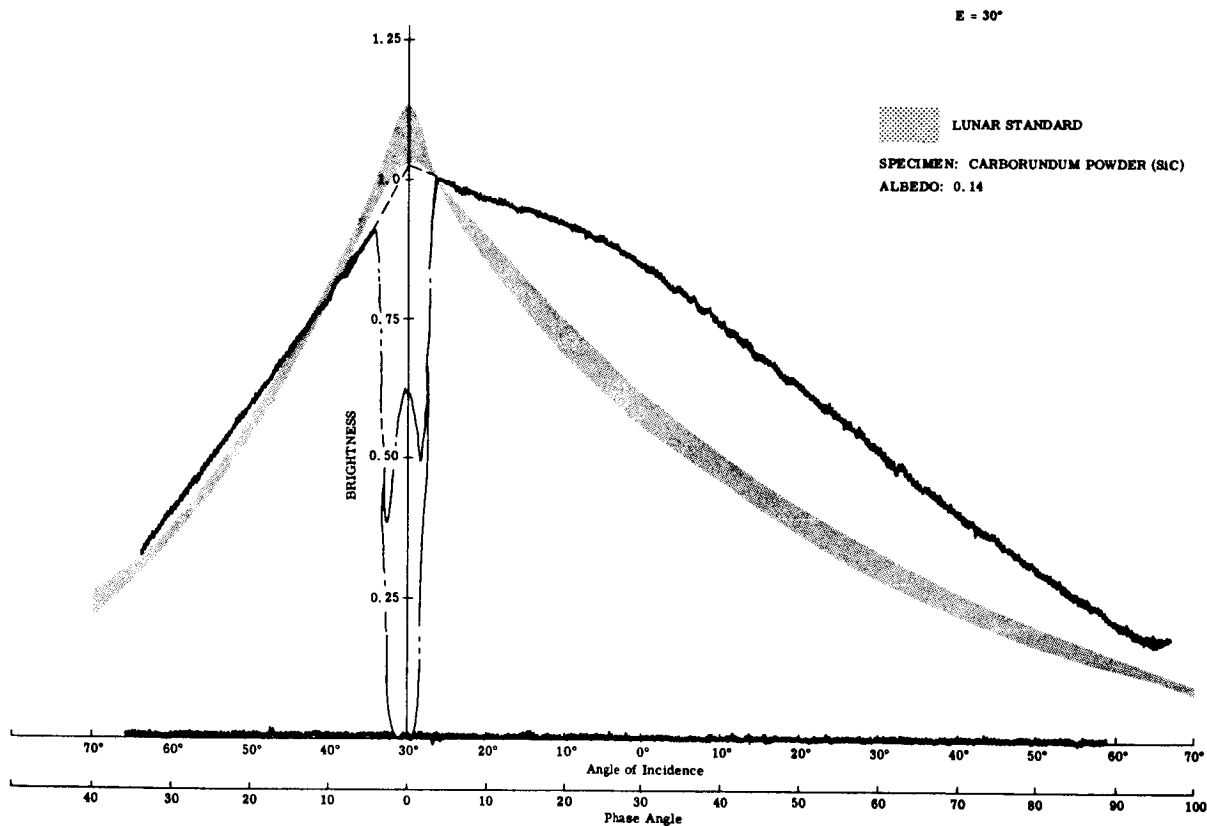
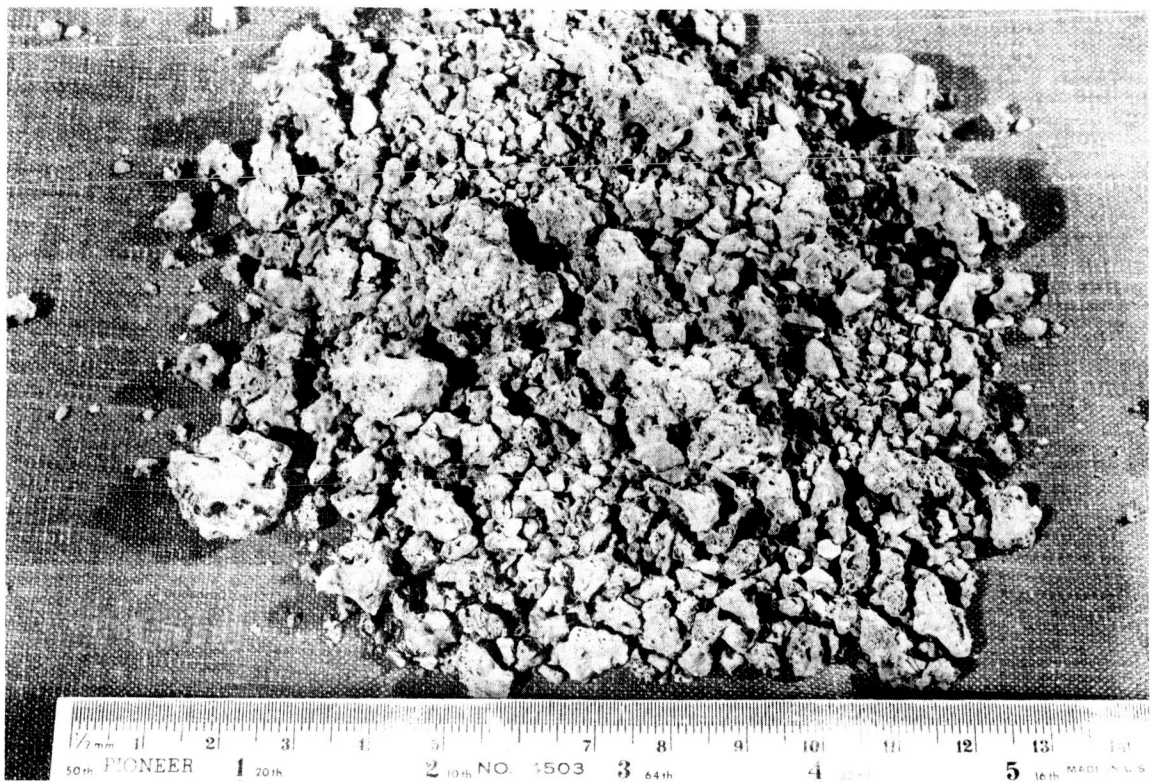
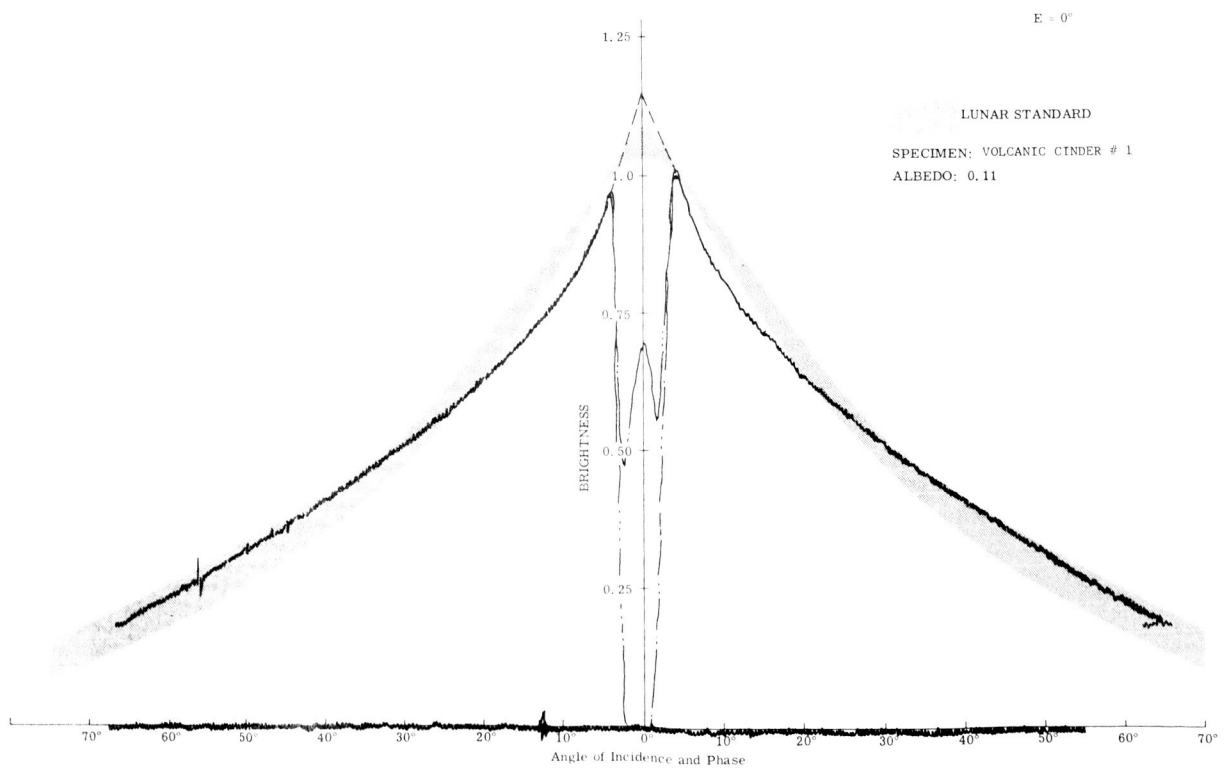


Figure 16. Carborundum Powder (Sheet 2 of 2)

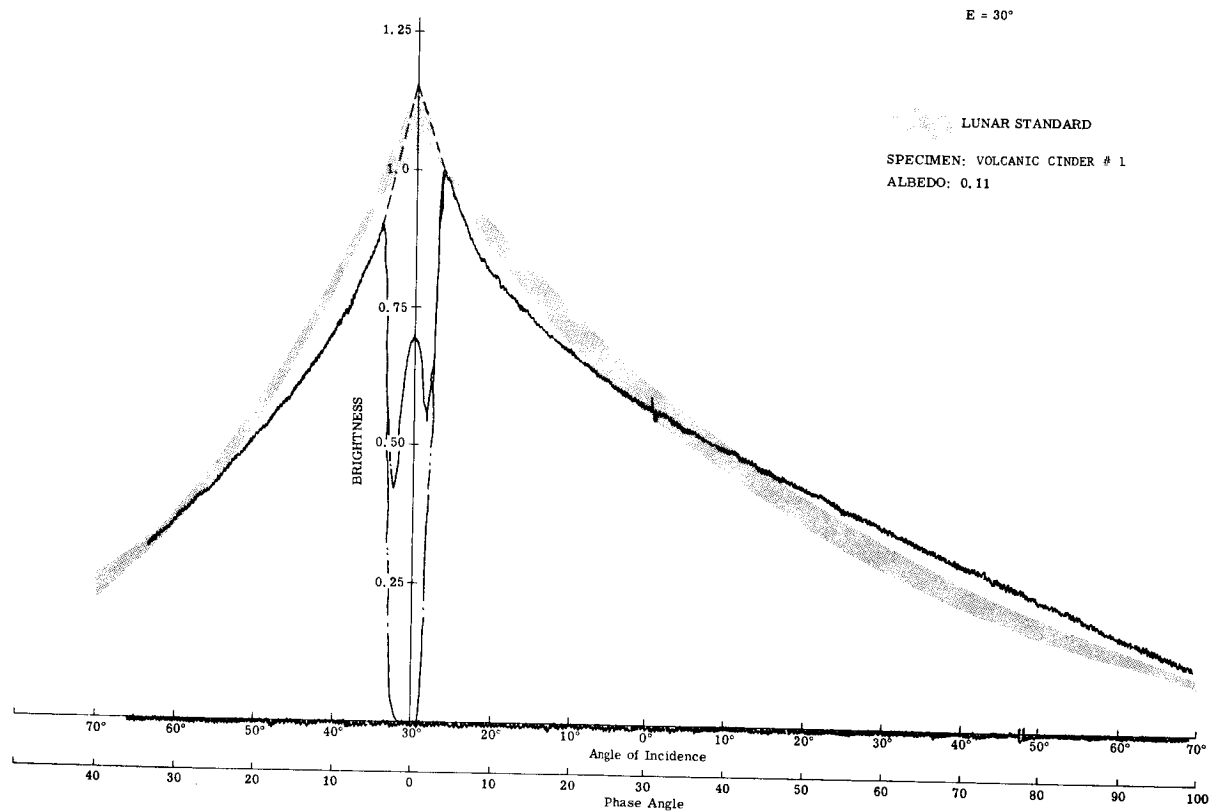


(a)

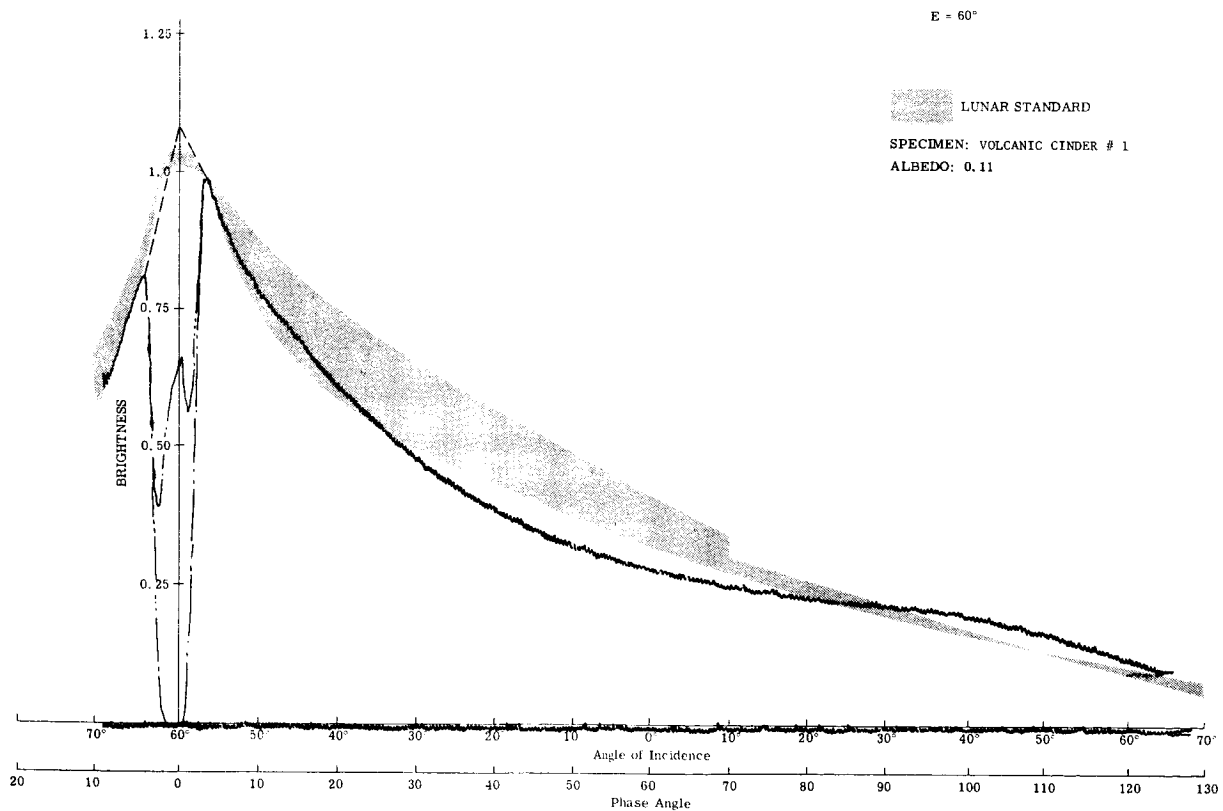


(b)

Figure 17. Volcanic Cinder #1 (Sheet 1 of 2)

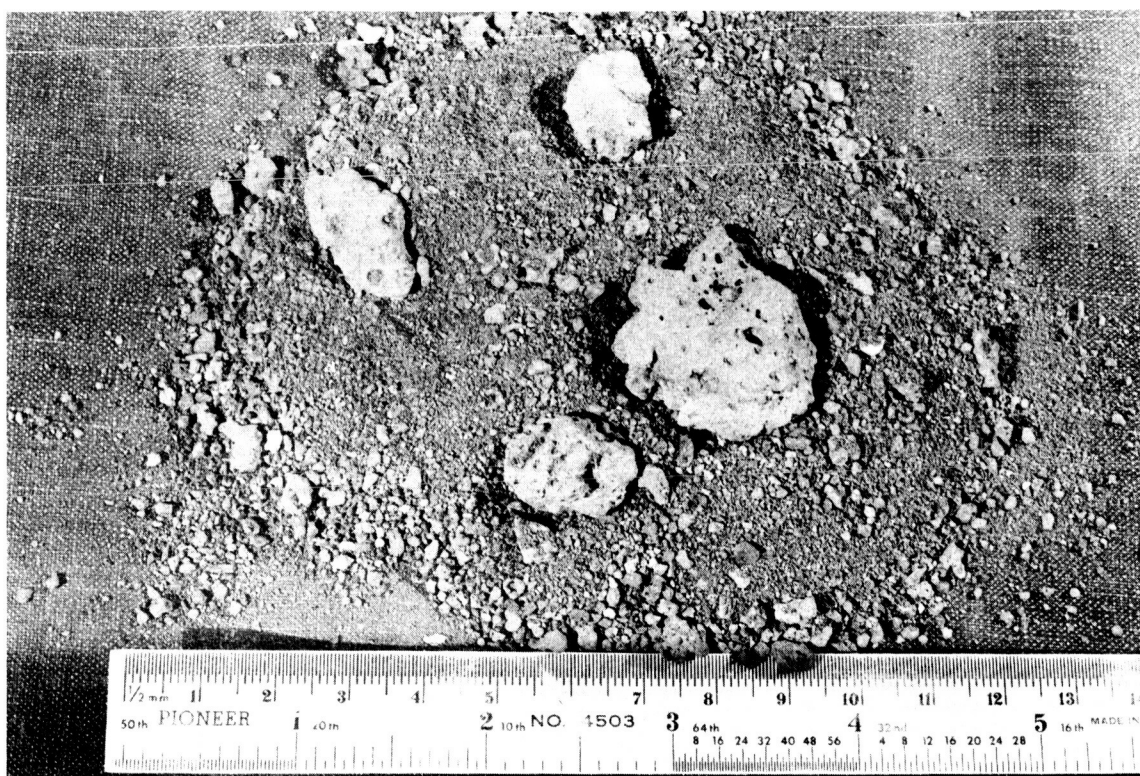


(c)

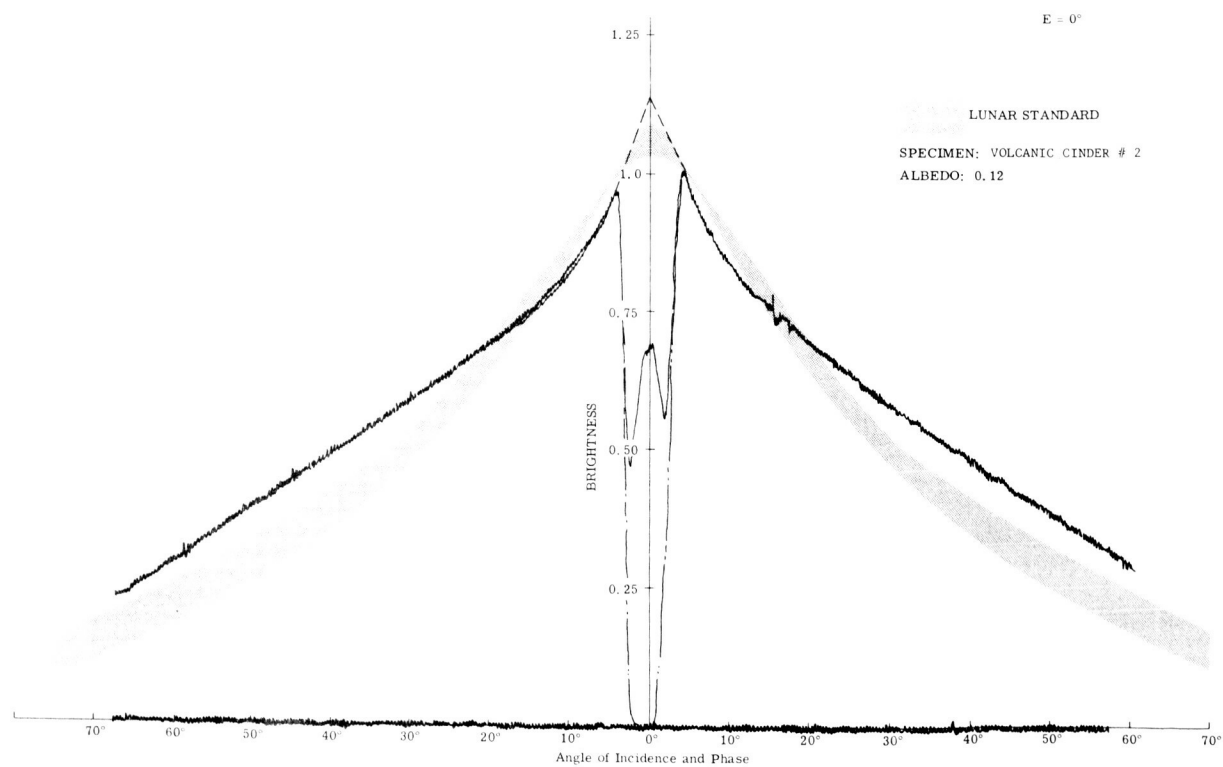


(d)

Figure 17. Volcanic Cinder #1 (Sheet 2 of 2)

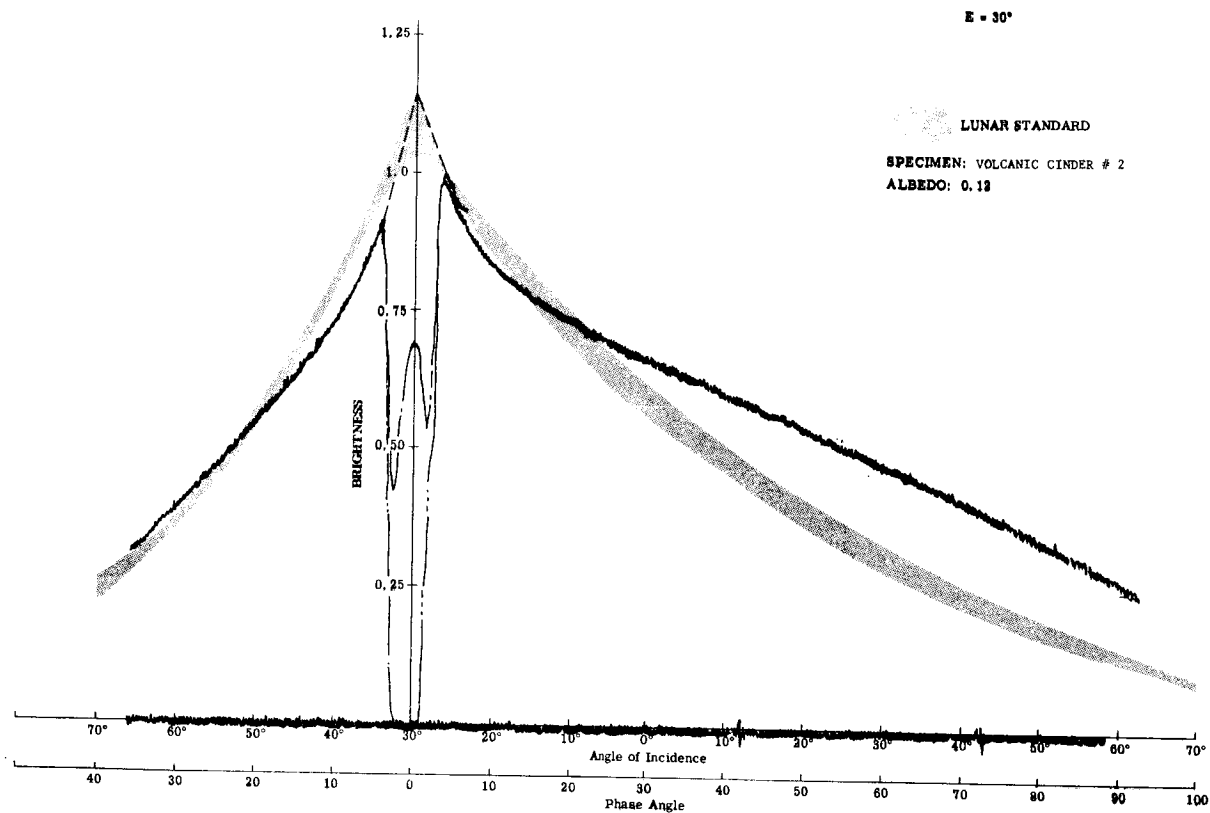


(a)

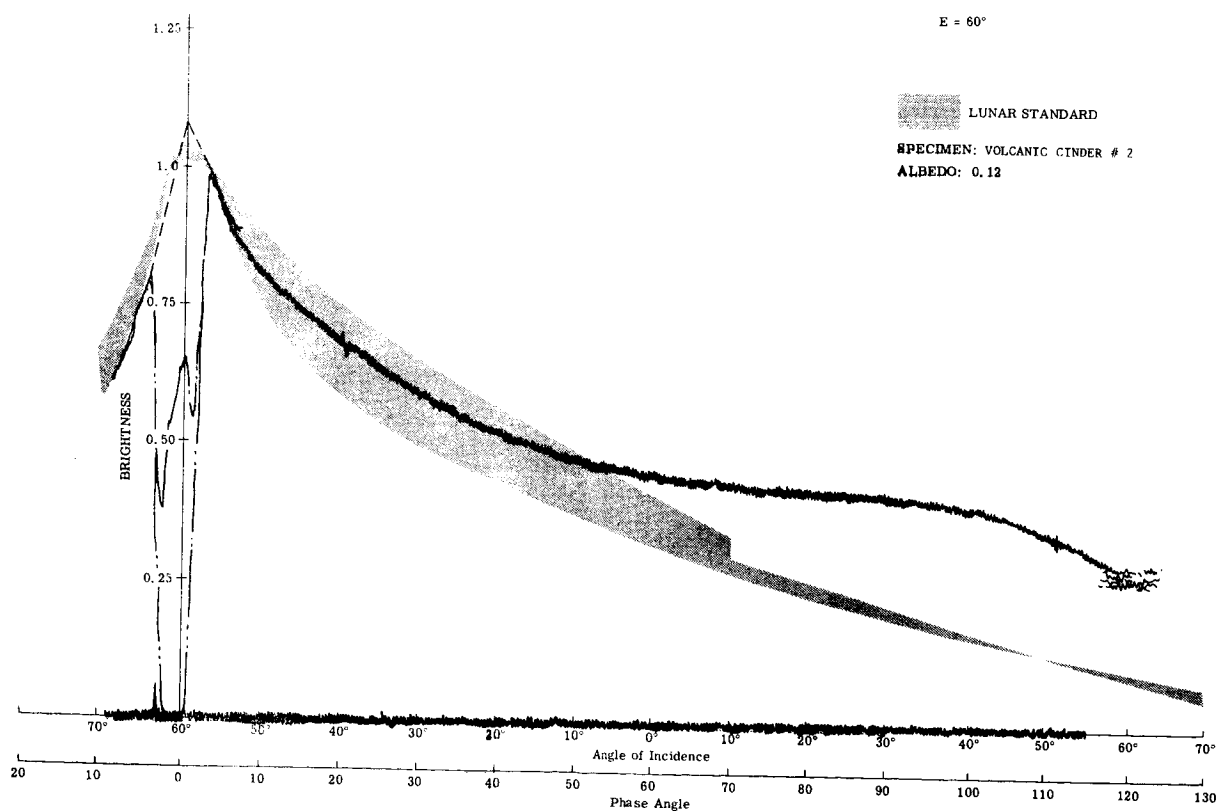


(b)

Figure 18. Volcanic Cinder #2 (Sheet 1 of 2)

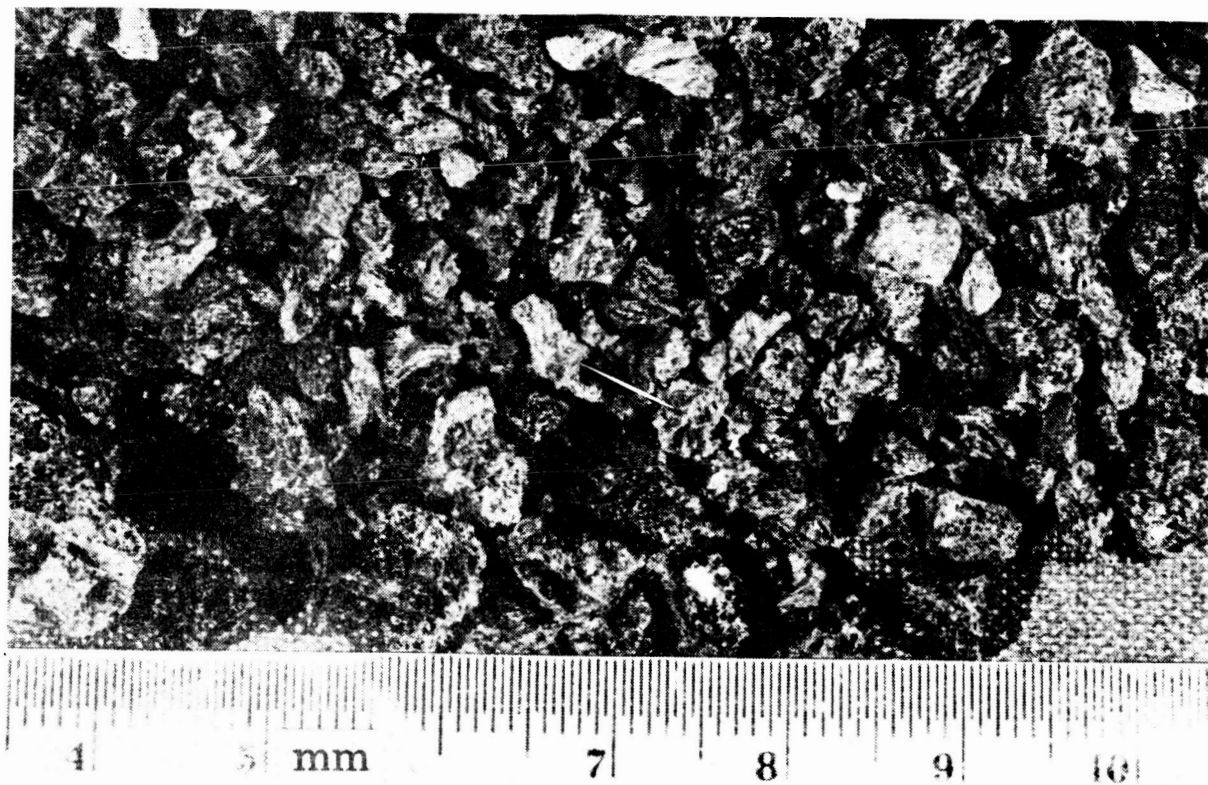


(c)

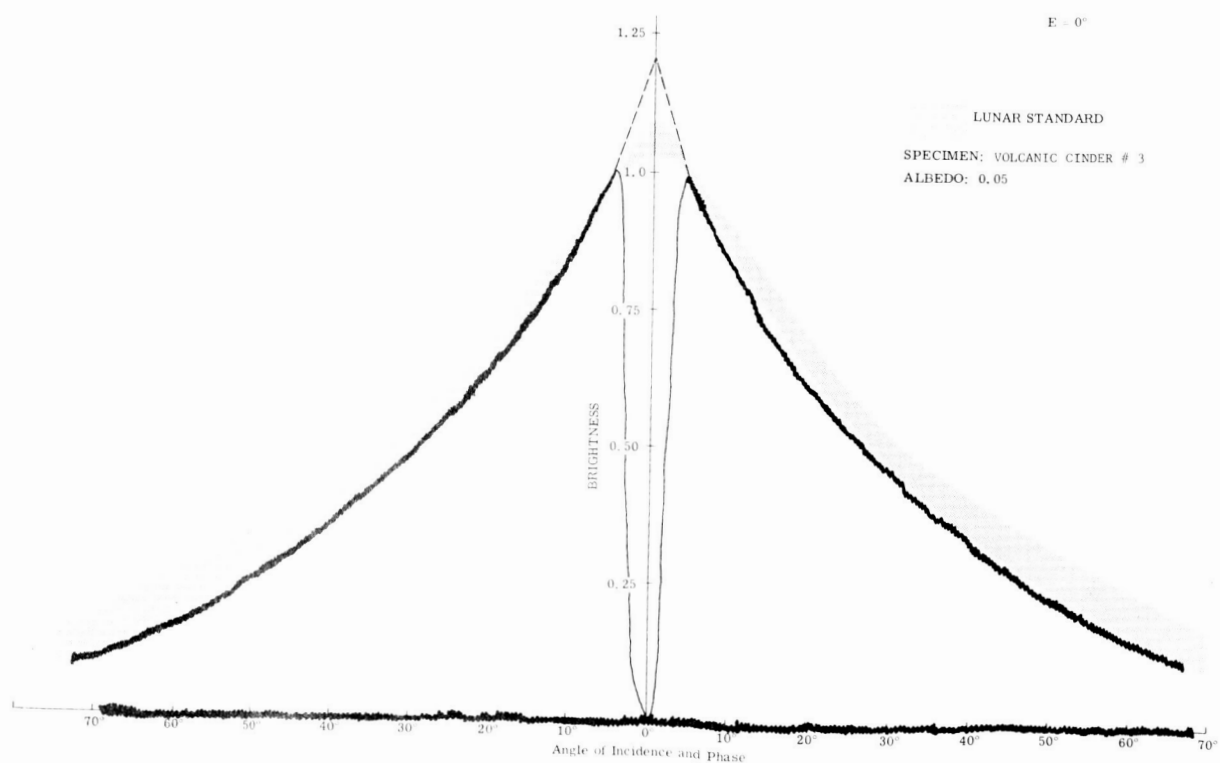


(d)

Figure 18. Volcanic Cinder #2 (Sheet 2 of 2)



(a)



(b)

Figure 19. Volcanic Cinder #3 (Sheet 1 of 2)

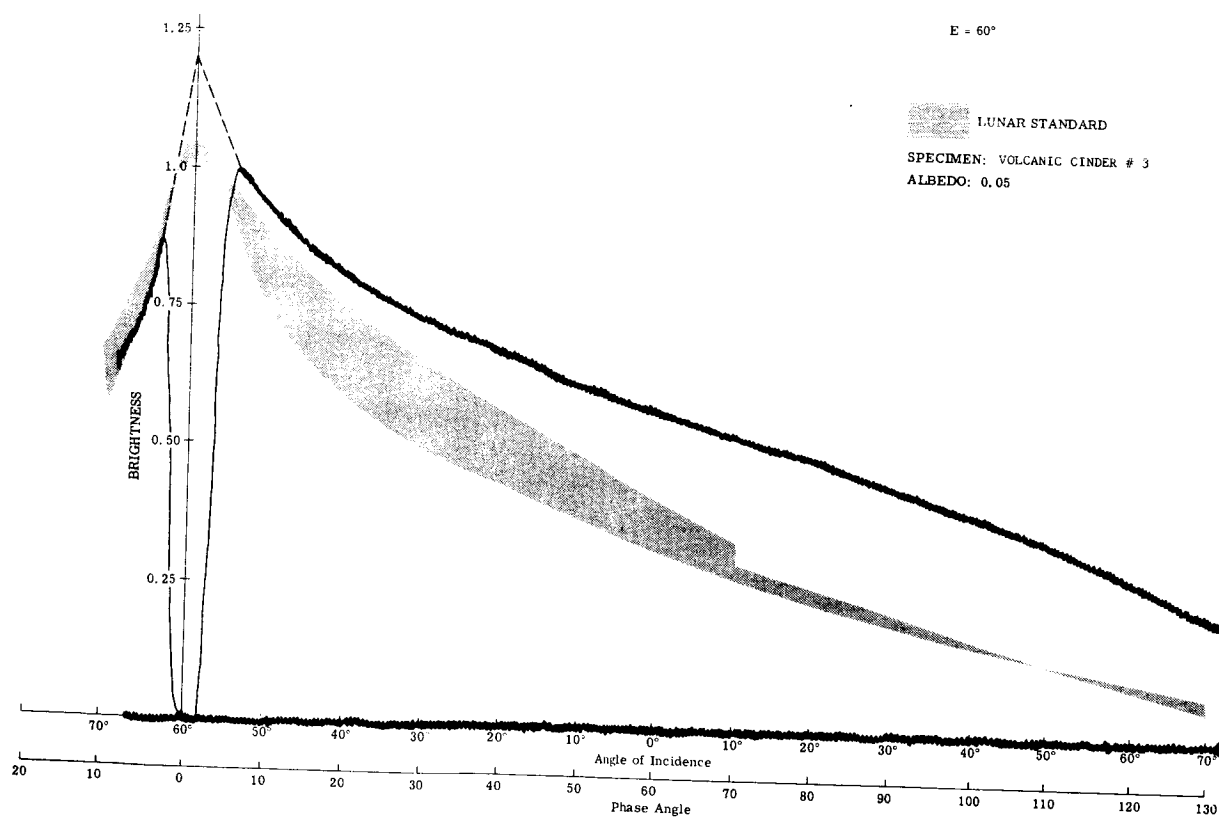
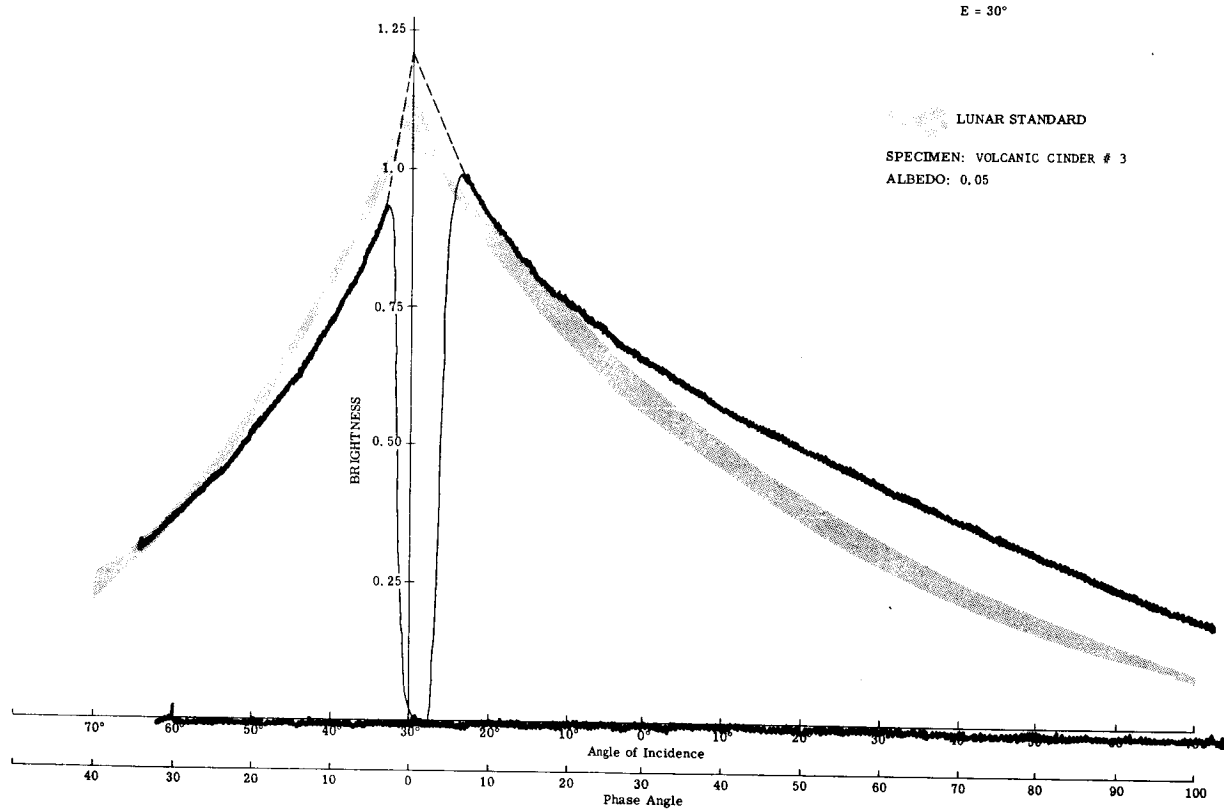
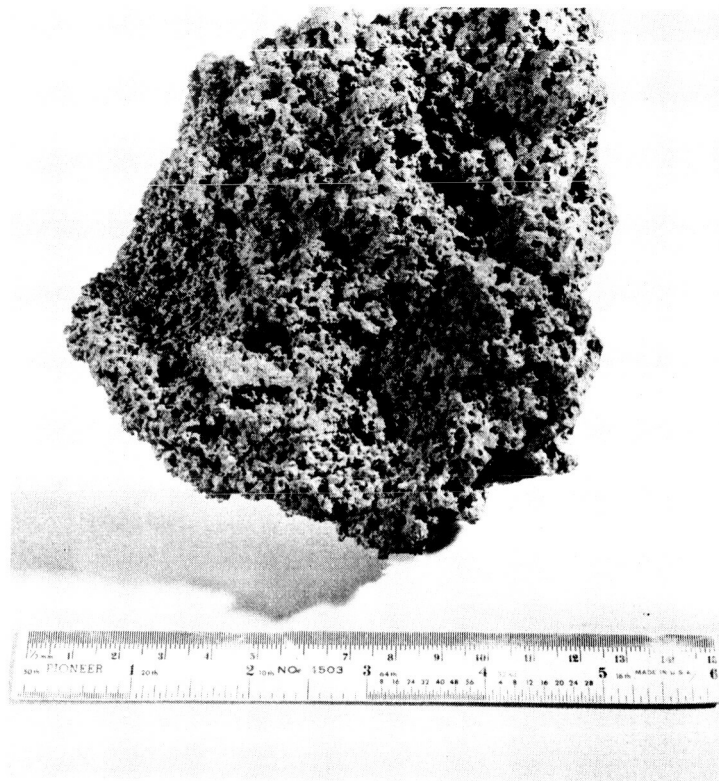
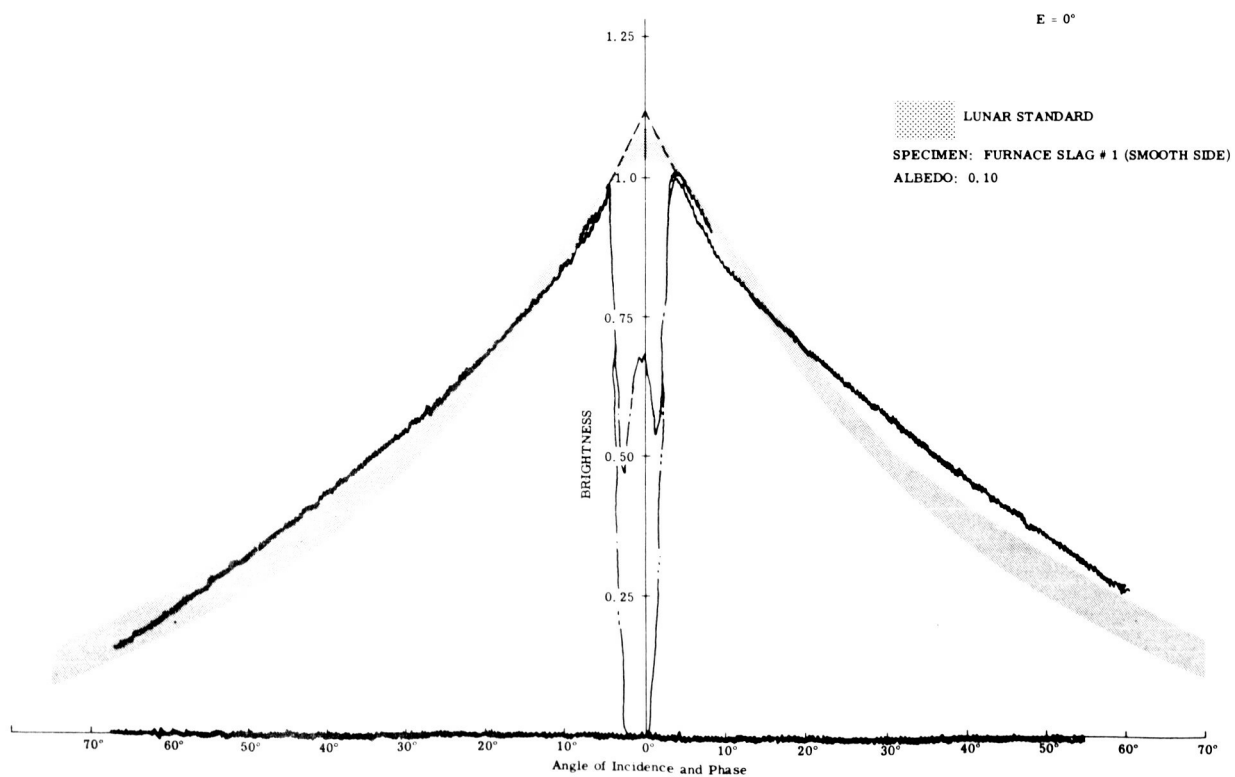


Figure 19. Volcanic Cinder #3 (Sheet 2 of 2)



(a)



(b)

Figure 20. Furnace Slag #1 (Sheet 1 of 2)

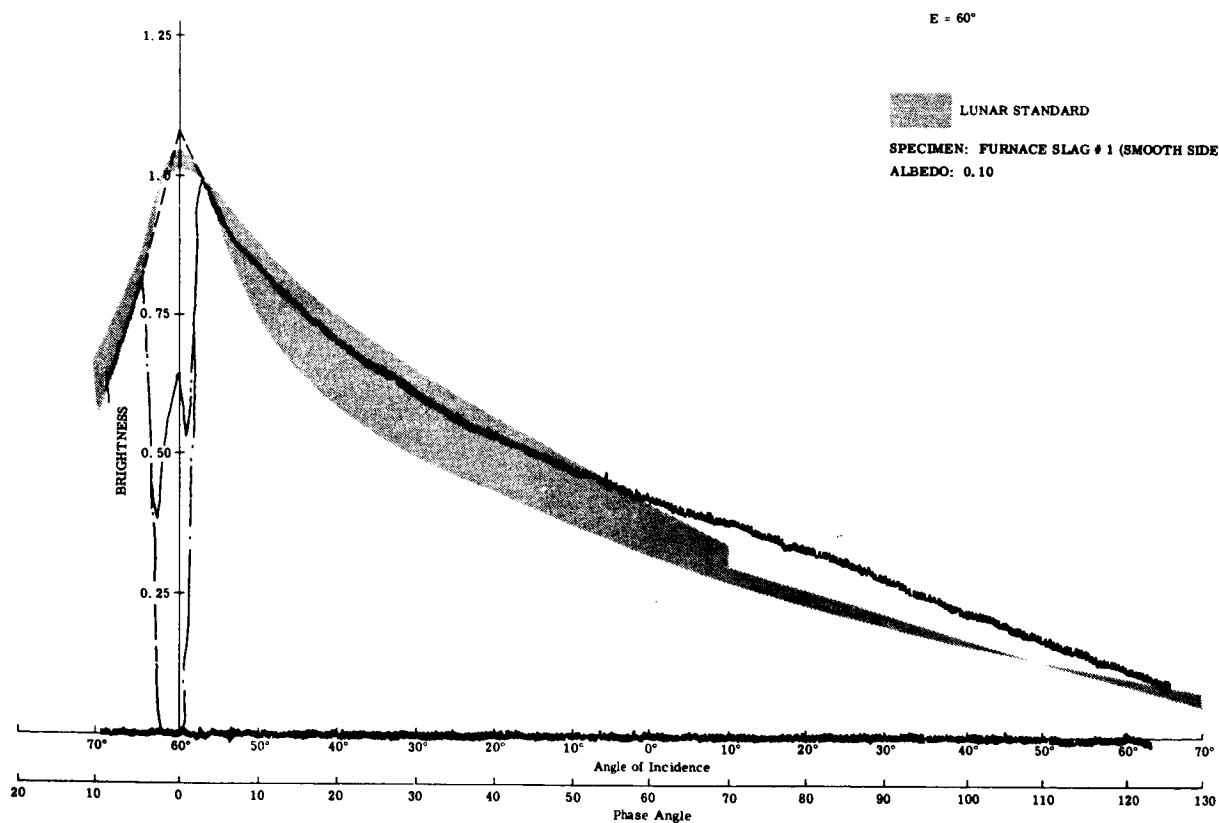
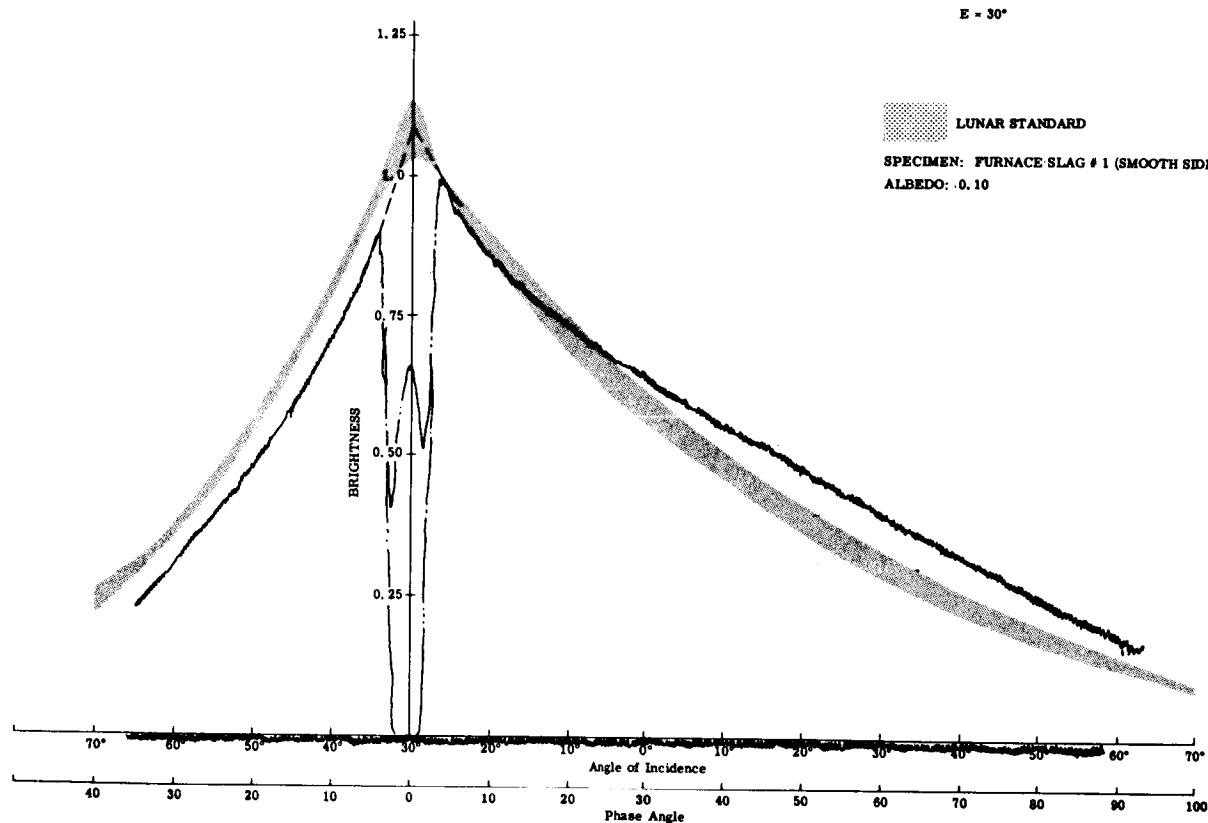
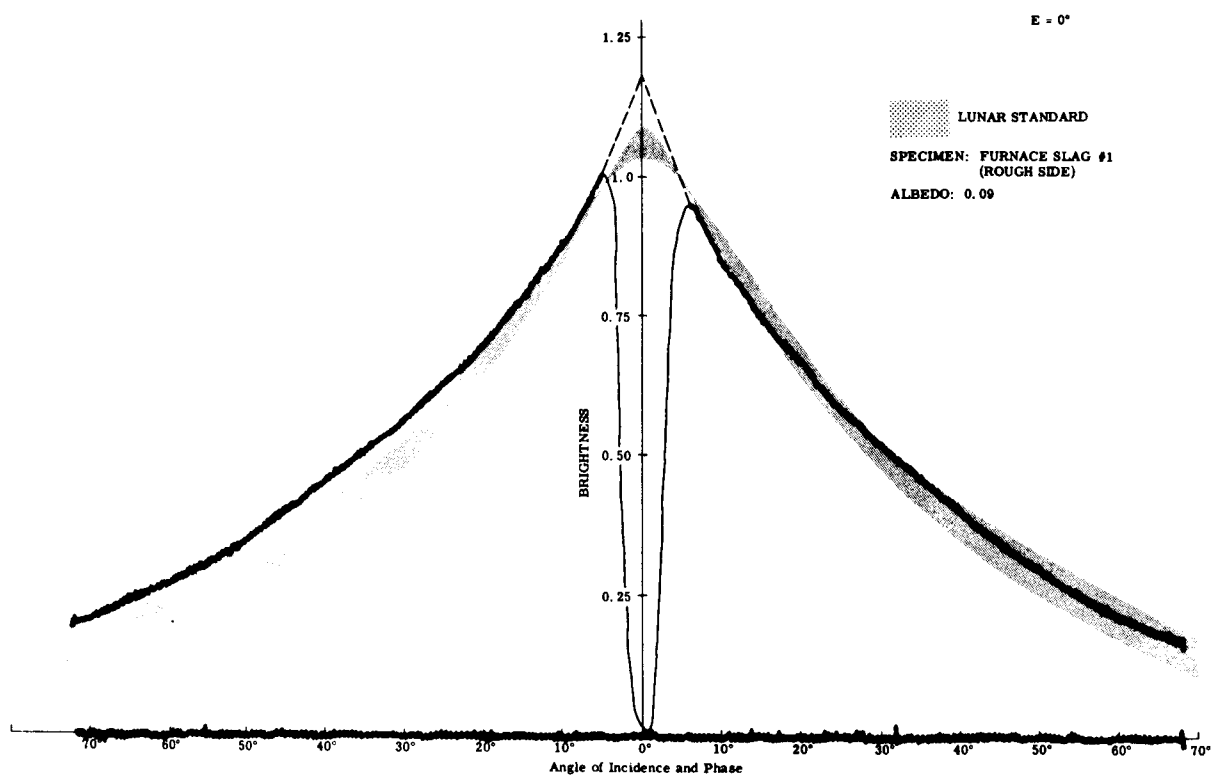


Figure 20. Furnace Slag #1 (Sheet 2 of 2)



(a)

Figure 21. Furnace Slag #1 (Sheet 1 of 2)

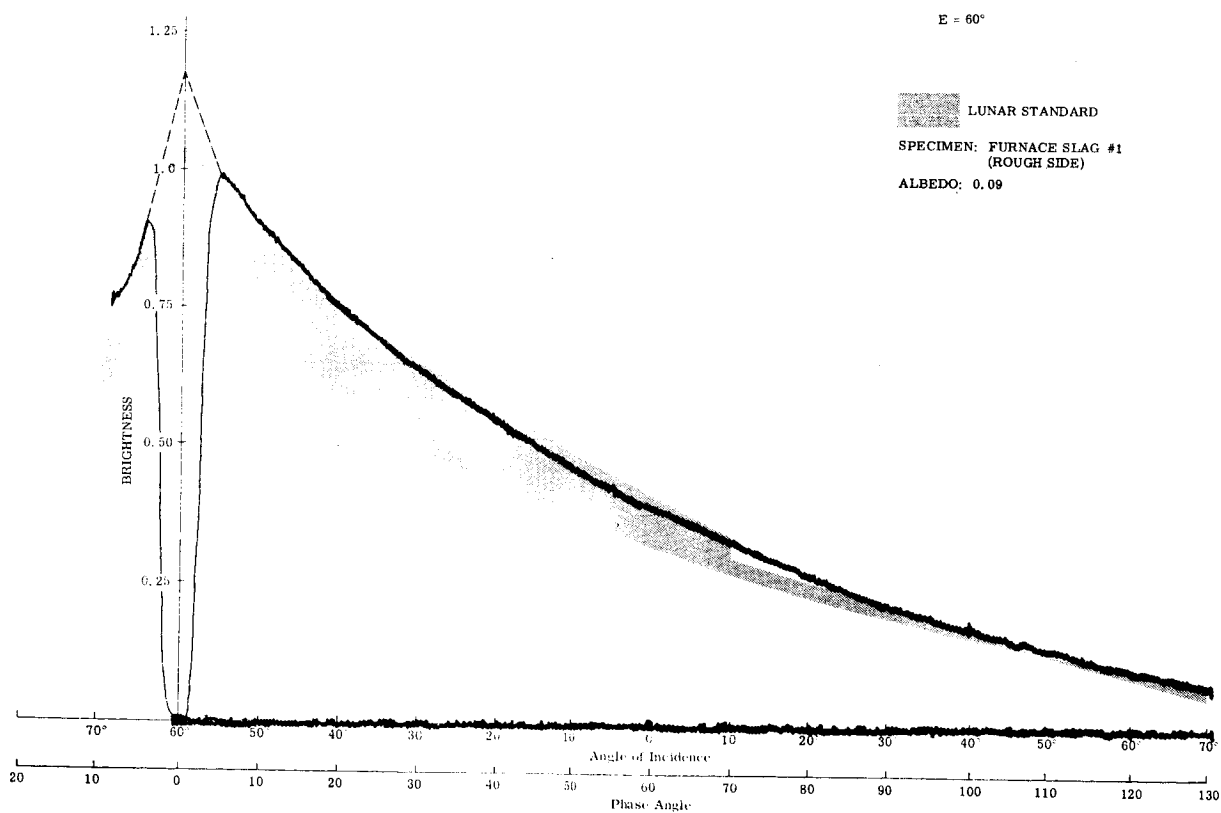
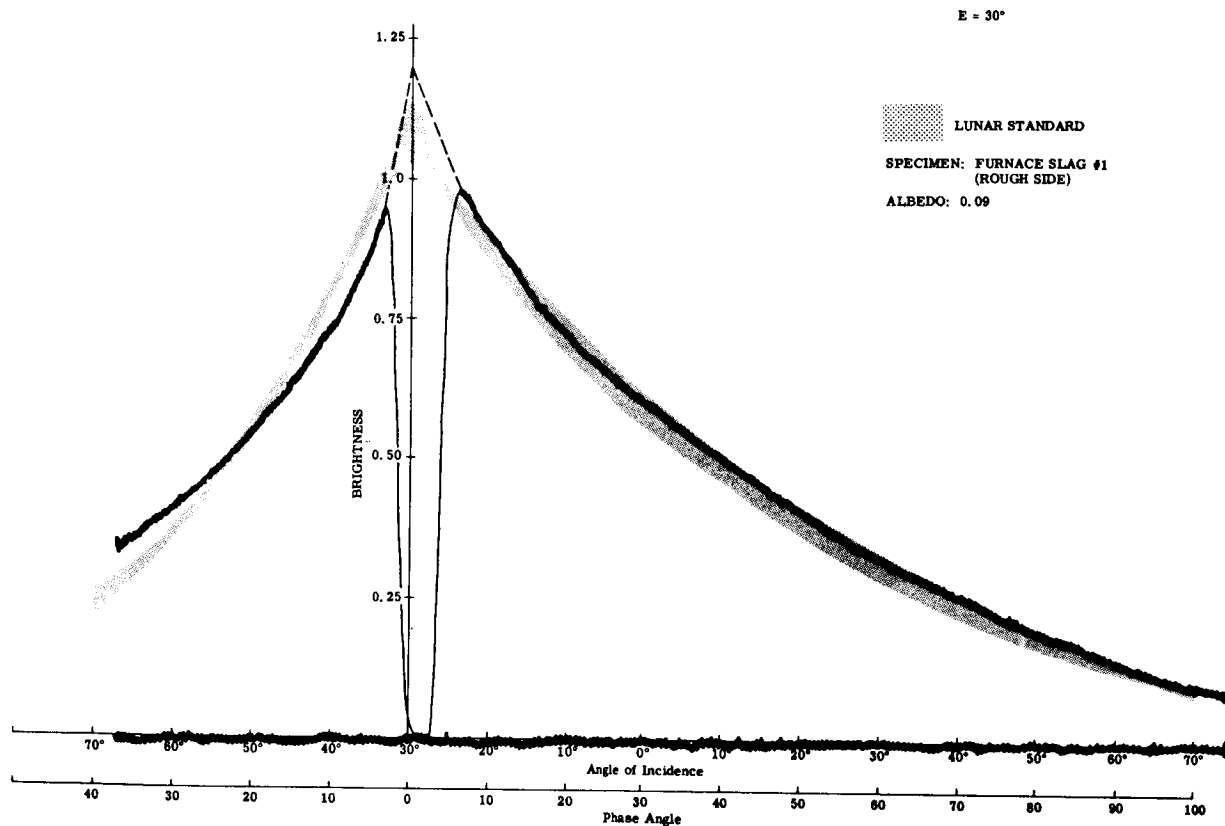
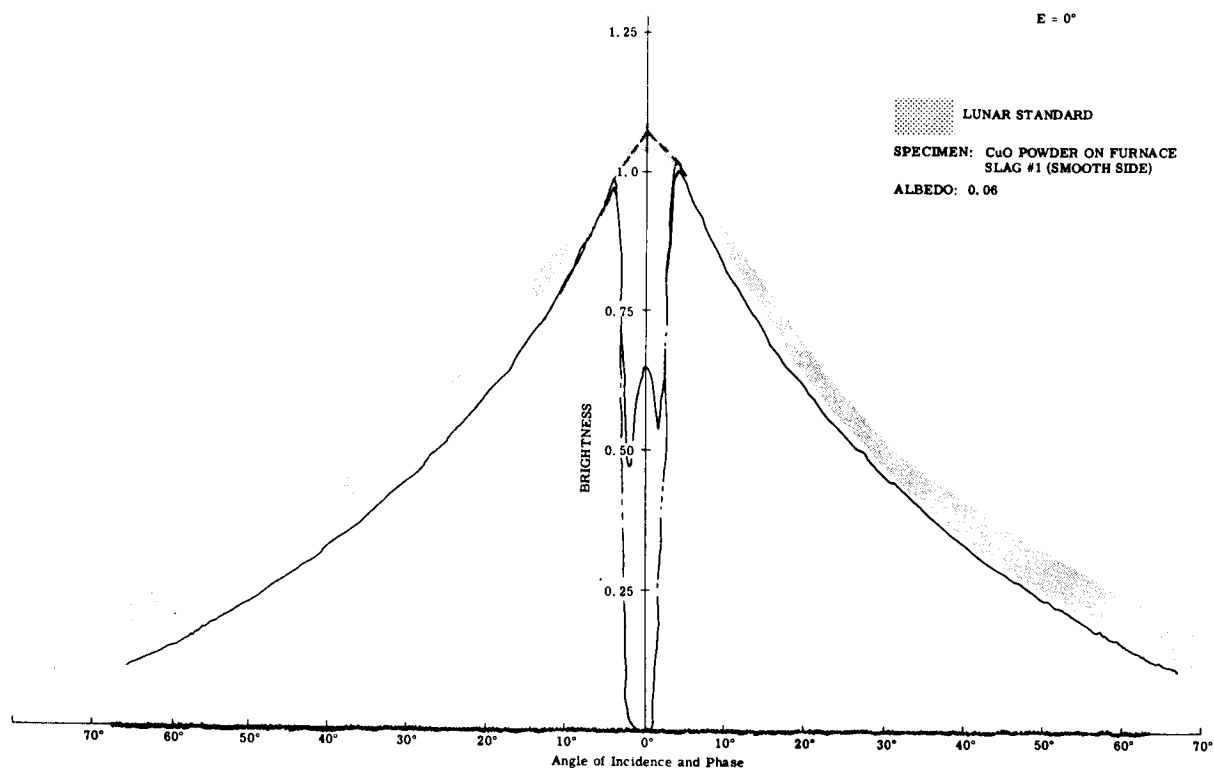
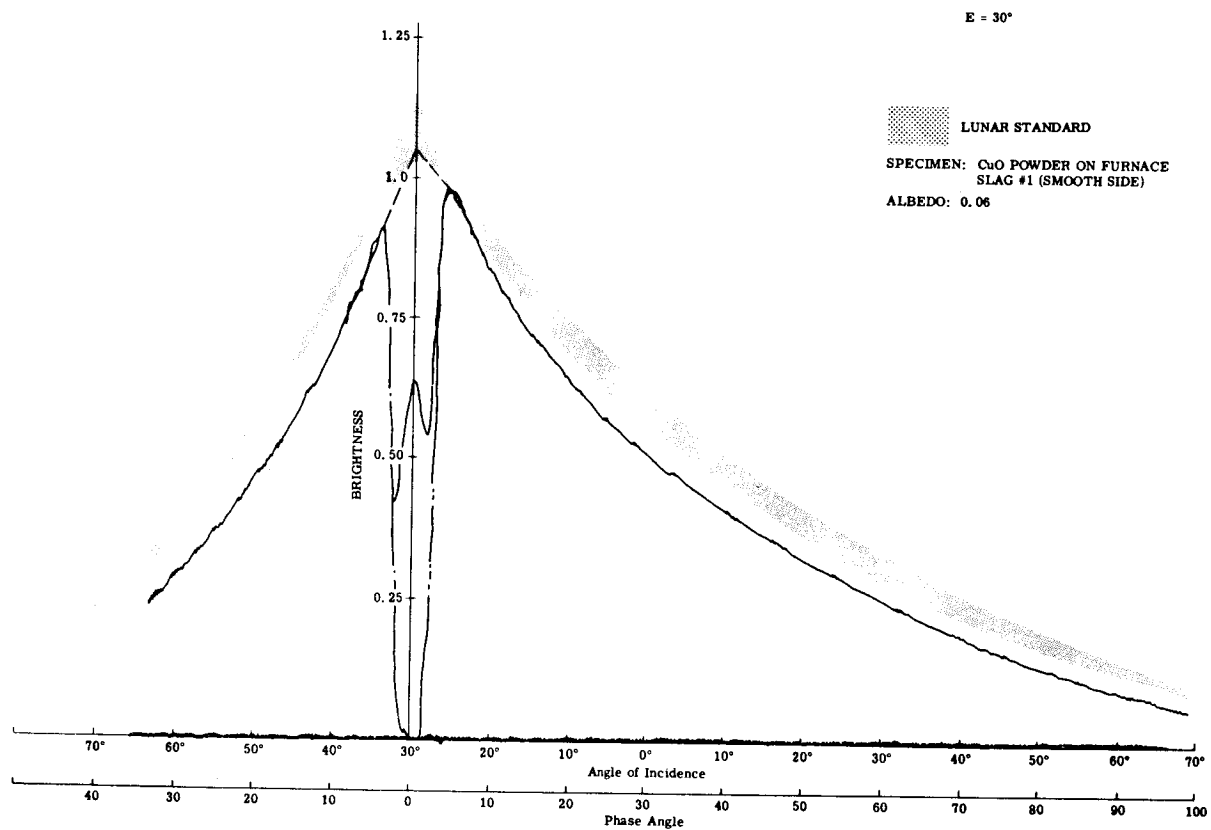


Figure 21. Furnace Slag #1 (Sheet 2 of 2)

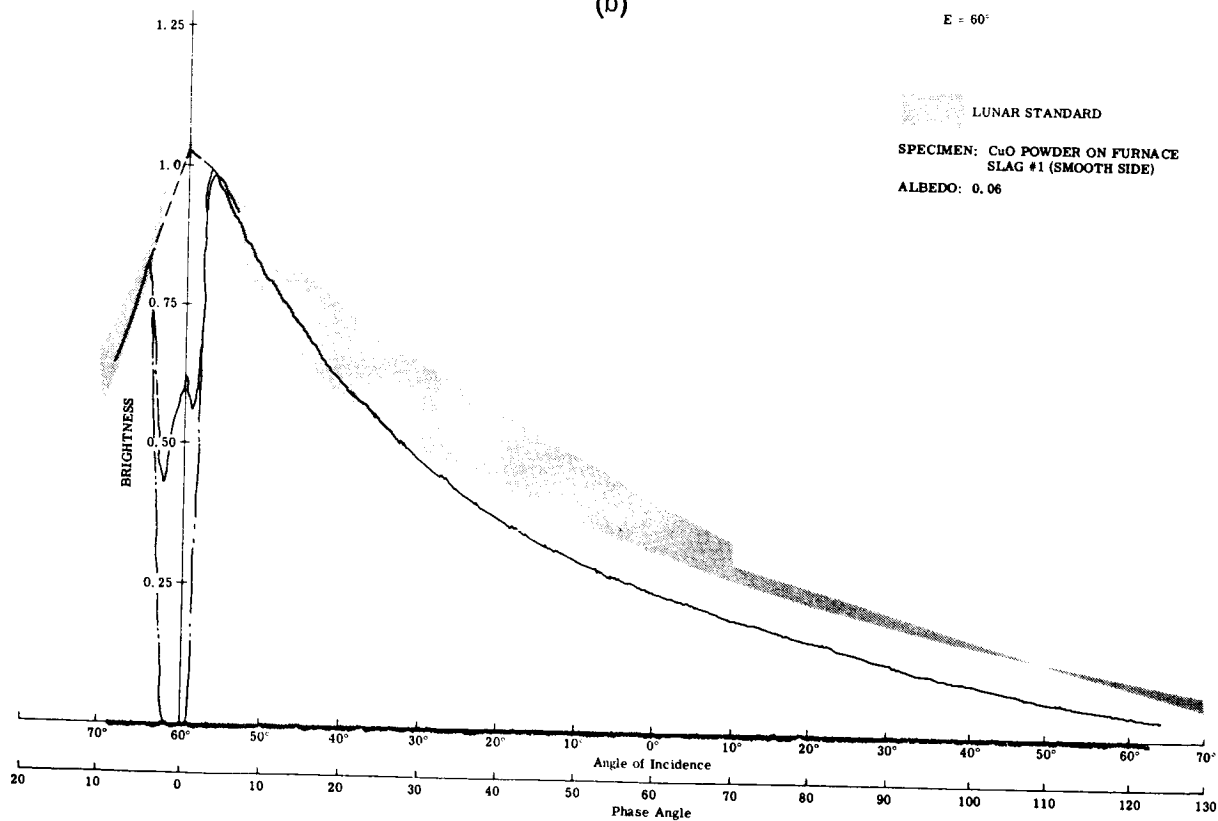


(a)

Figure 22. CuO Powder on Furnace Slag #1 (Sheet 1 of 2)



(b)

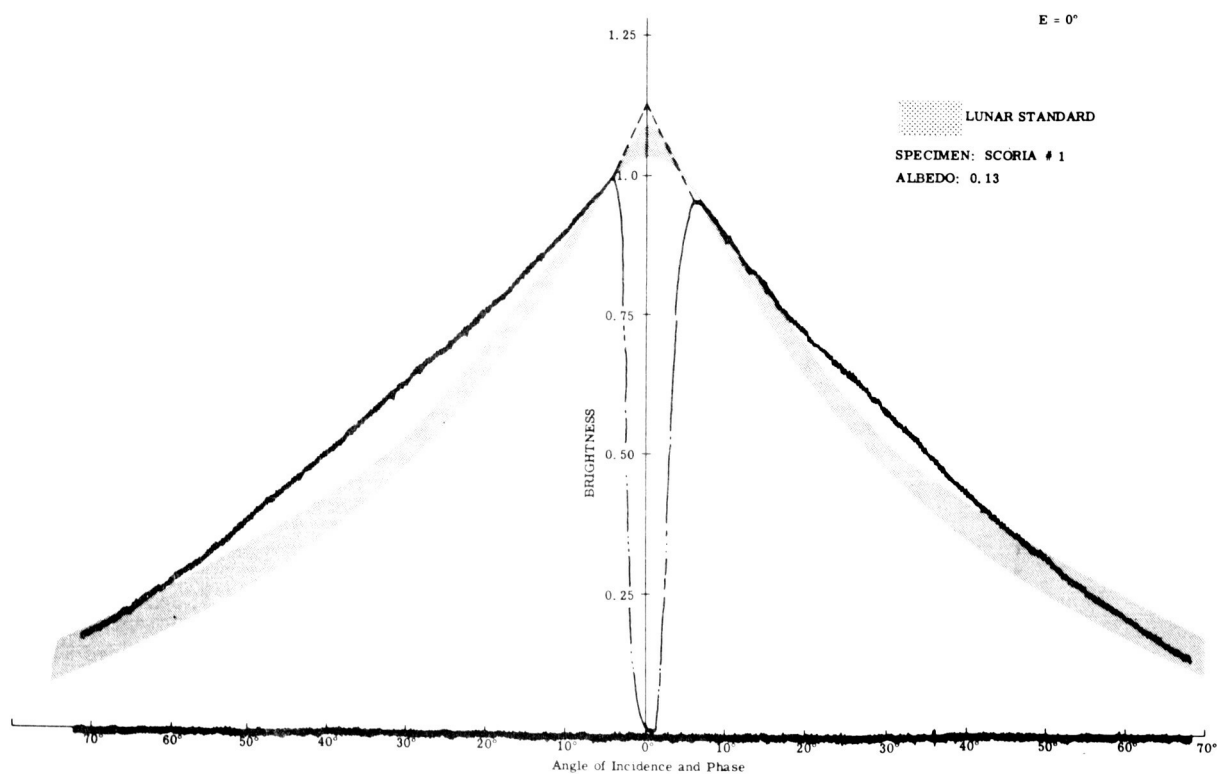


(c)

Figure 22. CuO Powder on Furnace Slag #1 (Sheet 2 of 2)



(a)



(b)

Figure 23. Scoria #1 (Sheet 1 of 2)

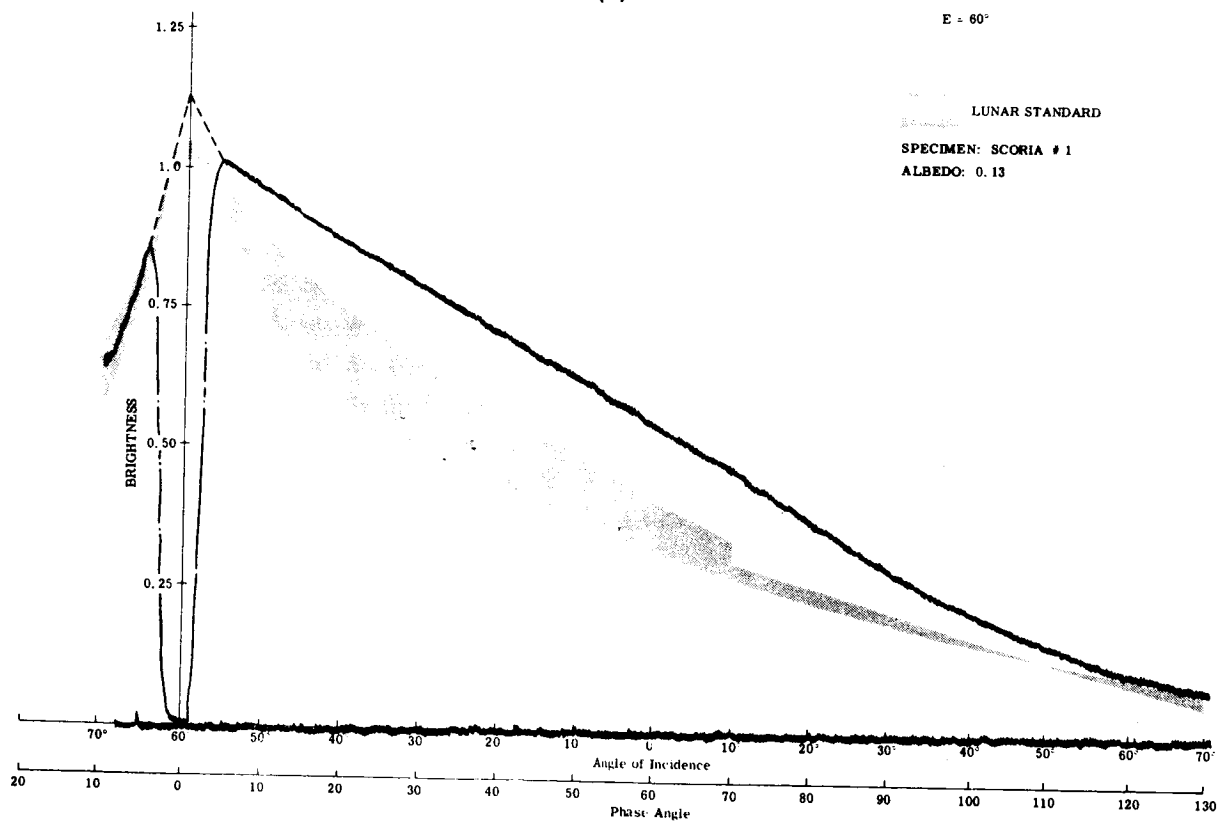
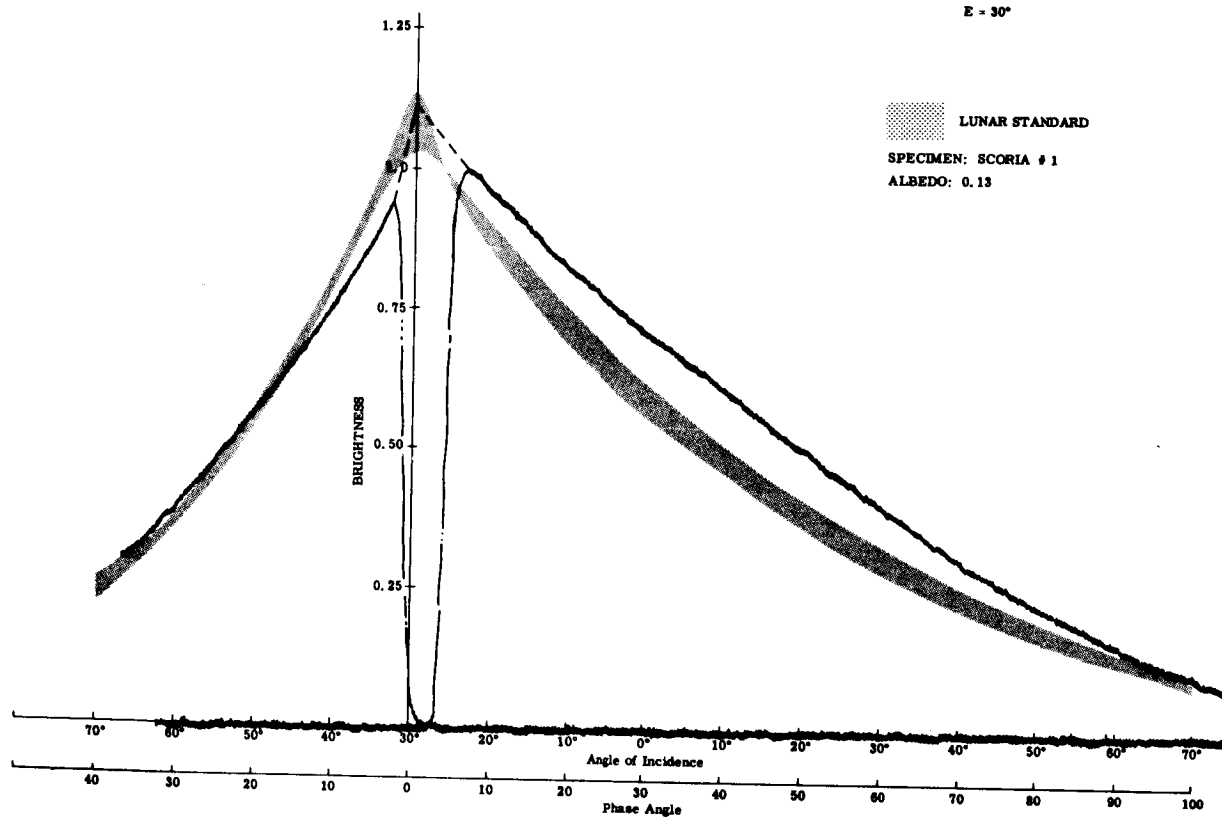
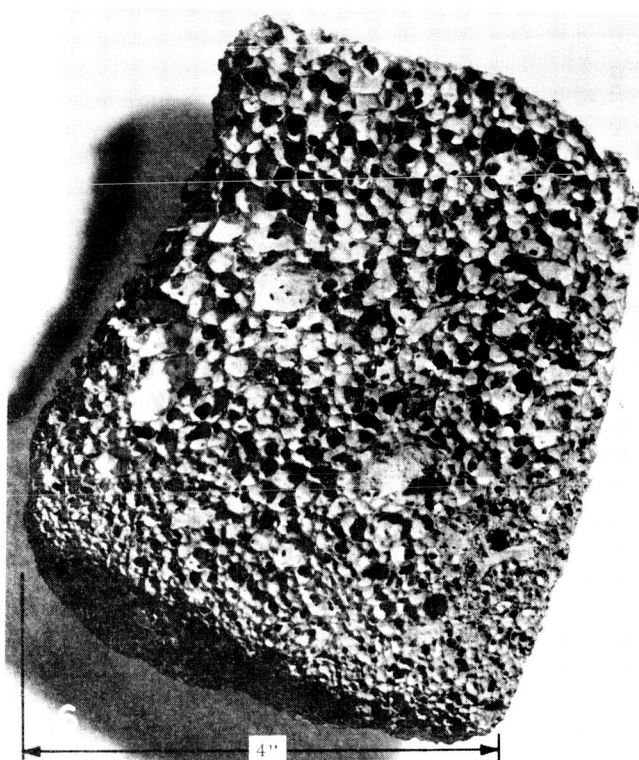
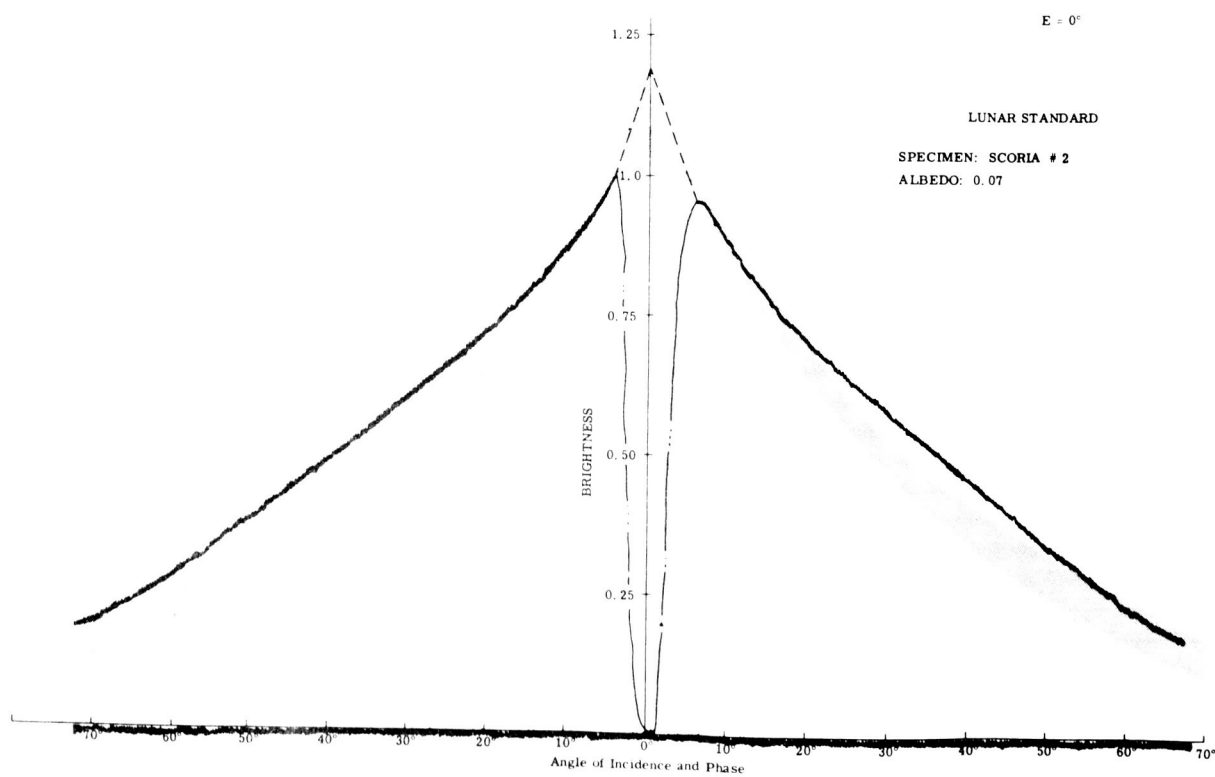


Figure 23. Scoria #1 (Sheet 2 of 2)

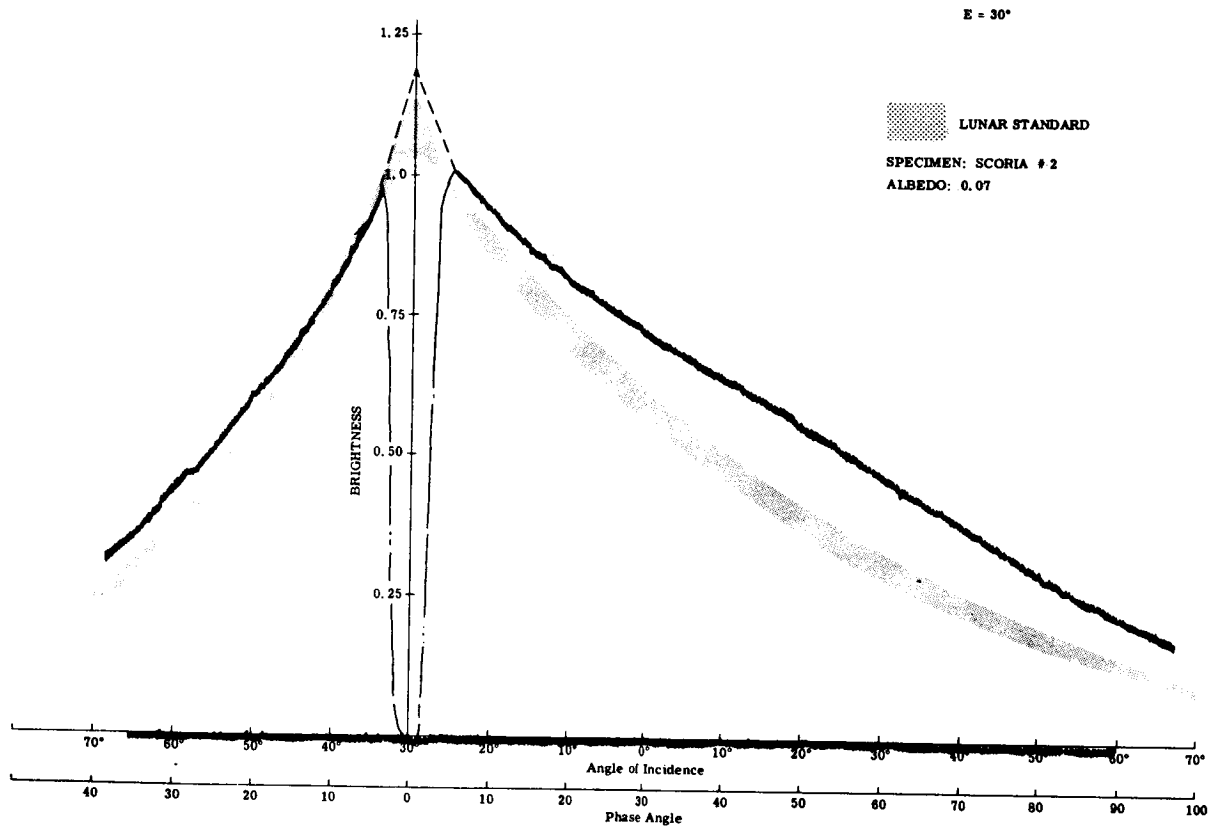


(a)

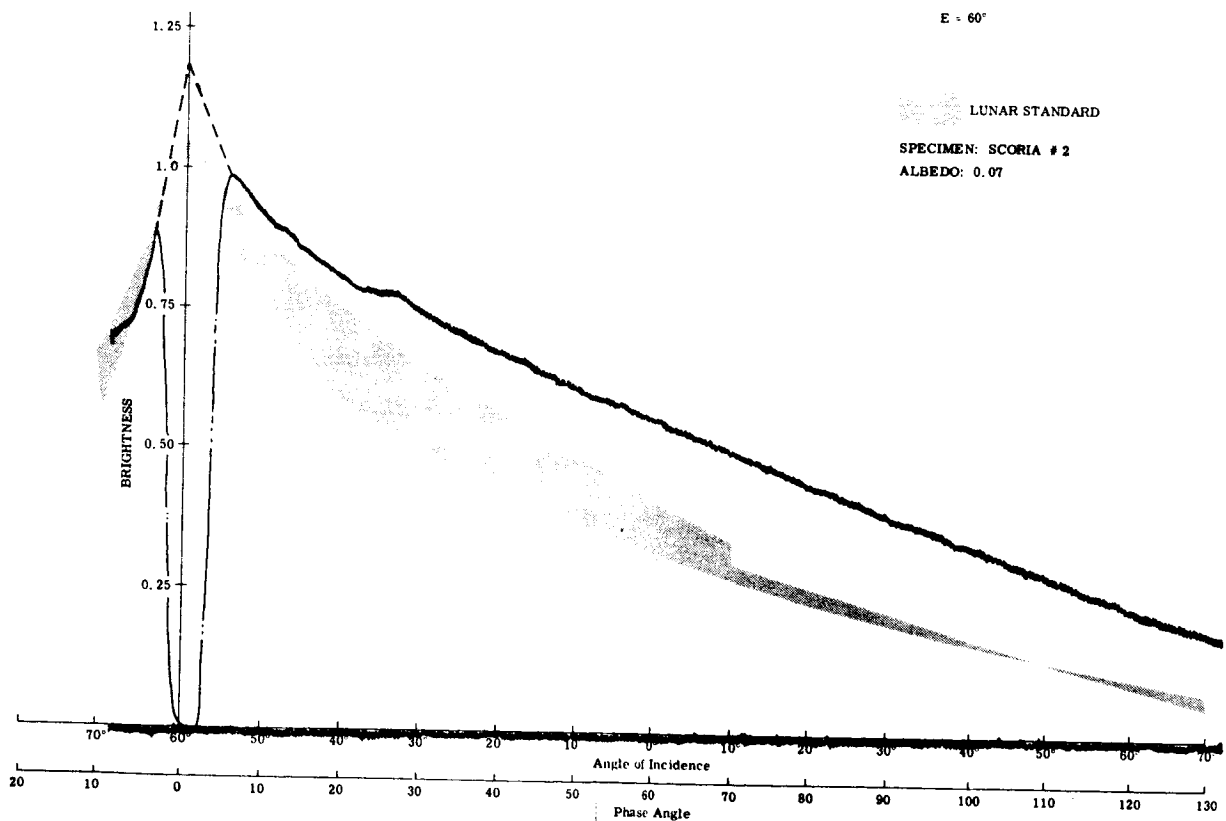


(b)

Figure 24. Scoria #2 (Sheet 1 of 2)

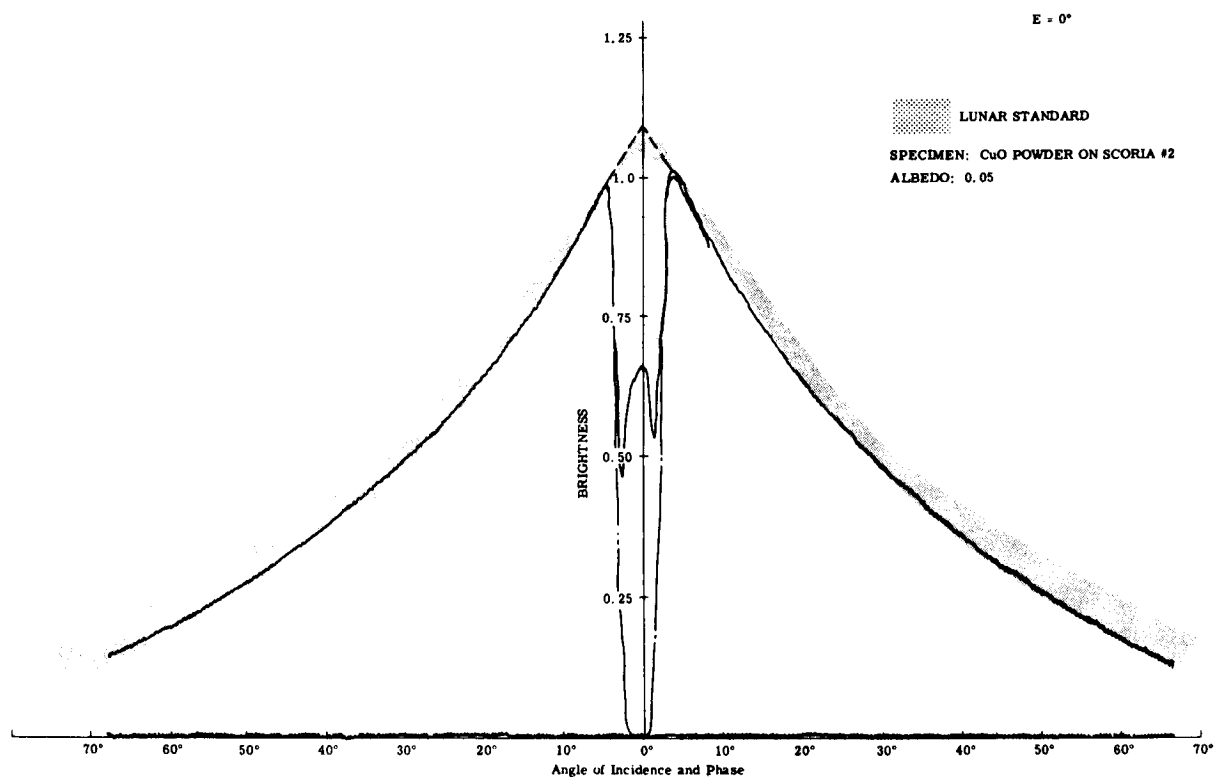


(c)



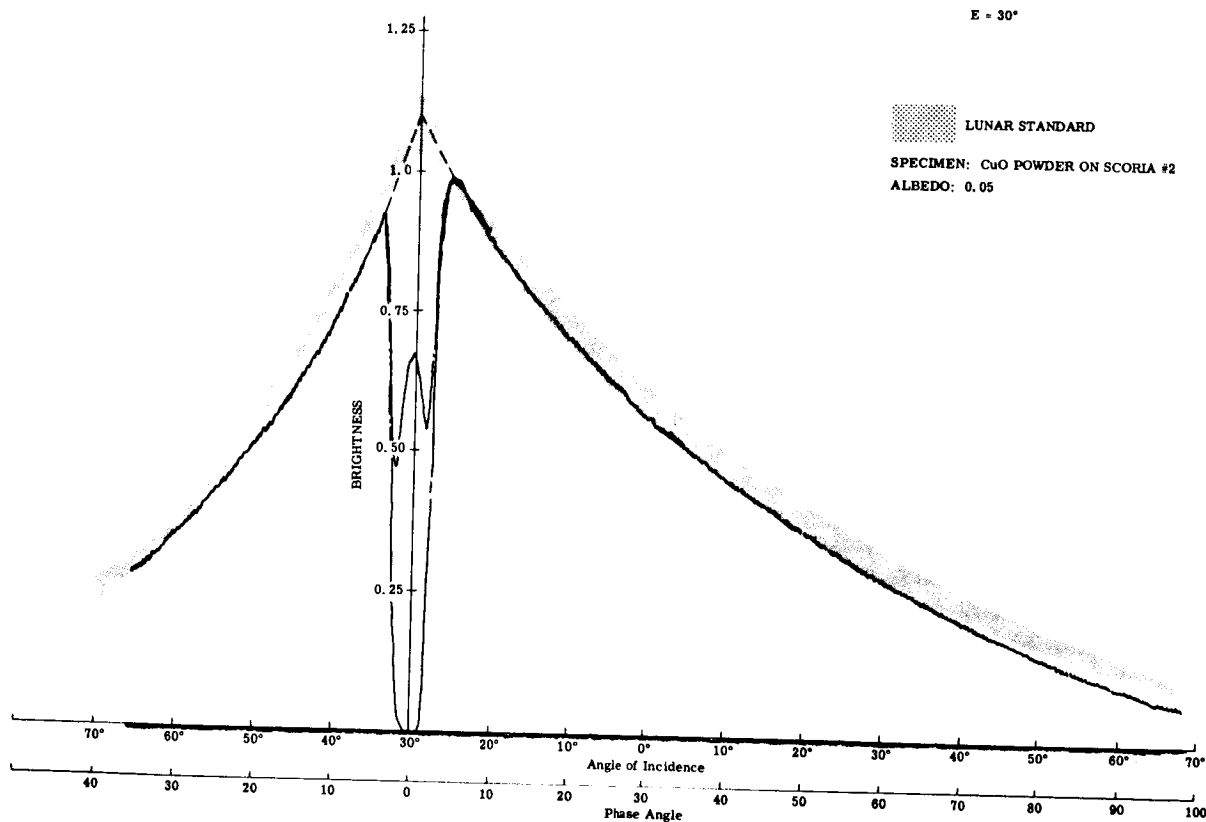
(d)

Figure 24. Scoria #2 (Sheet 2 of 2)

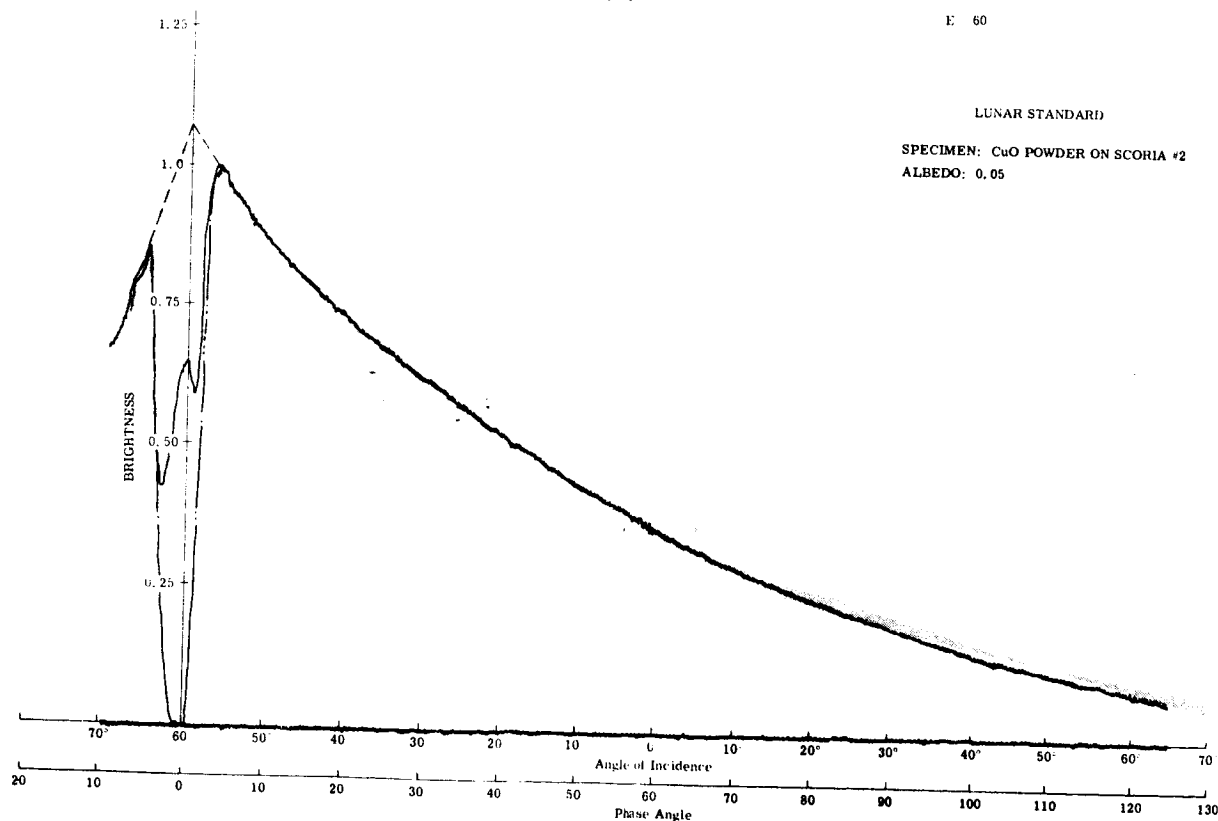


(a)

Figure 25. CuO Powder on Scoria #2 (Sheet 1 of 2)

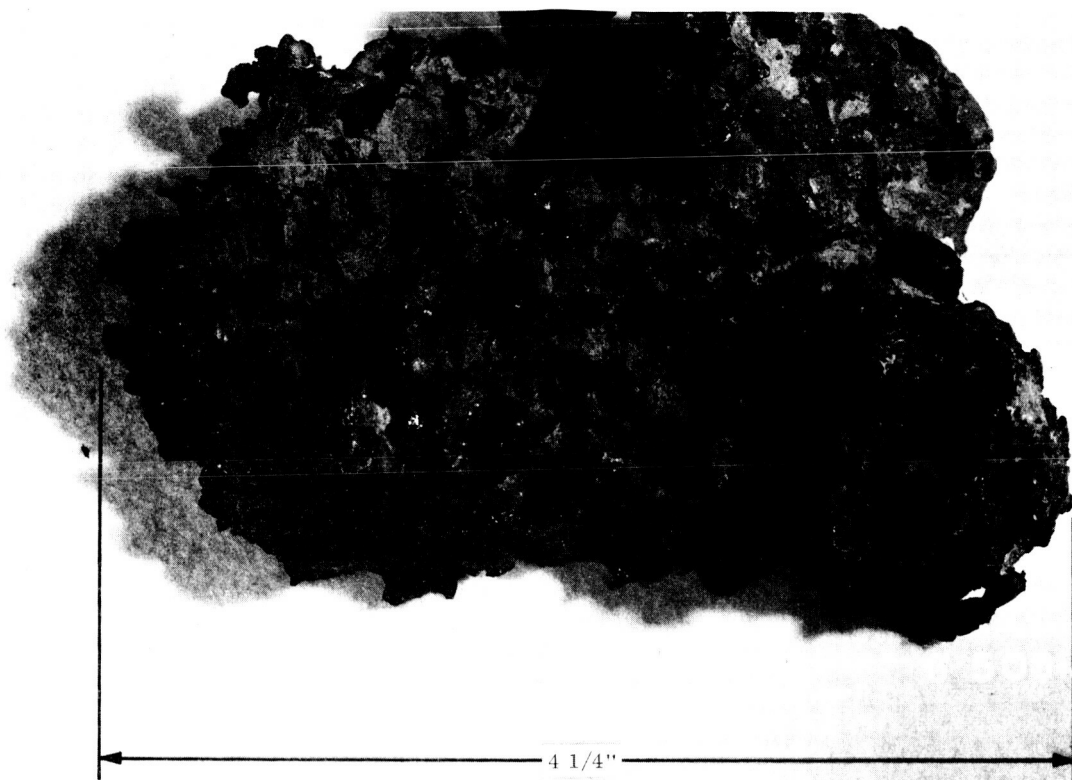


(b)

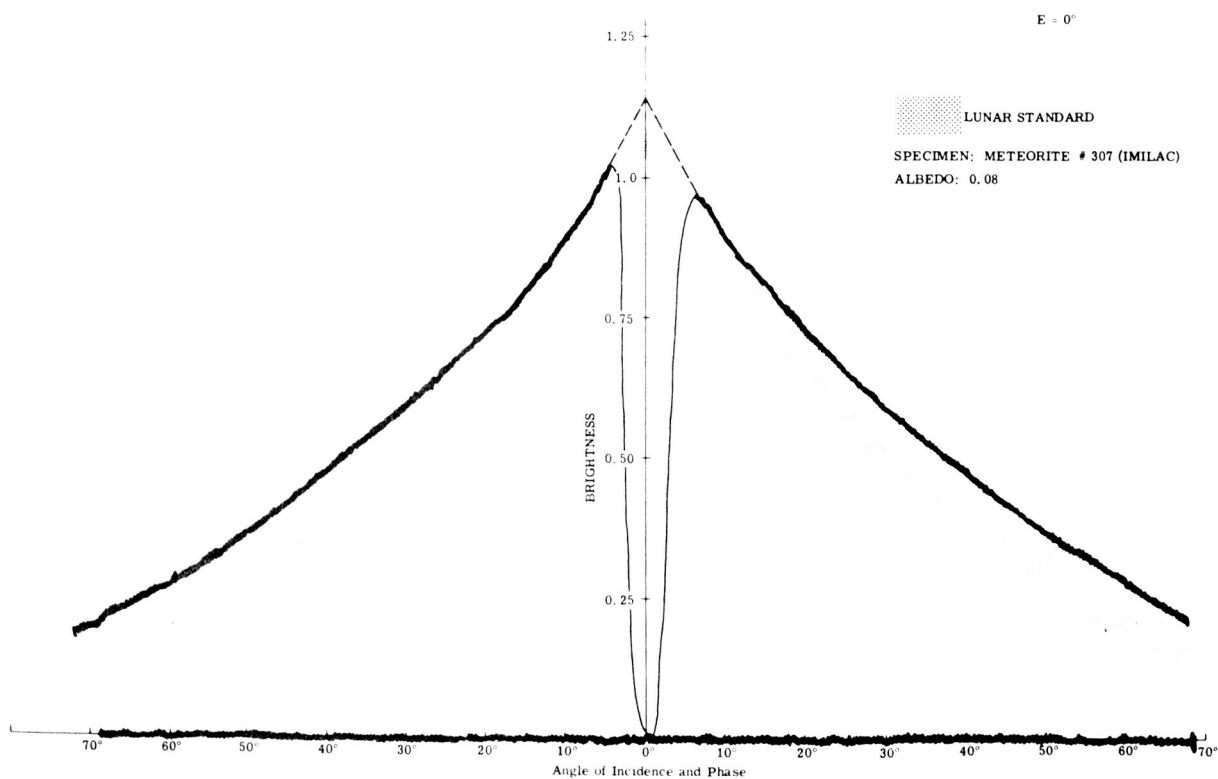


(c)

Figure 25. CuO Powder on Scoria #2 (Sheet 2 of 2).



(a)



(b)

Figure 26. Meteorite #307 (Sheet 1 of 2)

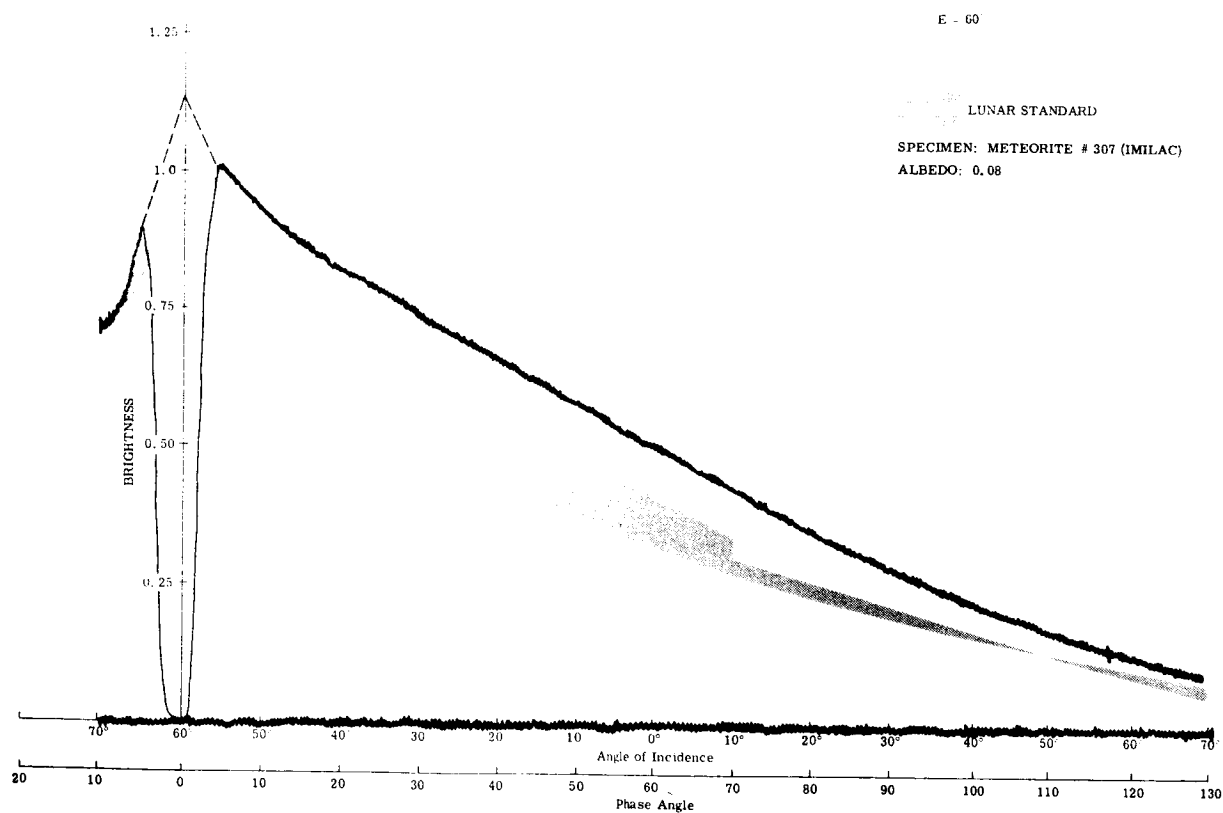
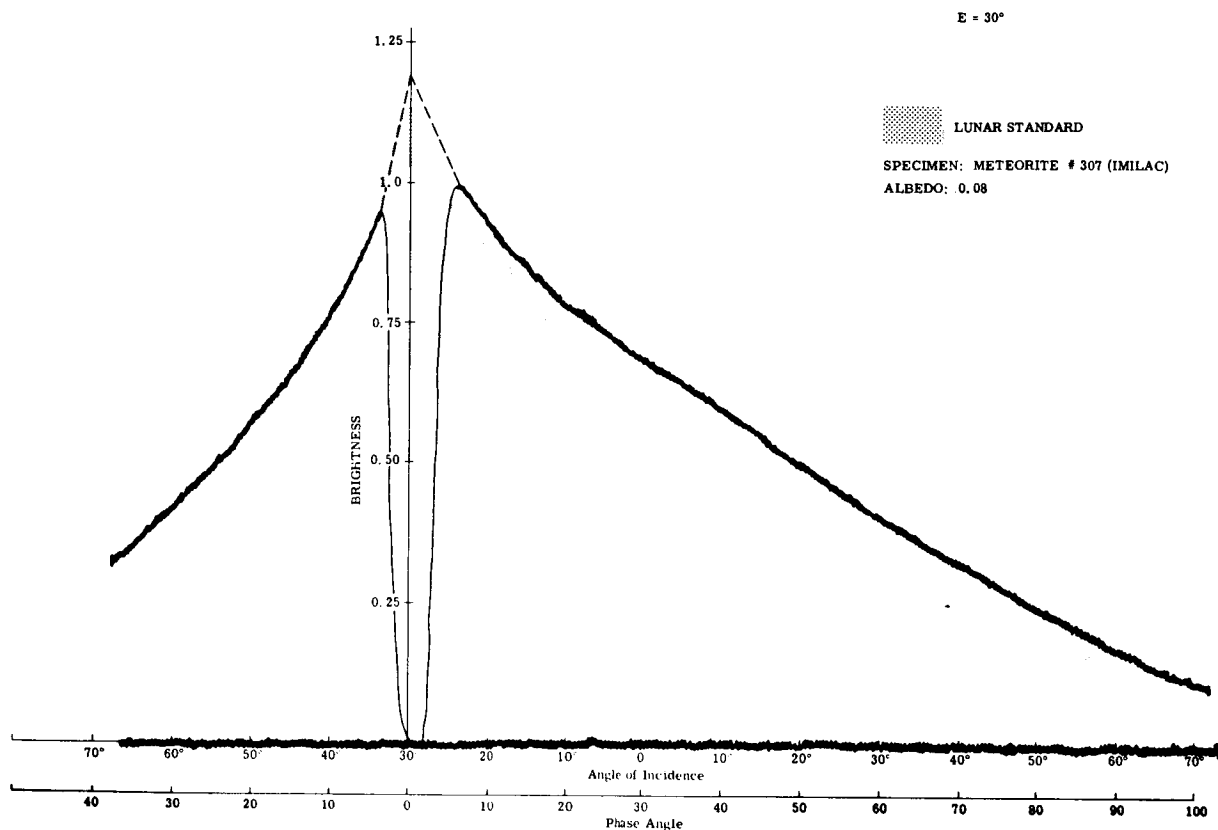
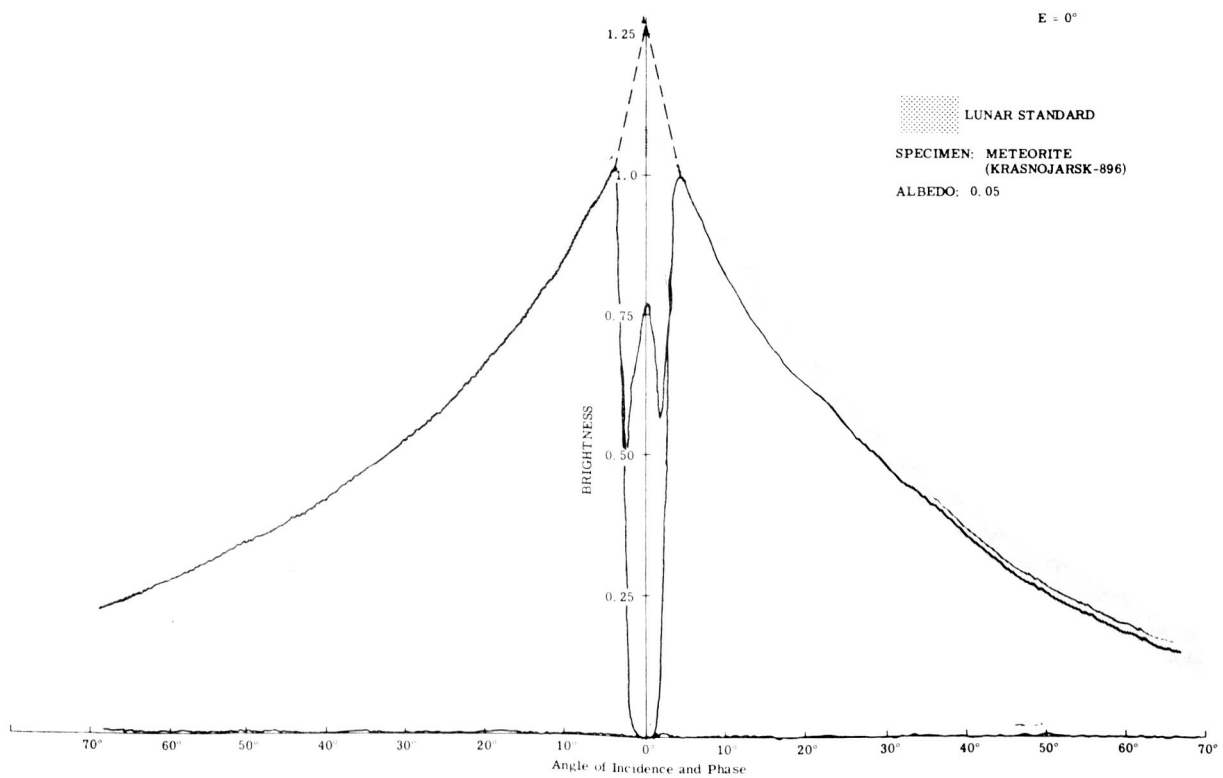


Figure 26. Meteorite #307 (Sheet 2 of 2)

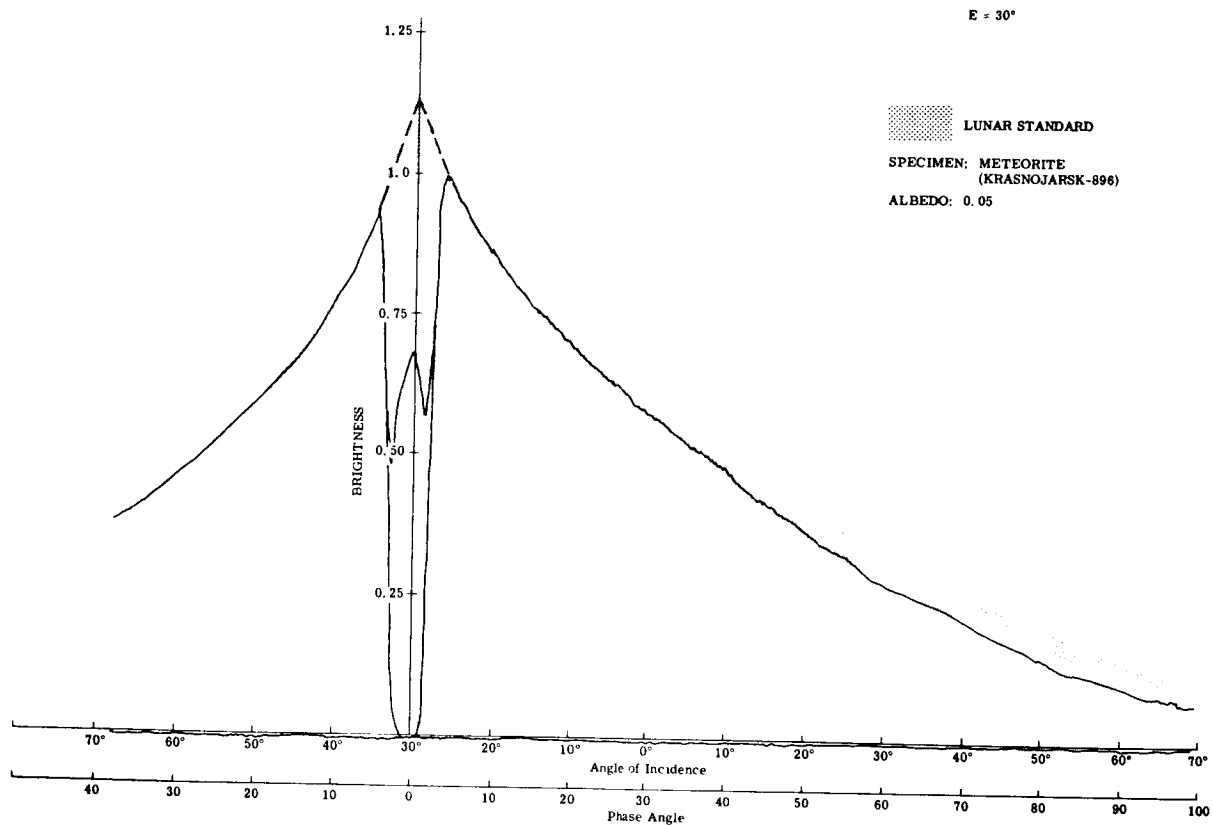


(a)

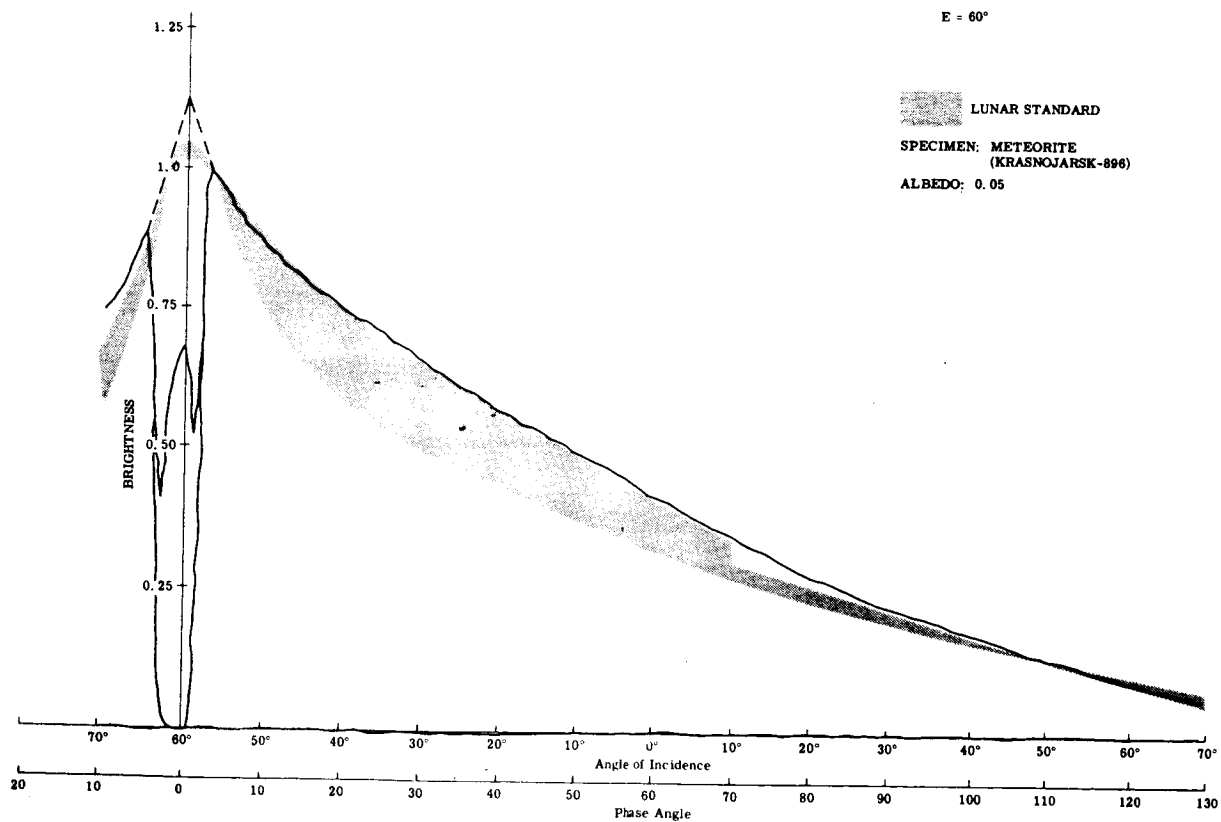


(b)

Figure 27. Meteorite (Sheet 1 of 2)



(c)

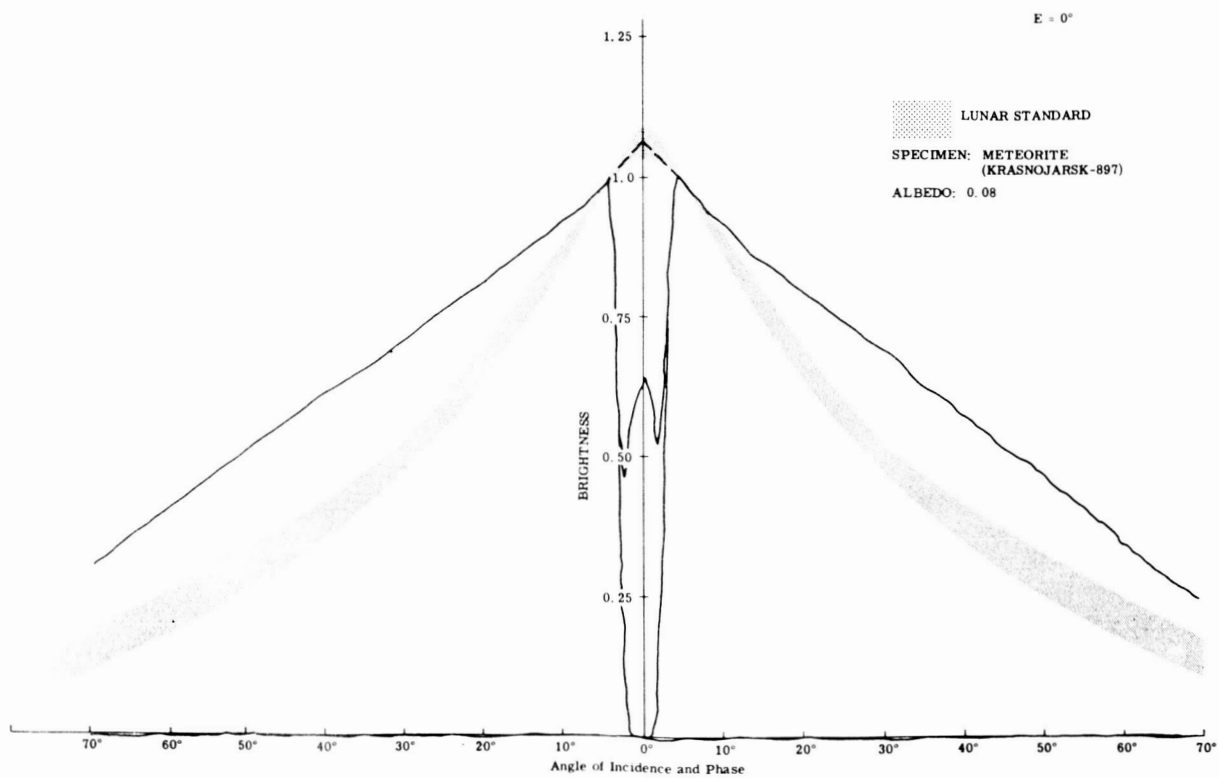


(d)

Figure 27. Meteorite (Sheet 2 of 2)



(a)



(b)

Figure 28. Meteorite (Sheet 1 of 2)

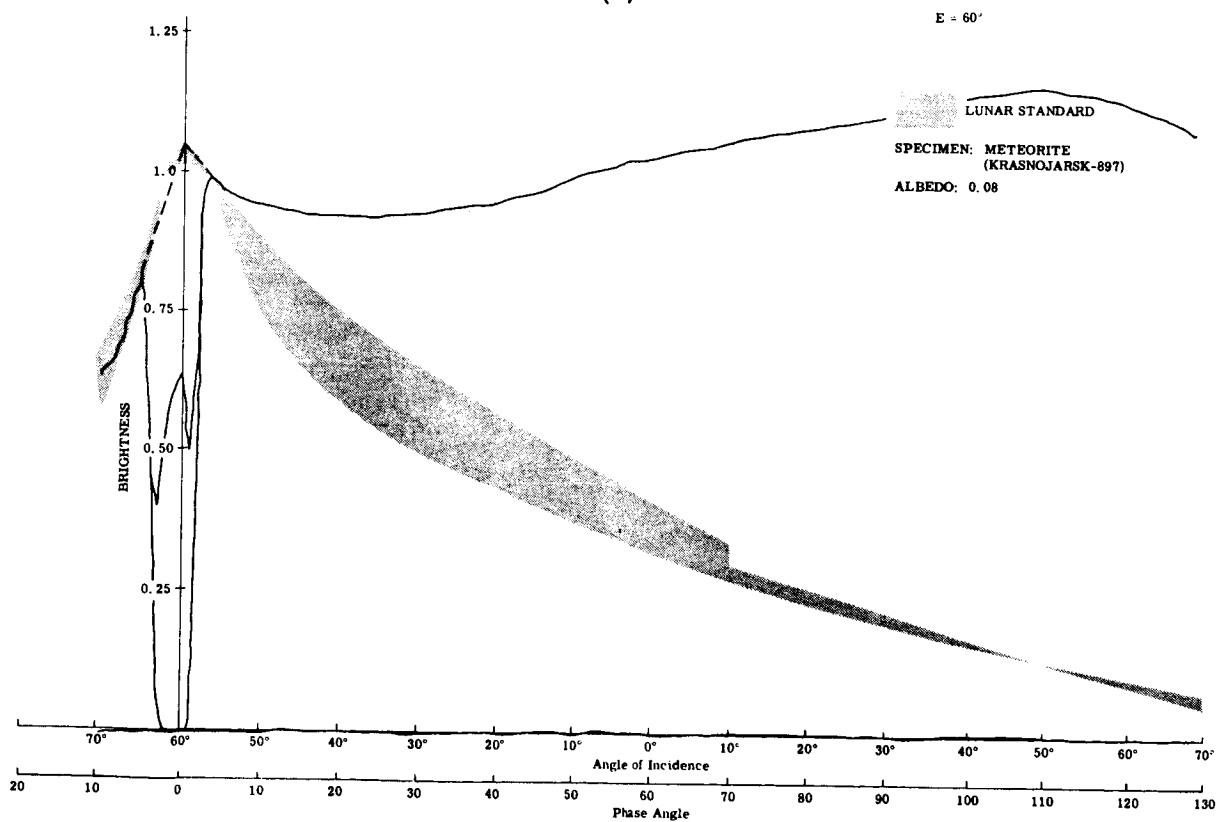
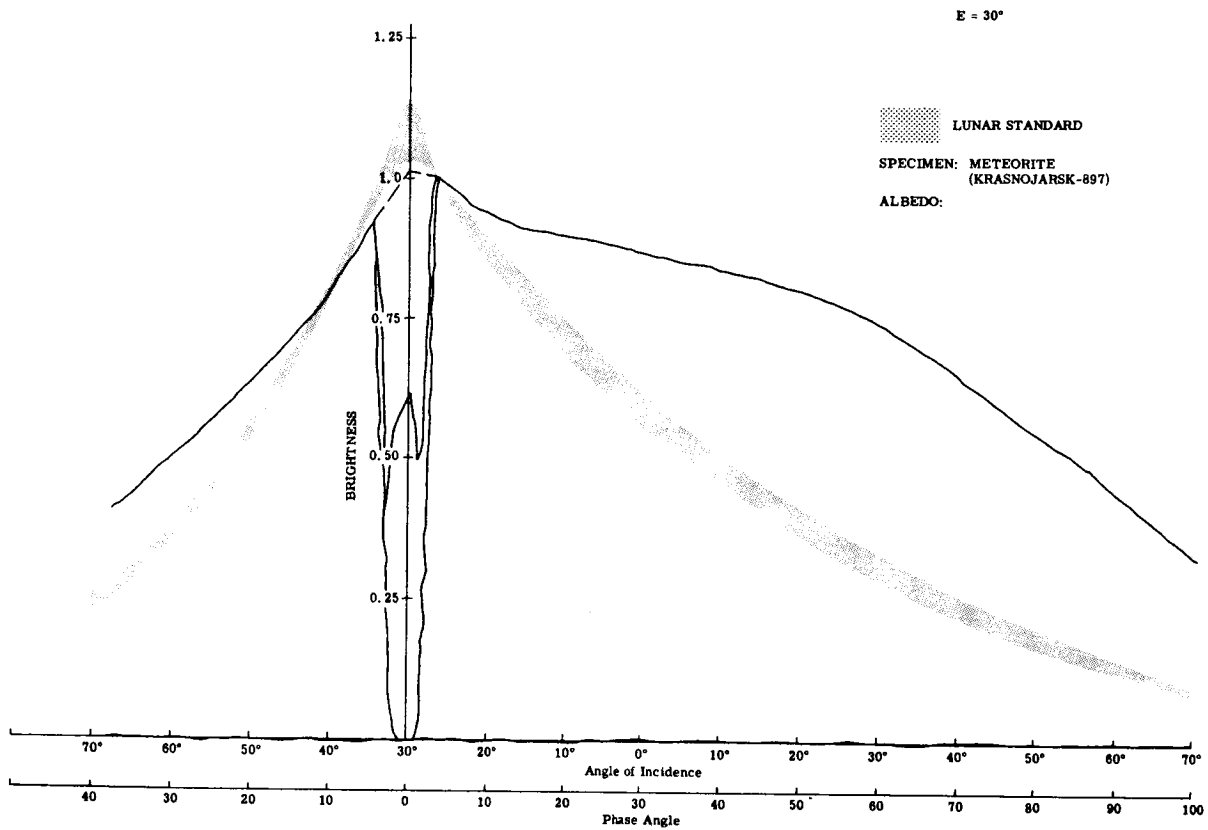
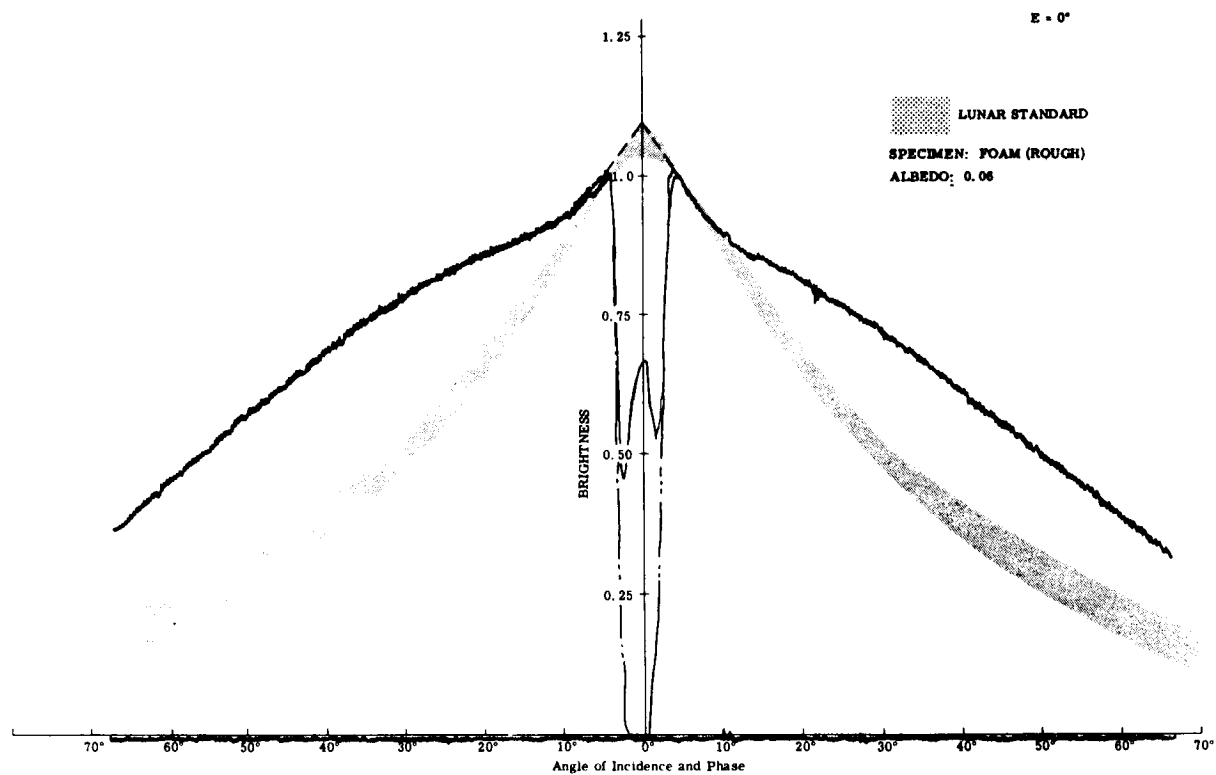


Figure 28. Meteorite (Sheet 2 of 2)



(a)

Figure 29. Foam (Sheet 1 of 2)

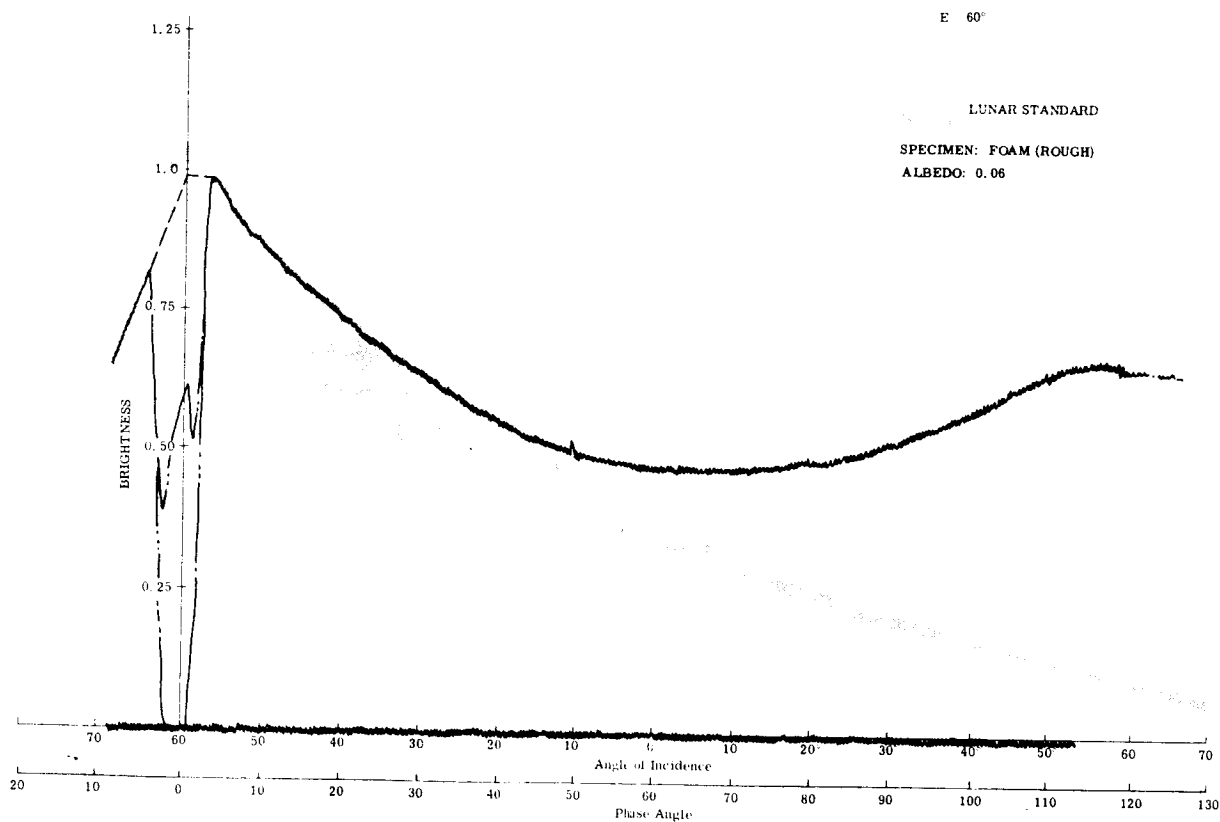
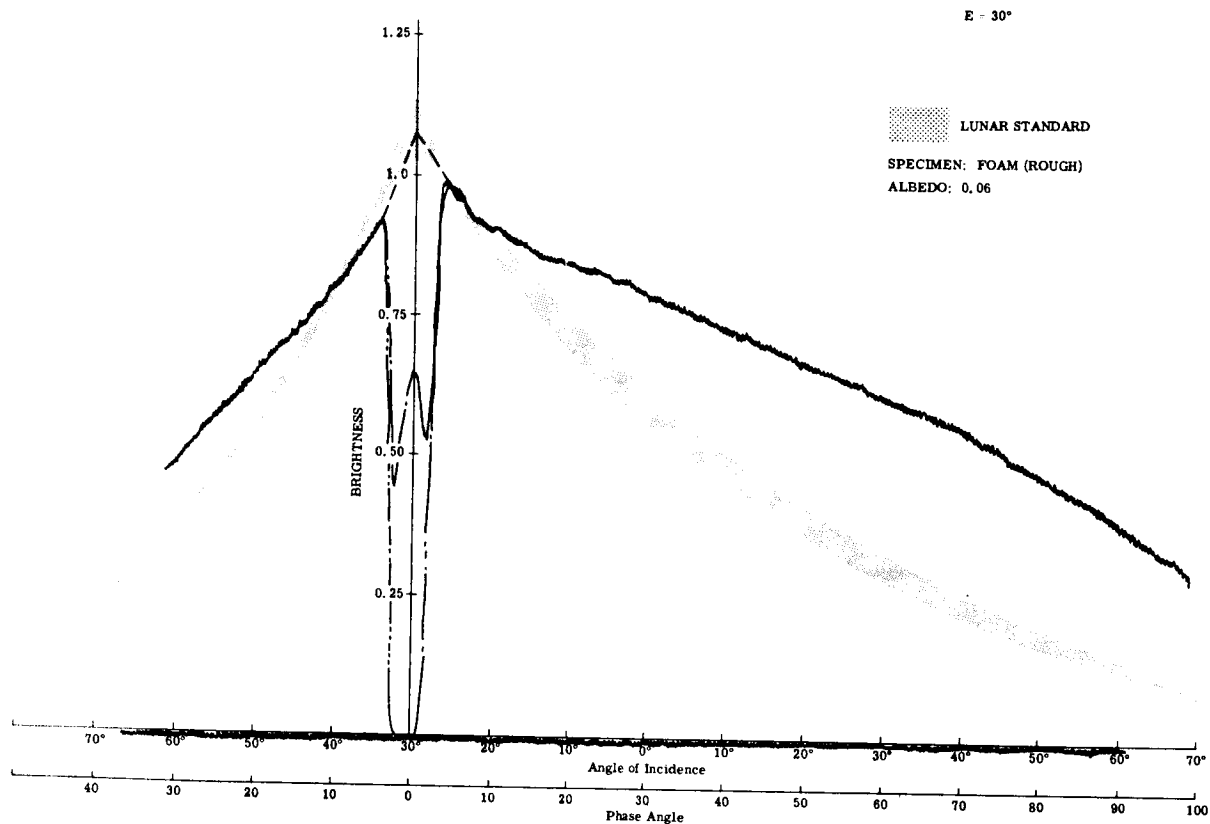
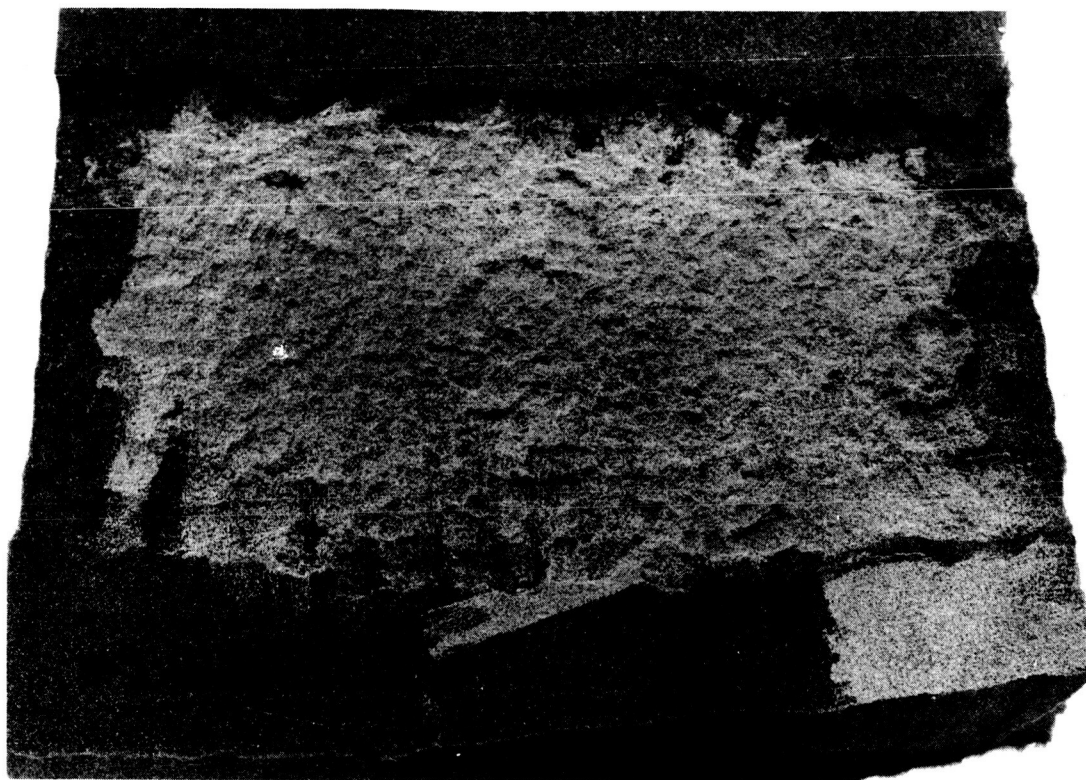
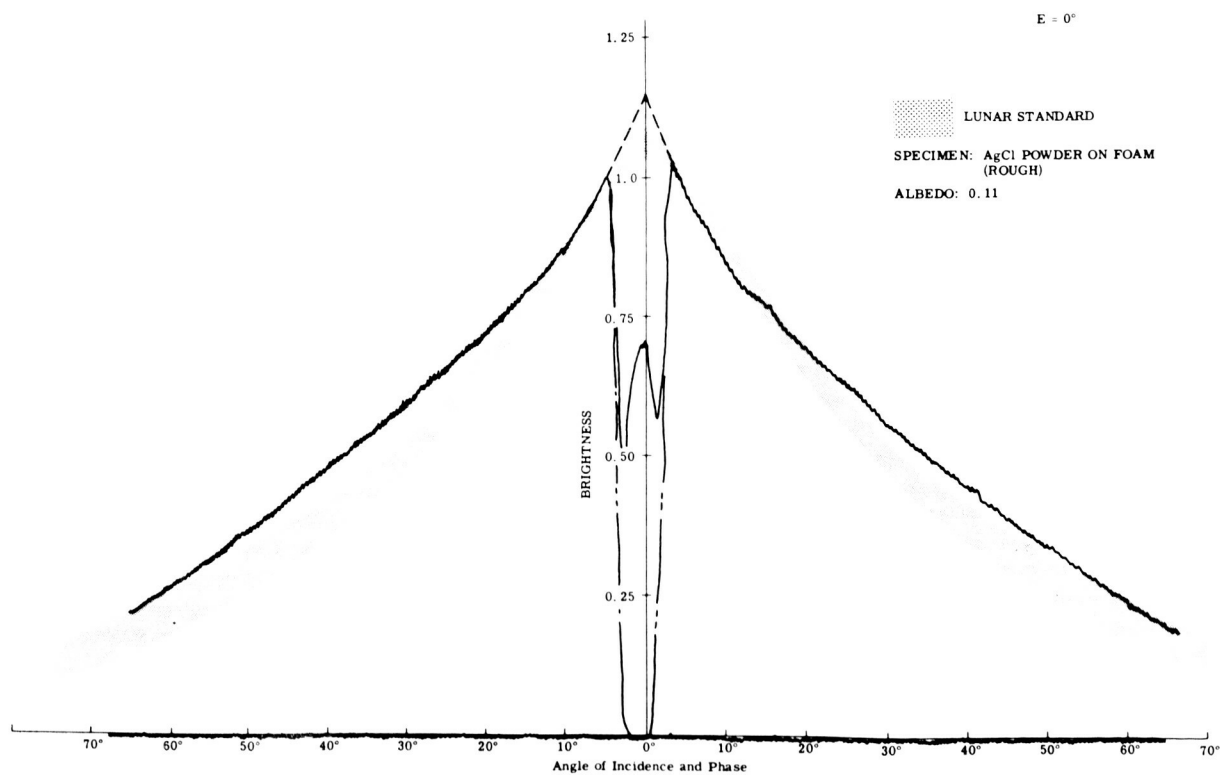


Figure 29. Foam (Sheet 2 of 2)



(a)



(b)

Figure 30. AgCl Powder on Foam (Sheet 1 of 2)

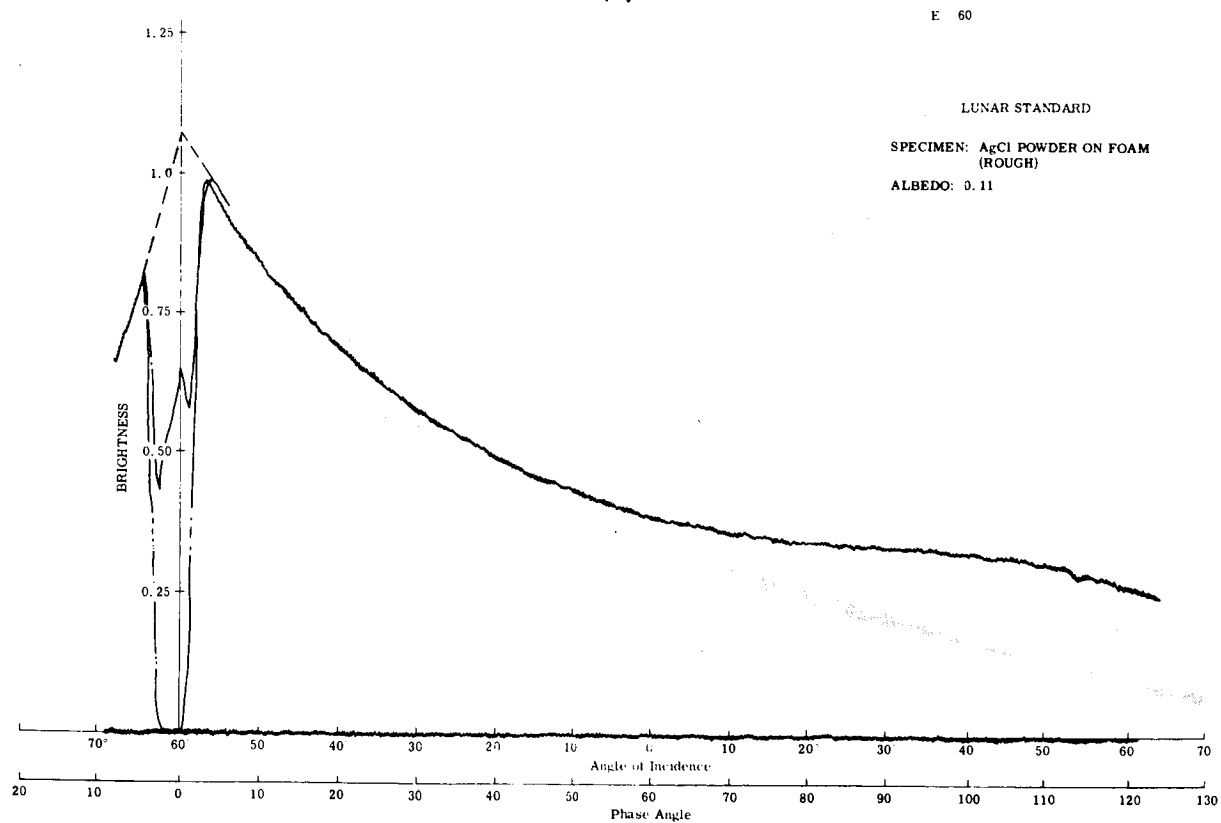
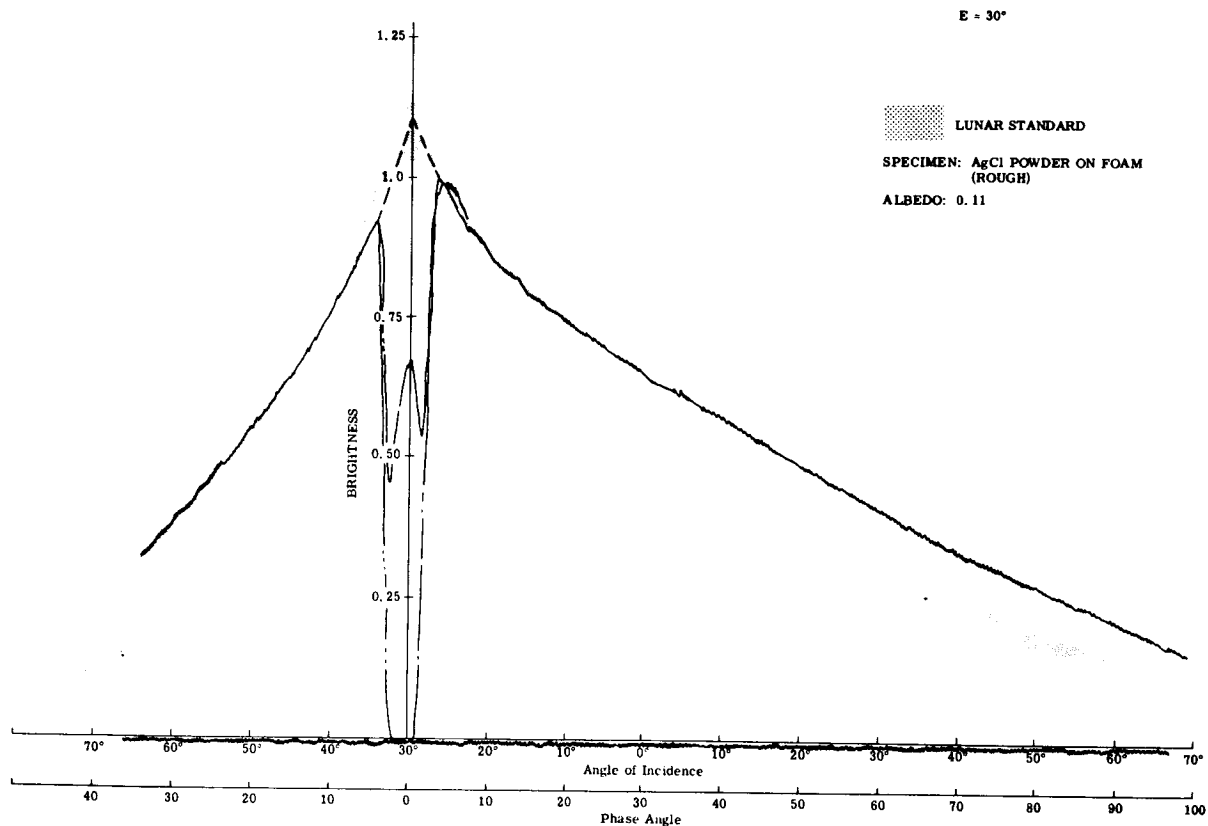
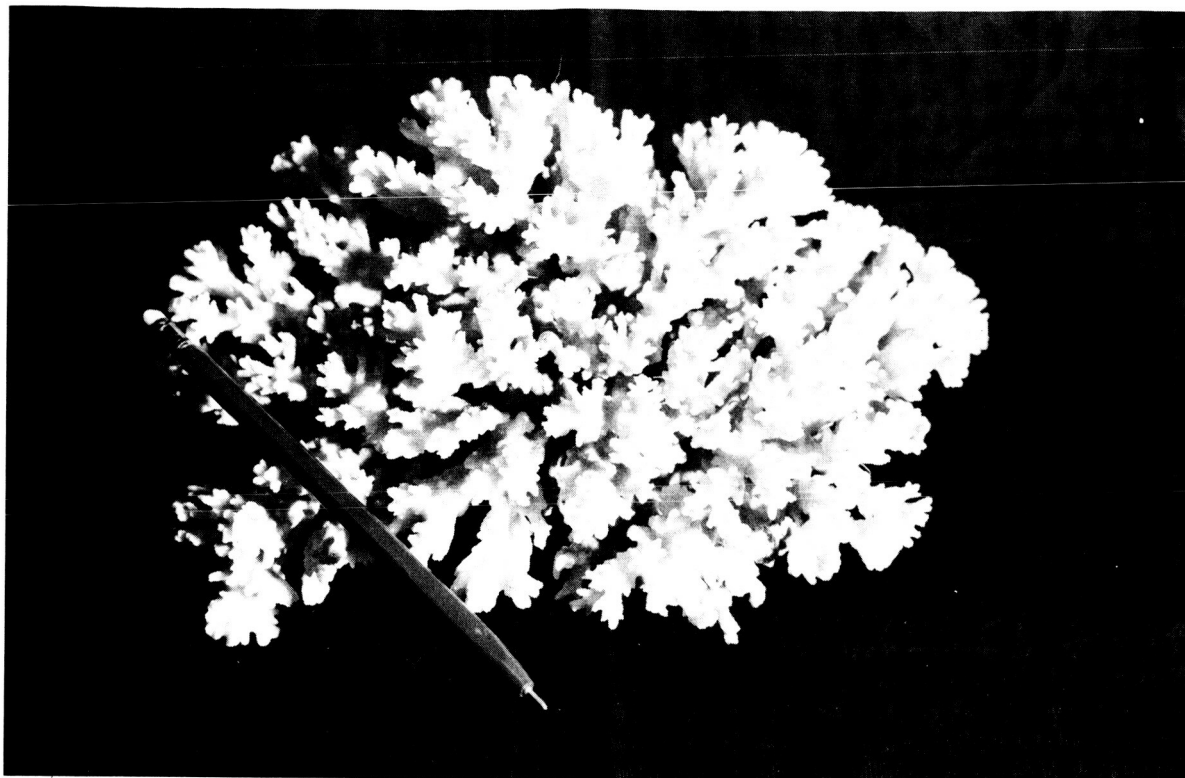
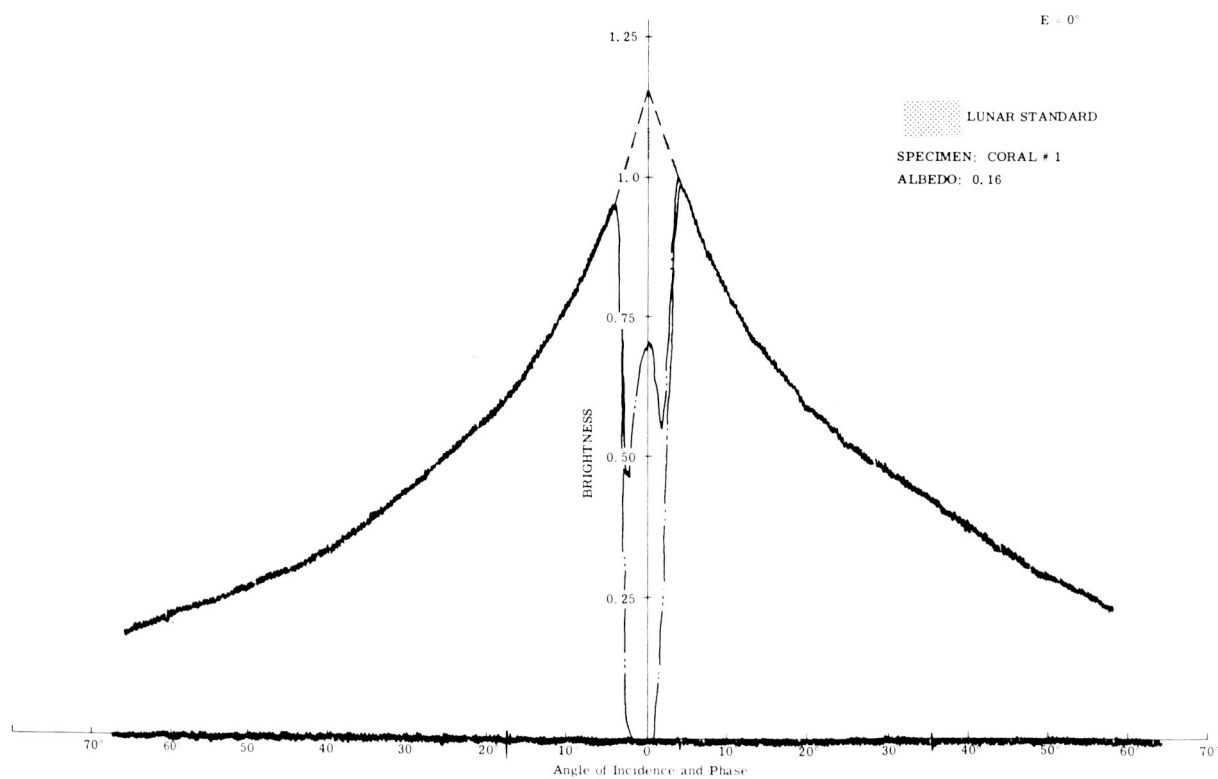


Figure 30. AgCl Powder on Foam (Sheet 2 of 2)



(a)



(b)

Figure 31. Coral #1 (Sheet 1 of 2)

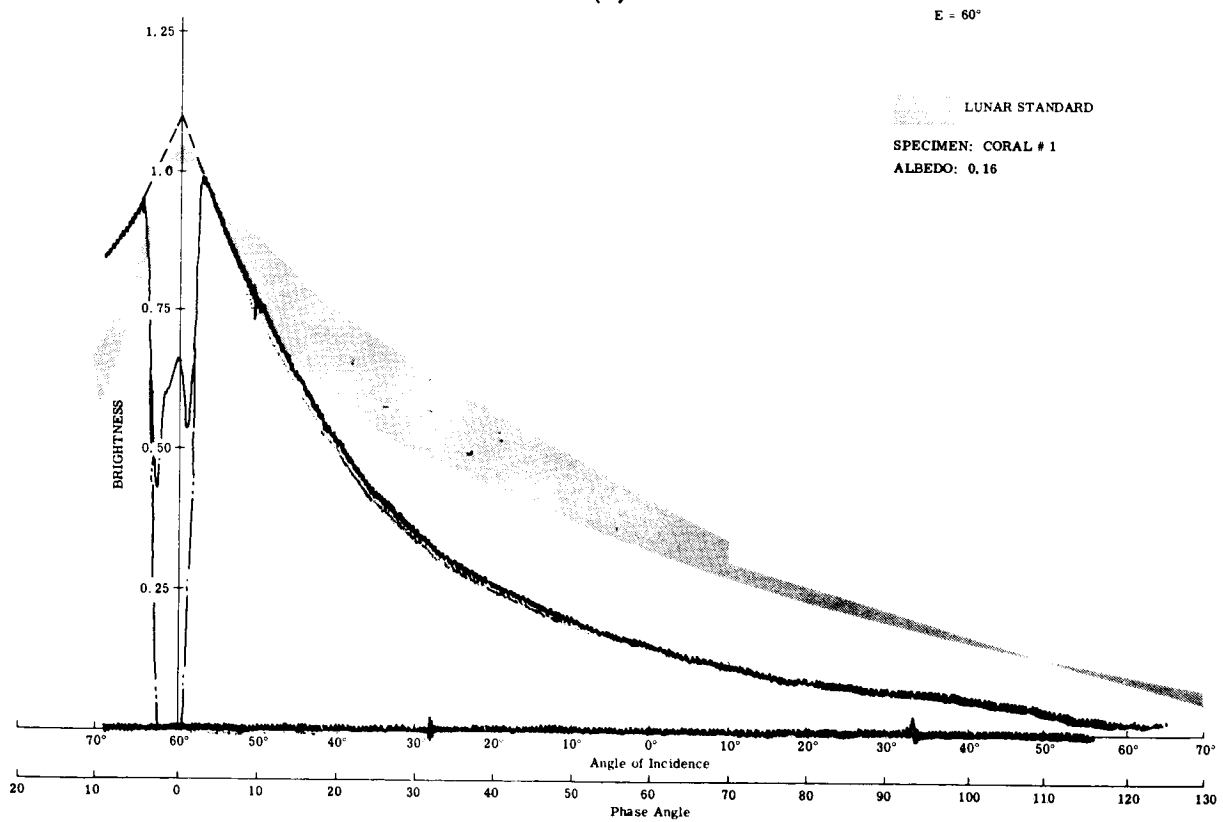
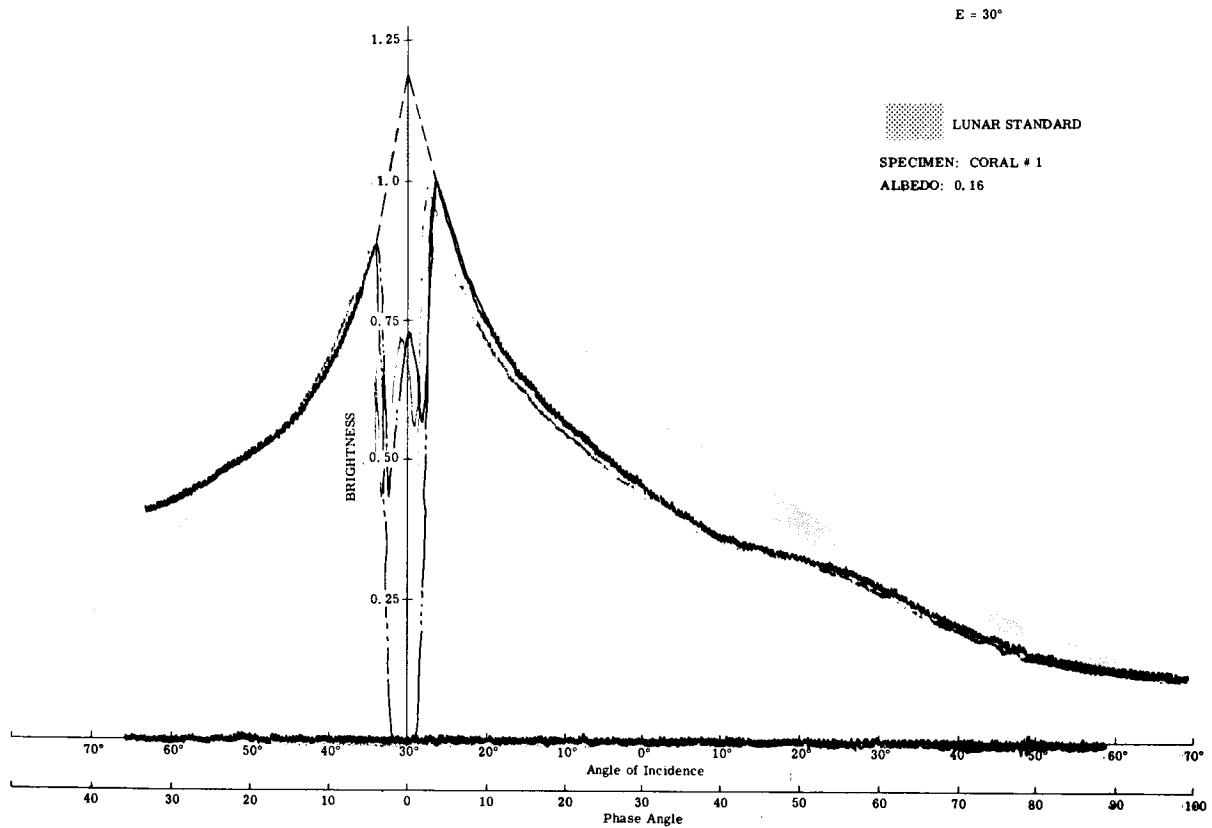
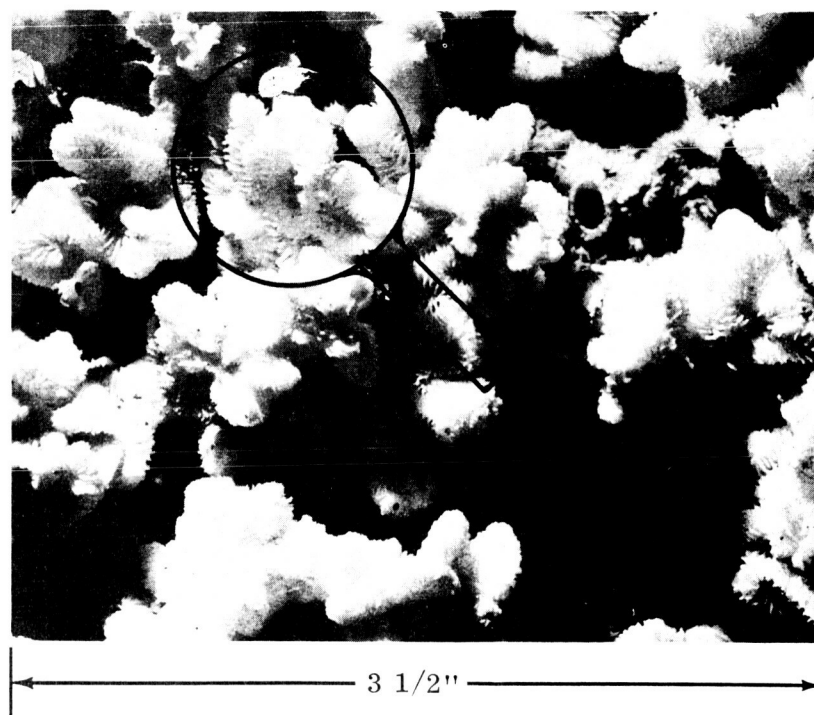
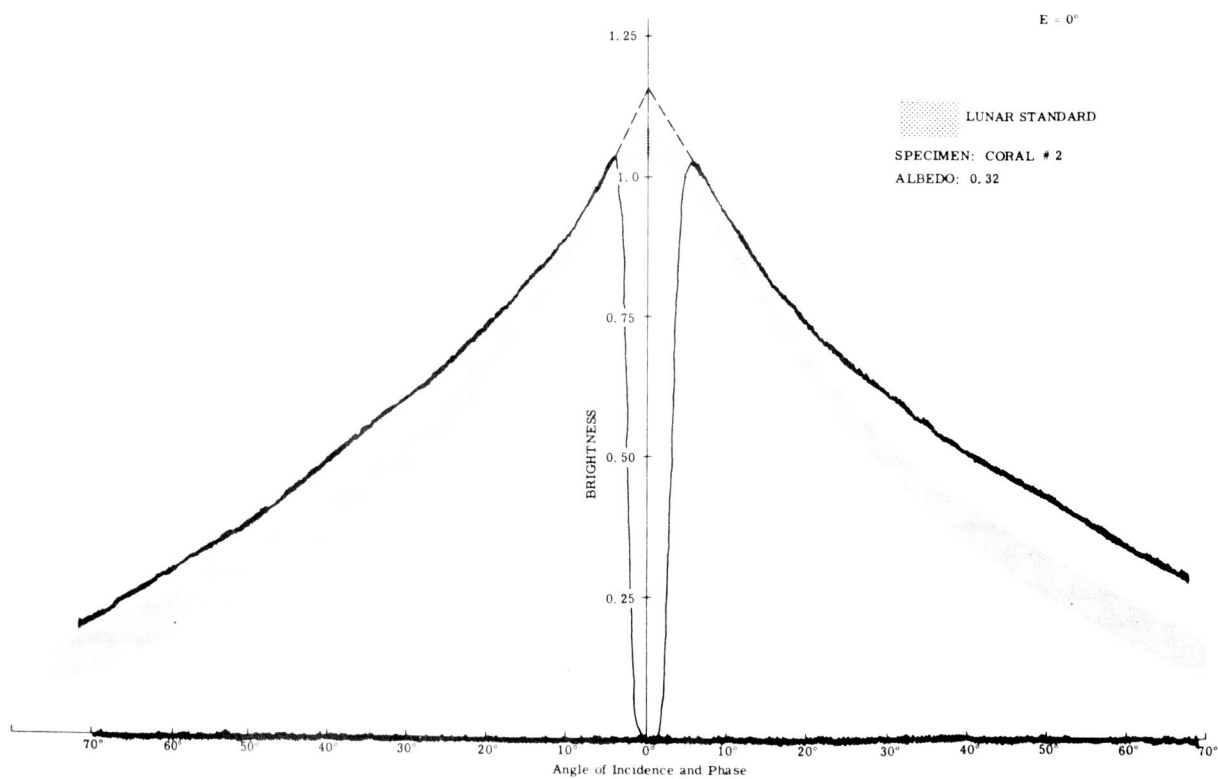


Figure 31. Coral #1 (Sheet 2 of 2)



(a)



(b)

Figure 32. Coral #2 (Sheet 1 of 2)

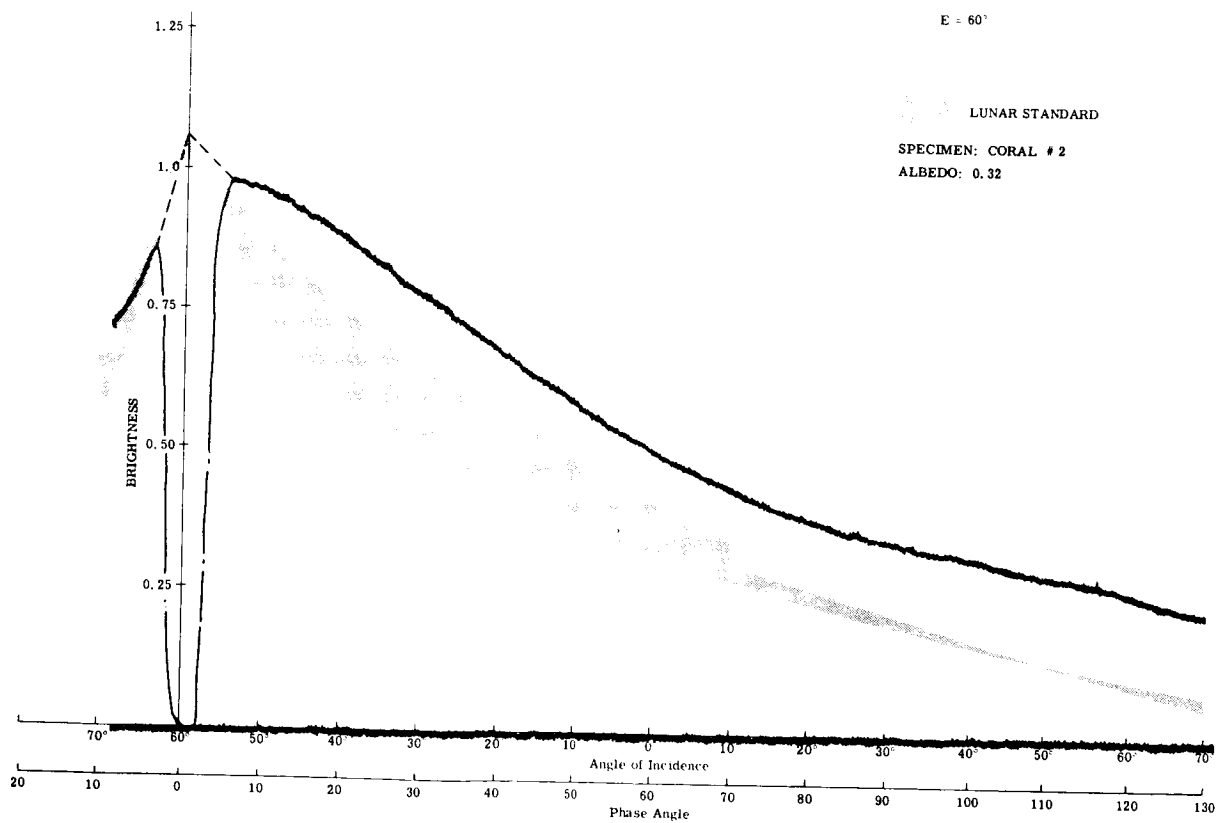
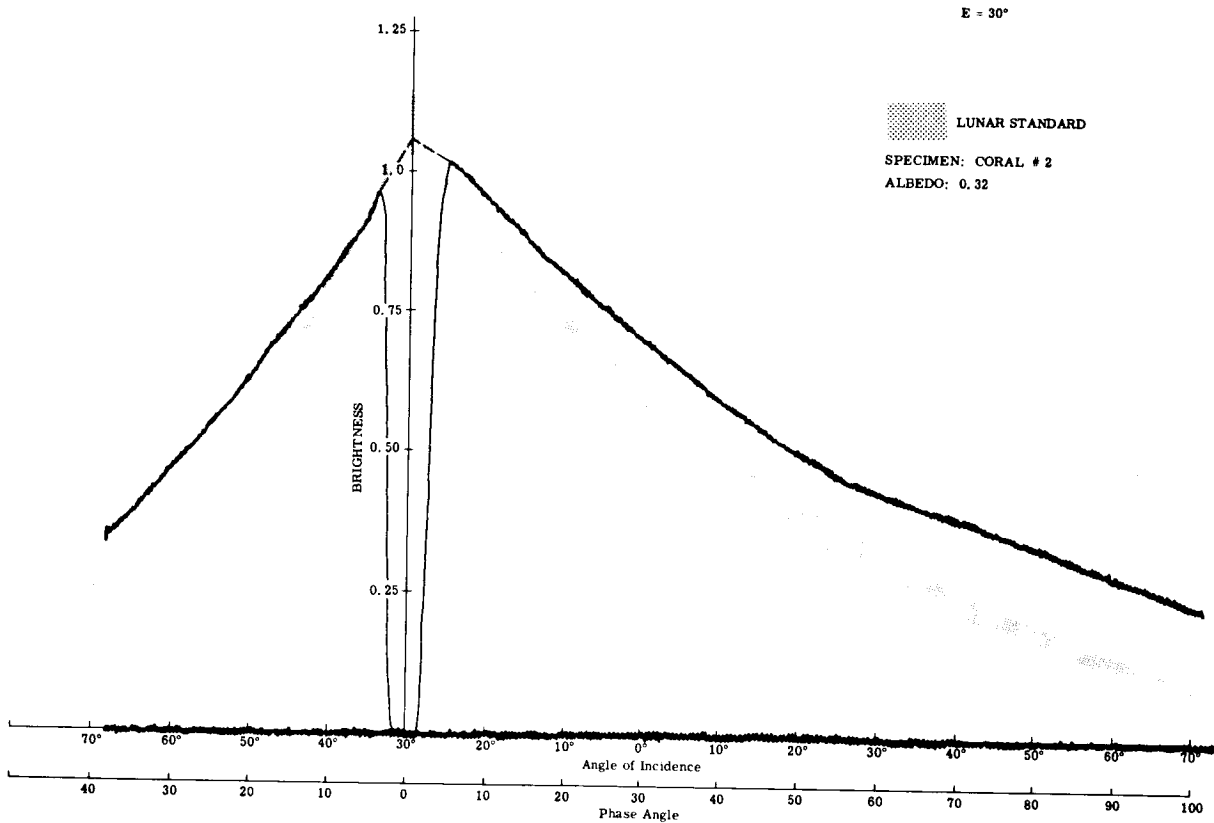
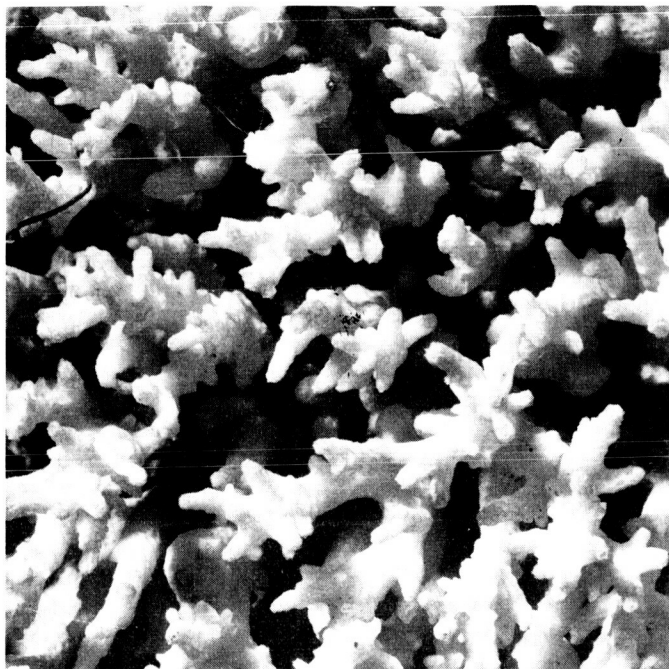
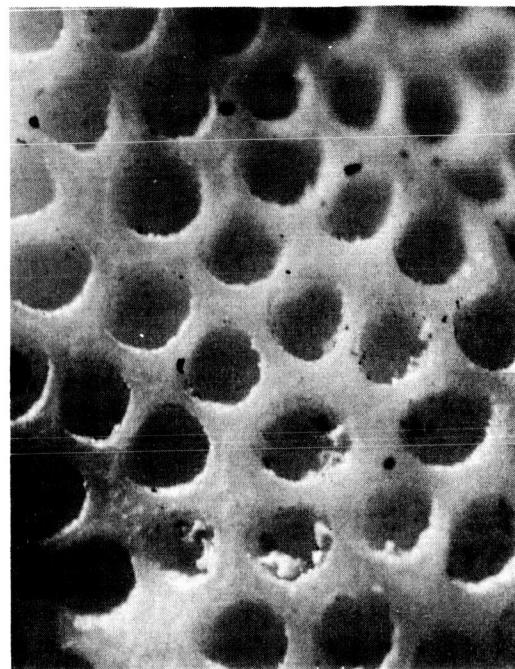


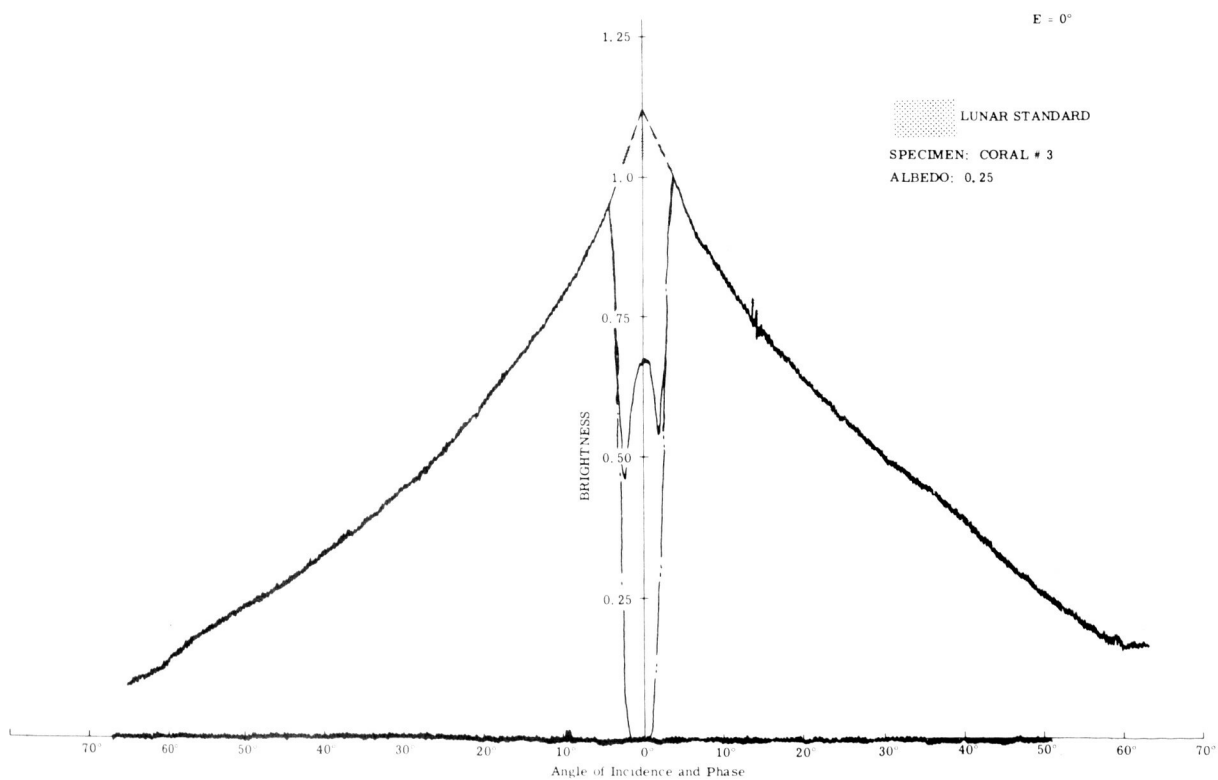
Figure 32. Coral #2 (Sheet 2 of 2)



(a)

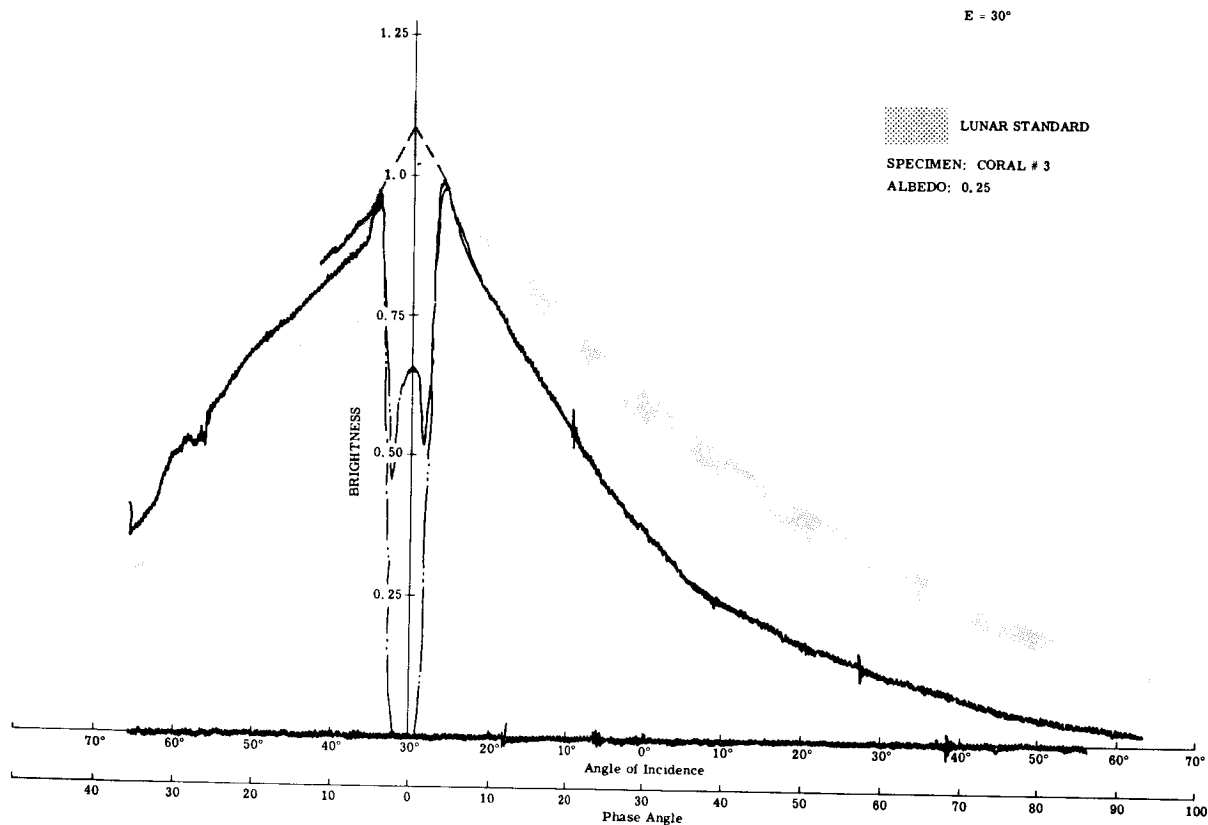


(b)

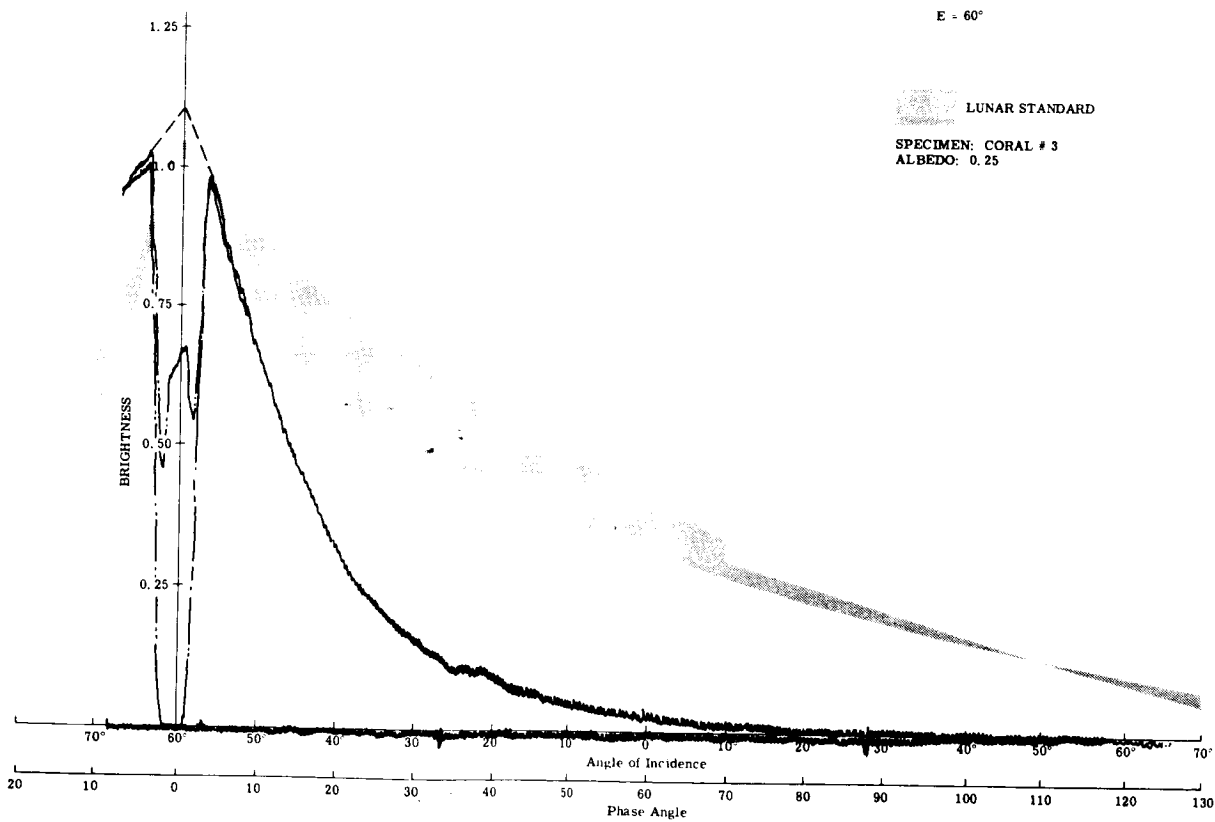


(c)

Figure 33. Coral #3 (Sheet 1 of 2)



(d)

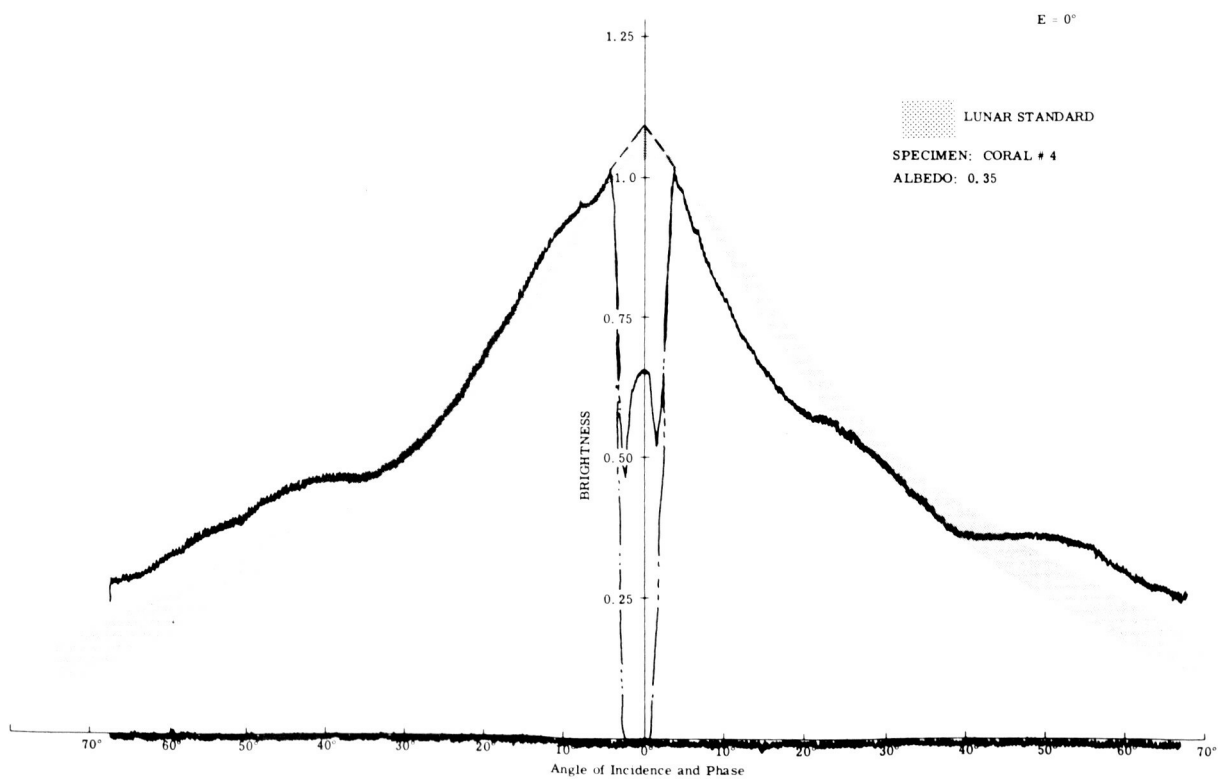


(e)

Figure 33. Coral #3 (Sheet 2 of 2)



(a)



(b)

Figure 34. Coral #4 (Sheet 1 of 2)

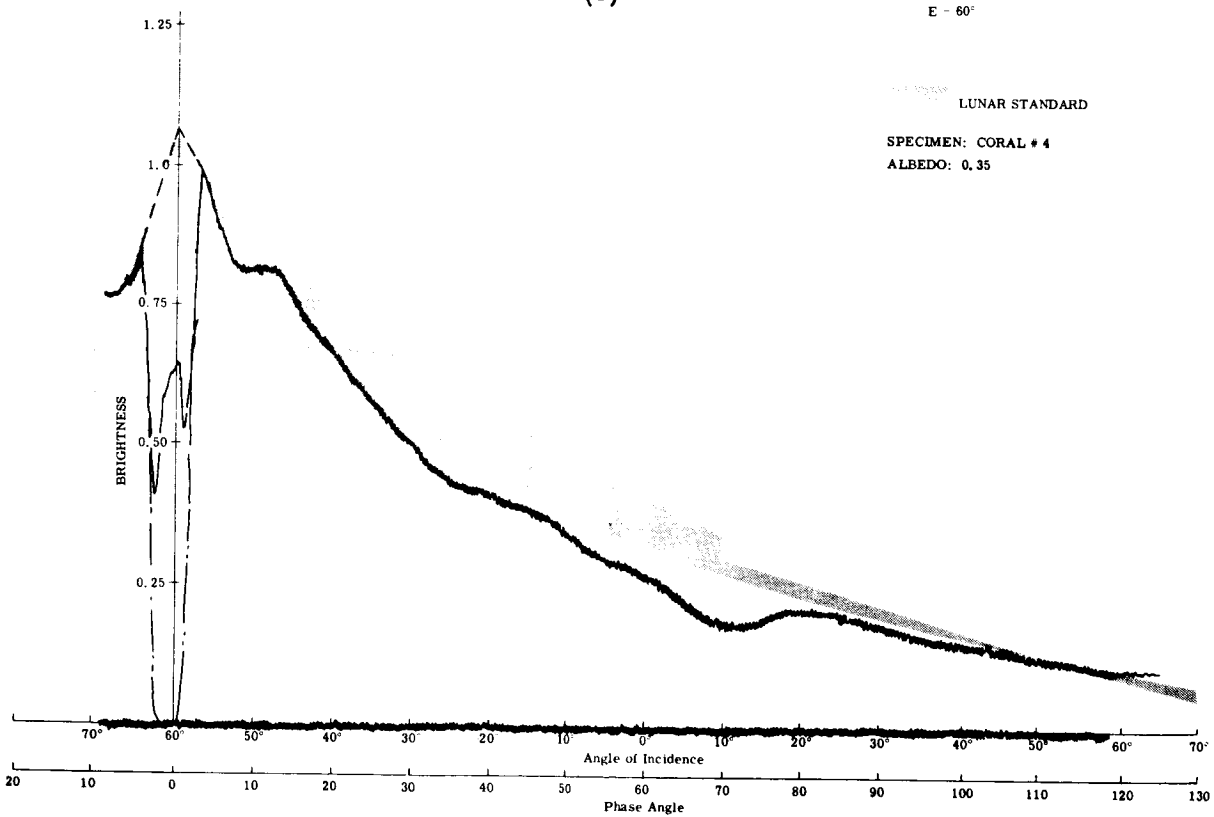
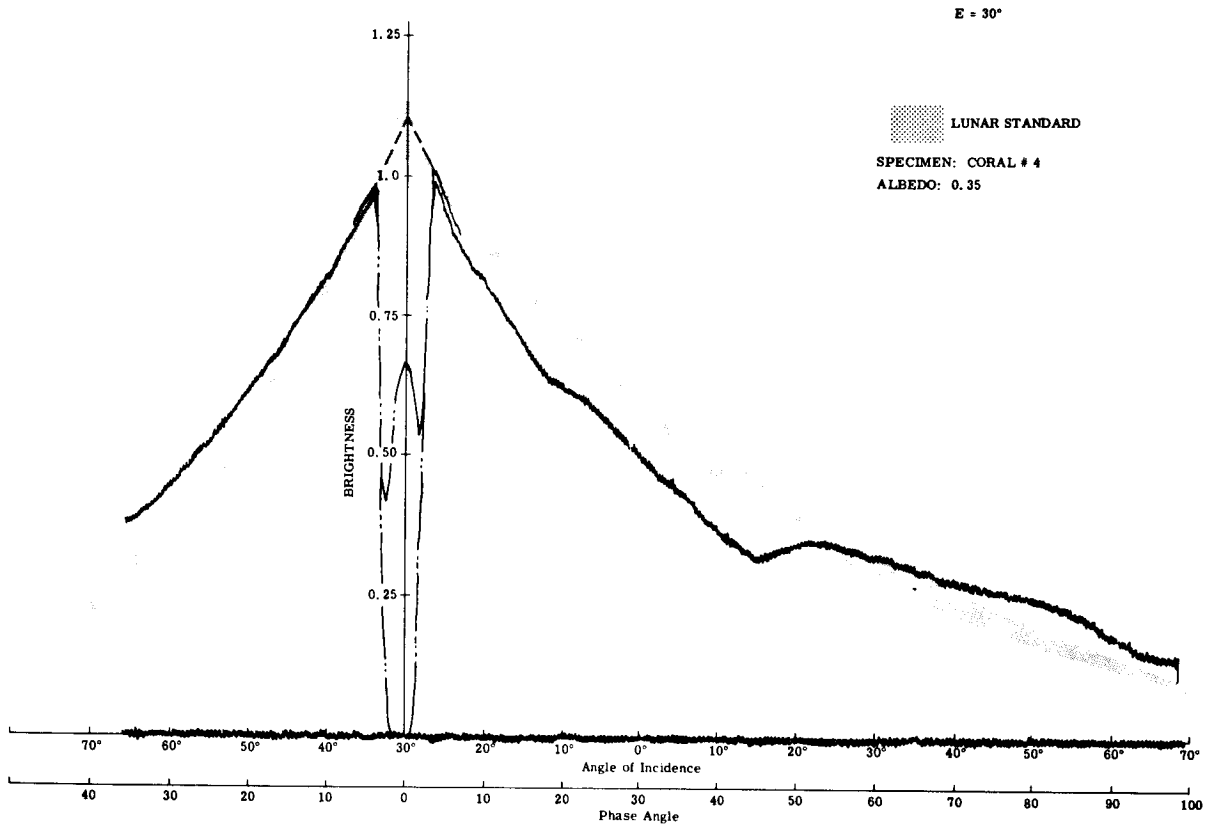


Figure 34. Coral #4 (Sheet 2 of 2)

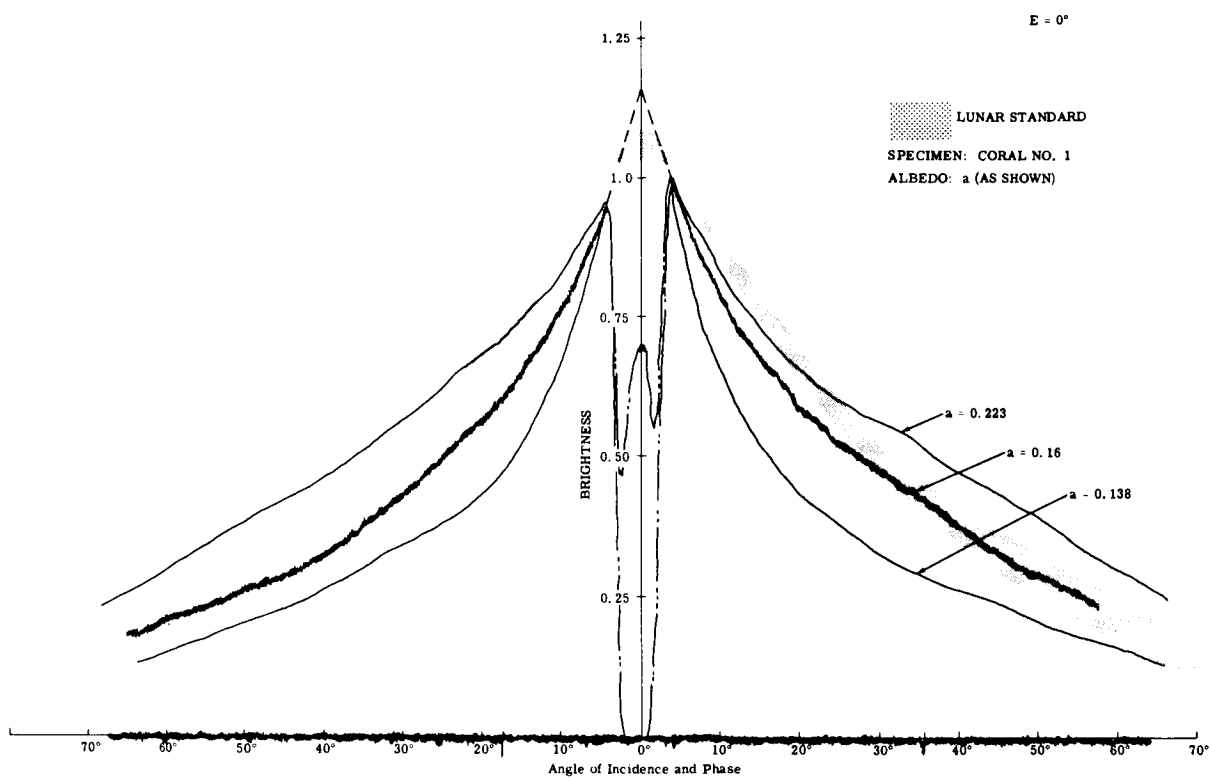


Figure 35. Coral #1 at Various Albedos

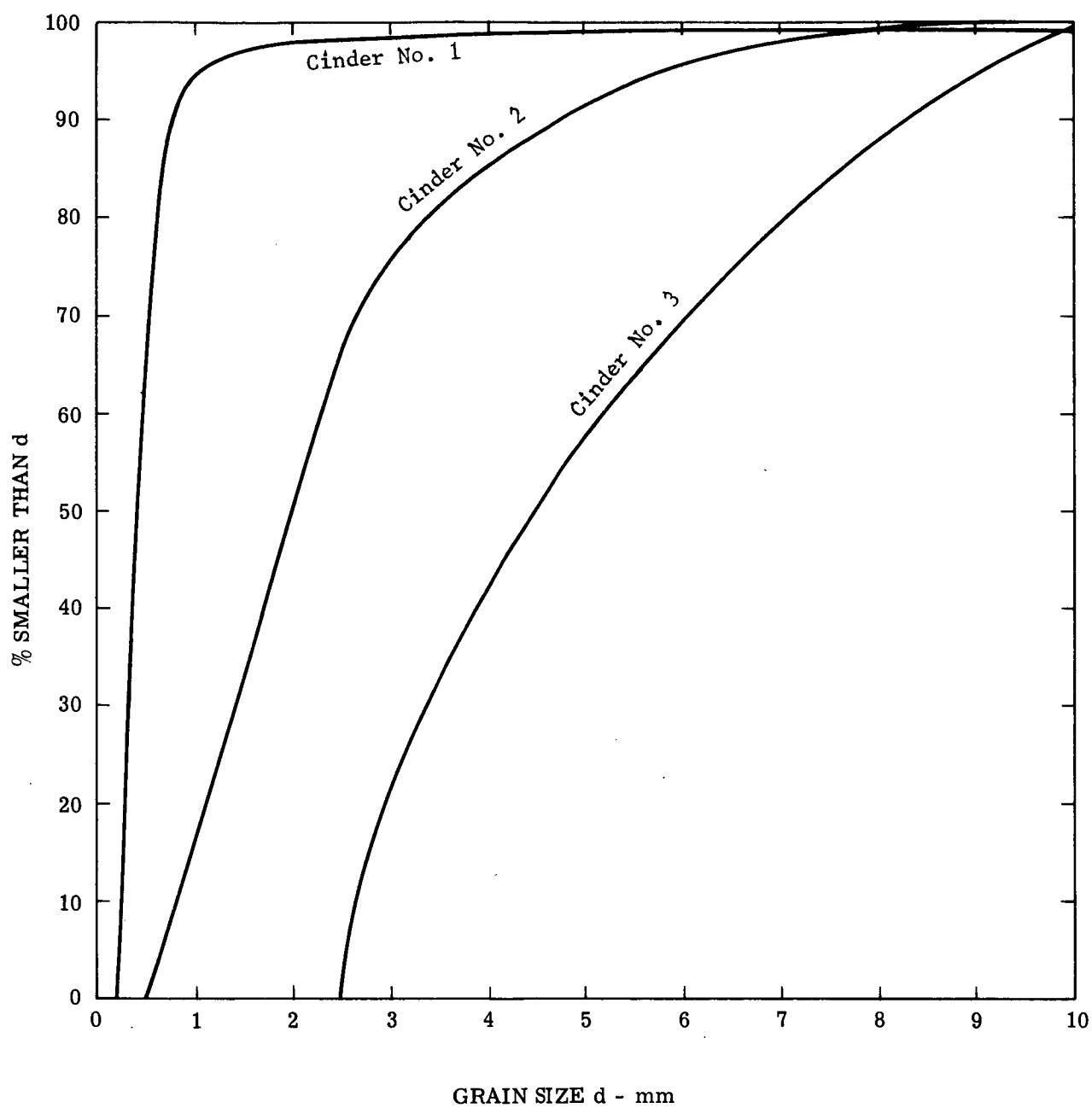
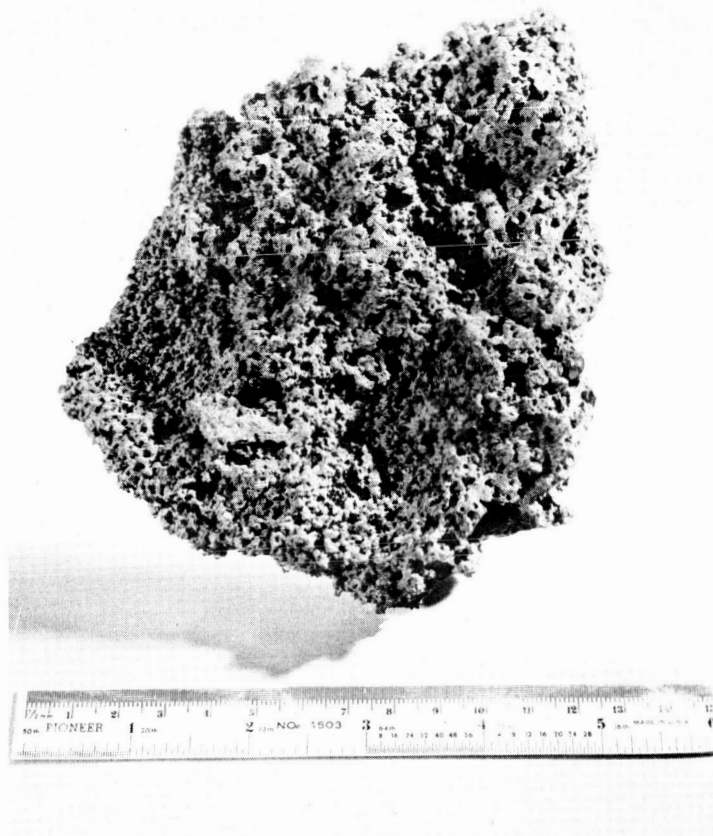
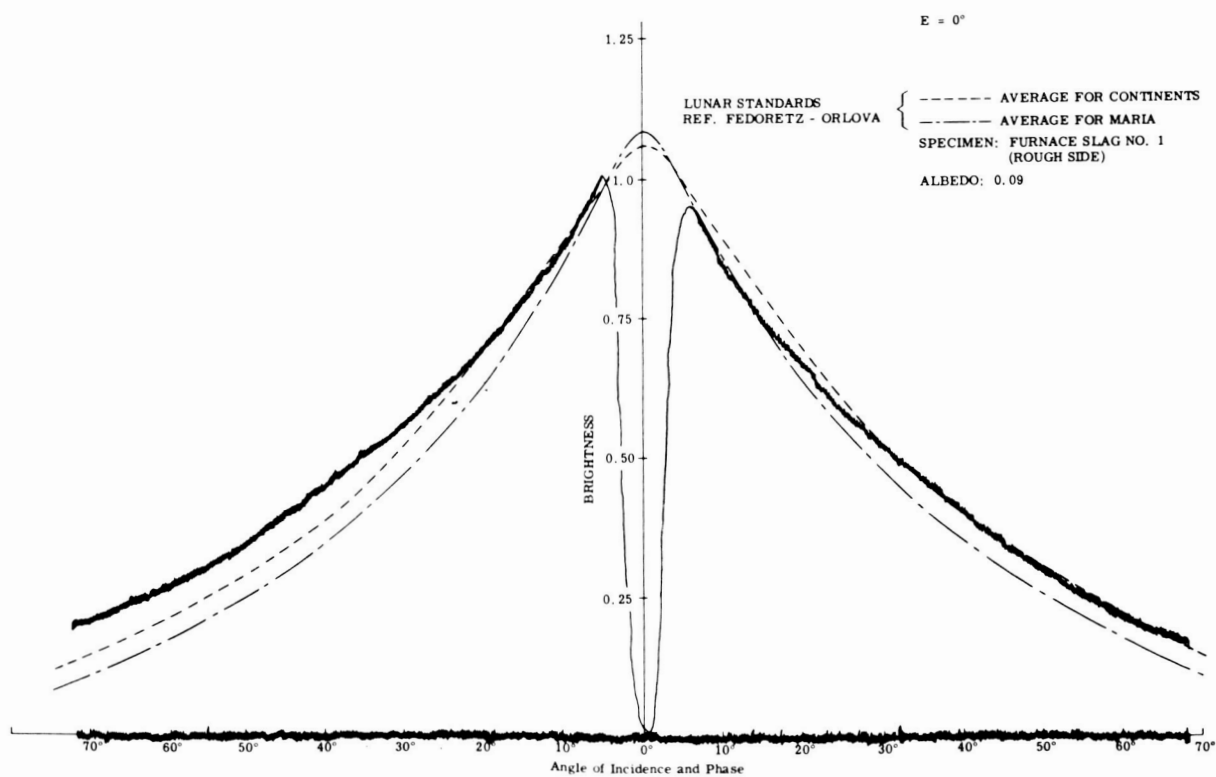


Figure 36., Grain Size Distribution of Hawaiian Volcanic Cinders



(a)



(b)

Figure 37. Furnace Slag #1 (Sheet 1 of 2)

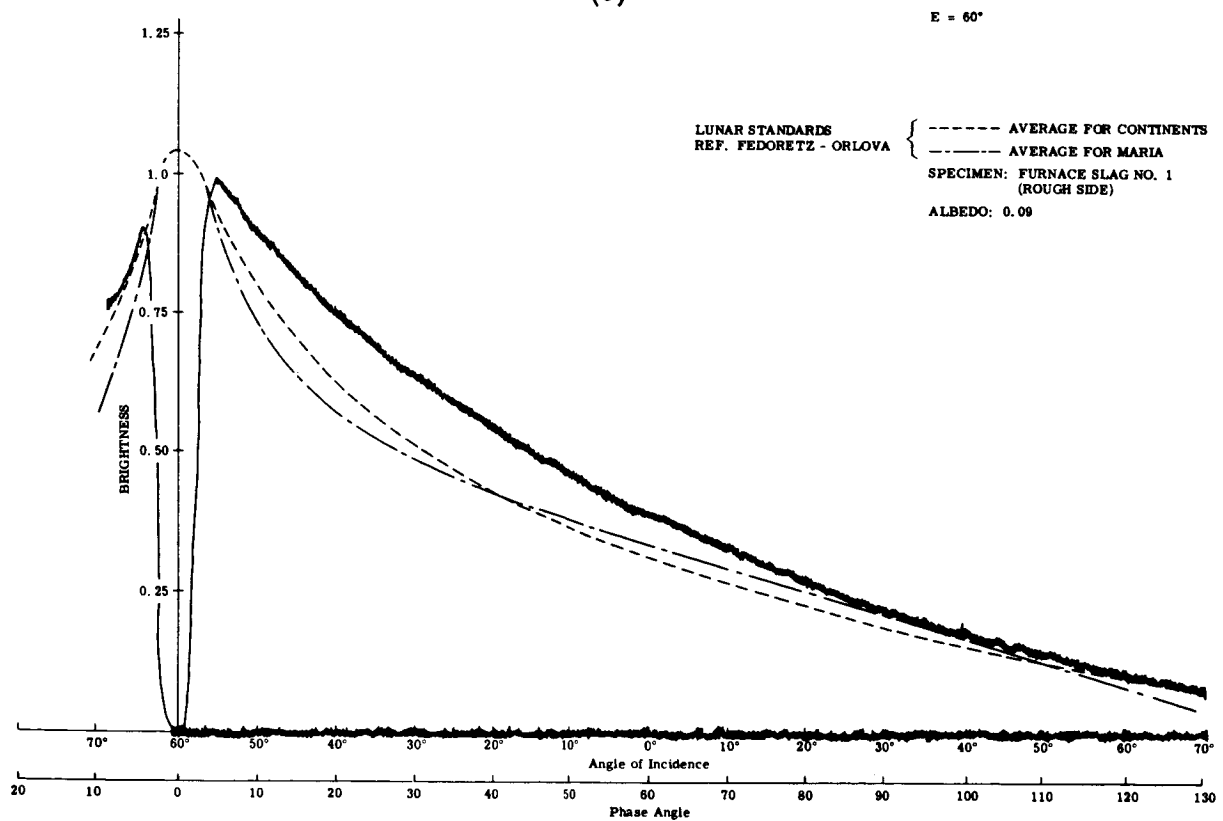
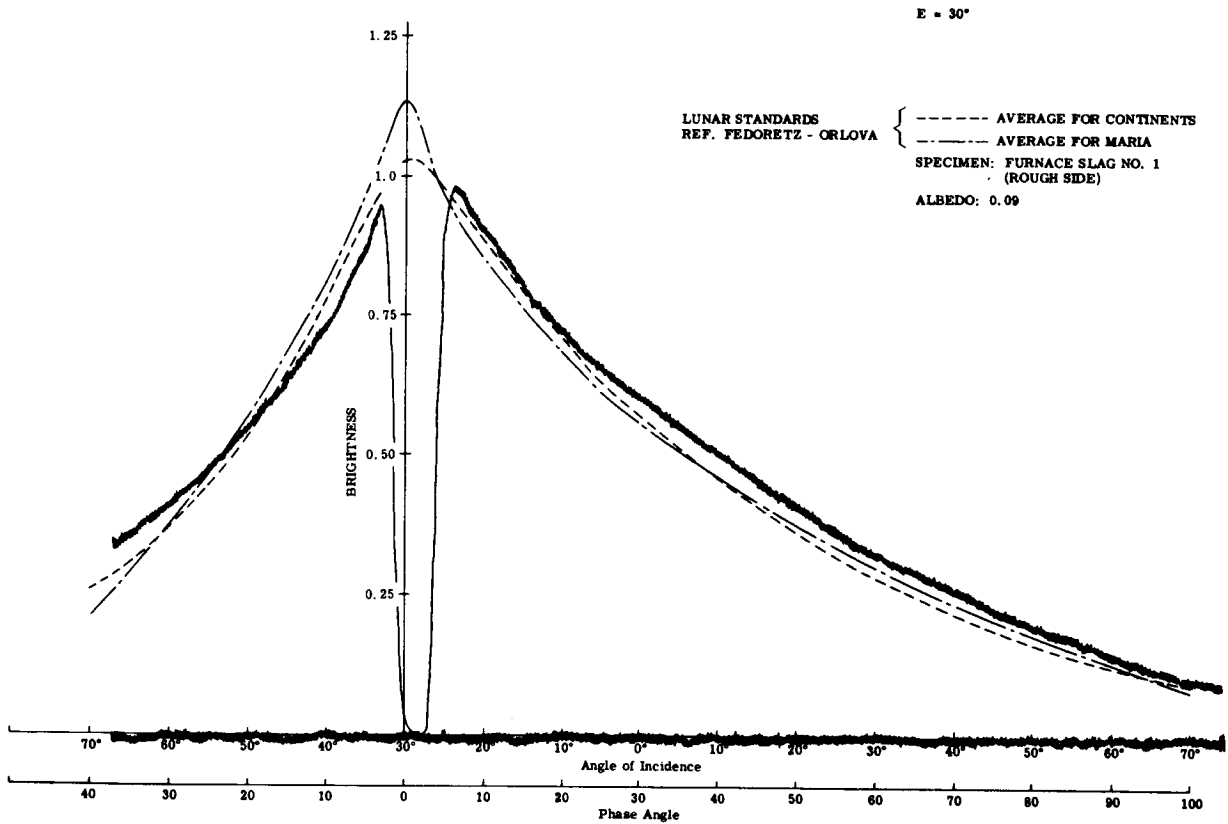
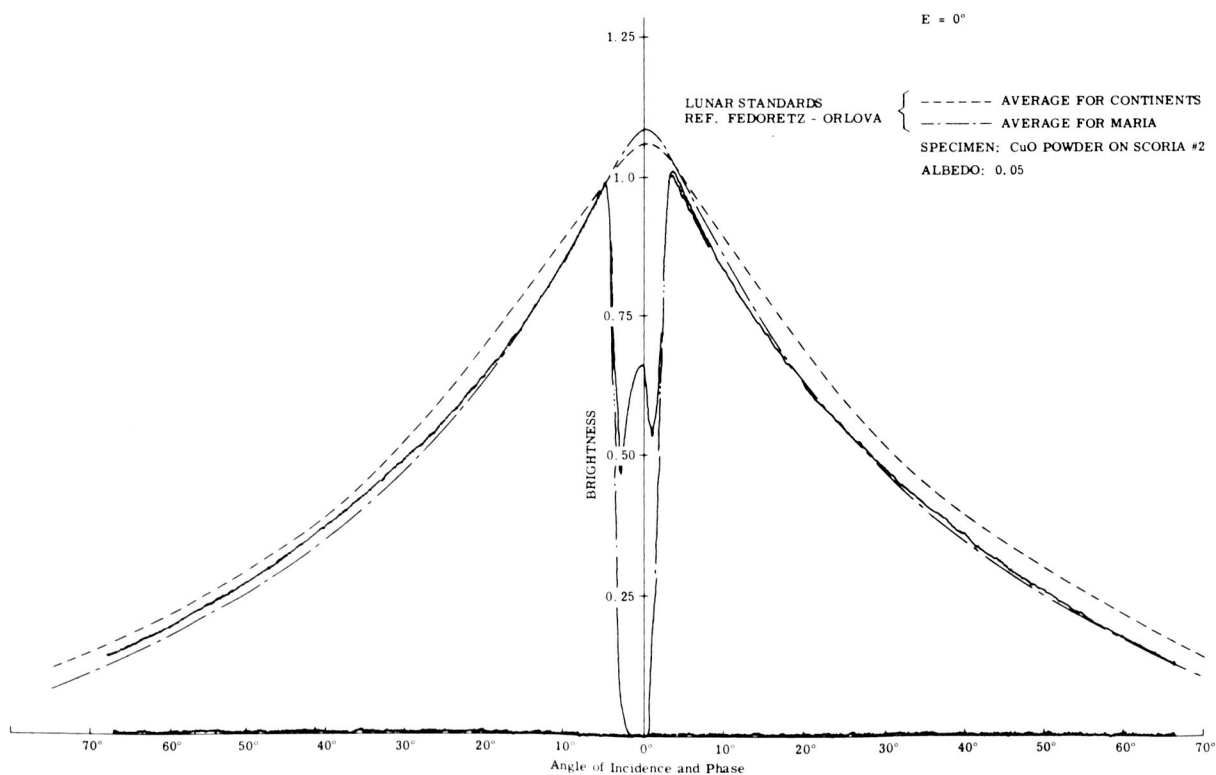


Figure 37. Furnace Slag #1 (Sheet 2 of 2)



(a) Without CuO Powder



(b)

Figure 38. CuO Powder on Scoria #2 (Sheet 1 of 2)

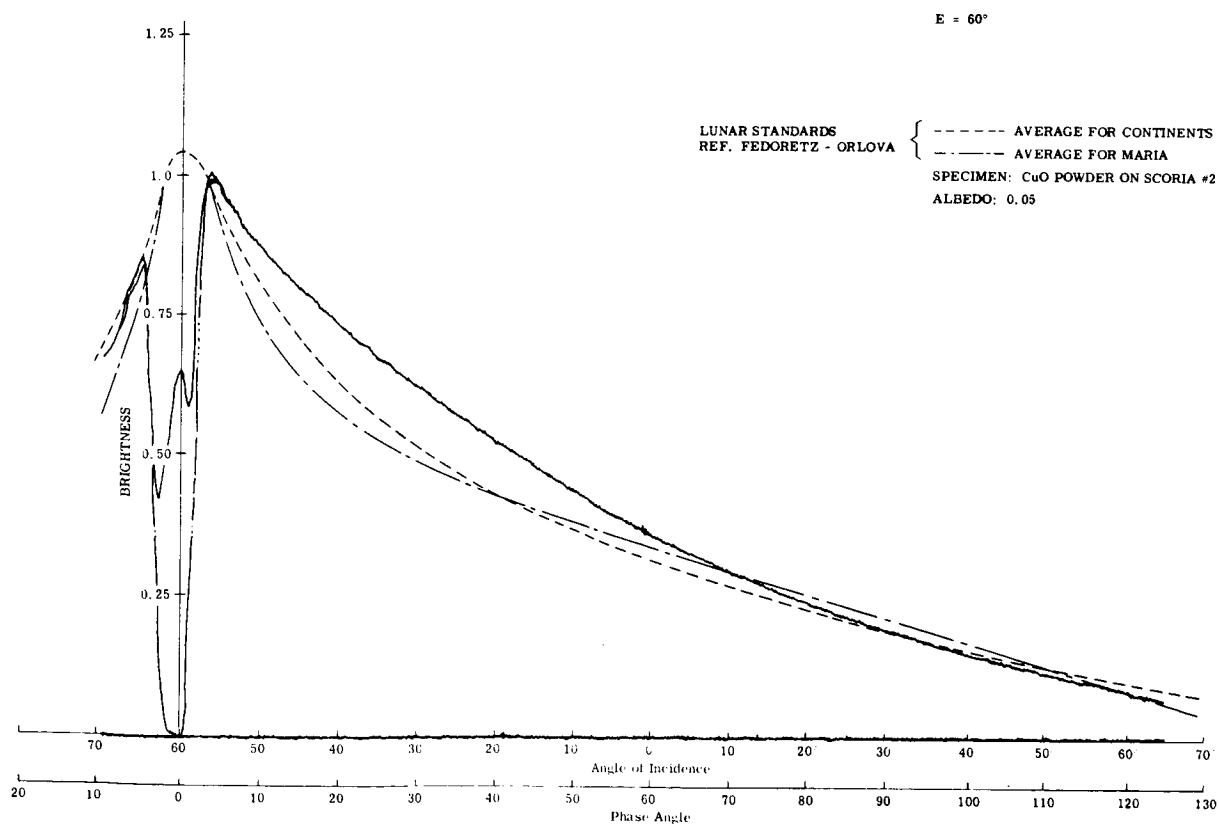
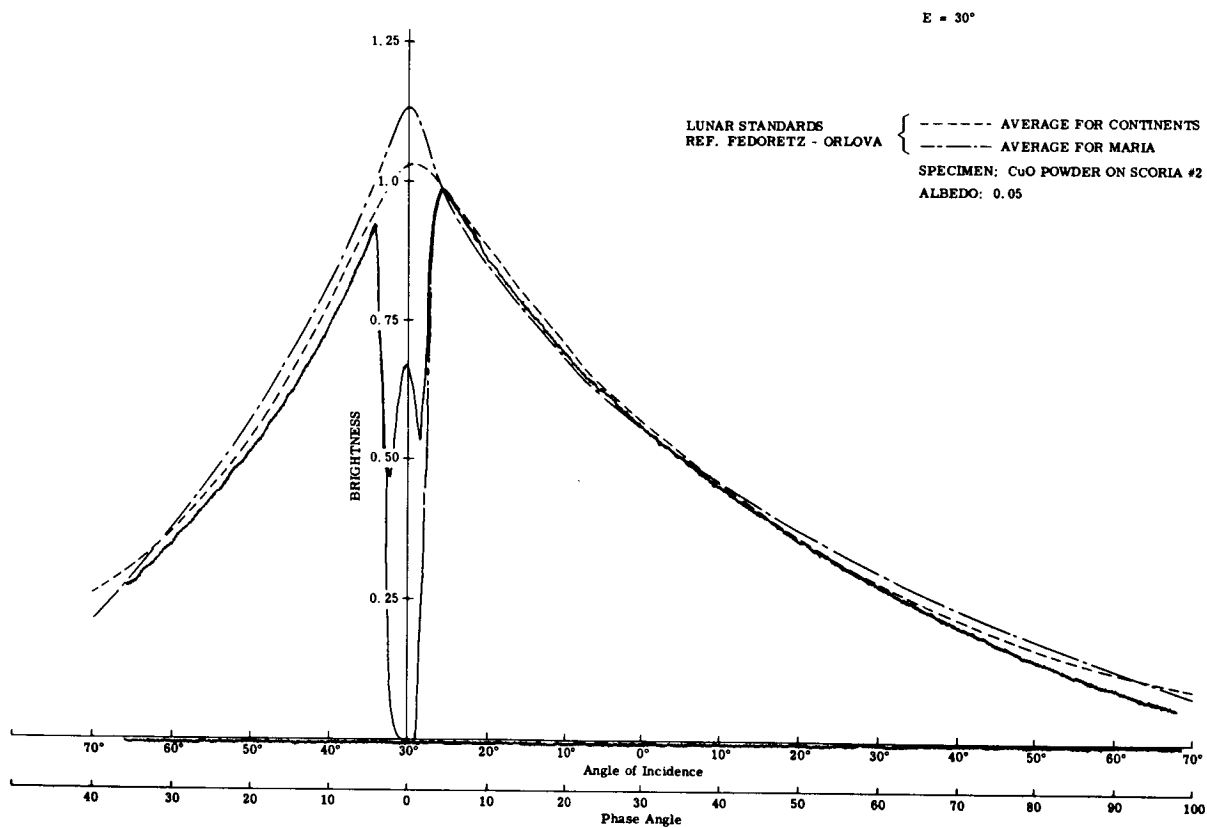
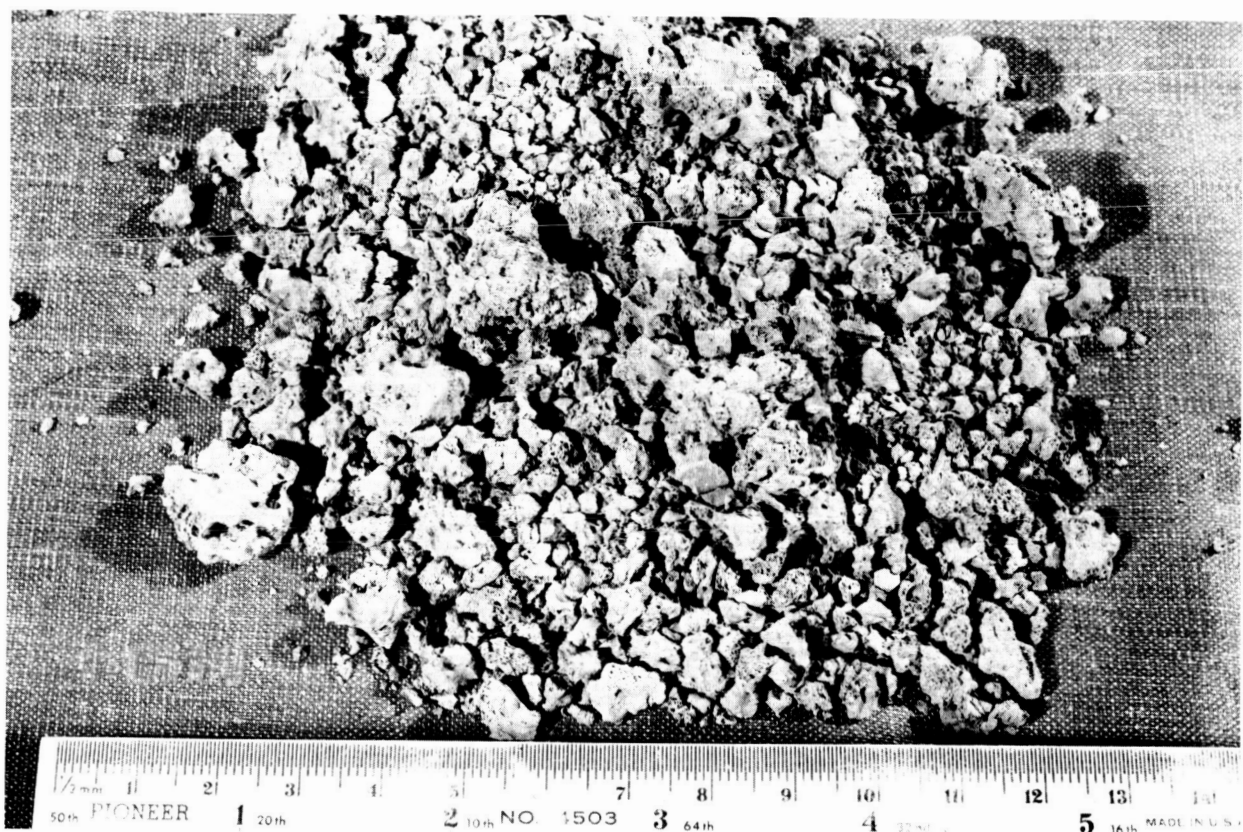
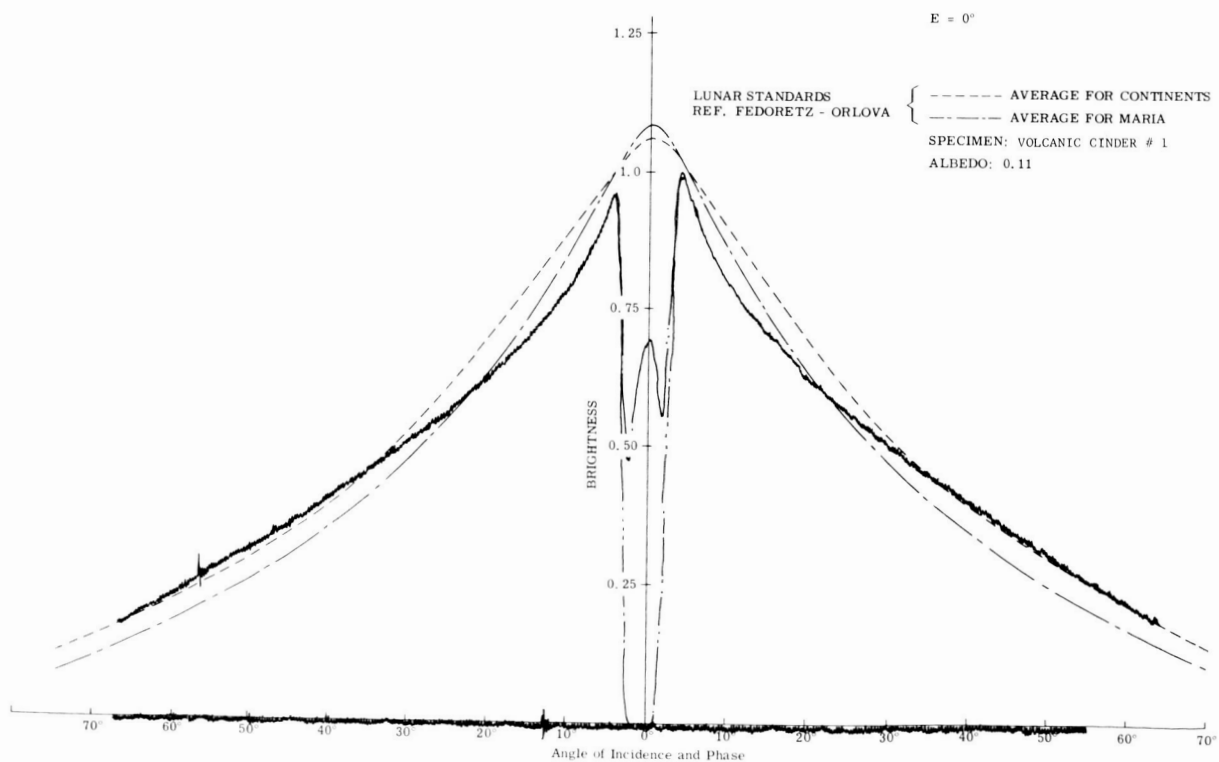


Figure 38. CuO Powder on Scoria #2 (Sheet 2 of 2)



(a)



(b)

Figure 39. Volcanic Cinder #1 (Sheet 1 of 2)

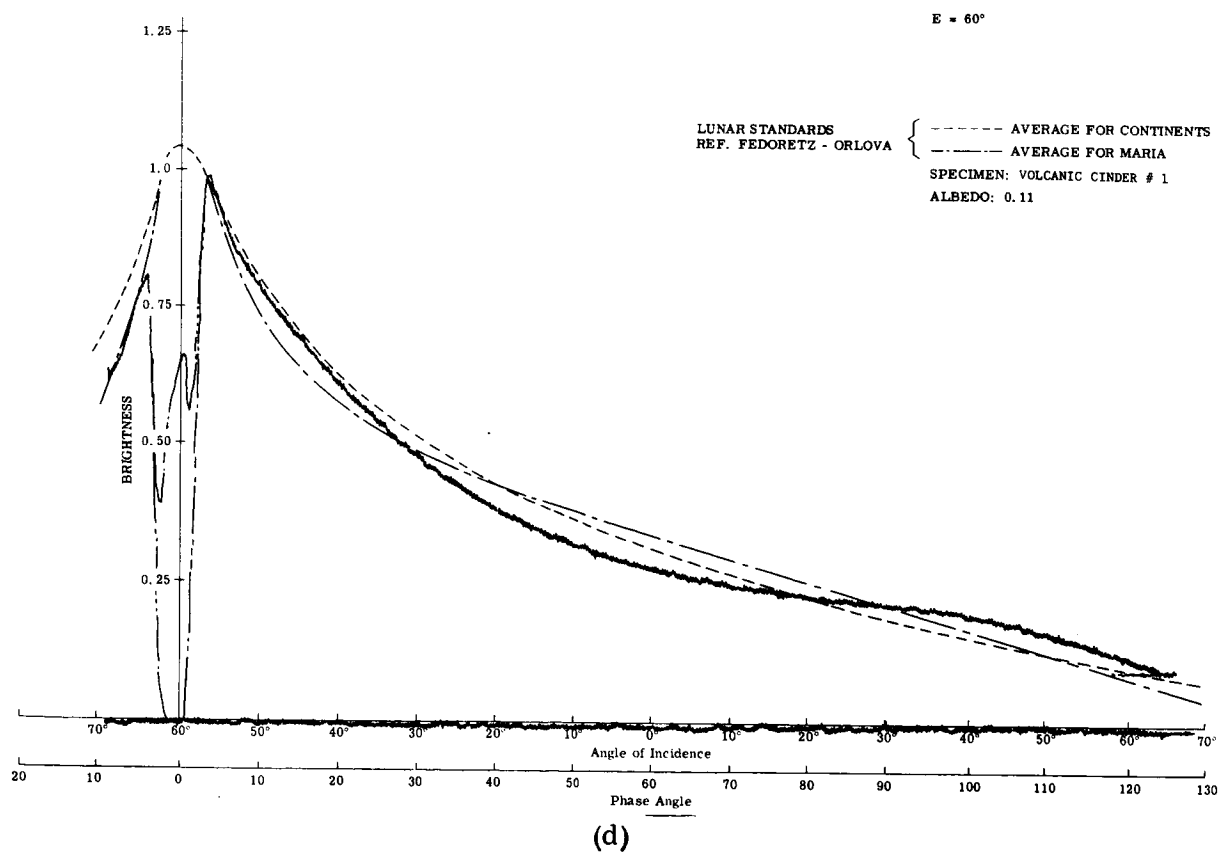
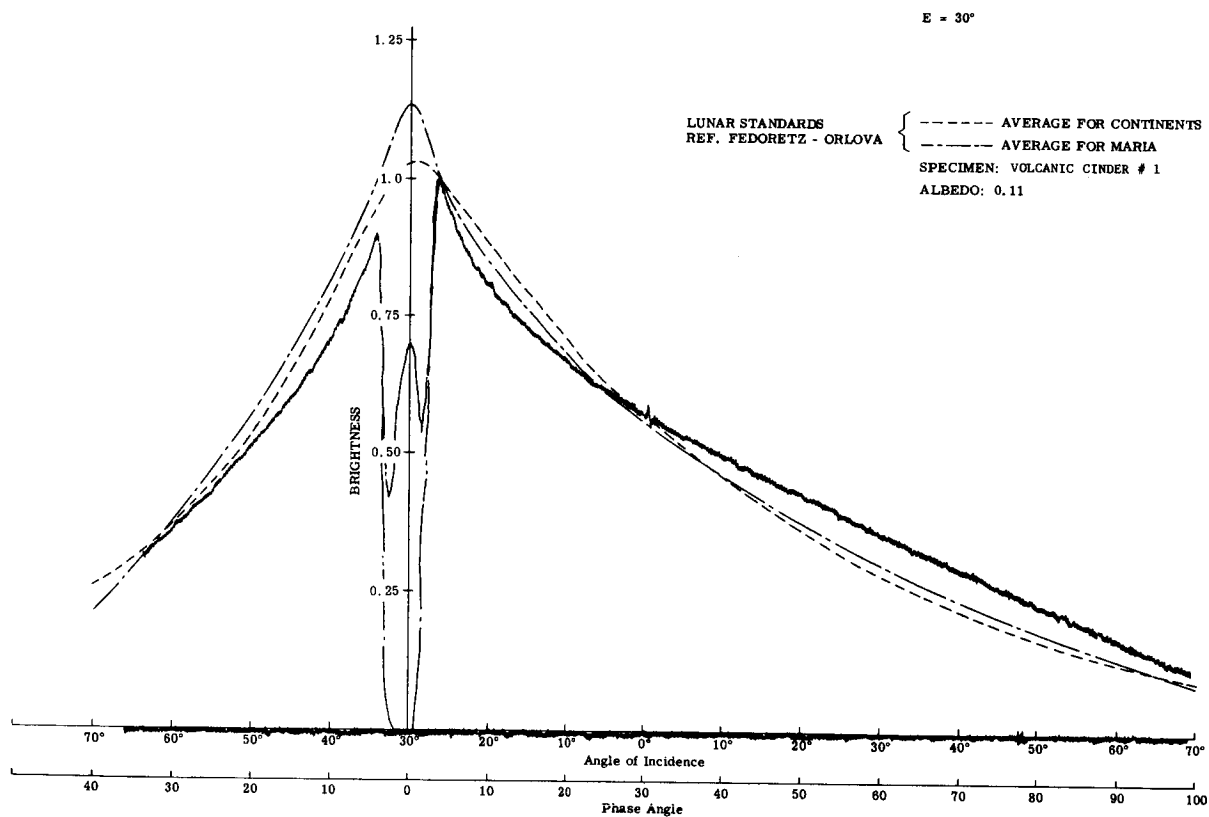
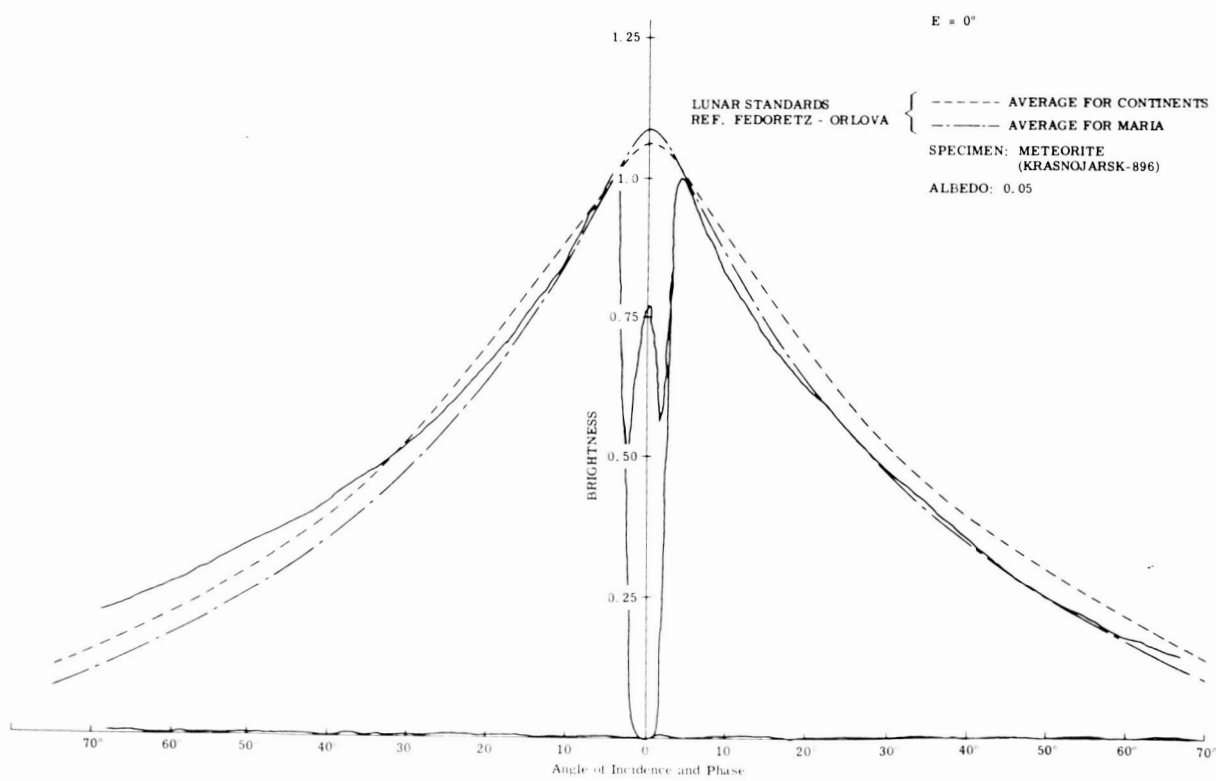


Figure 39. Volcanic Cinder #1 (Sheet 2 of 2)



(a)



(b)

Figure 40. Meteorite (Sheet 1 of 2)

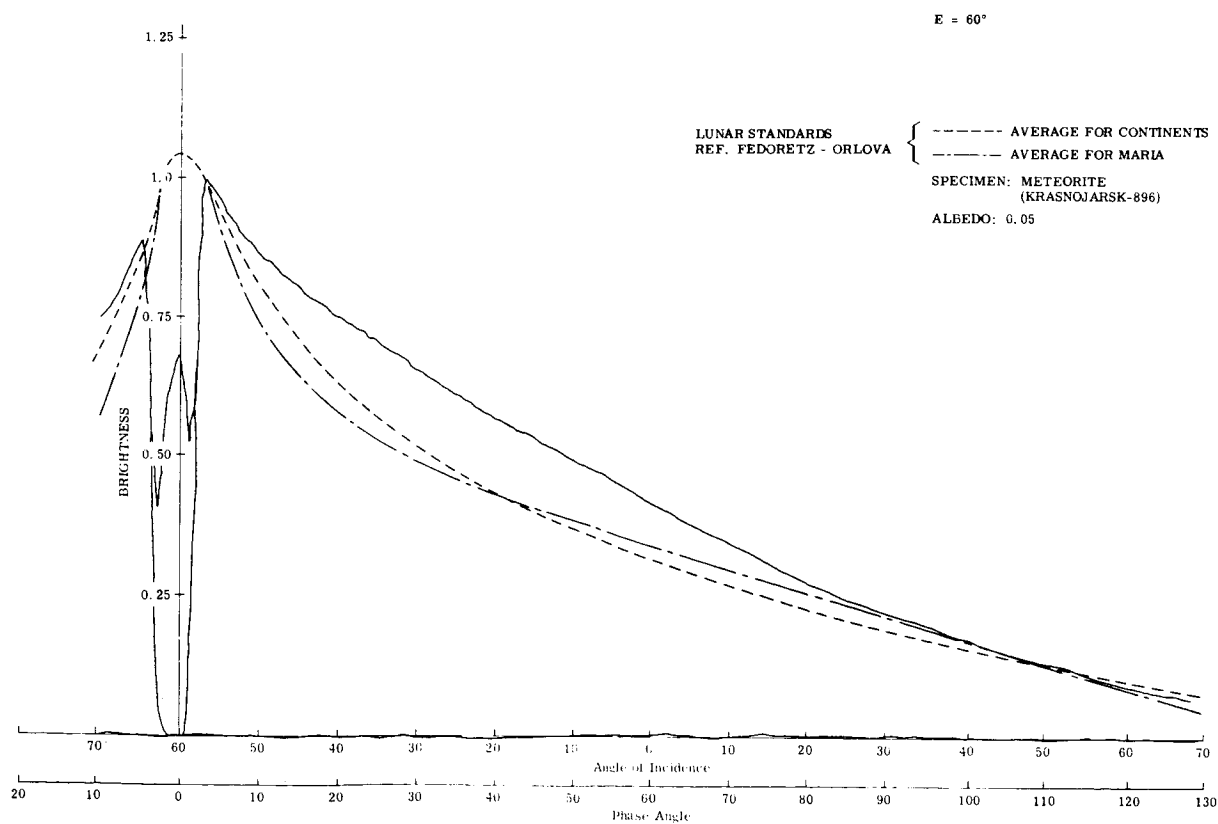
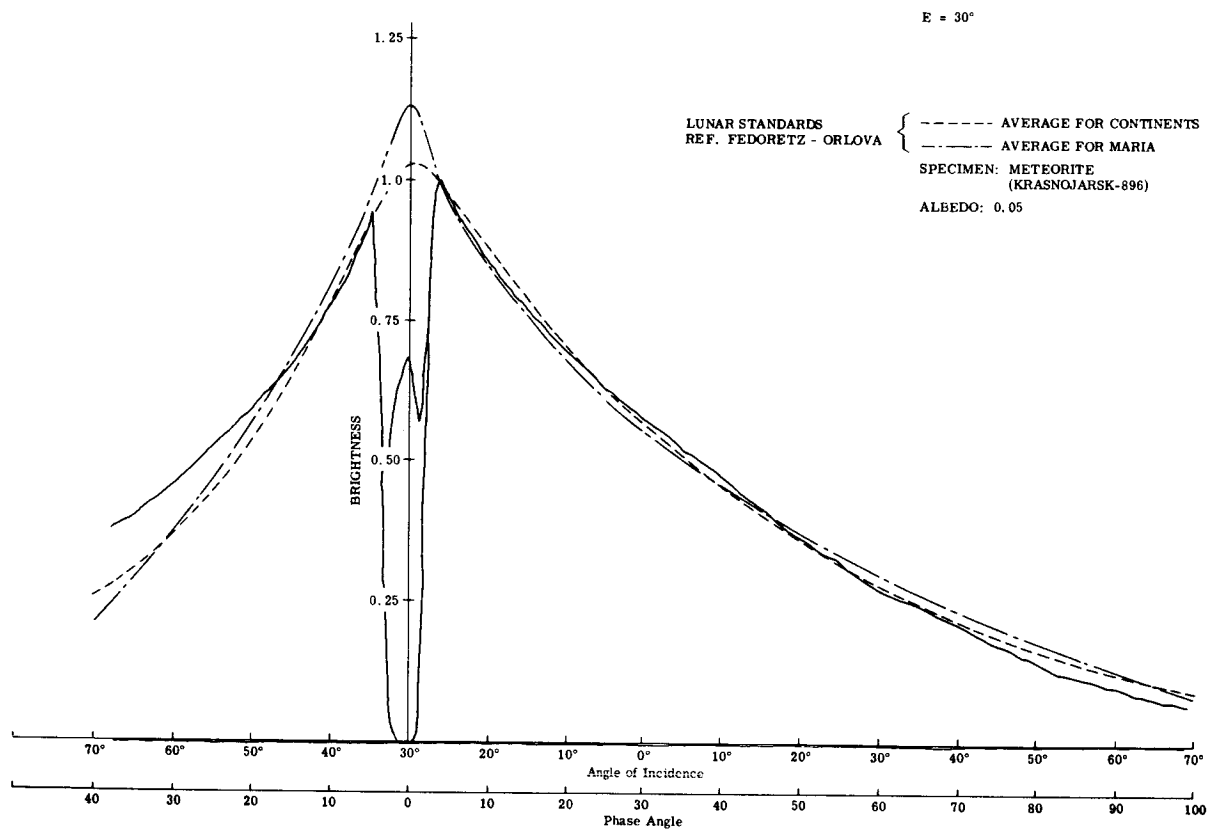


Figure 40. Meteorite (Sheet 2 of 2)

PHASE II — PHOTOMETRY OF ARTIFICIAL MODELS

Purpose

The experiments in this phase utilize test specimens that are artificially composed of "composite" (i.e., dust-covered) or "simple" elements devised for the purpose of developing an intuitive and, if possible, analytical grasp of the relationship of the geometrical and photometric properties of the lunar surface, or of any surface. More specifically, these investigations attempt to determine the relative contributions of micro and macroroughnesses and the albedo to the photometric function. Another significant objective of this phase is to develop simple models which simulate in an idealized form the microstructure of the lunar surface, and, unlike dust-covered models, lend themselves to controlled manipulations and graphical or mathematical analysis.

Test Specimens

The initial specimens in this phase consist (as originally proposed) of simple, wooden or metallic, geometrical solids of varying dimensions and slopes covered by a veneer of loosely sprinkled CuO and/or SiC (carborundum) powders of known albedo and photometric quality. The geometrical solids used were as follows: prisms, pyramids, cups and domes, and hexagonal depressions.

In the composite models, the CuO cover simulates the albedo and microroughness of the lunar surface, and the geometric shapes simulate the gross topographic features of the moon such as craterlets, bumps, ridges, and depressions. These models serve two distinct purposes. One of them is to determine the contribution of the gross features of the lunar surface to its photometric function. This is accomplished by changing the dimensions, slopes and location of the solids while keeping their albedo and microstructure unchanged. The other purpose these models serve is to provide the experience that is needed to create a contrived geometrical model that will match the lunar curves without the help of a backscattering powder veneer. It is desirable to eliminate the dust cover (without compromising the backscatter) because the "fairy castle" structures built by fine powders are too small and complex for detailed scrutiny, whereas those built by geometric, "macro" (i.e., visible to the naked eye) elements could lend themselves to quantitative analysis and could illustrate graphically the relationship of the changes of light and shadow on and within a porous model to their photometric signature.

As was anticipated, the knowledge acquired from the measurement and analysis of a sufficient number of composite models led to the creation of a simpler, more basic model essentially consisting of centimeter-size horizontal and vertical elements. This model is described and discussed in a succeeding section.

Experiments

Brightness vs. phase measurements were performed on various combinations of "simple" and "composite" models. Model geometry, albedo, viewing angle, and condition of illumination (i.e., relative position of the intensity equator with respect to model axis) during each measurement are listed next.

I. The following CuO-covered models were measured at 0° , 30° , and 60° viewing angles:

1. 60° pyramids, 1" high (Fig. 41a).
2. Hemispheric cups and domes, $3/4$ " in diameter, (Fig. 42a).
3. Hexagonal depressions, about $1/2$ " across (Fig. 42b).

II. The prismatic solids, covered with CuO powder, were examined at 0° viewing angle under the following conditions:

1. One to five 45° -prisms, 3rd column in Fig. 43.
 - a. Intensity equator parallel to ridges, Fig. 44.
 - b. Intensity equator perpendicular to ridges, Fig. 45.
2. 5-prism assemblies with 30° , 45° , and 60° base angles, fifth row in Fig. 43.
 - a. Intensity equator parallel to ridges, Fig. 46.
 - b. Intensity equator perpendicular to ridges, Fig. 47.

III. Mixtures of CuO and SiC powders in various proportions have been sprinkled on a 5-prism assembly and a flat plate. The results at 0° viewing angle are shown in Figs. 43 and 44.

IV. The "Thumb Tacks" model with and without vertical strips were measured at 0° , 30° , and 60° viewing angles. The results are shown in Fig. 54.

The specimens described in Parts I, II, and III above are termed "composite" models; those in Part IV are termed "simple" models, and are discussed in a separate section.

Discussion of Test Results of "Composite" Models

I. CuO-covered geometric solids examined at 0°, 30°, and 60° viewing angles. The albedo of all these models, regardless of the number of the gross features or viewing position, is the same, and is equal to that of the CuO powder on a flat surface.

1. 60°-pyramids, Fig. 41a. Four test curves are shown in Fig. 41b, taken at 0° viewing angle, representing the photometric properties of a CuO-covered flat surface occupied by one, five, and nine pyramids respectively. Notice that the addition of pyramids progressively increases the slope of the backscatter curve from a value less than the lunar backscatter to one slightly greater. Figures 41c and d show the test results at 30° and 60° viewing angles for the five and nine pyramid patterns. At these viewing angles the 9-pyramid pattern shows a larger deviation from the lunar data than at 0°. These curves clearly indicate that gross features do contribute to the backscattering of light from a surface, but, under the conditions of this experiment, this contribution is negligible compared to that of the microstructure and is within the lunar data scatter band, particularly at 0° viewing positions. It is interesting to note that the best fit is not given by the model "saturated" with pyramids, but by the checkered pattern in which the pyramids are interspaced by flat areas.

2. Hexagonal pits and hemispherical pits and domes. These models, shown in Figs. 42a and b, are made up of stamped metal plates covered with a thin layer of CuO powder. The photometric measurements at the three viewing angles are shown in Figs. 42c, d, and e. The curves for a flat surface covered with CuO are also shown in these figures for comparison. As in the case of the pyramids, there is an increase in the backscatter, but it is noticeably smaller probably due to the fact that the shadow-casting pits and domes are not so deep (or high) and so sharp in outline as the pyramids. The increase in backscatter is larger for the hemispheric shapes than for the hexagonal shapes, but the difference is not large enough to warrant further analysis at present.

II. CuO-covered prismatic solids at normal viewing angle. The photometric properties of these models depend upon the position of the intensity equator with respect to the prism ridges. The intensity equator is determined by the motion of the sun-source; the equator is located in the plane of vision which contains the specimen and viewer. Both directions of sun-source travel, i.e., parallel and perpendicular to the prism ridges, have been investigated, both analytically and experimentally. The discussion of test results is presented in terms of model combinations and lighting geometry.

Condition No. 1: One to five prisms, constant 45° base angle (column 3, Fig. 43); intensity equator parallel to the prism ridges.

The photometric properties of the CuO-covered 45° prisms at normal viewing angle are shown in Figs. 44a and b for one to five prisms. The test curves are all nearly identical, indicating that the number of prisms does not affect the photometry of the surface under this particular set of conditions; this set is, in effect, equivalent to a flat surface inclined to the horizontal at the same angle as the base angle of the prism. This equivalence is confirmed by analysis and actual measurement. The analysis is presented in Appendix A, and the measurement of a CuO-covered flat plane at 45° is shown in Fig. 44c. The test curve in this figure does not differ noticeably from the curve obtained from the CuO powder on a horizontal surface, shown in Fig. 2. Thus, it is not necessary to measure the photometric properties of the other prisms in Fig. 43 under this particular condition of illumination.

Condition No. 2: Same as Condition No. 1 except that intensity equator is perpendicular to the prism ridges.

The photometric properties of the CuO-covered 45° prisms at normal viewing angle are shown in Figs. 45a to e for one to five prisms respectively. In general, the test curves have a slightly sharper backscatter than measured in the previous condition, because under transverse lighting the prism ridges are in a position to cast shadows. The test curves differ from one another only to the extent that the "bend" at 45° phase shown by the single-prism curve, Fig. 45a, becomes gradually smoother with each additional prism, Figs. 45b to e. A typical analysis of the one-prism and three-prism configuration is presented in Appendix A. This analysis confirms the experimental curves, as indicated by the plotted points in Figs. 45a and c, and shows that the subsequent blending of the "bend" in the one-prism curve is due to the presence

of shadows in the trough of the prisms at phase angles larger than 45° . Since the single-prism configuration does not have any troughs, the entire face remains exposed to light beyond 45° phase and, consequently, registers a brighter signature.

The close fit between the analytical and test curves indicates that, in general, it is possible to predict the photometric behavior of a surface of known geometry, like the geometry of the prisms shown in Fig. 43, if the photometric function of an individual element, such as the face of a prism, is known. It is thus possible to derive analytically the photometric curve of the other models in Fig. 43, on the basis of a single measurement of a flat surface with the same composition as the prisms inclined to the horizontal at the same angle as the base angle of the prisms. Conversely, it may be possible to reconstruct a surface or surfaces to correspond to a known photometric function. The analytical technique developed for the purpose of verifying the prism curves might be used to build a physical photometric model that will obey the peculiar reflection laws of the moon. Past attempts to build such a model have not been very successful.

Condition No. 3: Five prisms, base angle 0° , 30° , 45° , 60° , (row 5 in Fig. 43); intensity equator parallel to the ridges.

In this condition and the following conditions, the number of prisms under observation remains constant, but the base angle of the prisms varies from 0° (a horizontal plane) to 60° . Under this condition the sun-source travels parallel to the prism ridges. In lunar terms, this particular combination of model and lighting is equivalent to increasing the latitude of the observed lunar areas at a given longitude. The lunar observational data shown in Fig. 46 indicates that the photometric properties of individual areas on the lunar surface are nearly independent of latitude. The test results shown in Fig. 47 agree with the lunar data. Both sets of curves show only a slight increase in backscatter with increasing latitude or base angle. It is believed that no useful additional knowledge will be gained by investigating the other models in Fig. 43 under this condition of illumination.

Condition No. 4: Same as Condition No. 3, except that the intensity equator is perpendicular to the prism ridges.

The photometric properties of the set of five prisms with varying base angles are shown in Fig. 48. The test curves reveal a progressive sharpening of the backscatter curves as a result of increasing base angle or decreasing ridge angle of the prisms. The

over-all increase in backscatter is more pronounced under the transverse mode than under the parallel mode of illumination. Since the albedo and the surface compositions of these models remain constant, the sharper backscatter could be attributed mostly to the shadows cast by the large scale features (i.e., prism ridges) at large phase angles under the transverse mode of illumination. It should be noted that the prisms cannot reproduce the lunar curve without the help of the CuO cover. However, these experiments indicate that it may be possible to achieve a match with the lunar curve using lambertian, centimeter-size elements alone, provided these elements have sharp edges and are arranged in the proper order -- which is, as yet, unknown. It is apparent that the investigation of prisms, pyramids, hemispheric, conical, or ellipsoidal pits and domes alone will not lead to this pattern, but sufficient knowledge has been gained from these experiments to explore other, less conventional geometries. The "Thumb Tack" model described below is an attempt in this direction and appears to be more rewarding than other similar attempts previously made at Grumman and elsewhere (Refs. 3, 4, and 28).

III. Models sprinkled with mixtures of CuO and SiC powders.

In these experiments an attempt is made to keep the roughness or geometry of the model unchanged and to vary its albedo within the range of lunar albedo values. Copper oxide and silicon carbide powders (having albedos of 0.06 and 0.15, respectively) are mixed in various proportions and sprinkled over a surface of known geometry. Both powders have about the same grain size, less than 0.037 mm. (passing through a 400 mesh screen).

The albedos of these mixtures were first measured at 0°, 30°, and 60° viewing angles. The result plotted in Fig. 49 show that silicon carbide, unlike copper oxide or the surface of the moon, does not have a constant albedo independent of viewing angle.

The photometric curves (at normal viewing angle) of a flat plate and a 5-prism assembly on which some of these mixtures are sprinkled, are shown in Figs. 50 and 51. The results indicate that the match with the lunar curve, or band, deteriorates with increasing albedo or SiC content. These results are somewhat similar to those obtained from the experiment in Phase I, Fig. 35, in which coral No. 1 was progressively darkened by a spray of paint. In this case, however, it is debatable whether the loss of backscatter can be caused entirely by an increase of albedo. The loss could also be attributed to the inability of the SiC particles to fluff up and form "fairy castles." An examination of the constituent

powders with a stereoscopic microscope revealed that this is indeed the case. The CuO particles, unlike the SiC particles, agglomerate to form intricate labyrinthine structures. Photomicrographs of these powders, shown in Figs. 15a and 16a, do not, unfortunately, illustrate the difference in their packing and tridimensional complexity to the degree revealed by stereoscopic viewing; however, they do show the difference in texture and, superficially, the degree of agglomeration; these photomicrographs show, in the case of the SiC powder, the presence of shiny, specular surfaces that are mainly responsible for their relatively high albedo and poor backscatter.

It may be concluded that the flattening of the photometric curve due to the addition of SiC powder could be due to a combination of albedo (i.e., multiple scattering) and geometry effects. The photomicrographs suggest evidence of both effects and indicate that the technique of mixing powders is not necessarily conducive to a meaningful study of these effects on the photometric function, since it is difficult to separate them and measure or compute their individual contributions. For this and other reasons mentioned above, it was found more desirable to deal with "simple" models having one order of roughness instead of two, i.e., "micro" and "macro," as represented by the dust cover and geometric solids respectively. However, the experiments with the composite models were useful in revealing the type of geometry that may be needed in order to backscatter light in the same manner as the moon without a cover of fine dust; this cover, as we have seen, is expedient to give a good match with the lunar data, but is not very helpful, other than in a qualitative sense, in giving an insight into the physics of the phenomenon.

An Analysis of the Basic Geometry of Backscattering Surfaces

It can be stated on the basis of the previous experiments that a "surface," which backscatters light like the moon, could have a pronounced tridimensional structure composed of opaque elements larger than the wavelength of visible light and arranged in such a manner that whatever light leaves by reflection through their interstices, must leave more or less in the direction of the source. These surfaces are sometimes said to have "negative gloss." The "natural" and "artificial" models investigated thus far exhibit this tridimensional structure, but to a degree too complicated to be subject to a useful analysis on the basis of the actual shape and contour of the surface. To overcome this difficulty, an attempt is made in this section to build a tridimensional

structure composed of elements of known geometry and albedo, arranged in a series of patterns, all of which are photometrically similar to the moon or to the natural specimens examined previously. These patterns may not necessarily conform to the random geometry of the natural specimen or lunar surface, but they may be considered as geometrically analogous to them in terms of relative roughness and, possibly, actual porosity.

The search for a lunar photometric model made up exclusively of "macrorough" features, which, unlike microscopic dust particles, lend themselves to easy manipulation and analysis, may begin with centimeter-size "lambertian" elements that are horizontal and/or vertical to the viewed area and are oriented in a direction perpendicular to the plane of vision including the intensity equator, as shown in Fig. 52.

To begin, consider the simplest possible tridimensional model composed of equal width opaque, horizontal strips of negligible thickness "suspended" over a flat surface, as shown in Fig. 53a. Assume all surfaces have the same albedo and that all scatter light according to Lambert's law. Let an observer or a photometer view this model at an angle, E , from the normal to the surface.

The following discussion is highly qualitative and ignores the fact that the flux projected on the surface varies with the angle between the local normal and the incident beam. The discussion is meant to provide a general feeling for what may be the behavior of these models; detailed quantitative analysis will be completed in subsequent work.

At zero phase angle, when the directions of sight and illumination coincide, the brightness of this model is at its maximum because the photometer sees 100% of the illuminated area, half of which consists of the top of the suspended strips and the other half consists of the AB-type areas on the base, as seen through the openings of the suspended strips, Fig. 53a. As the light moves counterclockwise along the intensity equator, area AB will be progressively darkened by the shadow of the upper element. The rate of change of the brightness vs. phase angle will depend of course upon the phase angle, the vertical distance between the base and the upper element and the width and spacing of the elements.

Neglecting multiple reflections, the brightness of this particular model will reach a minimum at phase angle α_1 , corresponding to the position where a suspended element casts its full shadow over area AB. At larger phase angles the shadow will move away, the brightness of the model as seen by the photometer will increase, and, unlike the geometry of the lunar surface, it will reach a second maximum at a phase angle α_2 which (as it can be seen in Fig. 53a) corresponds to the position where the light source, the next opening between the suspended strips and area AB are on a straight line. The height of the second brightness peak depends upon the angle of

incidence, i , and the geometry and nature (or finish) of the surfaces. It is clear that a tridimensional model made up of suspended elements only could give the peculiar "opposition effect" exhibited by the moon at small phase angles; however, the match with the lunar curve is very likely to deteriorate at larger phase angles.

Another tridimensional model, as simple as the preceding one, can be made up of equal height vertical elements only, as shown in Fig. 53b. This model, unlike the preceding one, will not behave, photometrically speaking, the same way at all viewing angles. For instance, at normal viewing, its brightness is expected to drop sharply (depending on the height and spacing of these elements) as the light moves away from a zero phase position, but at off-normal viewing angles, the drop in brightness near zero phase may follow a "cosine type" curve rather than a backscattering type curve, as shown in Fig. 53b. At larger phase angles, the vertical strips start casting their shadow over area AB, the brightness will drop at a faster rate; unlike the case of the previous model, no second brightness peak will appear. However, the vertical strips are equally unsatisfactory as a lunar model because they will not obey the reflection laws of the moon at all viewing angles. It would be interesting to verify this conjecture by experiments and/or analyses.

From the above discussion and sketches in Figs. 53a and b, it can be anticipated that a model consisting of a combination of horizontal and vertical elements as shown in Fig. 53c, may be free of the shortcomings of its constituents, namely, the second brightness peak exhibited by the horizontal strips and the "cosine type" curve at small phase and large viewing angles exhibited by the vertical strips. In the "T" model, shown in Fig. 53c, the vertical strips eliminate the second peak by preventing the light rays from reaching area AB for a second time during the same lunation, and the horizontal elements eliminate the "cosine type" curve by casting their shadow over area AB at all viewing angles. In the T-model, a slight, undesirable "bulge" is anticipated on the lower portions of the brightness-phase curve due to the Lambertian behavior of the exposed top of the horizontal strips being the only remaining illuminated elements of the model beyond phase angle α_1 . This portion of the curve could be improved easily by superimposing a "second order" roughness on top of the horizontal strips. This may be accomplished by adding a small vertical element or elements in the middle of the horizontal strip or two vertical elements or "lips" on the edges.

In the following section, an experimental account of the T-model is given. The results are preliminary, but they essentially bear out the validity of the approach.

Discussion of Test Results of "Simple" Models

The T-model discussed in the previous section was built in the following manner. The horizontal suspended elements were simulated by the heads of thumb tacks pinned in parallel rows into a flat base, the vertical elements consisted of two strips of blotting paper, each one fixed between two rows of thumb tacks as shown in Fig. 54a. It is safe to assume for the purpose of this investigation that the shadow cast by the stems of the thumb tacks is negligible. The entire model, excluding the vertical strips, was sprayed with a gray nonglossy paint. The results of albedo and photometric measurements at 0° , 30° , and 60° viewing angles, with and without the vertical strips, are shown in Figs. 54b, c, and d. The light source was moved in a direction perpendicular to the alignment of the thumb tacks.

The thumb tacks model in its present configuration is not photometrically homogeneous like the lunar surface or the natural specimens when examined under both directions of the intensity equator with regard to the alignment of the tacks. This, however, is not a serious shortcoming, since such a condition could be satisfied by arranging the tacks and the vertical elements in a checkered symmetrical pattern. Hence, by using the "aligned," nonsymmetrical pattern as a preliminary step, we do not depart as far from a realistic model as it would appear at first sight.

The experimental results, presented in Figs. 54b through d show, as predicted, that the model with vertical and horizontal strips is in better agreement with the lunar data than the model with only horizontal elements. For convenience, these models will be referred to as the "T" and the "suspended" models. The difference between these models is particularly noticeable at the 60° viewing position, Fig. 54d, where three points located at or near the inflection points of the photometric curves have been singled out for further scrutiny. Points 1, 2, and 3 are located on the suspended model curve, and points 1', 2', and 3' are located on the T-model curve.

Scaled cross sections of both models indicating the illuminated and shadowed areas seen by the photometer at phase angles 45° , 60° , and 100° are shown in Fig. 55. These sketches reveal the following points of interest:

1. In Fig. 55, the illuminated areas seen by the photometer on the T-model are smaller than those on the suspended model. This accounts for the fact that in Fig. 54d, points 1', 2', and 3' are lower on the scale of brightness than points 1, 2, and 3.
2. Unlike the lunar or the T-model curves, the curve for the suspended model ascends between points 1 and 3, indicating increasing brightness. This behavior is adequately explained by the increasing width of the illuminated areas in Fig. 55, that is,

$$C_1D_1 < C_2D_2 < C_3D_3 .$$

3. The second brightness peak anticipated in the discussion of the suspended model is confirmed by the test curve at 60° viewing angle. The illumination geometry drawn for this point in Fig. 55 does indeed show that area C_3D_3 on the base of the model, in full view of the photometer, is almost fully illuminated, whereas the same area in the corresponding cross section of the T-model is in the shadow of the vertical strip. The presence of this element is largely responsible for the better match with the lunar data at these critical phase angles. It is easy to see why the curve of the suspended model dips sharply past point 3, because area C_3D_3 in Fig. 55 is progressively shadowed by element E_3F_3 with increasing phase angles

It is not necessary to discuss all the peculiarities of the test curves in Figs. 54 b through d. Most of these could be reasonably accounted for by the surface and illumination geometries of the individual points as illustrated previously. It is important to point out that these experiments are preliminary, but they nevertheless, provide sufficient knowledge and confidence to enable one to improve the thumb tacks model or to create other contrived models so as to yield an improved match with the lunar data.

Significance of the Thumb Tacks Model

The purpose of the Thumb Tacks Model is not to replace the "natural" specimens investigated in this work or elsewhere, but to explain on the basis of macrostructure the reason why such specimens reproduce or fail to reproduce the lunar photometric data.

The dust-covered solids that we have thus far investigated suggest that the contribution of gross lunar features (within telescopic resolution) to the observed backscatter is less important than the contribution of innumerable small irregularities which, judging from close-up photographs relayed by the successful "Ranger" vehicles, are probably less than some centimeters in size. The partial failure of the composite models to provide a deeper insight into the geometric and photometric relationships of backscattering "surfaces," has made it necessary to build and investigate dust-free, though contrived, lunar photometric models. The Thumb Tacks model is a crude example of such models, but it marks a new departure toward the solution of the lunar photometric puzzle. It promises to be a valuable tool which

allows one to see and follow the sequence of shadowing, on and within a backscattering-type structure, with greater convenience and accuracy than would be possible with dust-covered and other complex natural specimens.

The Thumb Tacks model has confirmed that shadowing within a porous structure, more than any other optical phenomenon, is probably primarily responsible for the peculiar photometric properties of the lunar surface. The albedo of the surface and the subsurface (visible through the pores), particularly when uniform, appears to play a minor role in the backscattering process. In addition, the Thumb Tacks model has revealed that the shadow-casting elements in the porous crust (which appears to cover uniformly the entire visible surface of the moon) are made up predominantly of sharp edges and overhanging horizontal members. No conclusions can be reached, based on this model, about the actual scale of and the interfacial bond between these elements. It appears, however, that both quasi-horizontal and quasi-vertical members are necessary and that neither set of members is sufficient by itself to account for the reflection of the lunar surface at all phase and viewing angles. The horizontal or "suspended" elements, if properly arranged, could reproduce the unusual lunar "opposition effect" at very small phase angles, and fail to reproduce the rest of the lunar curves at larger angles. Vertical elements were introduced in the Thumb Tacks model in order to improve its backscattering property; this addition to the model may be very significant since such elements render

the model less tenuous and could possibly lend to it the stability and strength that is not associated with "suspended" models. However, this conclusion must remain tentative until further investigations of various "suspended geometries" are conducted.

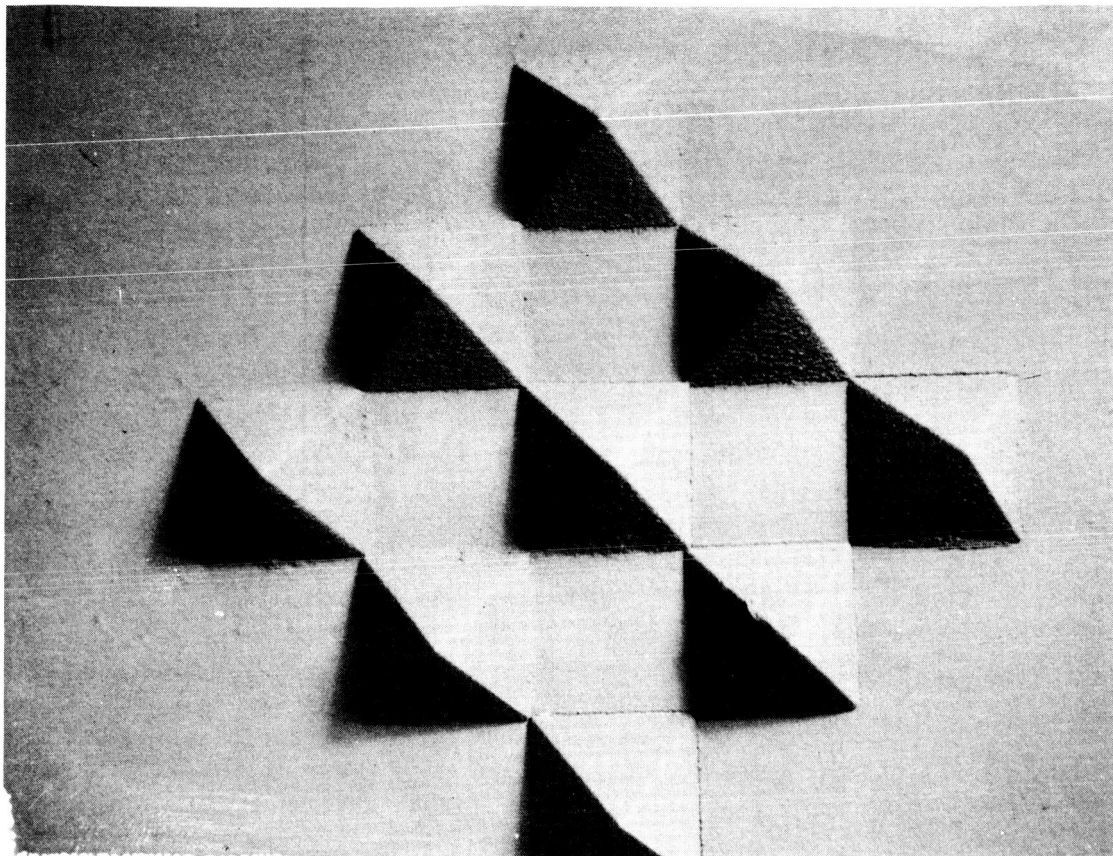
An equally significant aspect of the Thumb Tacks model and its future derivatives is that such models lend themselves more readily to an analytical formulation of the photometric function in terms of the illumination angles and the tridimensional geometry of the surface. Such a relationship is of more than academic interest. The porosity of the lunar surface, or a relatively narrow range of porosities dictated by the lunar photometric data, may be quantitatively assessed. As was indicated before, this information could, under certain conditions, complement the lunar radiothermal data in estimating the internal consistency, bearing strength, insulating, and other engineering properties of the lunar surface material.

A shortcoming of the Thumb Tacks and perhaps other "simple" models is the fact that such models, unlike the lunar surface or most of the natural specimens we have examined, do not or are not likely to exhibit a constant albedo at all viewing angles. This fact could be attributed mostly to the mathematical idealization of the shadow-casting elements. In the case of the terrestrial specimens, or the lunar surface, there is sufficient randomness in the distribution and orientation of the reflecting surfaces to minimize the variation of albedo with change in viewing angle. In the case of the contrived models, this difficulty could possibly be overcome (without compromising the integrity or realism of the model) by rounding off sharp corners, so that incident light could strike the surfaces at a more or less equal angle with respect to the local normal, and consequently, according to the principle of Lambertian reflection, yield a more uniform brightness or albedo at all viewing angles.

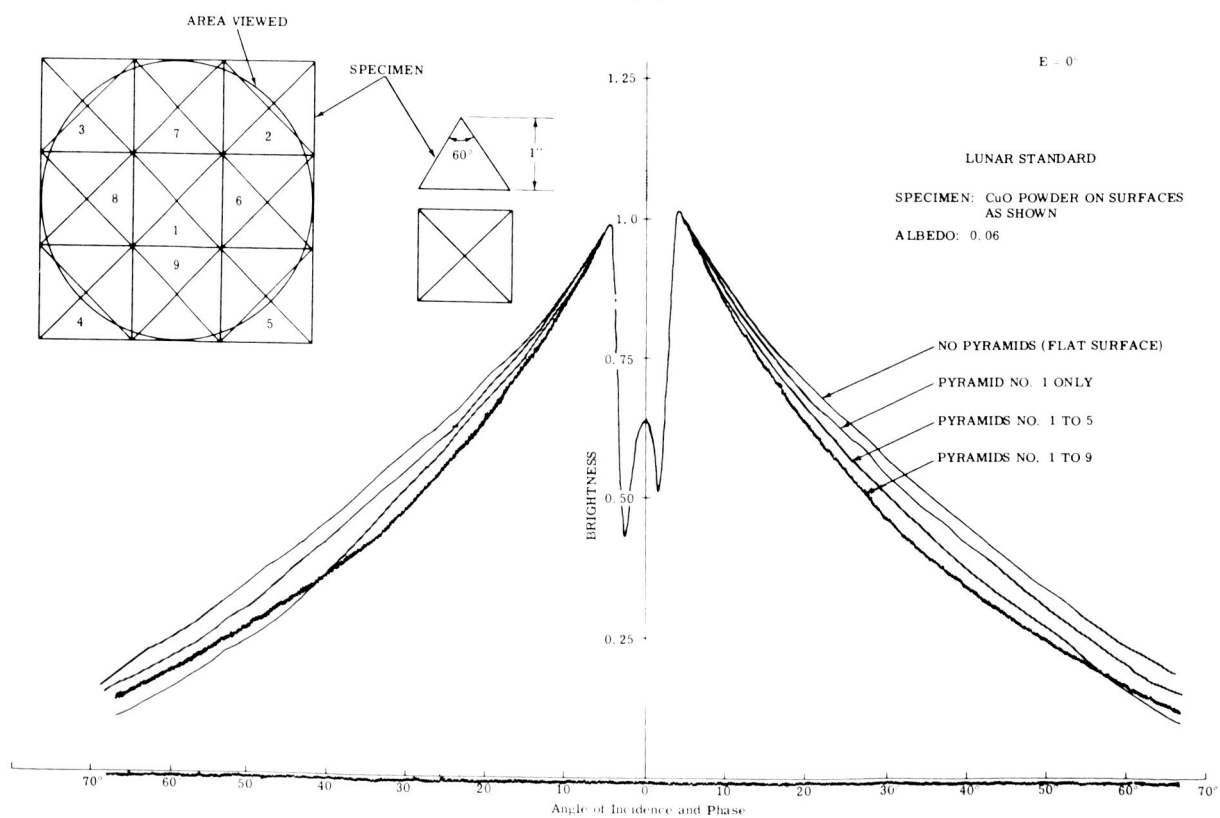
Contrived models like the Thumb Tacks, unlike the composite, dust-covered models, offer the advantage of enabling the experimenter to vary the albedo of a given model without incurring the risk of changing its structure (as we did when we mixed SiC and CuO powders). Specifically, varying the albedo within a given model would consist in painting the uppermost layer of the tridimensional model with a paint of different brightness than that in the interior of the pores. It is surprising that composite-albedo models, theoretical or experimental, have not been considered by previous investigators. Such models appear to be quite realistic in view of the possibility that the outermost surfaces on the moon

could be darkened (or reddened) more extensively by radiation and other mechanisms than the interior of the pores. The latest observational data by Gehrels et al. could be interpreted as lending support to this view. Thus it may not be necessary to postulate a tenuous cloud of particles in order to account, photometrically speaking, for the "opposition effect" at small phase angles. This particular phenomenon might be explained by the increased brightness of the interior of the pores which come into view at very small phase angles. In addition, the composite-albedo, tridimensional model might explain the "reddening" of the lunar surface at increasing phase angles (again reported by Gehrels), when we consider that the bright interiors of the pores (which could tend mostly toward the blue) become less and less visible at these angles, while the duller, "weathered" outermost surfaces, (likely to be darker or red), will contribute more and more to the observed color. This newly discovered peculiarity of the lunar surface imposes an additional constraint on model-matching experiments in lunar photometry. It would be very desirable to look for evidence of "red shift" in the natural specimens in Phase I that have passed the photometric test under integrated visible lighting. This may be accomplished by measuring the brightness vs. phase relationship of these specimens at discrete wavelengths in the visible spectrum. The reddening effect may conceivably affect the estimate of the porosity of the lunar surface material from the photometric data. This is because increasing the volume by undercutting the sides of the cavities between the shadow-casting elements has an effect on the backscatter curve similar to increasing the albedo of the interior of the cavities that come into view at small phase angles. Thus, a composite-albedo model exhibiting the reddening effect is likely to be less porous than one which has a uniform albedo. "Simple" models of the Thumb Tacks variety lend themselves very conveniently to the simulation and study of this newly observed lunar phenomenon.

Experimental studies involving the porosity and photometry of "natural" specimens having a uniform albedo are reported in the next phase.



(a)



(b)

Figure 41. CuO Powder on Pyramids (Sheet 1 of 2)

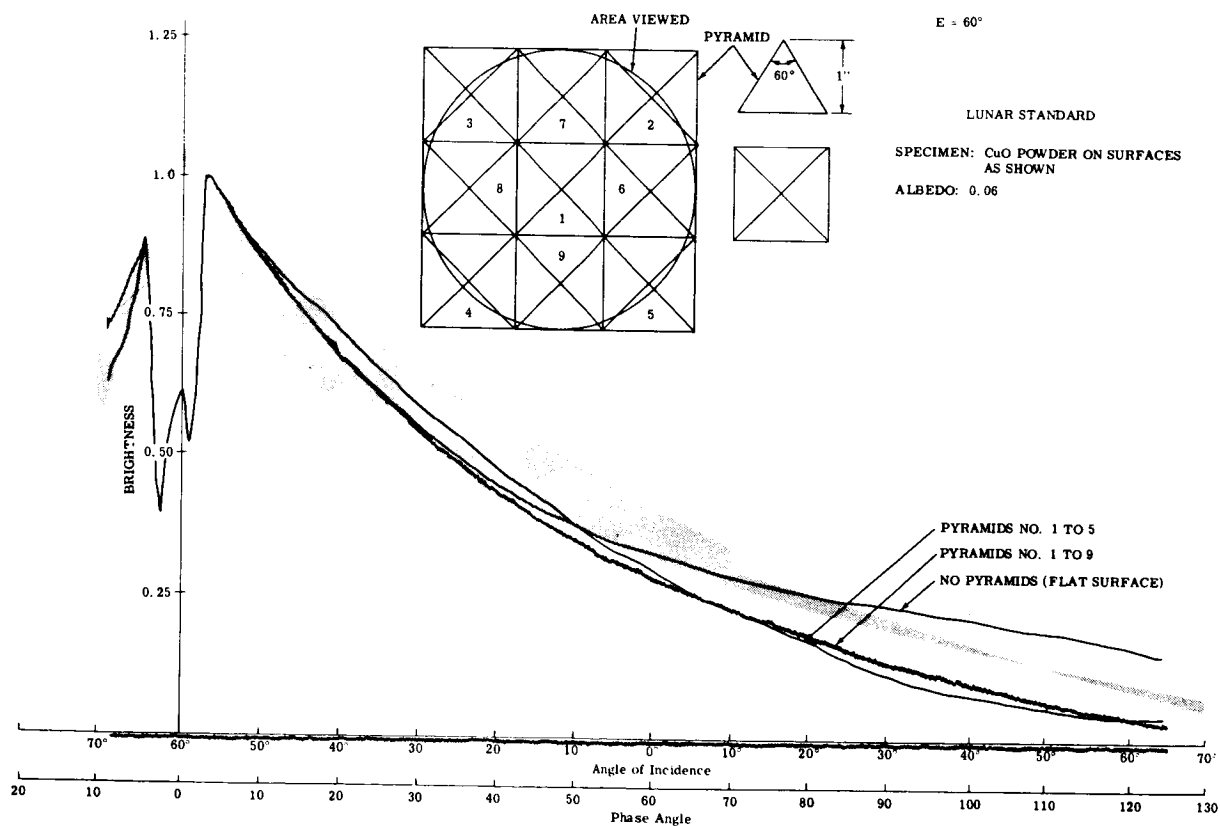
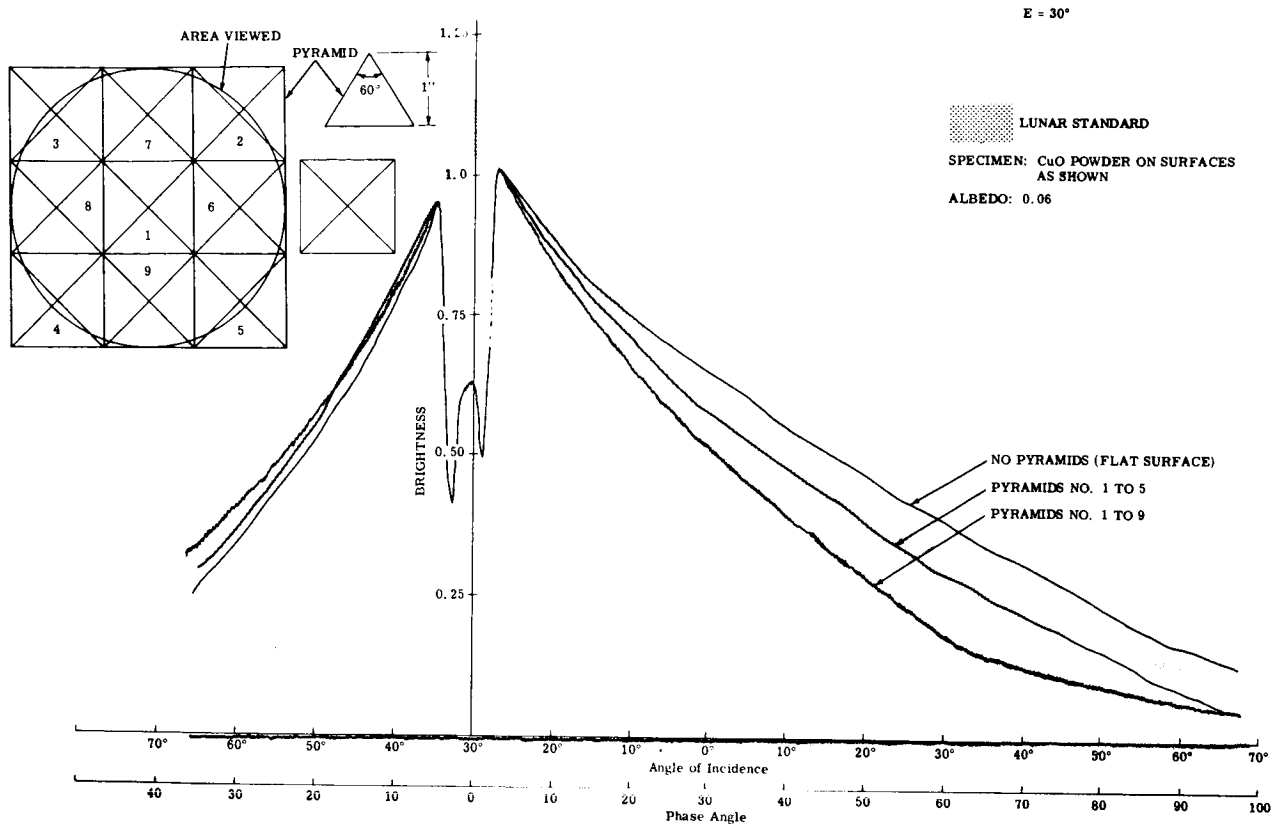
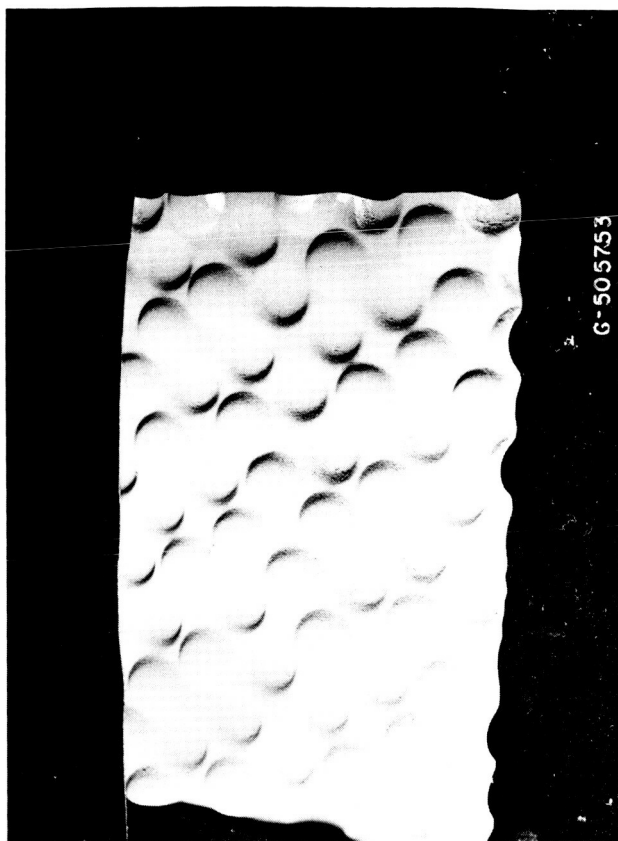
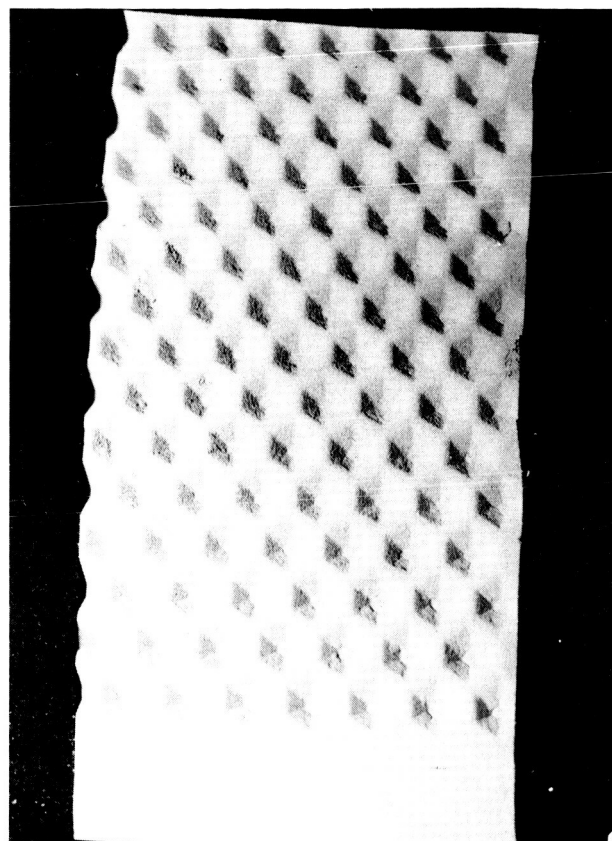


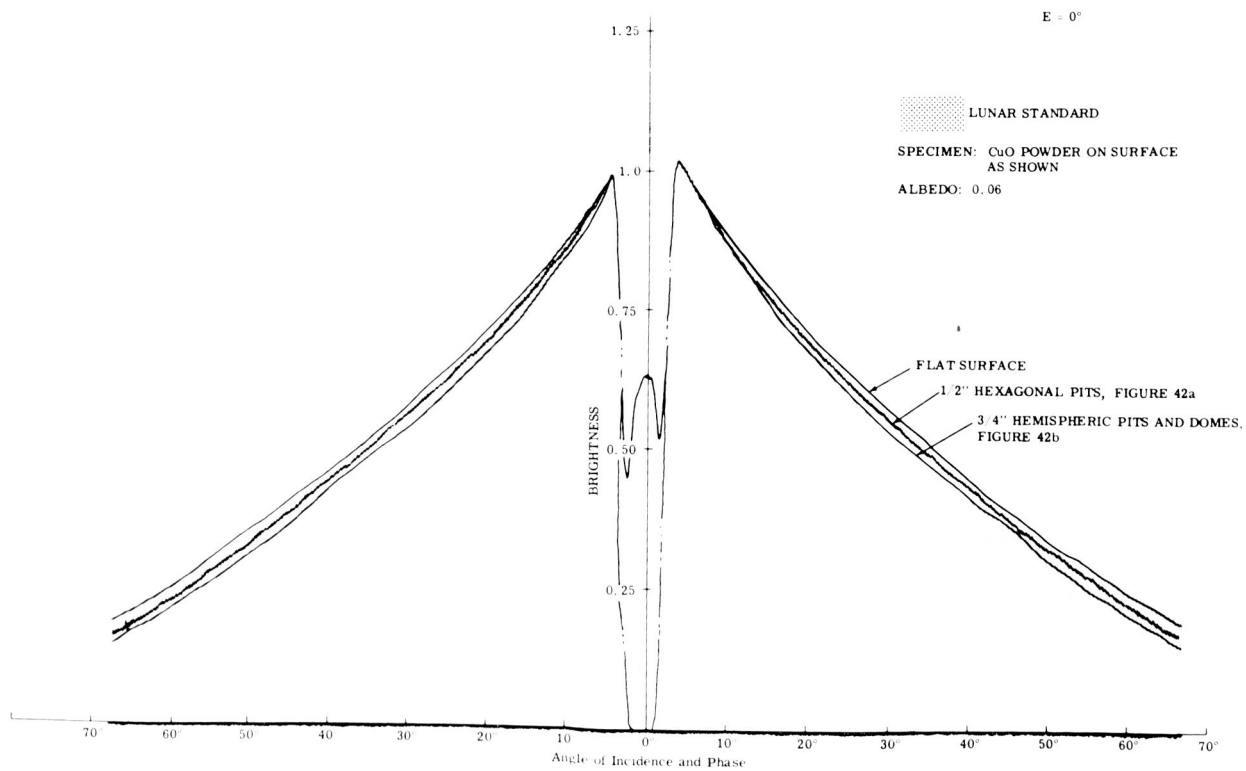
Figure 41. CuO Powder on Pyramids (Sheet 2 of 2)



(a)



(b)



(c)

Figure 42. CuO Powder on Surface as Shown (Sheet 1 of 2)

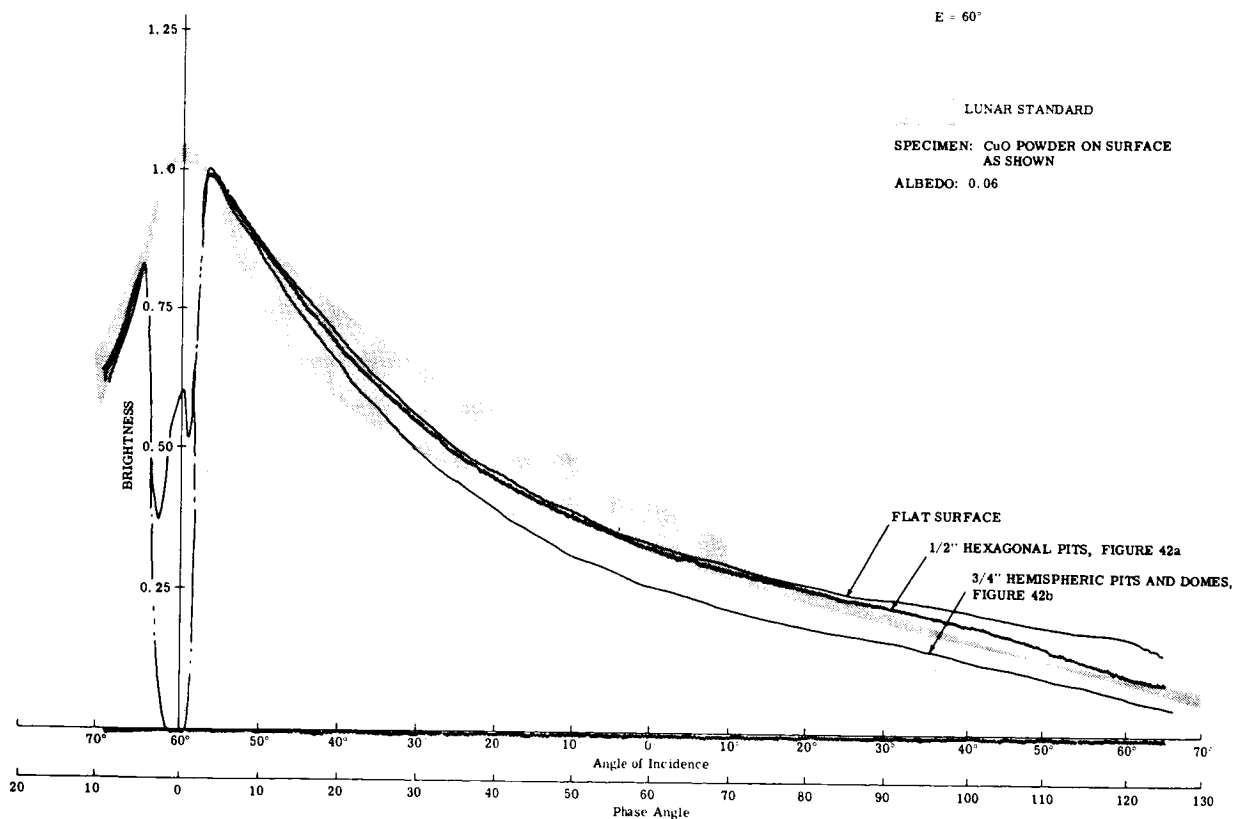
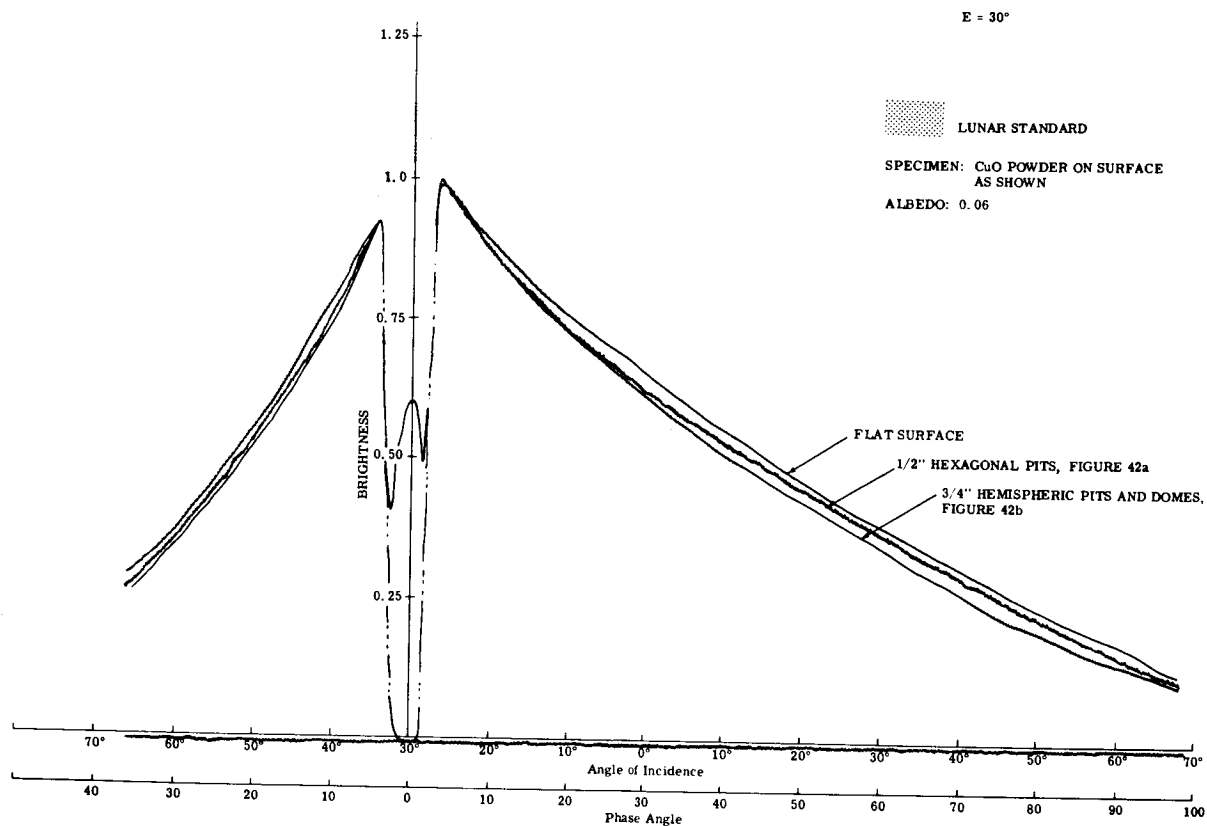


Figure 42. CuO Powder on Surface as Shown (Sheet 2 of 2)

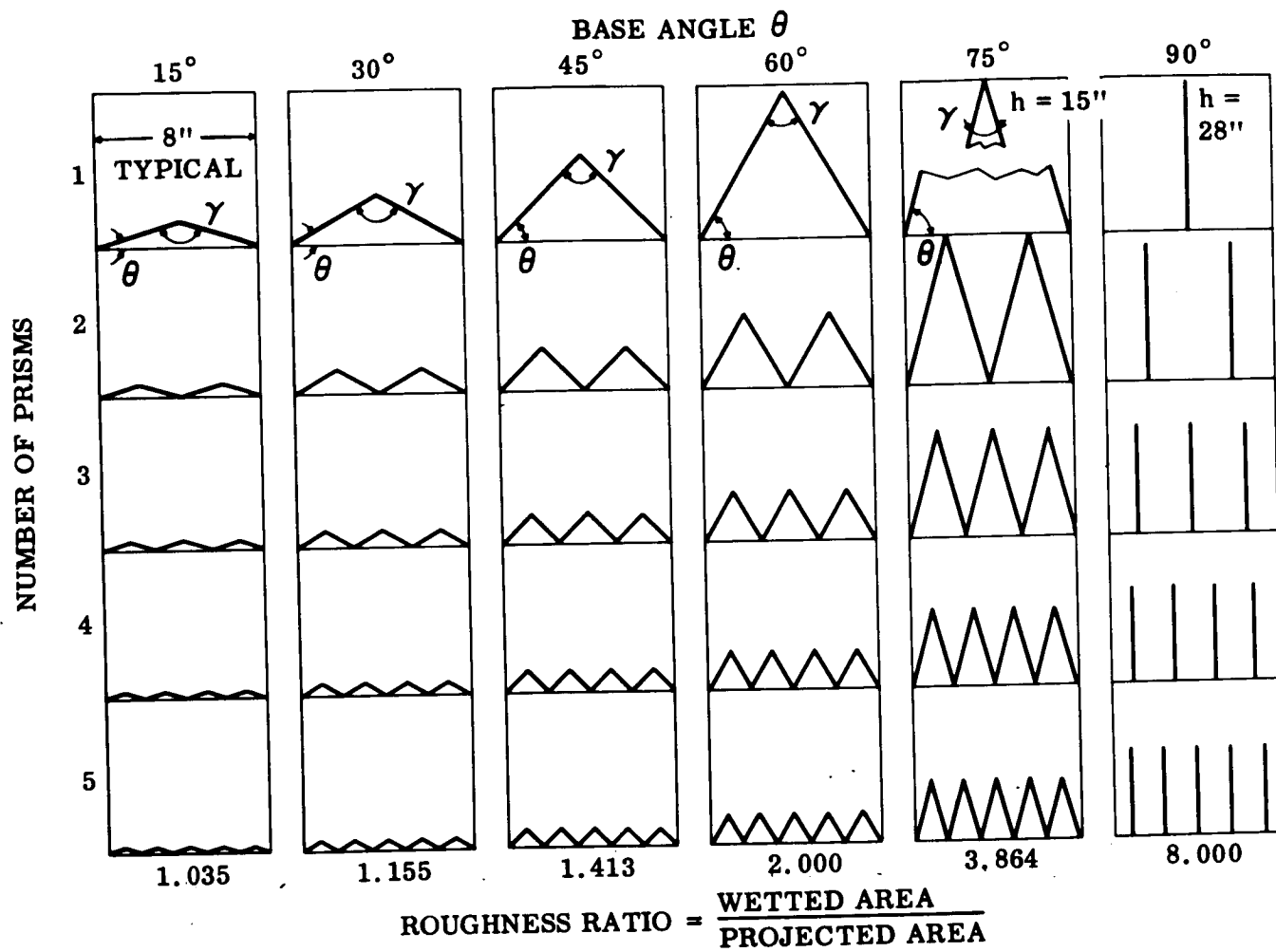


Figure 43. Cross Section of Prismatic Ridges

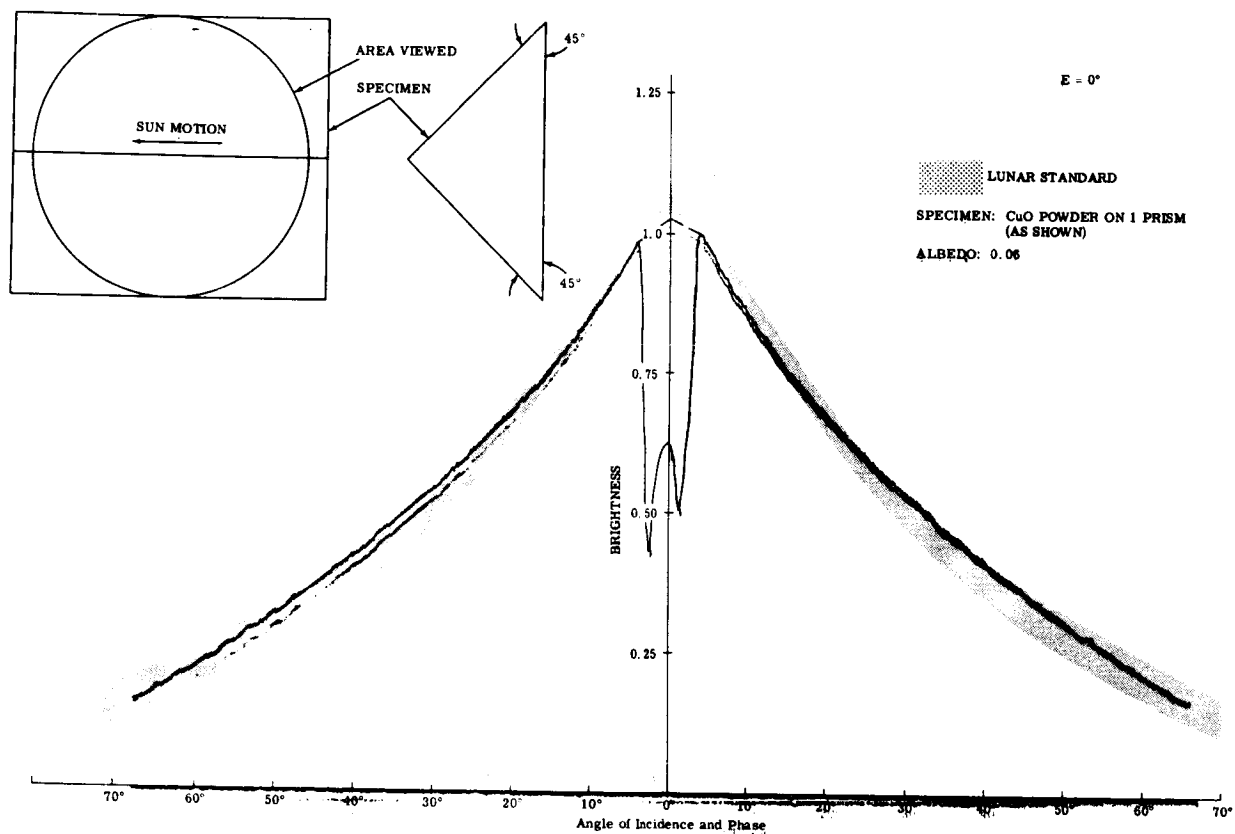


Figure 44a. CuO Powder on One Prism



LUNAR STANDARD

E = 0°

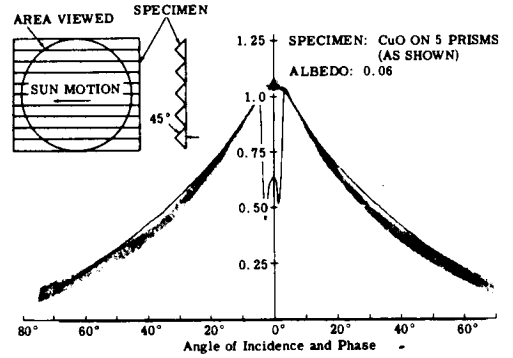
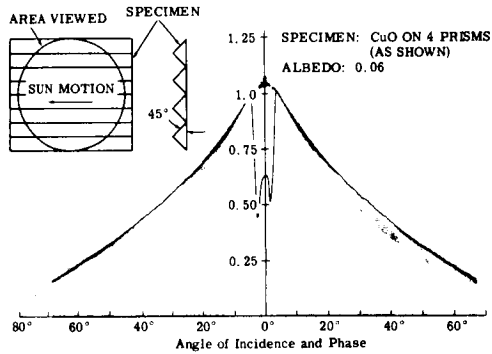
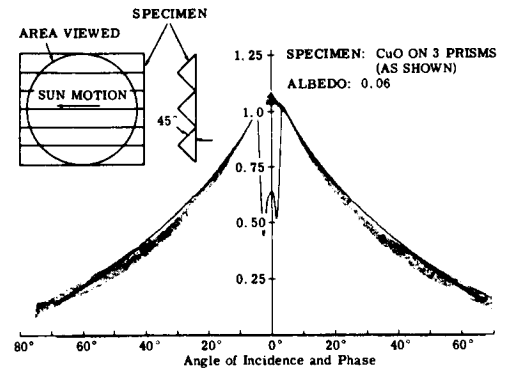
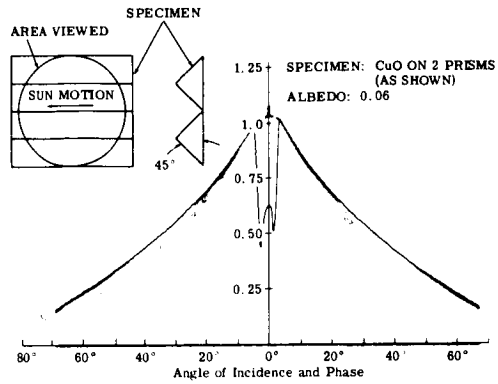


Figure 44b. CuO Powder on Two to Five Prisms

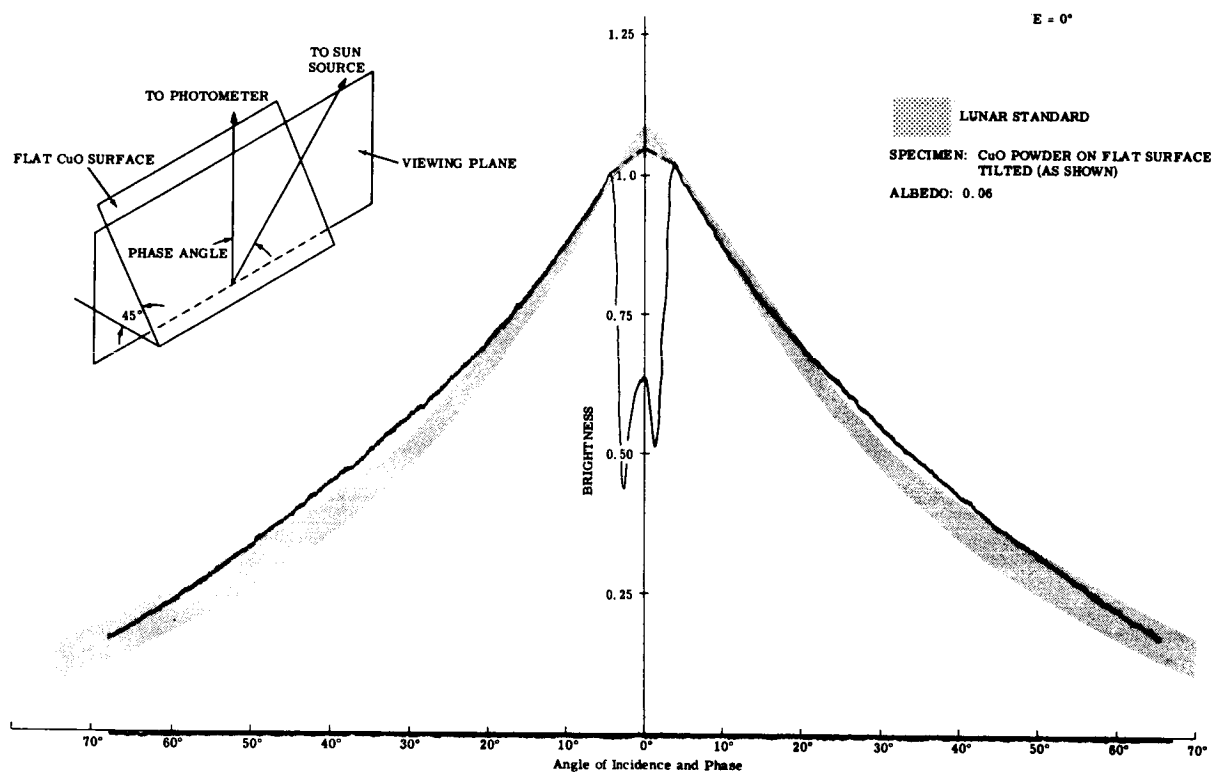
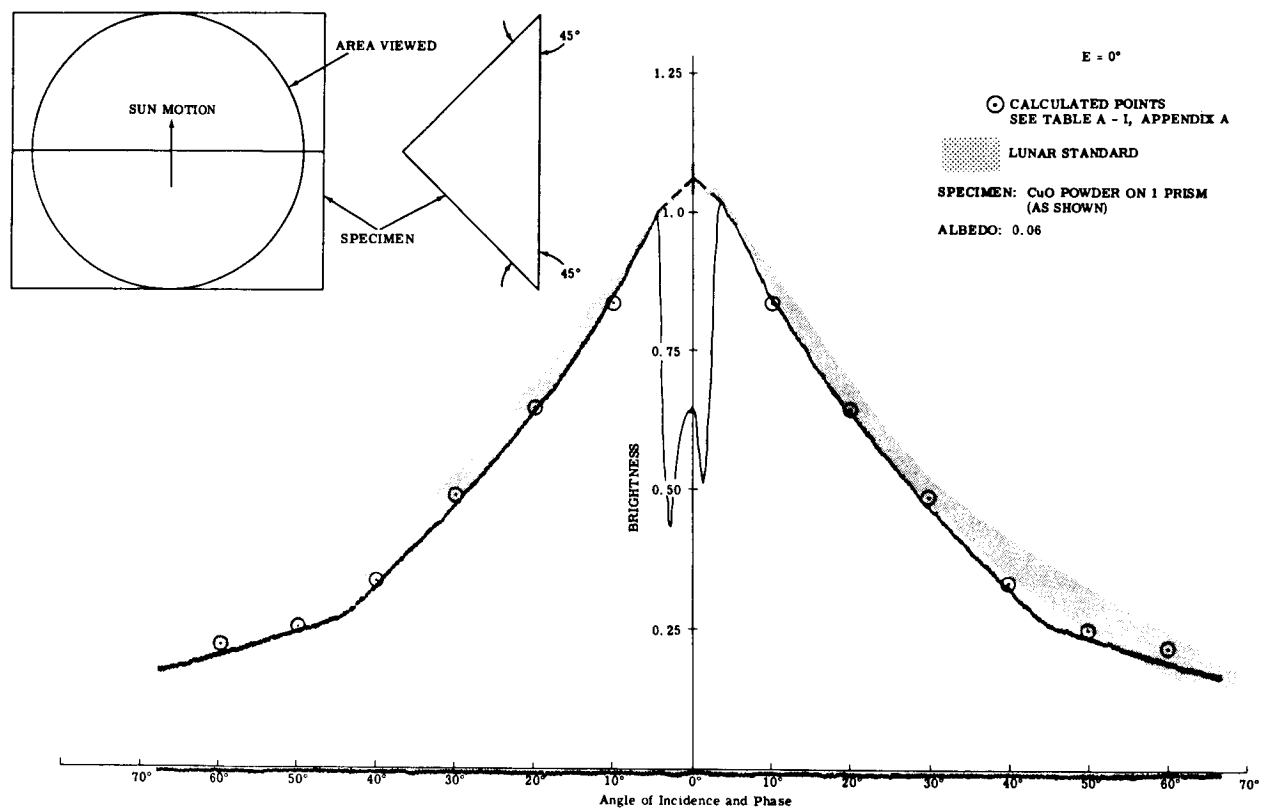
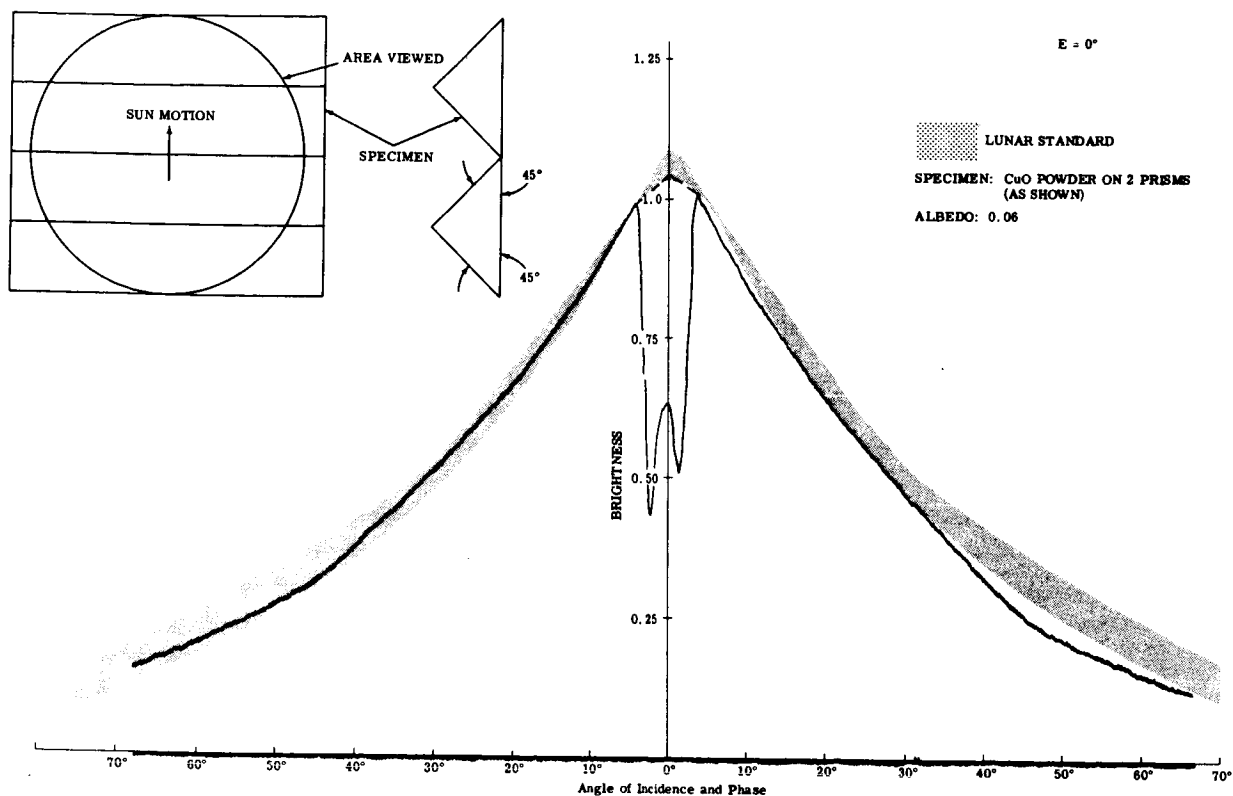


Figure 44c. CuO Powder on Flat Tilted Surface

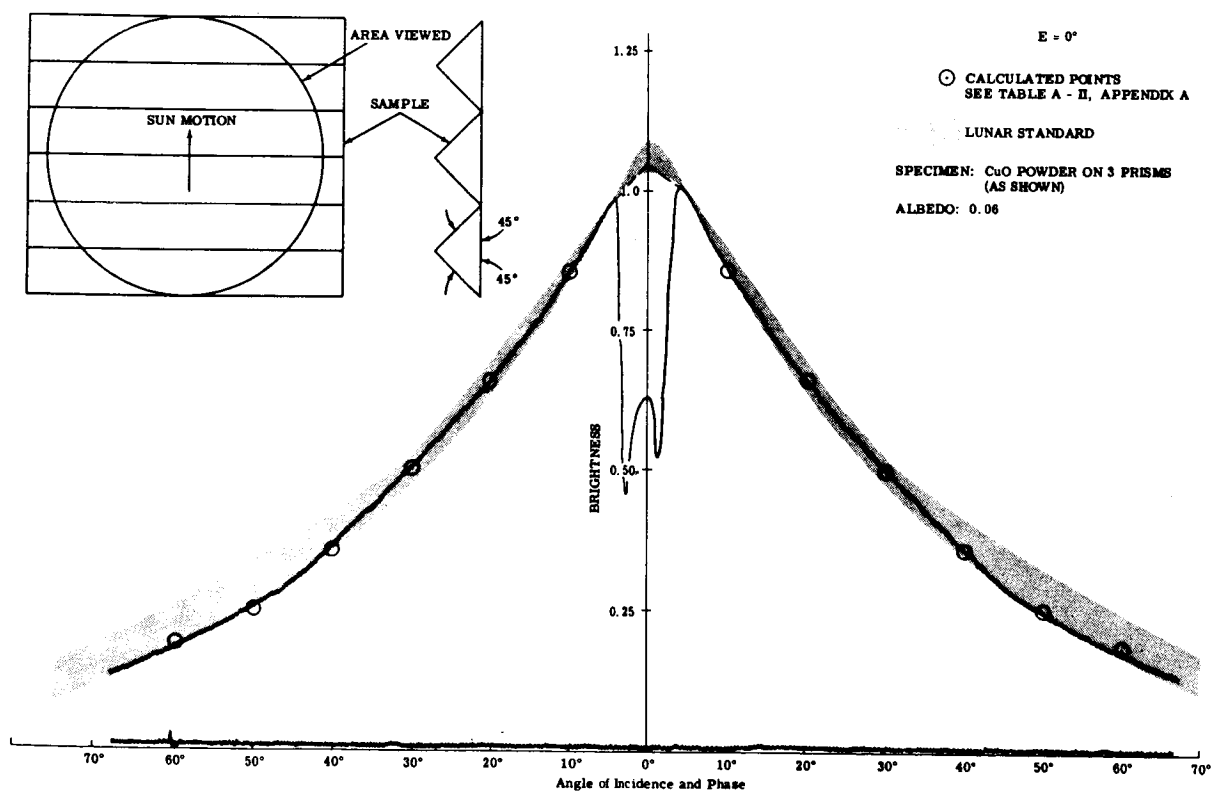


(a)

Figure 45. CuO Powder on Prisms (Sheet 1 of 3)

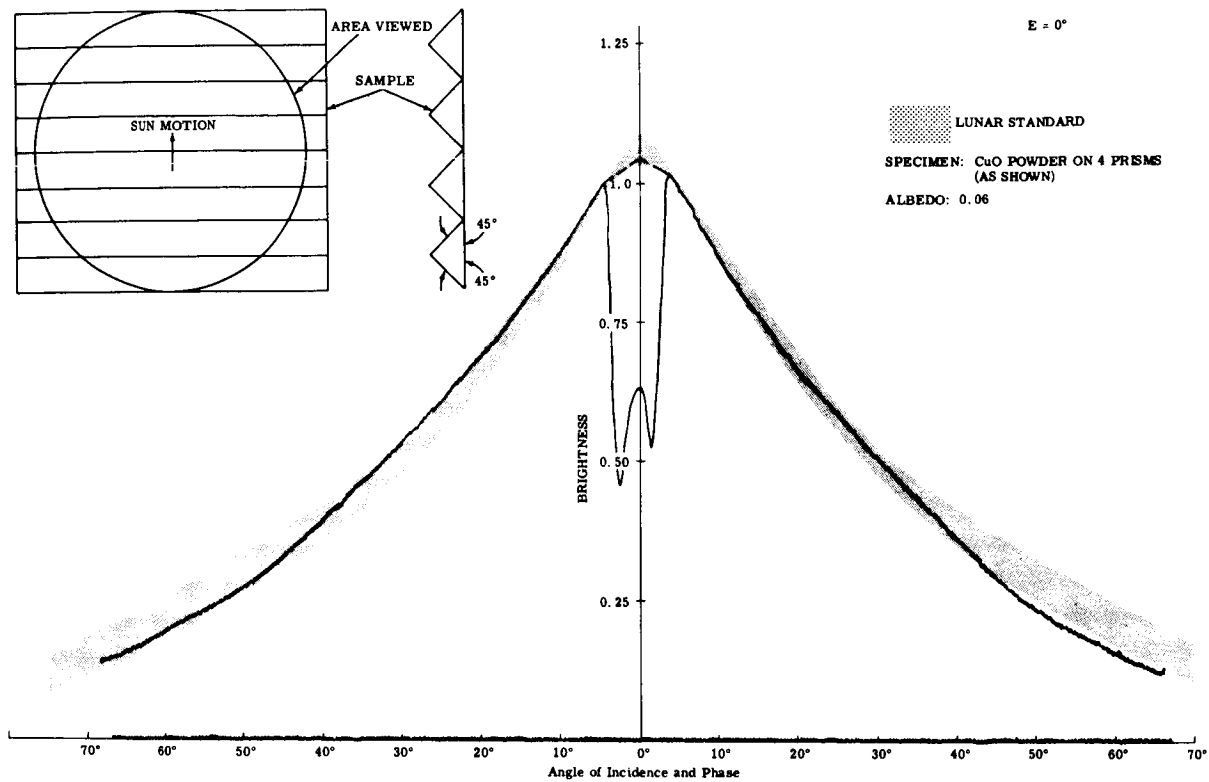


(b)

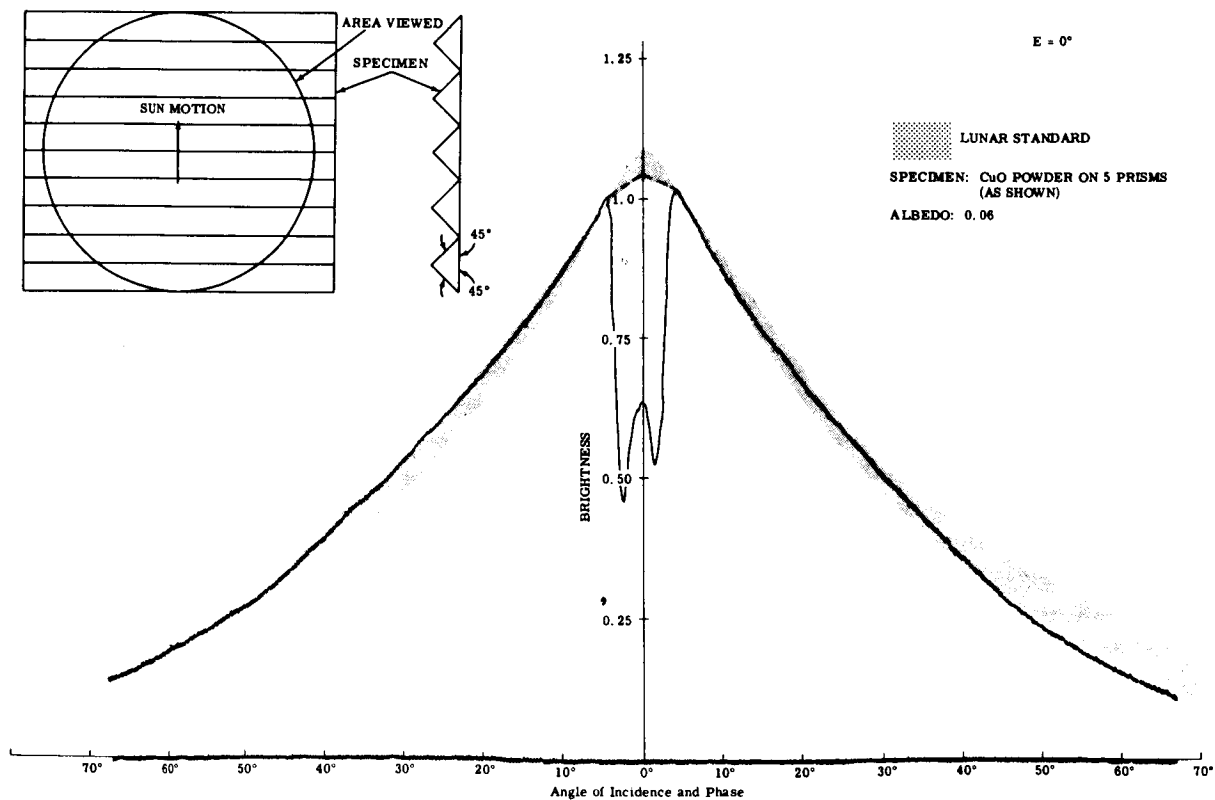


(c)

Figure 45. CuO Powder on Prisms (Sheet 2 of 3)



(d)



(e)

Figure 45. CuO Powder on Prisms (Sheet 3 of 3)

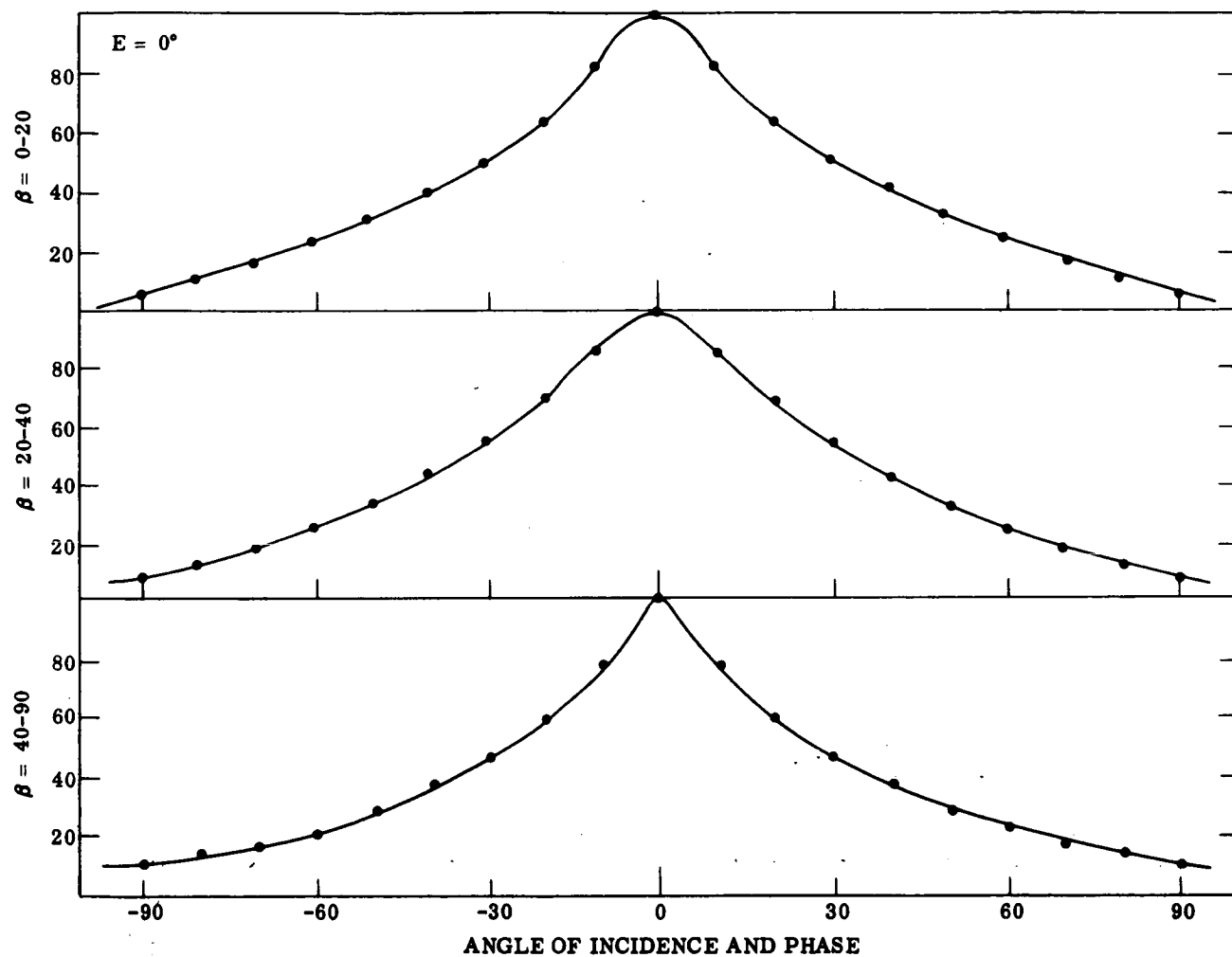


Figure 46. Lutation Curves of 0° to 10° Longitude Crescent; β = Latitude (Ref 28)

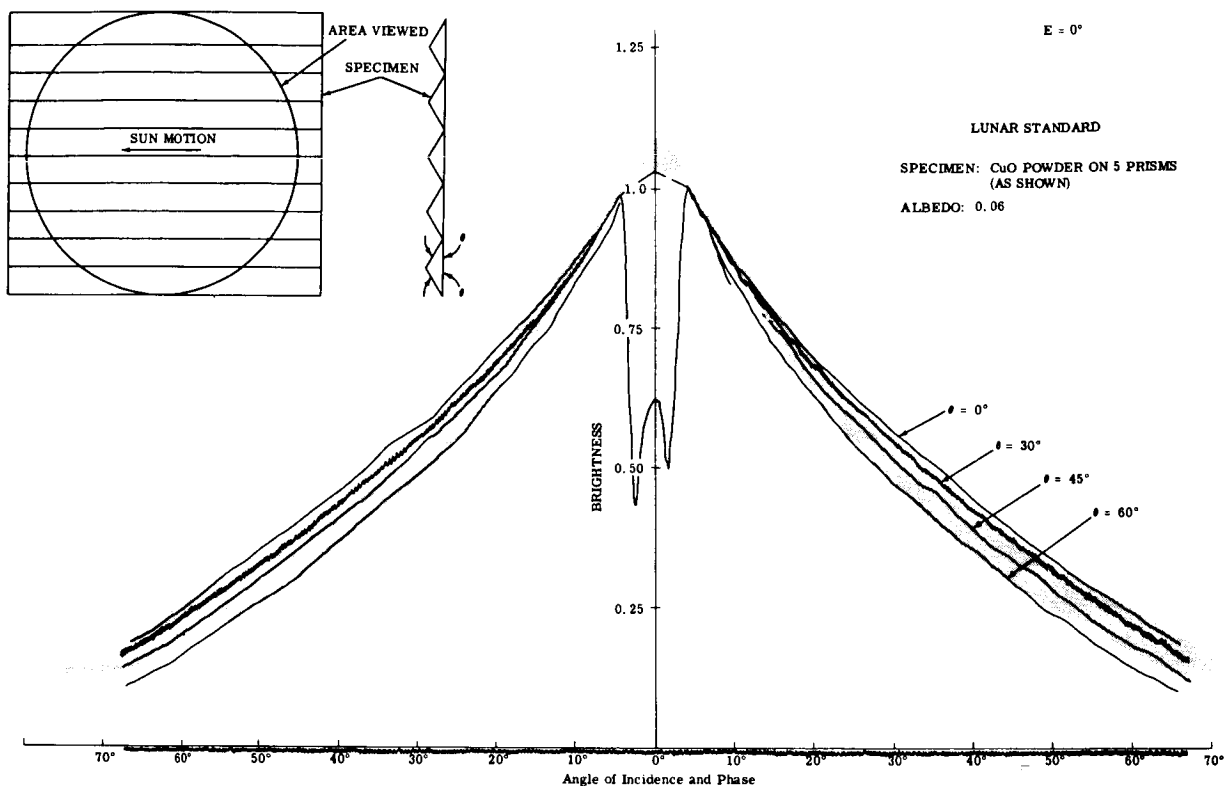


Figure 47. CuO Powder on Five Prisms Intensity Equator Parallel to Ridges

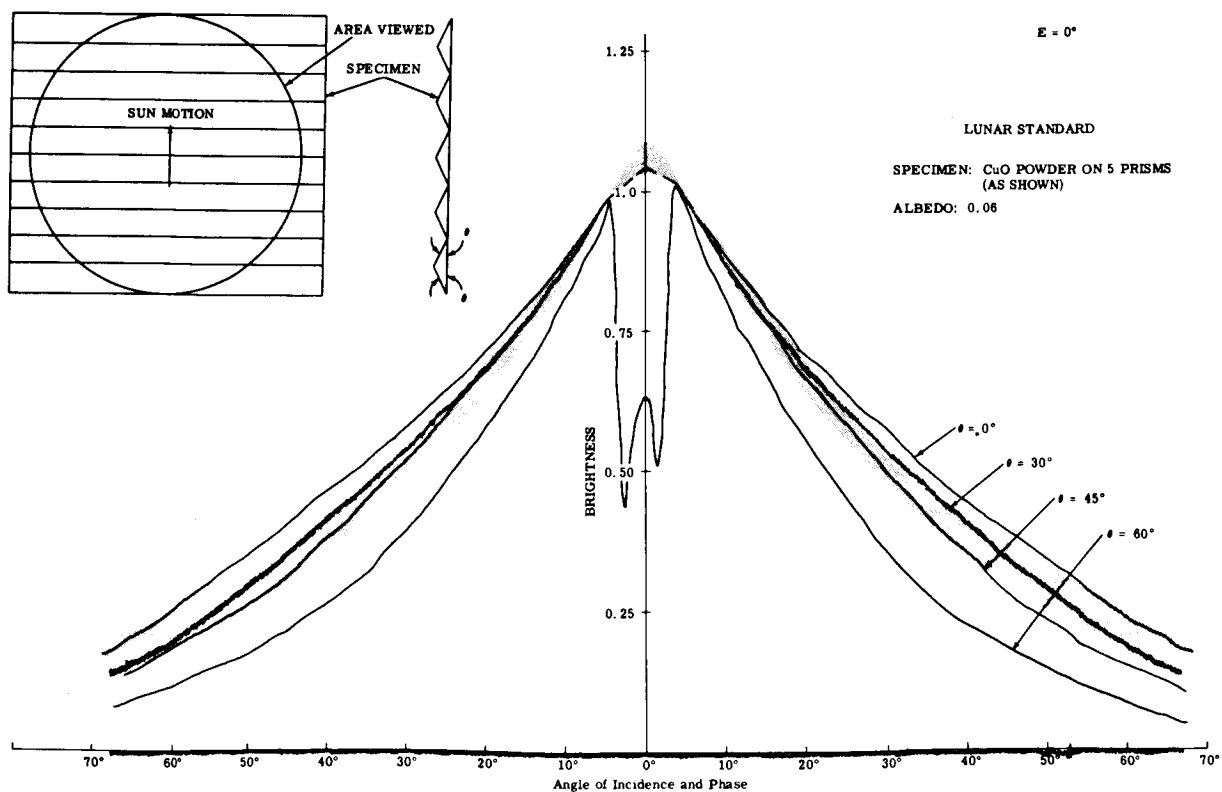
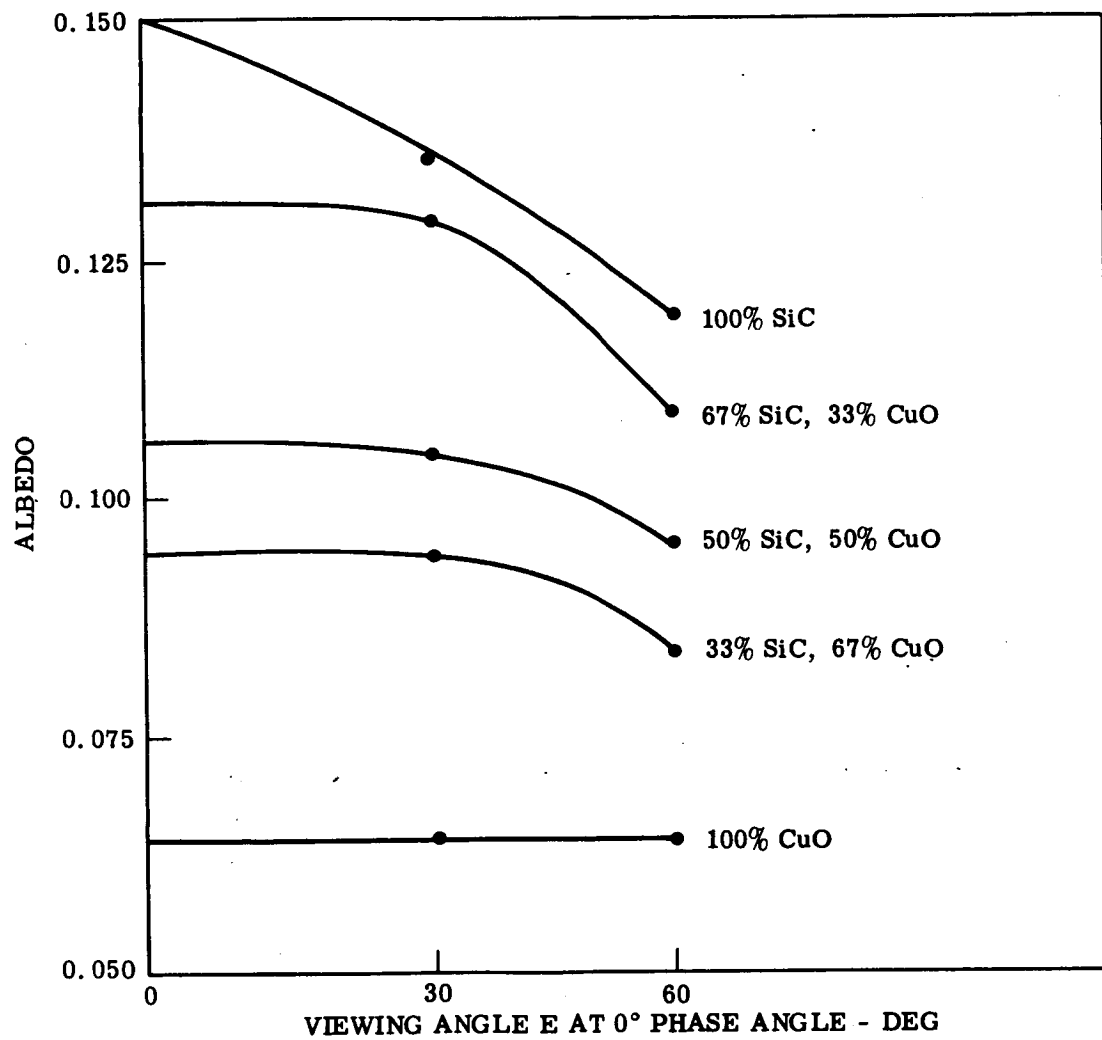


Figure 48. CuO Powder on Five Prisms Intensity Equator Perpendicular to Ridges



NOTE: PERCENTAGES GIVEN BY VOLUME

Figure 49. Albedo vs Viewing Angle of CuO and/or SiC Powders.

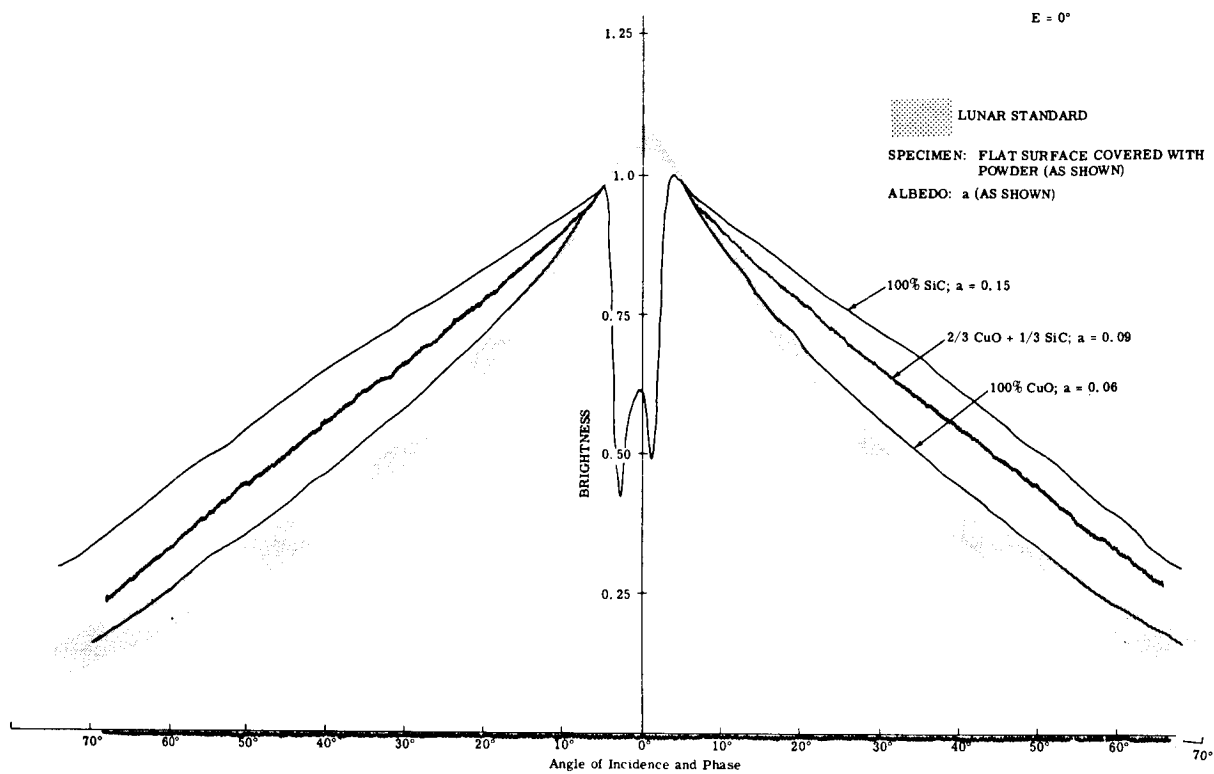


Figure 50. Mixed Powders on Flat Surface

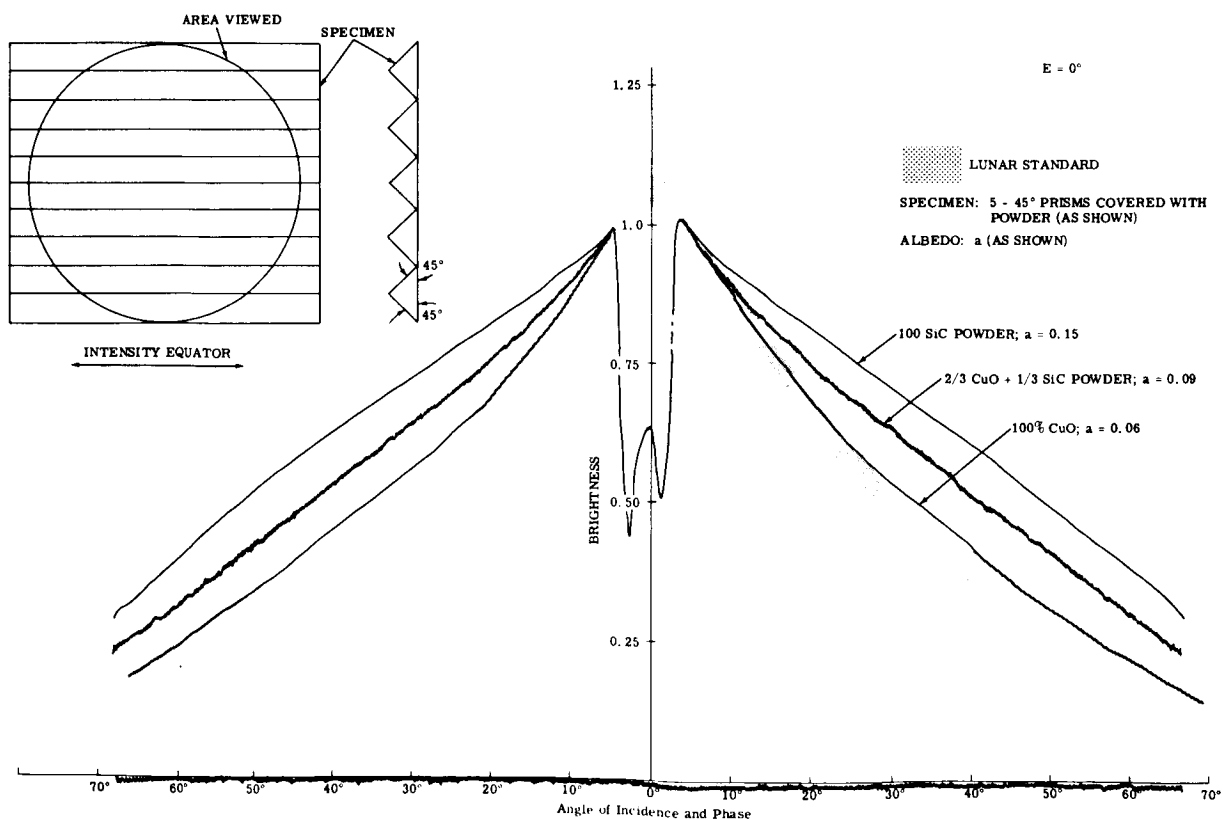


Figure 51. Mixed Powders on Prisms

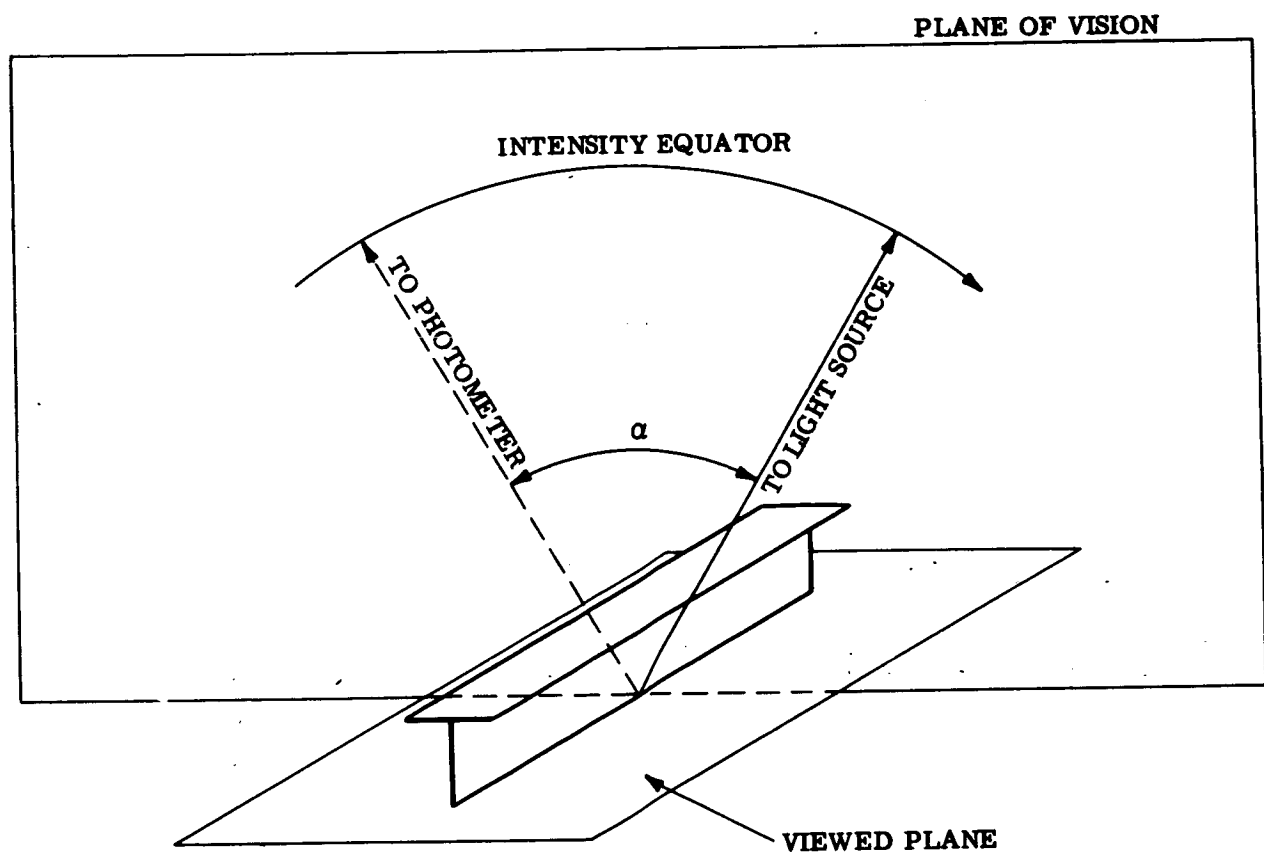
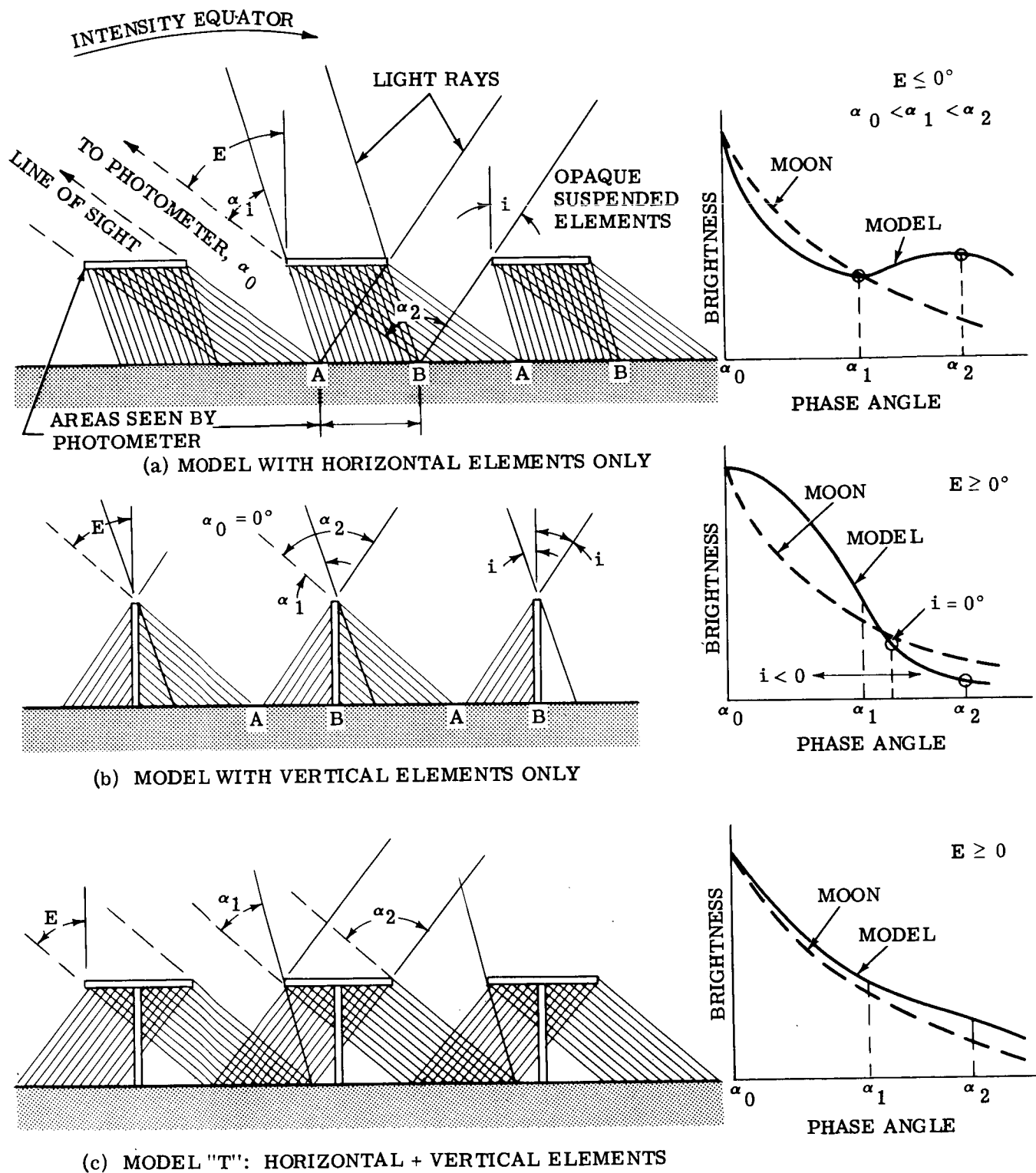


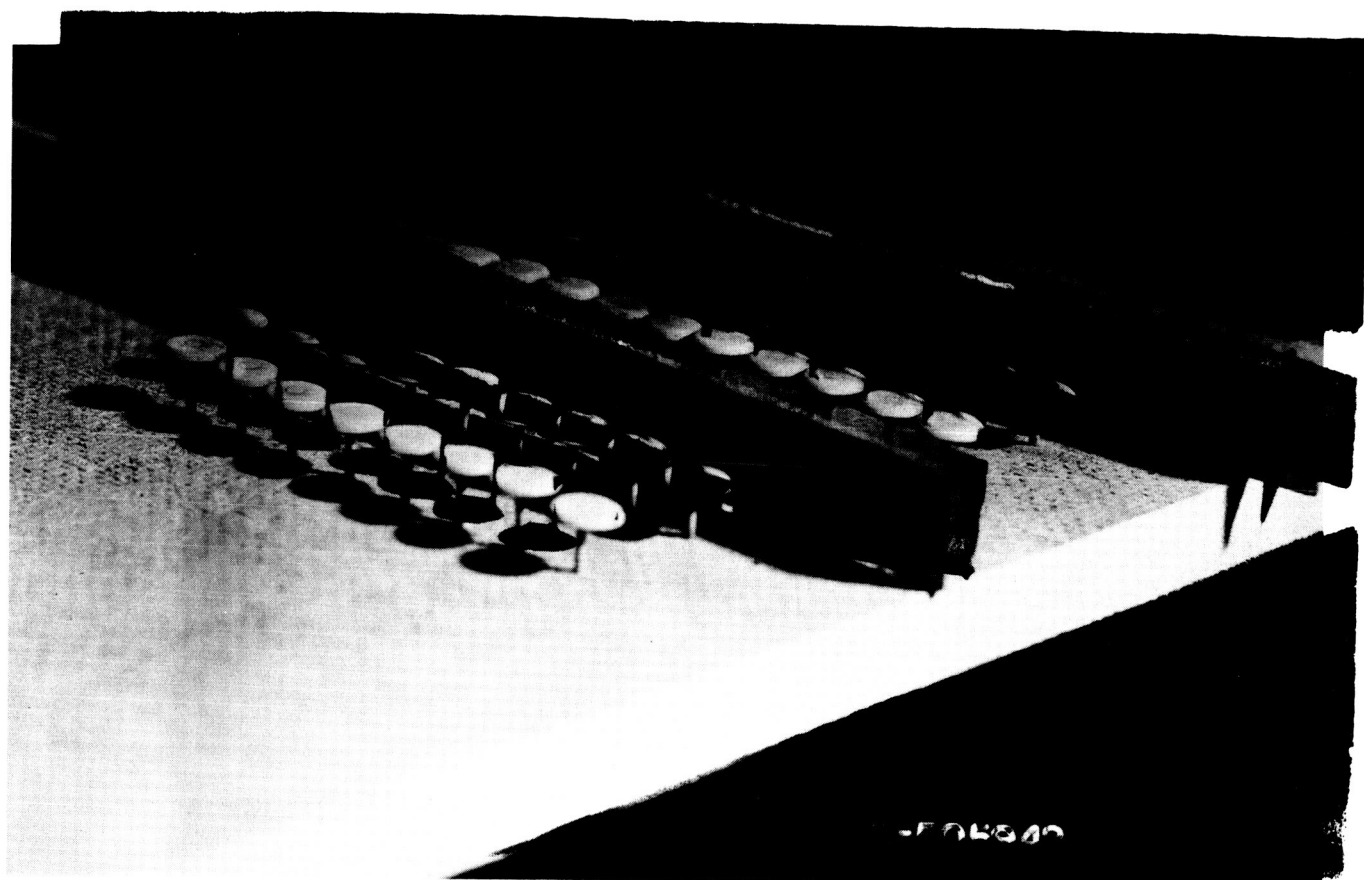
Figure 52. Intensity Equator and Model Orientation.



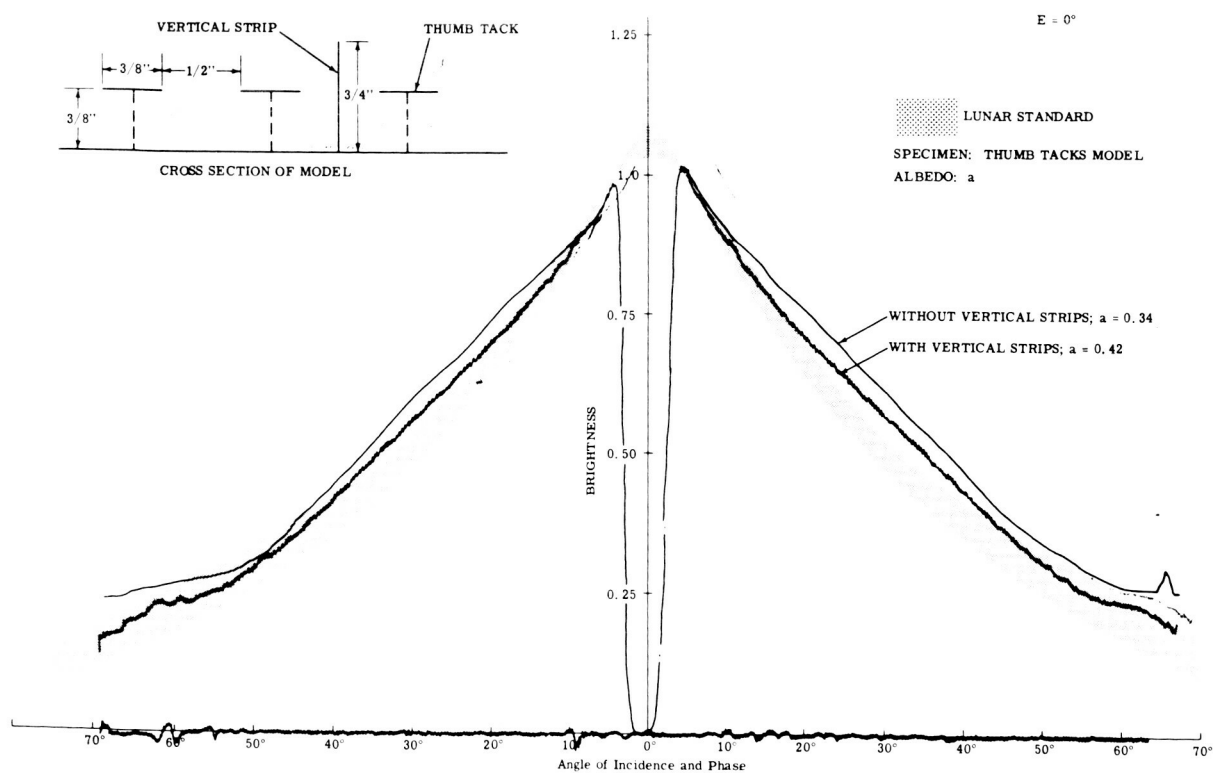
Note:

All Surfaces Assumed Lambertian
and Cross Sections in Plane of Vision

Figure 53. "Simple" Models and Their Probable Photometric Function

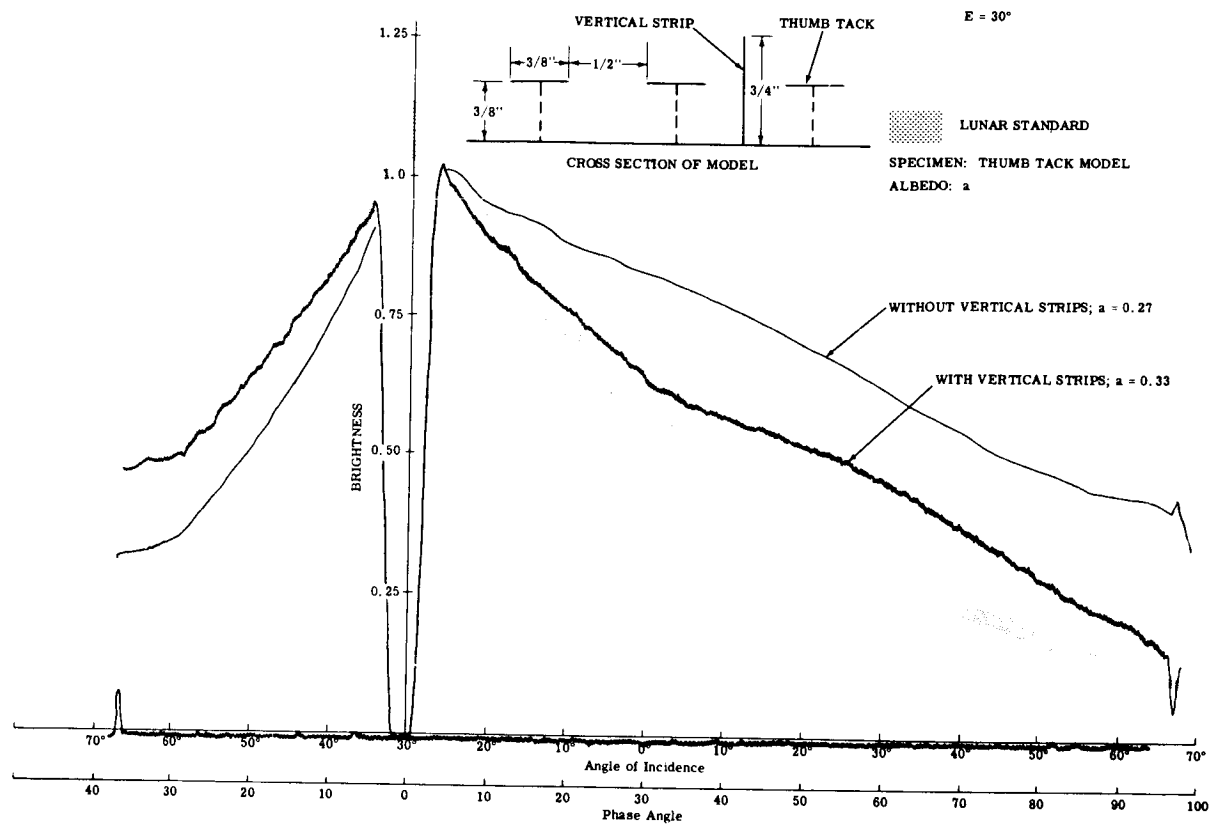


(a)

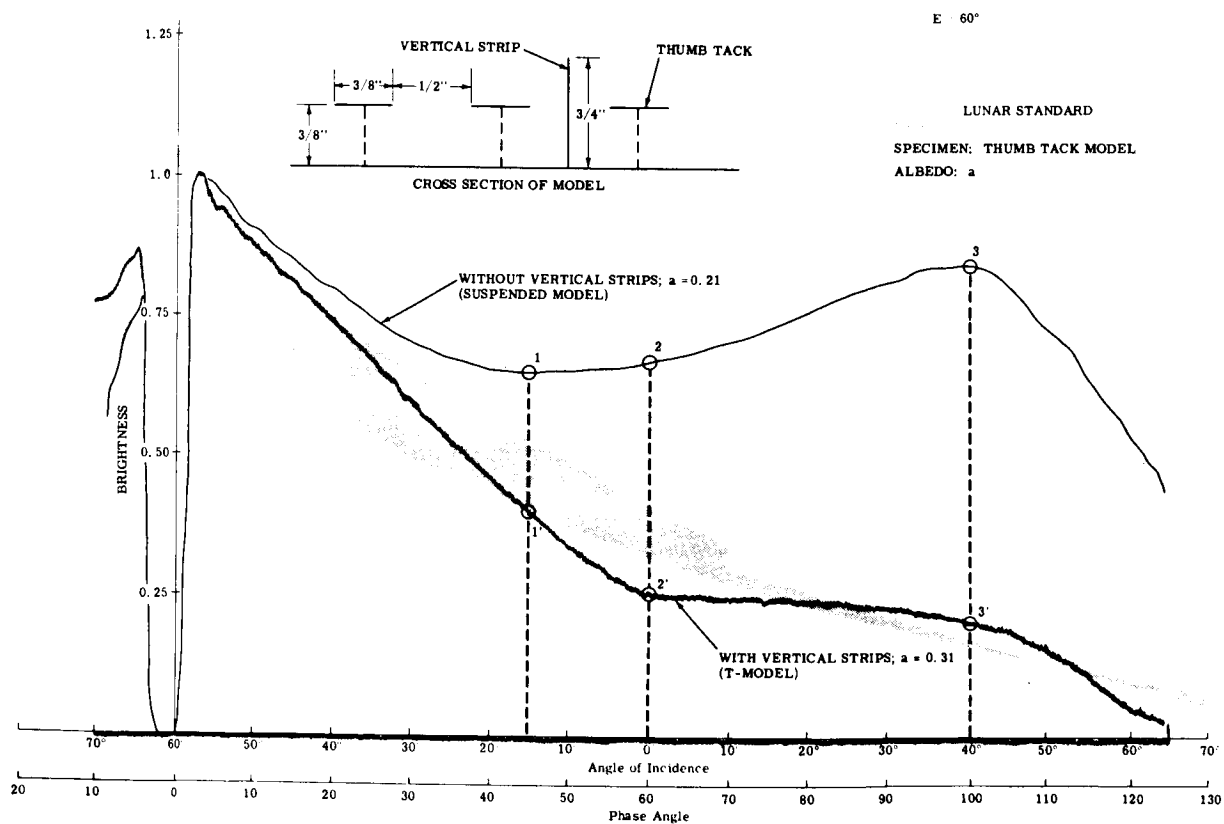


(b)

Figure 54. Thumb-Tacks Model (Sheet 1 of 2)

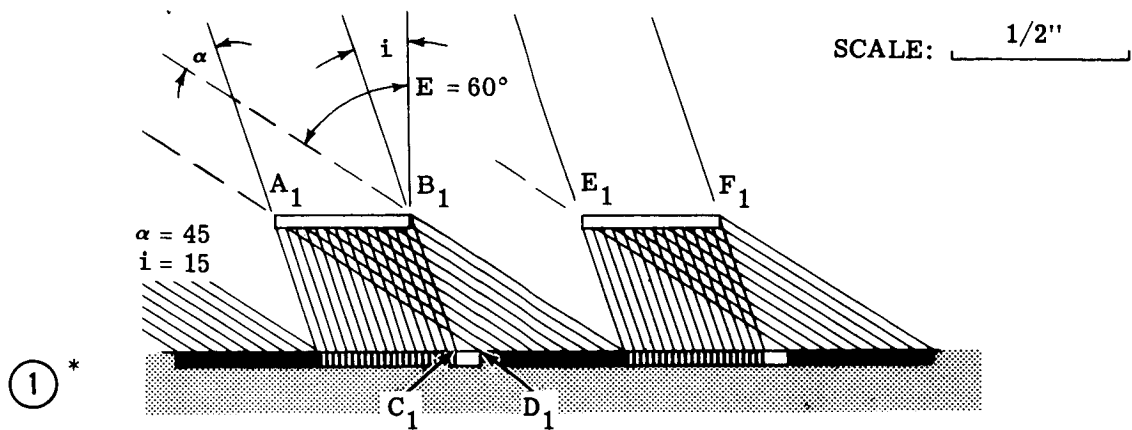


(c)

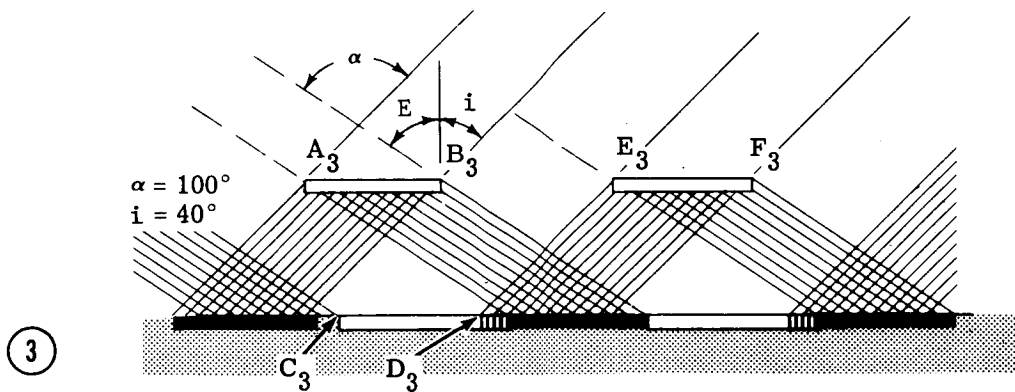
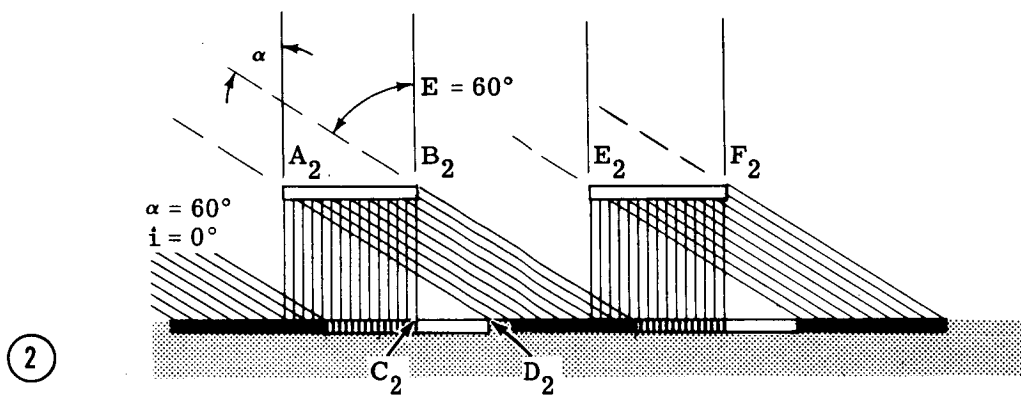


(d)

Figure 54. Thumb-Tacks Model (Sheet 2 of 2)



* See Figure 54d for Location of Points on Lunation Curves



(a) WITHOUT VERTICAL STRIP

LEGEND

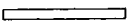
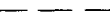



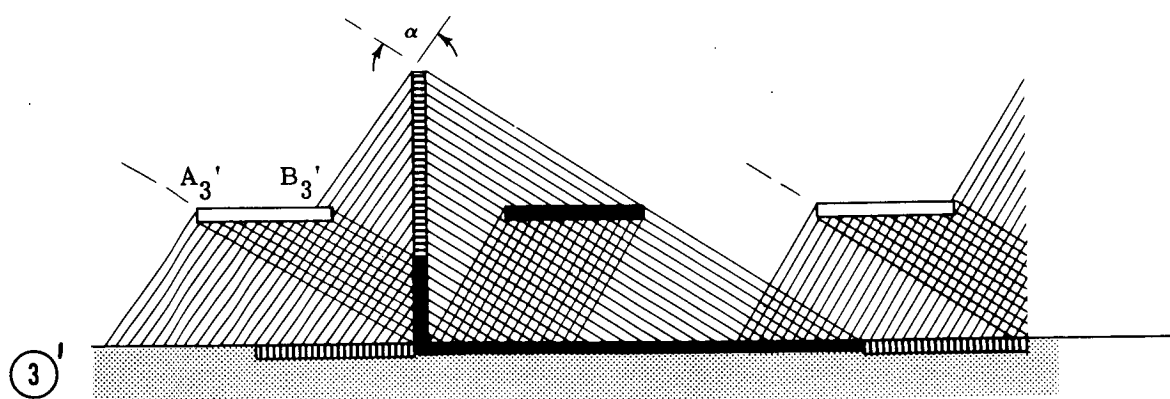
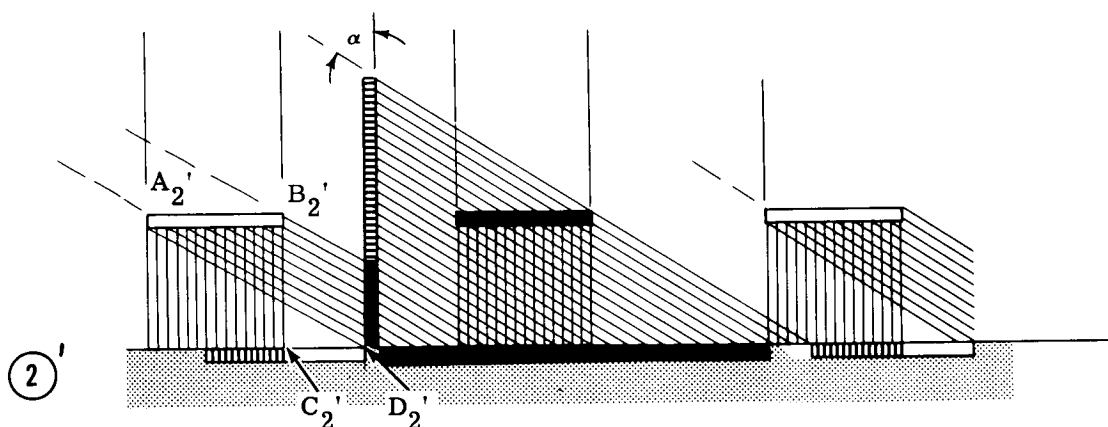
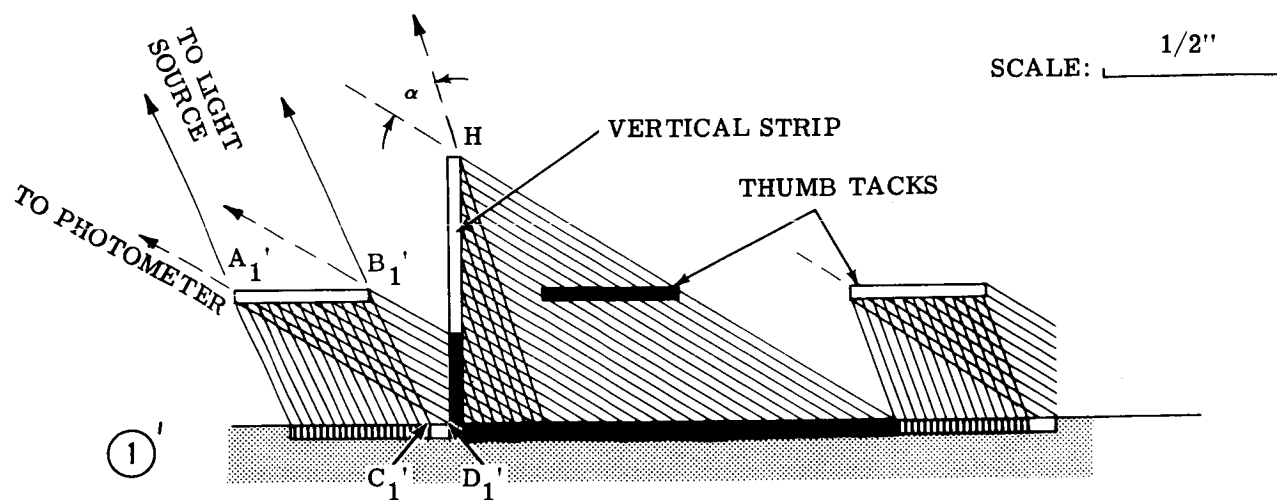
	Illuminated Areas Seen by Photometer		Line of Sight
	Shadow Zone		Ray of Light
	Occultation Zone		

Figure 55a. Cross Sections of and Shadowing Sequence in Thumb-Tack Model



(b) WITH VERTICAL STRIP

LEGEND


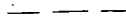



- | | | | |
|---|--------------------------------------|---|---------------|
|  | Illuminated Areas Seen by Photometer |  | Line of Sight |
|  | Shadow Zone |  | Ray of Light |
|  | Occultation Zone | | |

Figure 55b. Cross Sections of and Shadowing Sequence in Thumb-Tack Model

PHASE III — PHOTOMETRY OF "CONTROLLED" PARTICULATE SPECIMENS

Purpose

It is the purpose of this phase to investigate the effect of grain size, porosity (or apparent density), and albedo on the photometric function, and to attempt to clarify some of the confusion that has obscured the interpretation of the lunar photometric data.

Test Specimens

The test specimens in this phase consist of particulate materials only. Such materials may be made up either of artificial spheres of any controlled size, or of randomly comminuted, irregular particles ranging in grain size from microns to centimeters. In the study of porosity effects on the photometric function, the porosity of such materials may be varied by either one of the following techniques:

1. Ordered packing: Select "macro" spheres (i.e., of the order of millimeters or a centimeter) of uniform albedo and diameter (material composition is not important so long as the spheres are opaque), and arrange them in various "stable" or "unstable" packing patterns. The porosity of stable patterns may range from a minimum of 26% for the face-centered cubic packing to 66% for the diamond cubic. Higher porosities, approaching 100%, may be obtained by either bonding the spheres or physically suspending them using thin elements of negligible shadow casting capability.
2. Random packing: Use comminuted powders sorted into various particle sizes. Such powders, when loosely sifted, assume varying degrees of porosity depending upon the importance of two opposing effects; one of these effects would favor a high porosity when the particles are small enough to be susceptible to inter-particle cohesive forces, whereas the other effect would favor a high porosity when the

particles are large and contain micropores. When the large porous particles are broken down into finer elements, one may expect a gradual decrease in porosity due to the destruction of the micropores. However, one may reach a limit of particle size below which the porosity of a loosely sifted powder could increase again due to the predominance of surface forces over body forces.

The first technique, unlike the second, has the advantage of lending itself to accurate control of grain size and albedo during the process of varying porosity. However, the "random packing technique" was adopted in these experiments because it is much less laborious than the "ordered packing technique," and, moreover, because it allows the "dissection" of the Phase I natural specimens that were investigated in their "as is" condition. The purpose of this attempt is not to create new photometric models, but to account better for the photometric properties of the original specimens in terms of their porosity, grain size, and albedo.

Two specimens, volcanic cinder and furnace slag, successfully investigated in Phase I, were selected for further photometric analysis. Since the original specimens were not sufficient for the needs of this operation, new batches were ordered from their respective sources. Six specimens of volcanic cinders (differing in color, albedo and surface texture) were received from Hawaii. These samples originated from the summit of Haleakala on the Island of Maui (in the area known as Red Hill and Kolekole). According to Dr. W. R. Steiger (Ref. 25) who was instrumental in securing these samples, four of them, Nos. 4, 5, 6, and 9 (reddish-brown in color) were from the surface and thus were considerably weathered. Sample Nos. 7 and 8 (black in color) were taken from a cut, and thus they are relatively unweathered. The age of these volcanic cinders is estimated to be between 0.4 and 0.9 million years. Their composition is not well known, but they are believed to belong to the Alkalic Basalt group. Their probable chemical composition, given by Dr. Steiger, is as follows:

SiO ₂	43%
Al ₂ O ₃	14%
Fe Oxides	15%

MgO	6%
CaO	11%
Na ₂ O	4%
K ₂ O	1%
TiO ₂	6%

All six specimens were investigated photometrically at all viewing angles in an "as-received" condition in order to select the most suitable one for crushing and screening. The results are shown in Figs. 57a through d. All the specimens show appreciable backscatter and reproduce the lunar data reasonably well. Volcanic cinder No. 4, showing one of the best fits with the lunar curves, was selected for further investigation. Its original grain size distribution is shown in Fig. 56. In Figs. 57a through d, it is of interest to note that volcanic cinders No. 7 and 8 show the poorest fit with the lunar curves despite their low albedo. This anomaly is probably due to their relatively smoother, unweathered surfaces as pointed out by Dr. Steiger.

Several new specimens of furnace slag were selected from a new shipment from NASA Manned Spacecraft Center, Houston, Texas, and were photometrically measured at all viewing angles. The results of three specimens, labeled Nos. 2, 3, and 4, are shown in Figs. 59a through d. These figures also include the Furnace Slag No. 1 curves obtained in Phase I. None of the new specimens reproduce the lunar curves as closely as Furnace Slag No. 1. Since there was not a sufficient quantity of this particular specimen for comminution and segregation, the next best furnace slag, No. 4, was chosen.

Experiments

The volcanic cinder and furnace slag specimens chosen for further analysis were ground and screened into seven gradations of particle sizes, ranging from centimeters to microns as shown in Tables I and II and Figs. 61 and 63. For both specimens, the original, unbroken lot is labeled as No. 1 and the seven ground and segregated lots of powders are labeled as Nos. 2 through 8 in order of decreasing grain size.

TABLE I
GRAIN SIZE, POROSITY AND ALBEDO OF VOLCANIC CINDER NO. 4 POWDERS

Curve No. Ref. Fig. 58	Grain Size		Weight of Solids, W_s g	Apparent Volume, V_a cm ³	Volume of the Solids, V_s cm ³	Apparent Density, g/cm ³ $\rho_a = \frac{W}{V_a}$	Real Density g/cm ³ $\rho_r = \frac{W}{V_s}$	% Porosity* $n = 100(1 - \frac{\rho_a}{\rho_r})$	Albedo @ Viewing Angle		
	Range mm	Avg. mm							0°	30°	60°
1	80								0.14	0.14	0.14
2	6.35-2.83	4.6	4.9	5.8	1.8	0.85	2.72	71	0.14	0.14	0.14
3	2.83-1.19	2.0	4.7	4.7	1.6	1.00	2.94	64	0.14	0.14	0.14
4	1.19-0.50	0.85	6.4	5.5	2.1	1.16	3.05	60	0.14	0.14	0.14
5	0.50-0.21	0.35	5.5	4.0	1.8	1.38	3.05	53	0.14	0.14	0.14
6	0.21-0.088	0.15	6.3	4.8	2.1	1.31	3.00	55	0.14	0.13	0.13
7	0.088-0.037	0.062	6.5	5.4	2.3	1.20	2.82	59	0.14	0.13	0.12
8	0.037	0.02	4.4	5.5	1.5	0.80	2.93	73	0.18	0.17	0.16
Average ρ_r							2.93				

*Based on average ρ_r

TABLE II.
GRAIN SIZE, POROSITY AND ALBEDO OF FURNACE SLAG NO. 4 POWDERS

Curve No.	Grain Size Range mm	Avg. mm	Weight of Solids, W_s g	Apparent Volume, V_a cm^3	Volume of the Solids, V_s cm^3	Apparent Density, g/cm^3 $\rho_a = \frac{W}{V_a}$	Real Density g/cm^3 $\rho_r = \frac{W}{V_s}$	% Porosity* $n = 100(1 - \frac{\rho_a}{\rho_r})$	Albedo " Viewing Angle	0°	30°	60°
1		≈ 80								0.11	0.11	0.11
2	6.35-2.53	4.6	5.7	3.6	1.3	1.59	4.4	65		0.10	0.10	0.10
3	2.83-1.19	2.0	5.9	3.0	1.2	1.97	4.8	56		0.09	0.09	0.09
4	1.19-0.50	0.85	6.9	3.8	1.4	1.82	4.9	60		0.08	0.08	0.08
5	0.50-0.21	0.35	5.5	2.9	1.2	1.90	4.6	58		0.08	0.08	0.07
6	0.21-0.088	0.15	6.4	3.6	1.5	1.78	4.3	60		0.08	0.07	0.07
7	0.088-0.037	0.064	6.3	3.9	1.4	1.60	4.5	65		0.11	0.11	0.10
8	< 0.037	0.02	4.3	3.0	1.0	1.44	4.3	68		0.12	0.12	0.19

Average ρ_r

*Based on average ρ_r

For the photometric measurements, the powders were loosely sifted from a height of a few inches onto a flat board. Likewise, in order to determine the porosity of the specimens, each lot of powder was loosely sifted into a narrow graduated tube up to a height of about 3 inches. The weight and volume of the powder were measured in order to determine its apparent density, ρ_a . The real density, ρ_r , was determined by measuring the volume of the solid particles by the water displacement method. These measurements, including the calculated porosities are shown in Tables I and II for the volcanic cinder and furnace slag, respectively.

The experimental data on apparent density, porosity, and albedo as a function of grain size are plotted in Fig. 61 for the volcanic cinder and in Fig. 63 for the furnace slag.

The albedo and photometric properties for each lot of powder at the three viewing angles were measured. The results for the volcanic cinder constituents are shown in Figs. 58b through d, those for the furnace slag are shown in Figs. 60b through d. They are analyzed in the next section in terms of their grain size, porosity, and albedo.

Discussion of Test Results

The size reduction of the particles or elements of an initially good lunar photometric model was originally conceived as a means of varying the porosity of that model; it was proposed as an experiment largely based upon the notion that the progressive reduction of the size of the particles "could give a poorer match with the lunar data (mostly due to a reduction in porosity) perhaps including the micron range despite the fluffing caused by the predominance of the surface forces over body forces." This statement was made in a preproposal inquiry (Ref. 11) preceding this work. The expected failure of the fine particles in the micron (i.e., "fairy castle") range to reproduce the lunar data was attributed at that time to a possible increase of the albedo of the powder in these size ranges. These predictions are largely corroborated by the results of our experiments that include measurements of porosity, albedo, and photometric function of two comminuted specimens segregated into grain sizes covering a spectrum of three orders of magnitude (0.01 mm to 10 mm).

An inspection of Figs. 61 and 63 reveals the following points of interest:

As expected, both specimens show an increase of albedo with decrease of particle size. This increase is more sudden below a grain size of 0.1 mm, than is gradual throughout the spectrum. Above 0.1 mm the albedo of volcanic cinder is constant, whereas that of furnace slag shows a slight but surprising increase with increasing grain size.

The predicted porosity vs. grain size relationship is obeyed by both specimens. Figures 61 and 63 show a dip in the porosity curve (or a peak in the apparent density curve). The loss of porosity around the middle of the spectrum is due (as discussed in a preceding section) to the fact that the micropores within the individual particles are destroyed without, as yet, being compensated by the fluffing action of surface forces. The point of minimum porosity is reached sooner by the furnace slag (at a grain size of about 0.7 mm) than by the volcanic cinder (at a grain size of about 0.3 mm). Both specimens exhibit the same minimum and maximum porosities, about 55% and 70% respectively. The 70% maximum is experienced at both ends of the particle size spectrum.

The real densities of the specimens, unlike their porosities, differ appreciably. The average real density of 2.93 g/cm^3 for the volcanic cinder is comparable to basaltic rocks, whereas a value of 4.5 for the furnace slag is indicative of appreciable metallic content. The fact that both specimens have similar porosity-grain size relationships, despite differences in real densities, indicates that the cohesive forces between the furnace slag particles are stronger than those between volcanic cinder particles. Of course, the ambient gravity field does play a role in the porosity-grain size relationship. It is conceivable that both of these specimens would assume measurably higher porosities in the lower gravity field of the moon, particularly toward the low end of the particle size spectrum.

For convenience in assessing qualitatively the photometric test results, all measurements taken on the constituents of a given specimen at a given viewing angle are plotted on the same chart. Figures 58b through d and 60b through d show clearly that the predicted deterioration of the match with the lunar data at reduced grain sizes is largely confirmed for both specimens. This observation should not necessarily be interpreted to mean that fine, micron-size powders are less likely to exist on the moon than coarse, millimeter to centimeter-size particles. It is the

purpose of these experiments to show that grain size, per se, is not a key photometric property, and that information on albedo and porosity are needed for a meaningful interpretation of test results.

The data in Figs. 58 and 60 are plotted in a different form in order to show, in a quantitative manner, the progressive deviation of curves labeled 1 to 8 from the lunar standard band. Figures 62 and 64 show the actual extent of this deviation as a function of particle size for volcanic cinder and furnace slag respectively. The expression "match index" is used as a measure of this deviation and is defined as the ratio of the area under the test curve to the area under the lunar curve. The latter curve is determined by a line bisecting the gray lunar standard band. Both areas are delimited to the left by a vertical line at 0° phase angle and at the top by a horizontal line at ordinate 1.0. Assuming no local irregularities in the test curves, a match index of 1.0 would suggest a good match with the lunar data. The greater the deviation of the index from the value 1.0, the poorer is the match with the lunar data. Indices less than one indicate that the specimen has a sharper backscatter than the lunar surface. Match-index vs. grain size curves are plotted for each viewing position. The curves for both specimens at all three viewing angles, begin with I_m equal to about one at the coarse end of the particle size spectrum and rise noticeably in the direction of the fine particles. This rise, which actually represents a deterioration of the backscattering function, is not continuous, but reverses itself toward the middle or fine end of the spectrum, (about 0.1 mm particle size). A glance at the porosity vs. grain size chart on the opposite page reveals that this reversal, (which in effect is an improvement of the backscattering function) is due largely to an increase of porosity caused by the fluffing action of surface forces. However, at around 70% porosity, at the fine end of the spectrum, the match index does not go all the way back to 1.0, from which it started at the coarse end of the spectrum, but stops around 1.5. The most probable explanation of this phenomenon may be found in the behavior of the albedo vs. grain size curves. We notice in Figs. 62 and 63 that the albedo of both specimens increases rather suddenly below 0.1 mm particle size. This increase, predicted on the basis of data by Hapke, is about 30% for volcanic cinder and 40% for furnace slag. It is conceivable that multiple reflection in a high albedo medium could lighten the shadows that are primarily responsible for the backscatter. The experiments in Phase I with Coral No. 1 having varying albedos (Fig. 35) give sufficient evidence of this effect, and justify the conclusion that in complex random surfaces such as may be found

on the moon, a high porosity, of the order of 70%, is necessary, although not sufficient without a sufficiently low albedo to account for the photometric properties of the lunar surface. The other important conclusion to be derived from these experiments is that the grain size of the material covering the lunar surface cannot be inferred directly from its photometric properties. However, there are a number of reasons why the grain size of laboratory specimens should be known and preferably controlled: it should be known because, as we have demonstrated, grain size influences other physical properties that are photometrically relevant, such as porosity, (particularly when the particles are fine and are loosely sifted) and albedo (in the absence of darkening due to an external agent); it should be controlled because there is a lower and upper limit of grain size beyond which photometric measurements may lose their meaning. The lower limit, of the order of a few microns, is determined by the loss of opacity of the grain or diffraction when the grains and the spacing between them are not too large in comparison with the wavelength of visible light. The upper limit is determined by the size of the area viewed by the photometer. The grains must be small enough (of the order of a few centimeters in our case) for a representative number of them to be included under the area of observation. A more accurate determination of the grain size boundaries as a function of the wavelength of light and viewing area is very desirable but beyond the scope of this study.

These experiments render the thick single layer lunar dust theory less tenable in view of the incompatibility of fine rock dust with the low albedo of the moon, unless, of course, it be demonstrated that certain mechanisms operating on the moon could darken the rock dust without fusing or cementing it. Sytinskaya claims, on the basis of extensive albedo-color matching tests, that darkening on the moon can only be explained by the fusion of meteorites and target material due to the heat generated at impact.

A Reevaluation of Former Photometric Models

Essentially, the results of the above experiments confirm previous findings. They make it clear that the best known lunar photometric models, such as van Diggelen's "peat moss" (a vegetal material), and Hapke's "fairy castles" (made up of loosely sifted fine metallic oxide powders) appear to owe their success to their high porosity, low albedo, and intricate structure rather than to their grain size, chemical composition, or degree of internal cohesion.

In addition, our experiments help to narrow existing areas of disagreement. For instance, contradictory statements made by Barabashev and van Diggelen regarding the photometric properties of volcanic cinders, could be resolved in the light of the above experiments. Both of these investigators measured the photometric properties of volcanic cinder specimens of known albedo and grain size, but of unknown porosity. Their results are shown in Figs. 6 and 7. The specimen measured by Barabashev had particle sizes of 2 mm and coarser, whereas, van Diggelen's specimen had an average grain size of 0.1 mm. These data and our own porosity vs. grain size curves show that the porosity of these specimens significantly differed from one another, and that this fact may be sufficient to account for their conflicting photometric properties.

Figure 61 indicates that the porosity of volcanic cinder at the grain size of 0.1 mm, used by van Diggelen, is about at its minimum (50%), hence, it is most unlikely to reproduce the lunar data. This particular region of the grain size spectrum seems to represent the point where the grains are too small to contain micropores and too large to be susceptible to the fluffing action of interparticle cohesive forces. As to the specimen used by Barabashev, (2 to 6 mm grain size) it is safe to assume, on the basis of Fig. 61 data, that it had a porosity of about 70%, hence is most likely to pass the photometric test. Our photometric experiments confirm the conflicting results reported by van Diggelen and Barabashev, and our porosity measurements adequately account for this conflict. It may be concluded that it is premature to infer the presence or absence of volcanic cinder on the moon on the basis of the photometric data, and that the existing contradiction can be resolved if the photometric properties of terrestrial volcanic cinders are interpreted in terms of their porosity and albedo primarily, rather than in terms of their grain size or chemical composition.

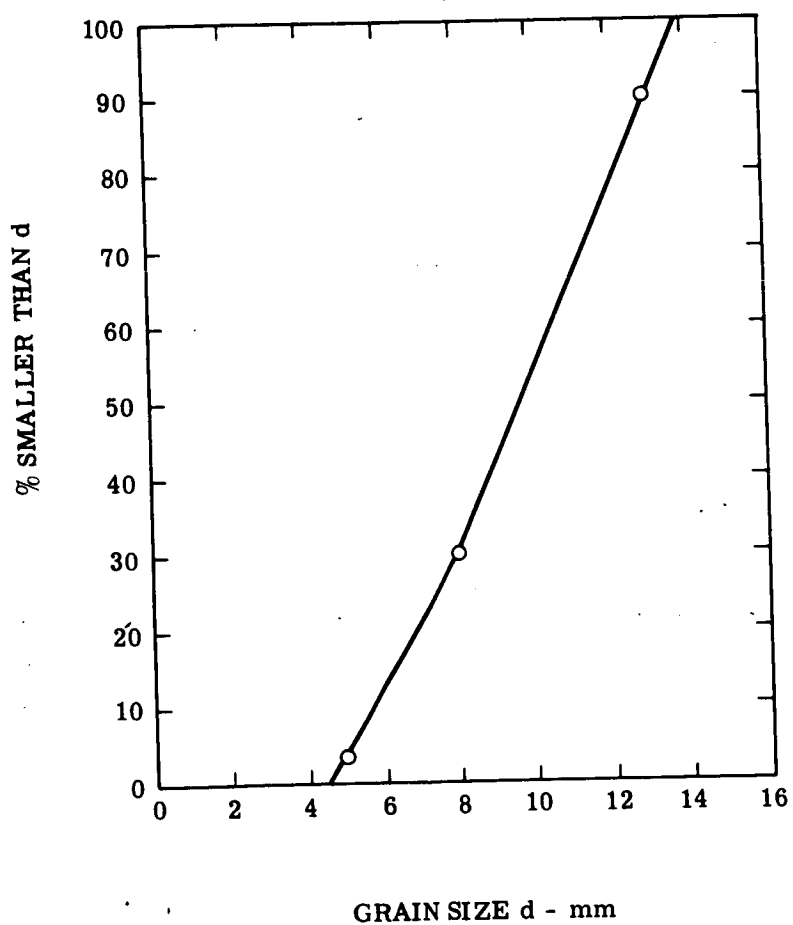


Figure 56. Grain Size Distribution of Hawaiian Volcanic Cinder No. 4



(a) Cinder No. 4



(b) Cinder No. 5

Figure 57. Photometry of Coarse-Grained Hawaiian Volcanic Cinder Specimens
(Sheet 1 of 5)

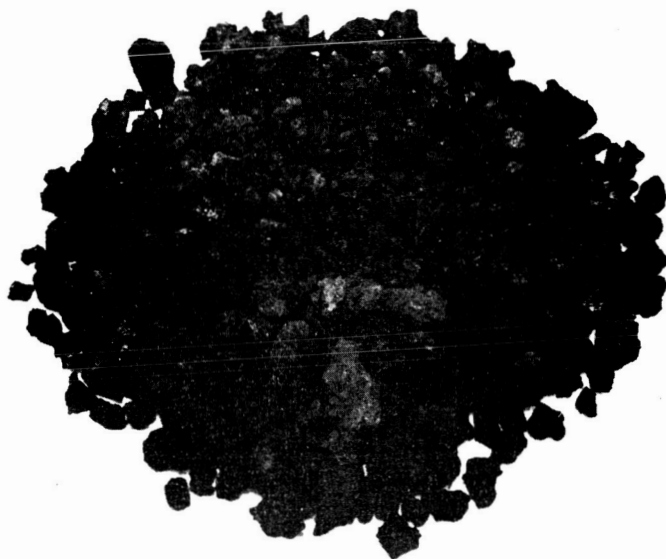


(c) Cinder No. 6



(d) Cinder No. 7

Figure 57. Photometry of Coarse-Grained Hawaiian Volcanic Cinder Specimens
(Sheet 2 of 5)



(e) Cinder No. 8



(f) Cinder No. 9

Figure 57. Photometry of Coarse-Grained Hawaiian Volcanic Cinder Specimens
(Sheet 3 of 5)

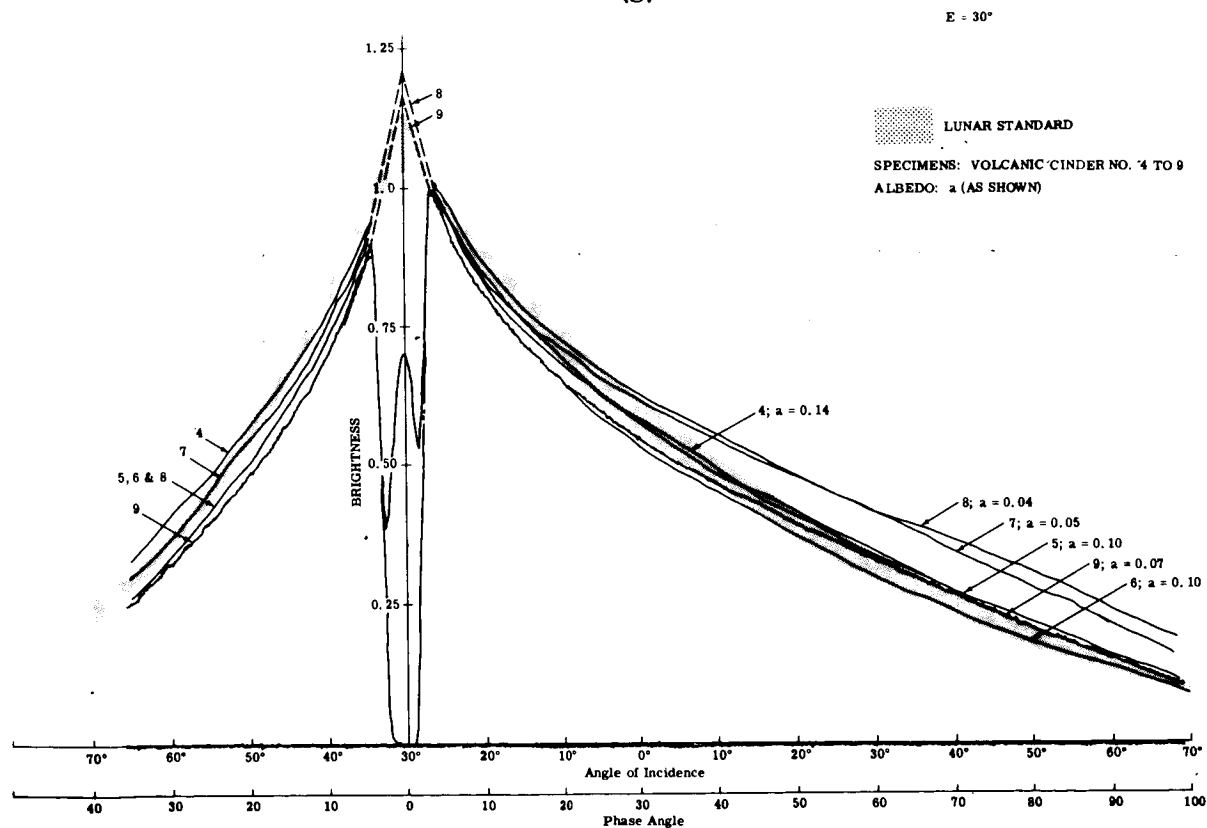
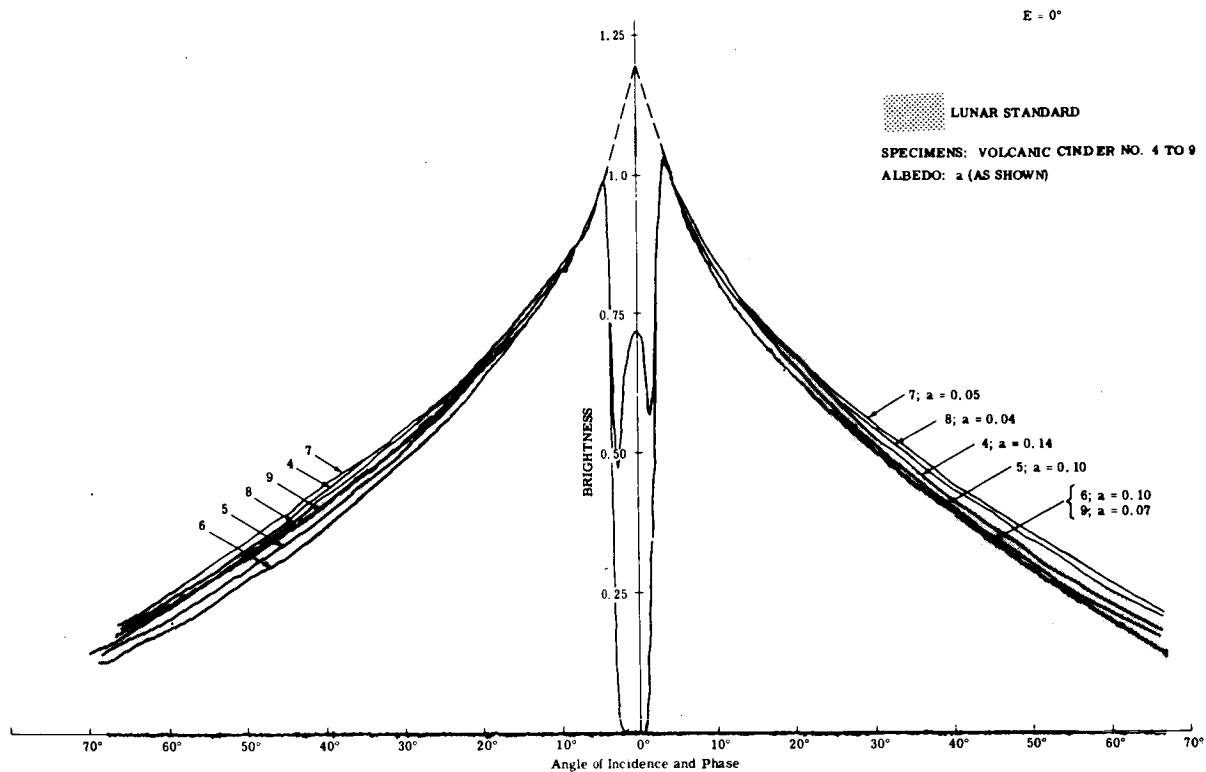
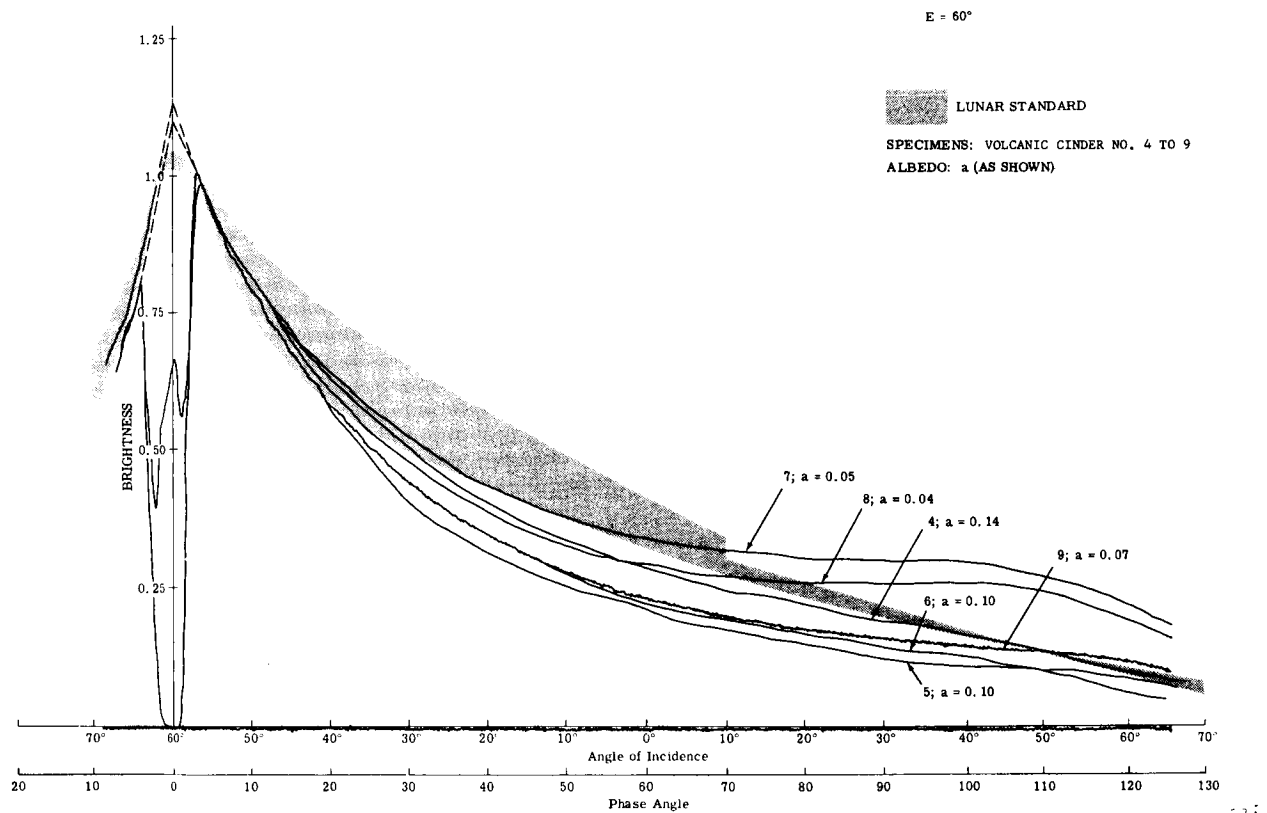
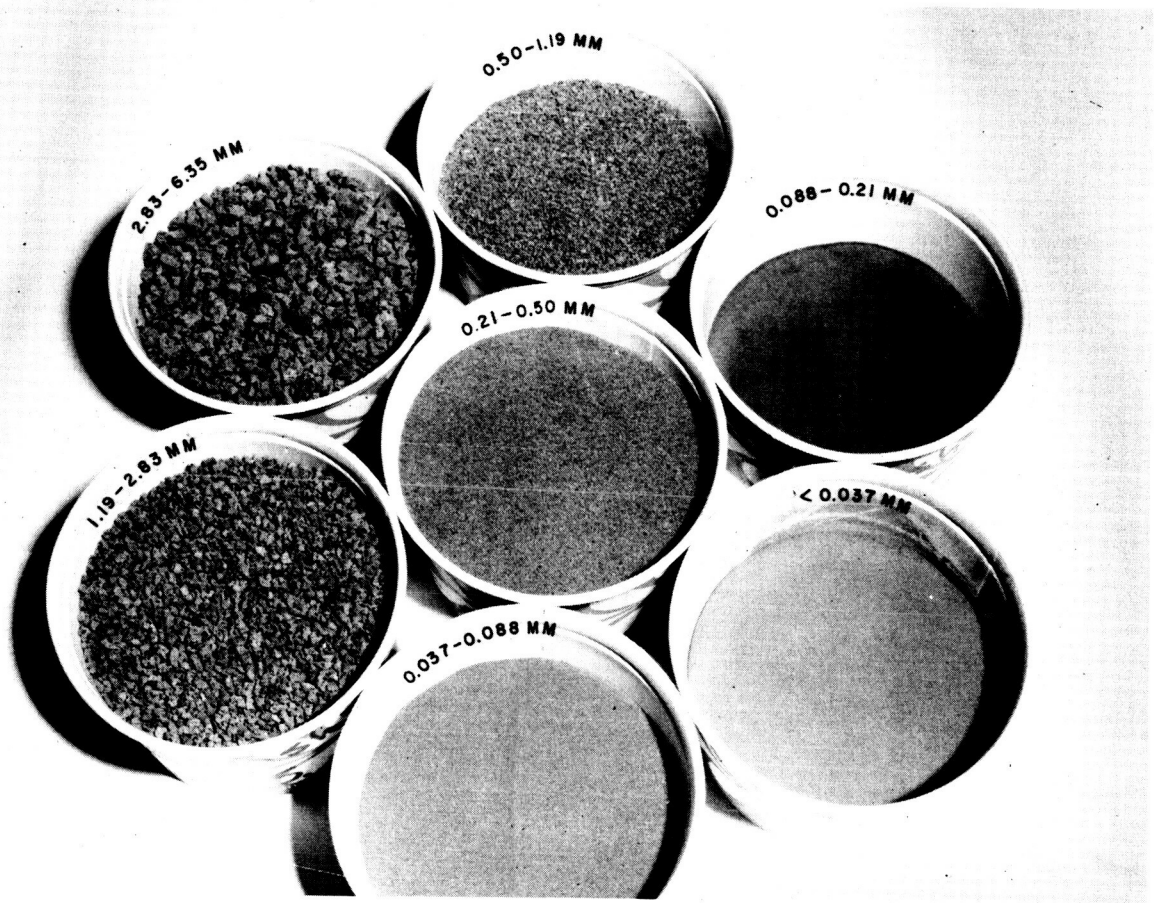


Figure 57. Photometry of Coarse-Grained Hawaiian Volcanic Cinder Specimens
(Sheet 4 of 5)

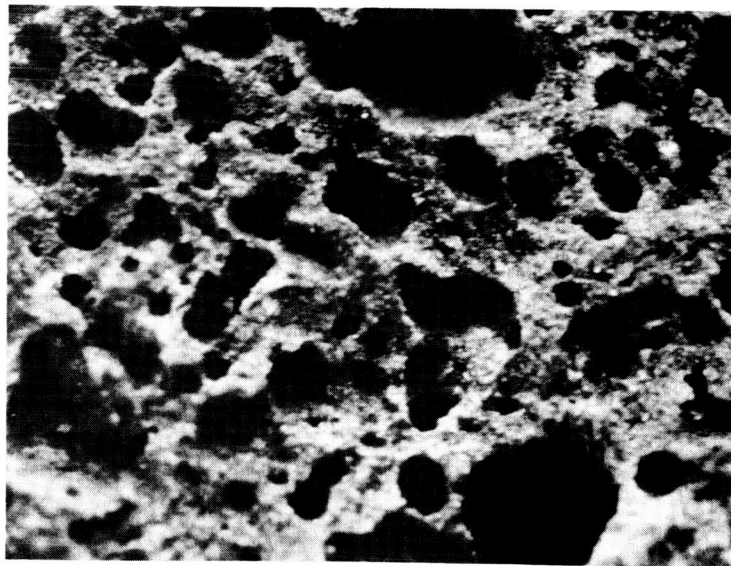


(i)

Figure 57. Photometry of Coarse-Grained Hawaiian Volcanic Cinder Specimens
(Sheet 5 of 5)

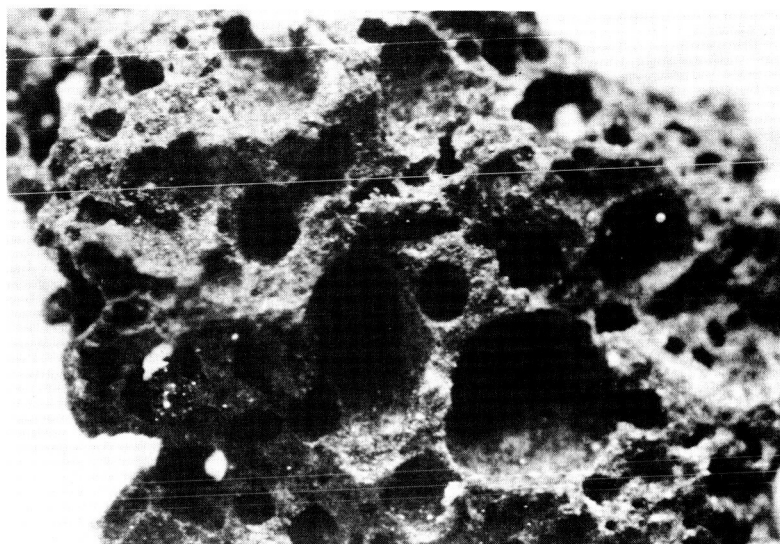


(a) Cinder # 4, Ground and Sorted



(b) Grain Size (Magnified 21X)

Figure 58. Photometry of Volcanic Cinder # 4 as Function of Grain Size, Porosity, and Albedo (Sheet 1 of 5)



(c) Magnified 20X



(d) Magnified 25X

Figure 58. Photometry of Volcanic Cinder # 4 as Function of Grain Size, Porosity, and Albedo (Sheet 2 of 5)

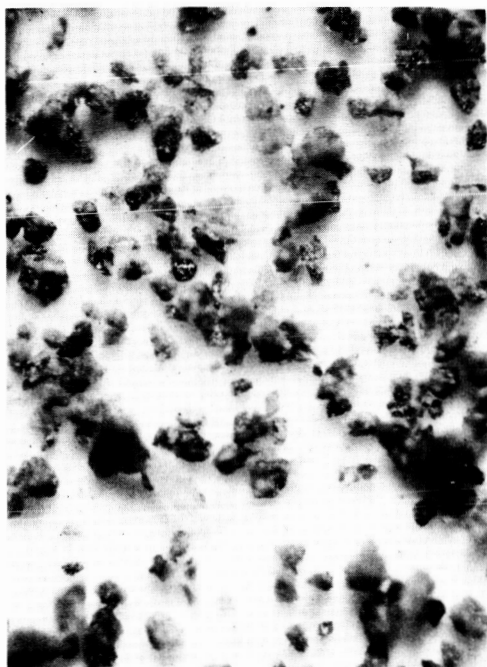


(e) Magnified 25X

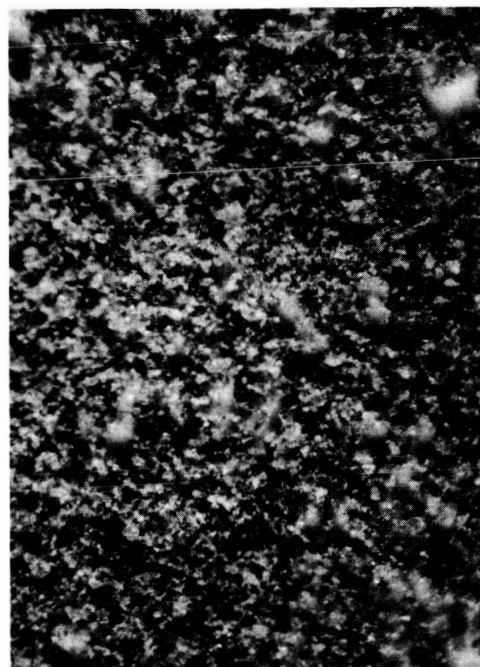


(f) Magnified 65X

Figure 58. Photometry of Volcanic Cinder # 4 as Function of Grain Size, Porosity, and Albedo (Sheet 3 of 5)



(g) Magnified 65X



(h) Magnified 65X

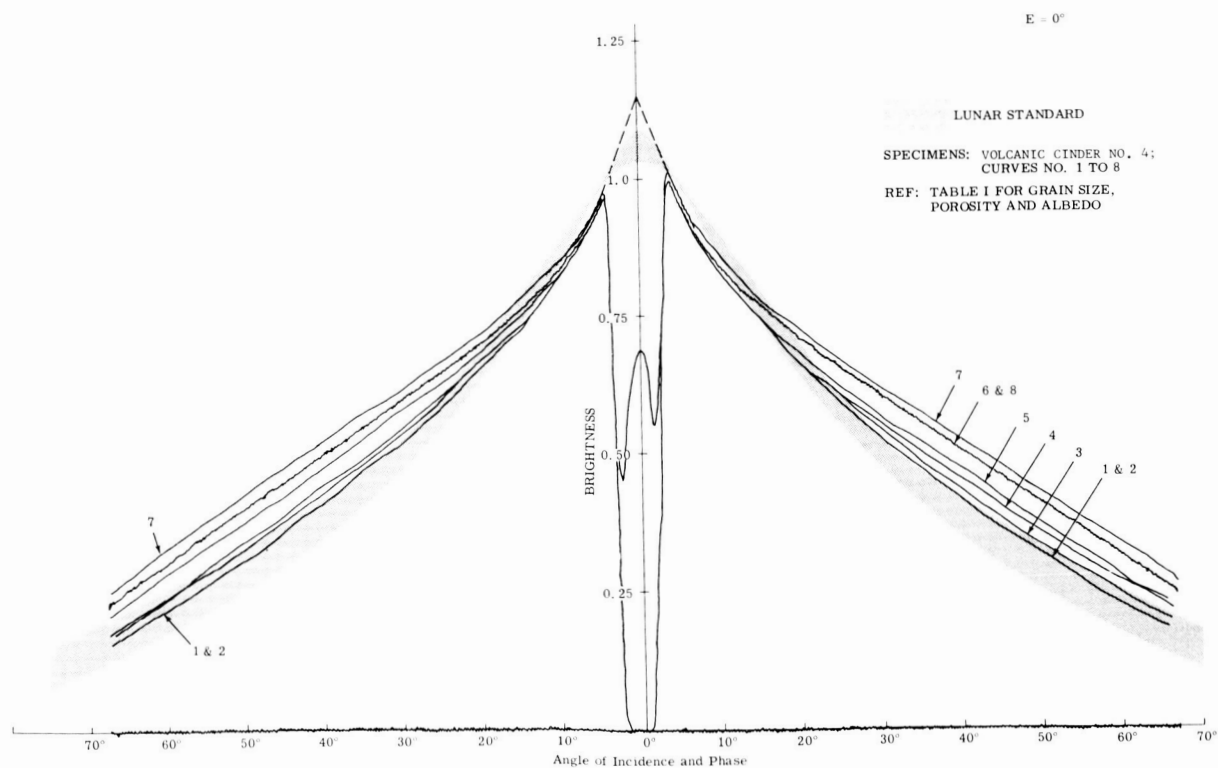


Figure 58. Photometry of Volcanic Cinder # 4 as Function of Grain Size Porosity, and Albedo (Sheet 4 of 5)

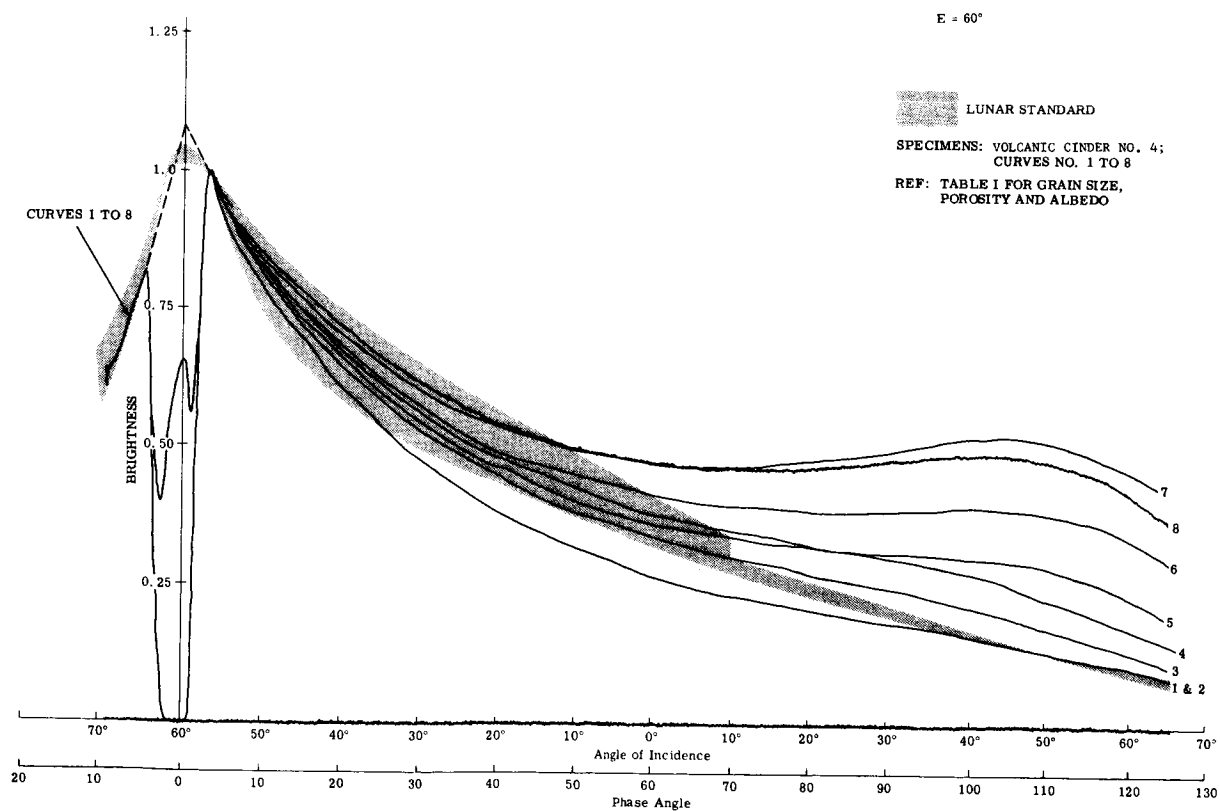
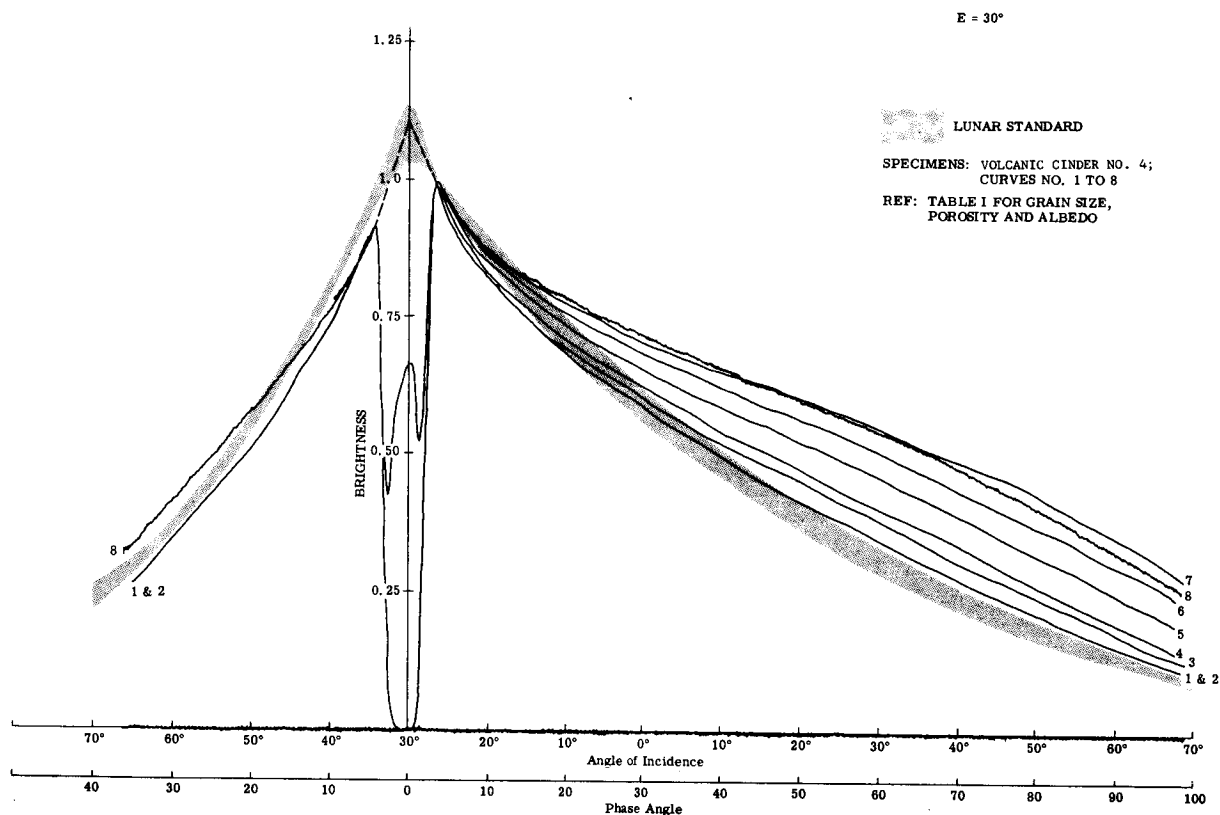


Figure 58. Photometry of Volcanic Cinder # 4 as Function of Grain Size, Porosity, and Albedo (Sheet 5 of 5)



(a)

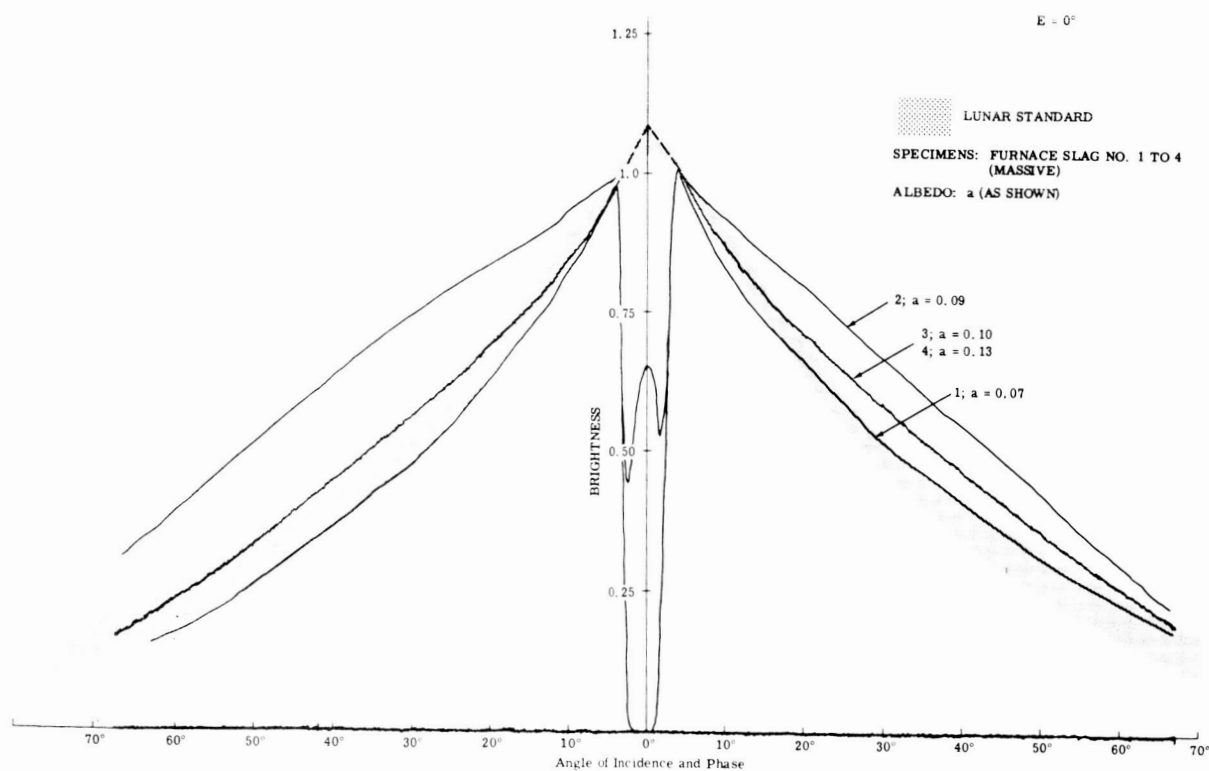


(b)

Figure 59. Photometry of Massive Furnace Slag Specimens (Sheet 1 of 3)



(c)



(d)

Figure 59. Photometry of Massive Furnace Slag Specimens (Sheet 2 of 3)

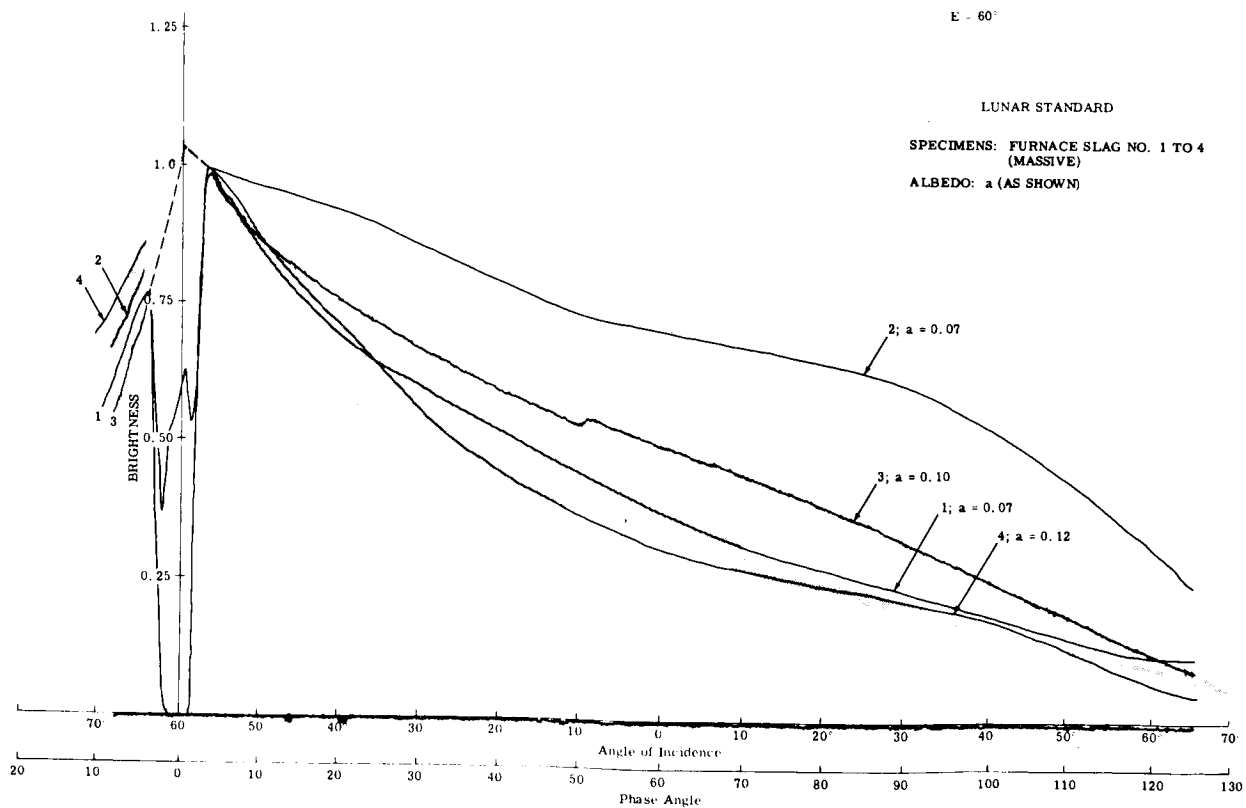
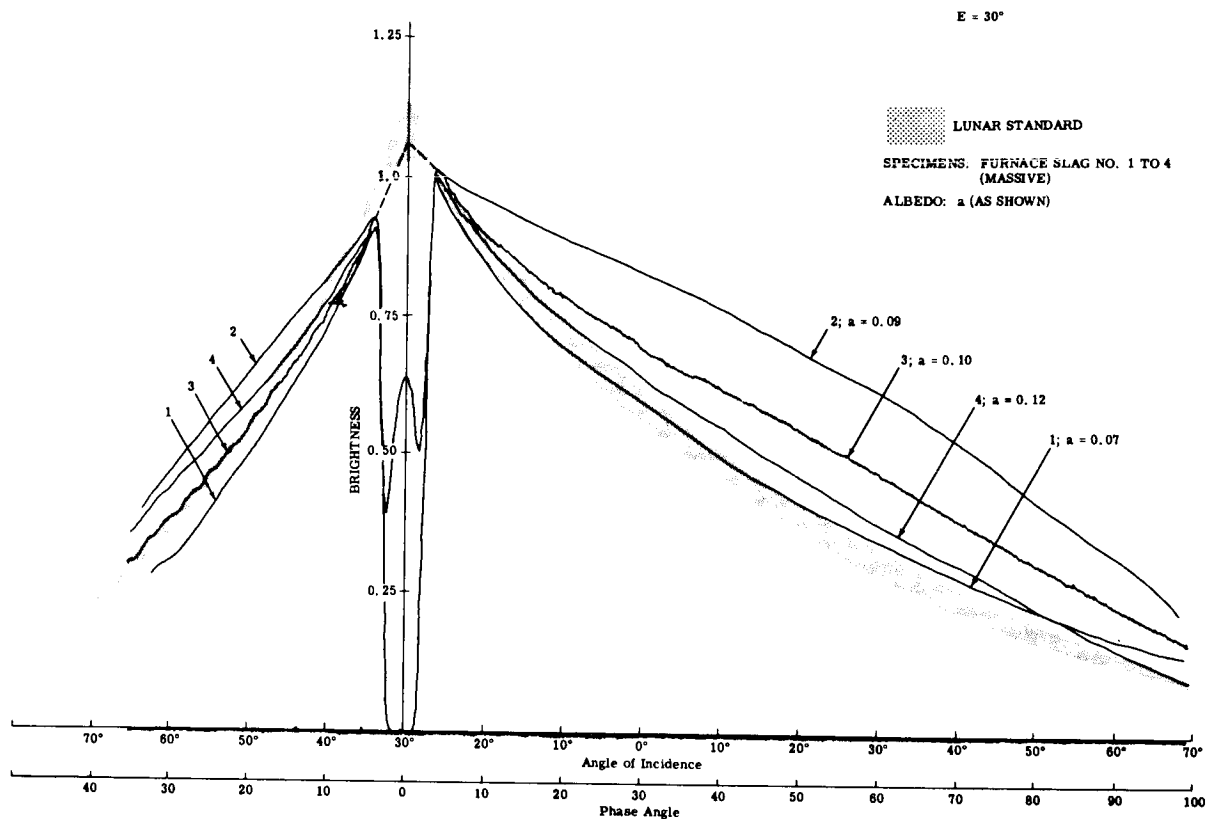
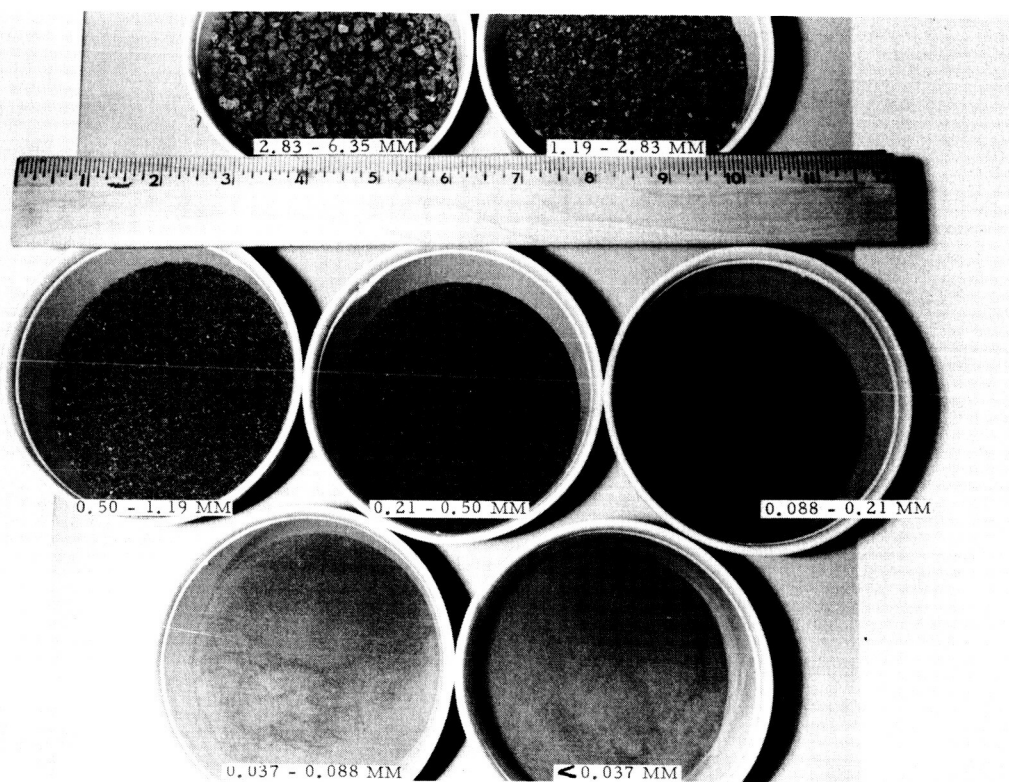
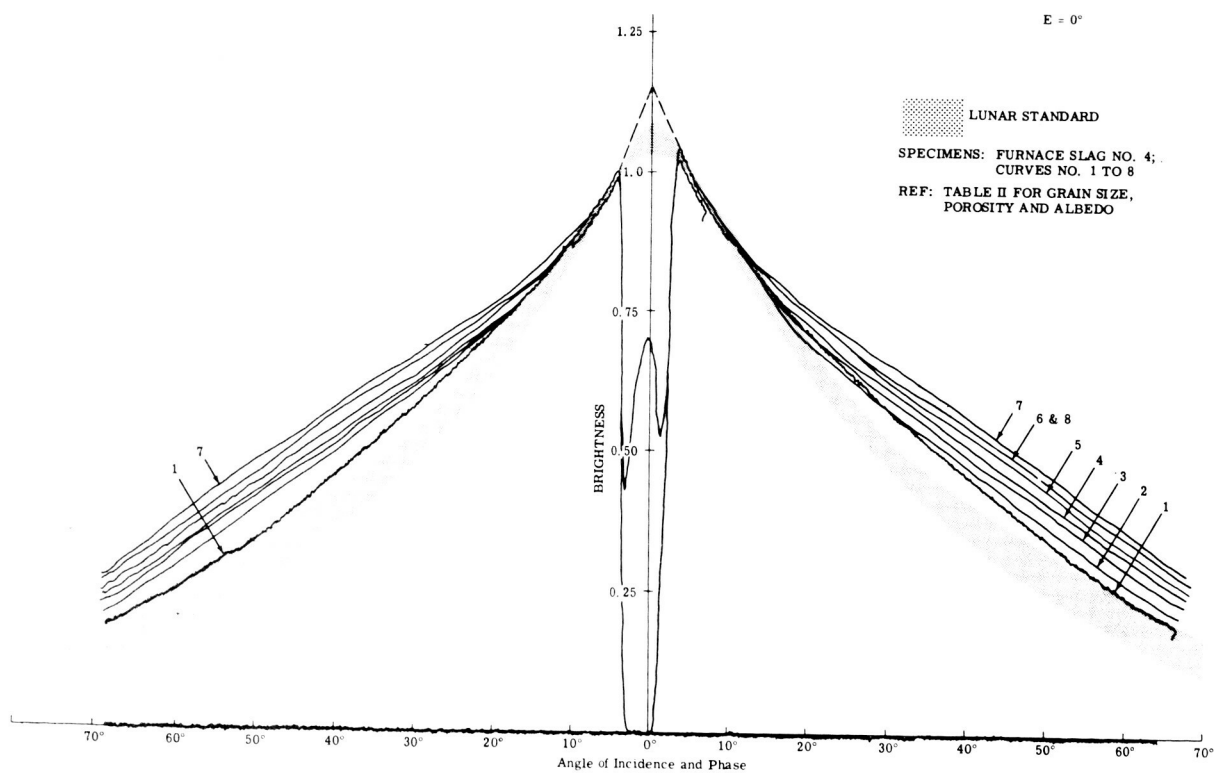


Figure 59. Photometry of Massive Furnace Slag Specimens (Sheet 3 of 3)



(a)



(b)

Figure 60. Photometry of Furnace Slag as Function of Grain Size, Porosity, and Albedo
(Sheet 1 of 2)

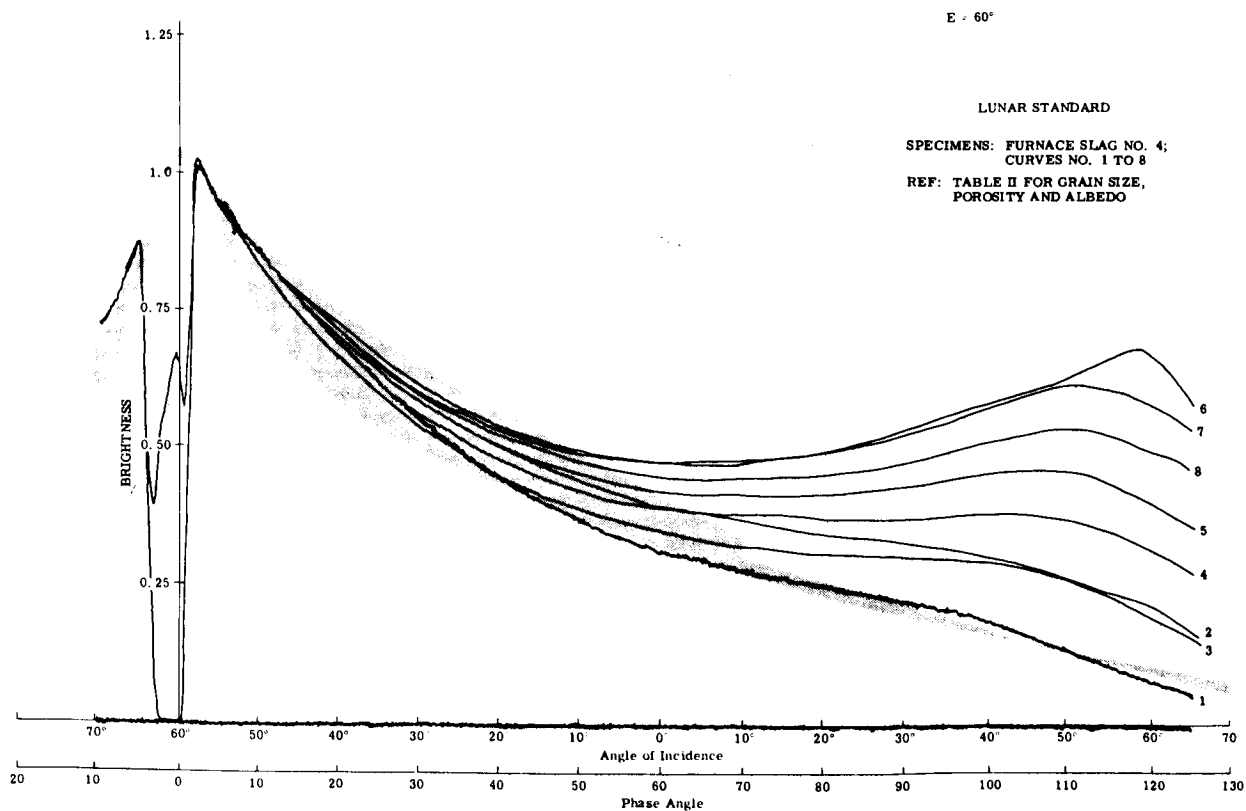
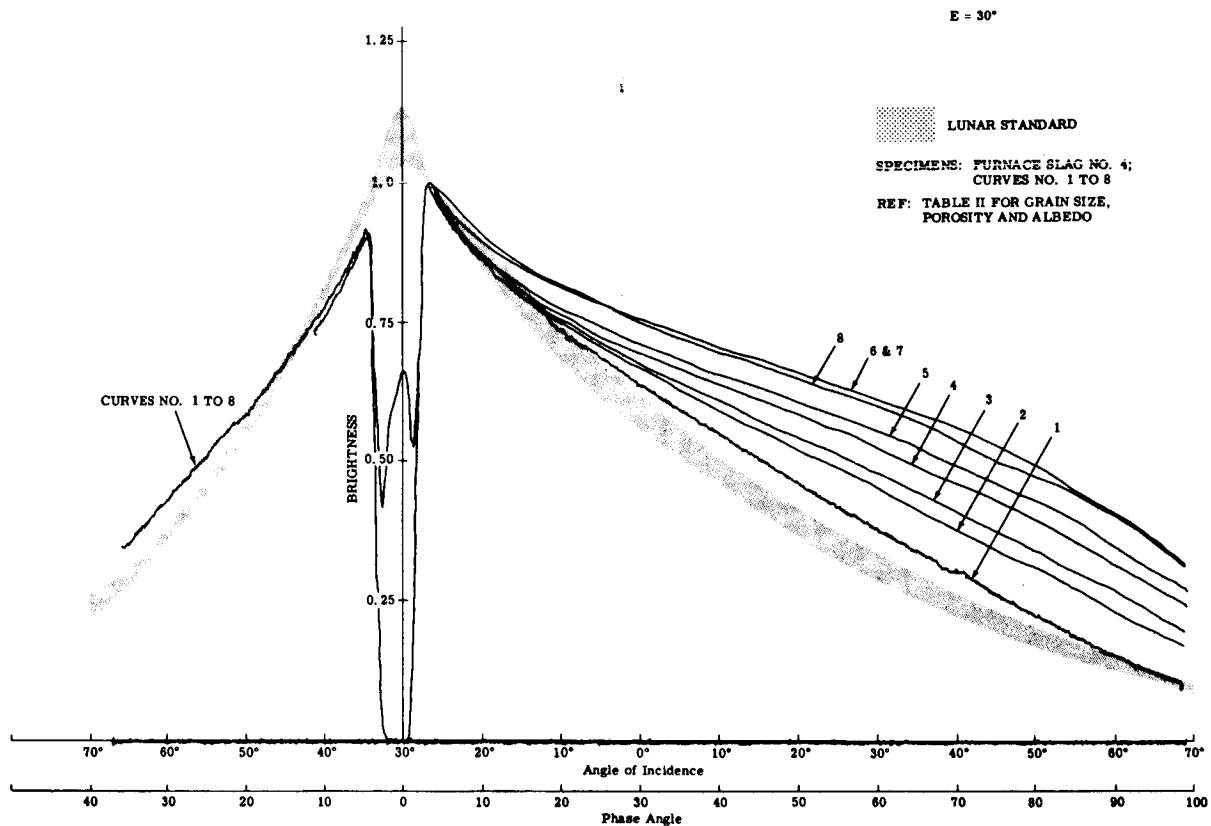


Figure 60. Photometry of Furnace Slag as Function of Grain Size, Porosity, and Albedo
(Sheet 2 of 2)

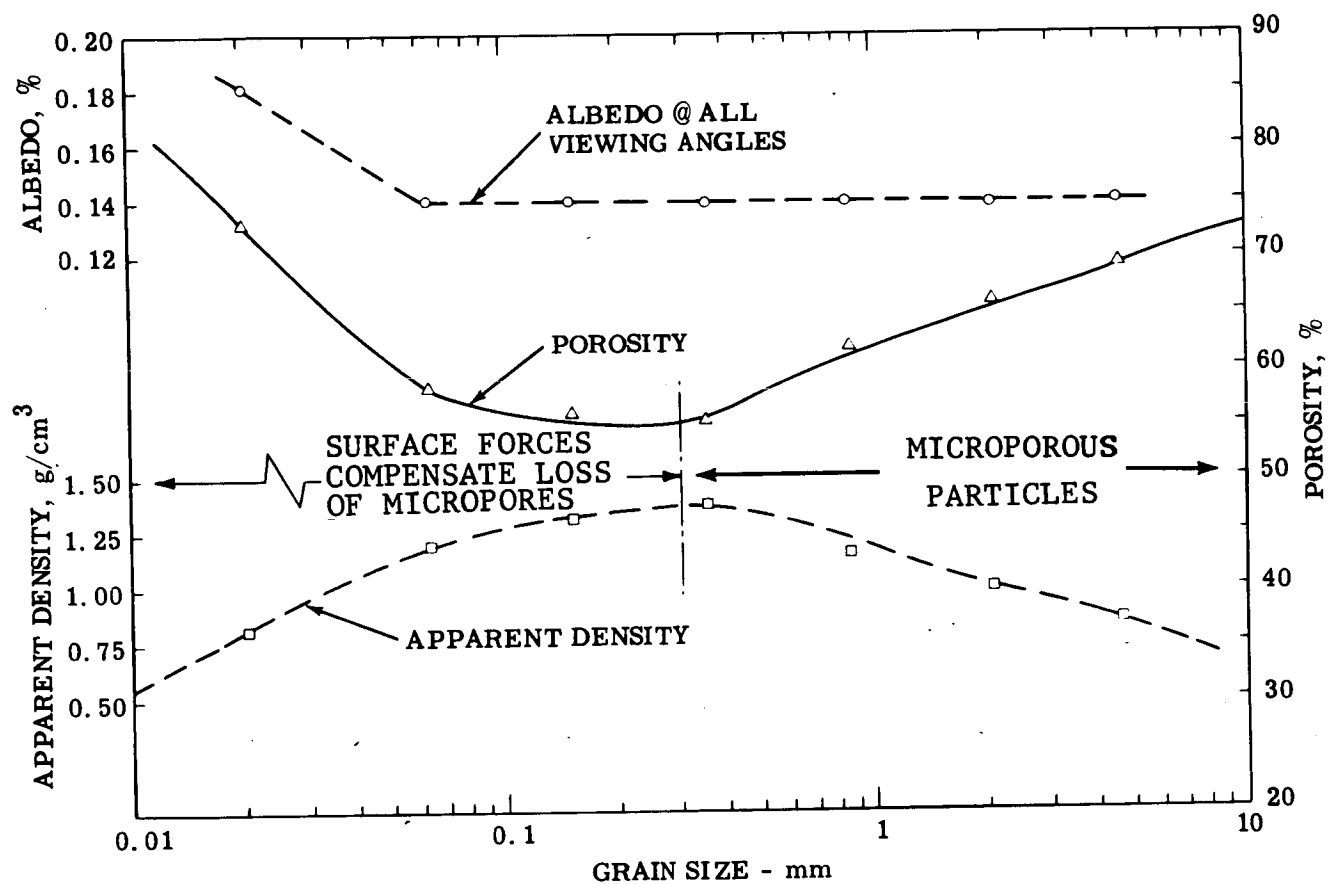


Figure 61. Albedo and Porosity of Volcanic Cinder Powders vs Grain Size

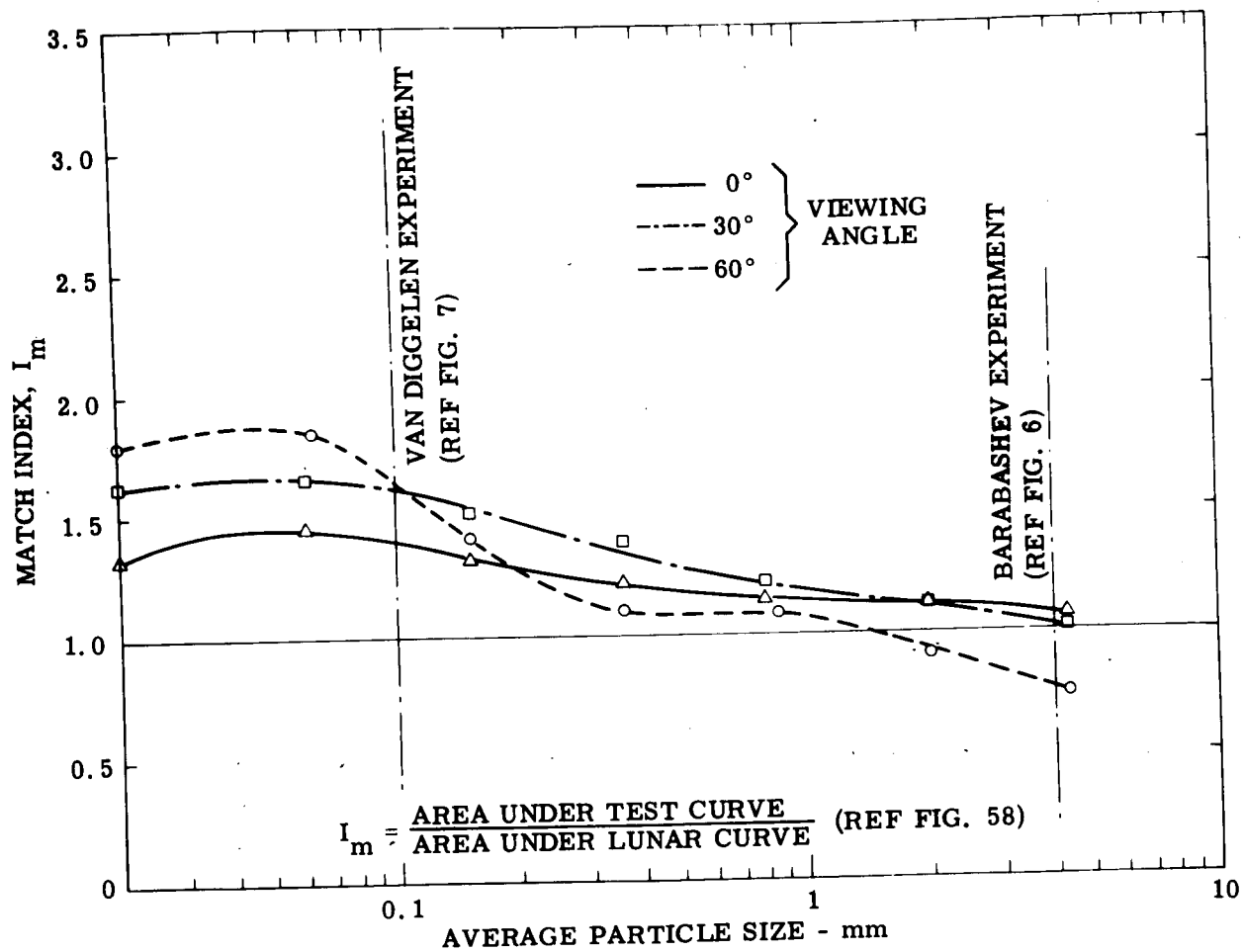


Figure 62. Photometric Match Index vs Grain Size of Volcanic Cinder # 4

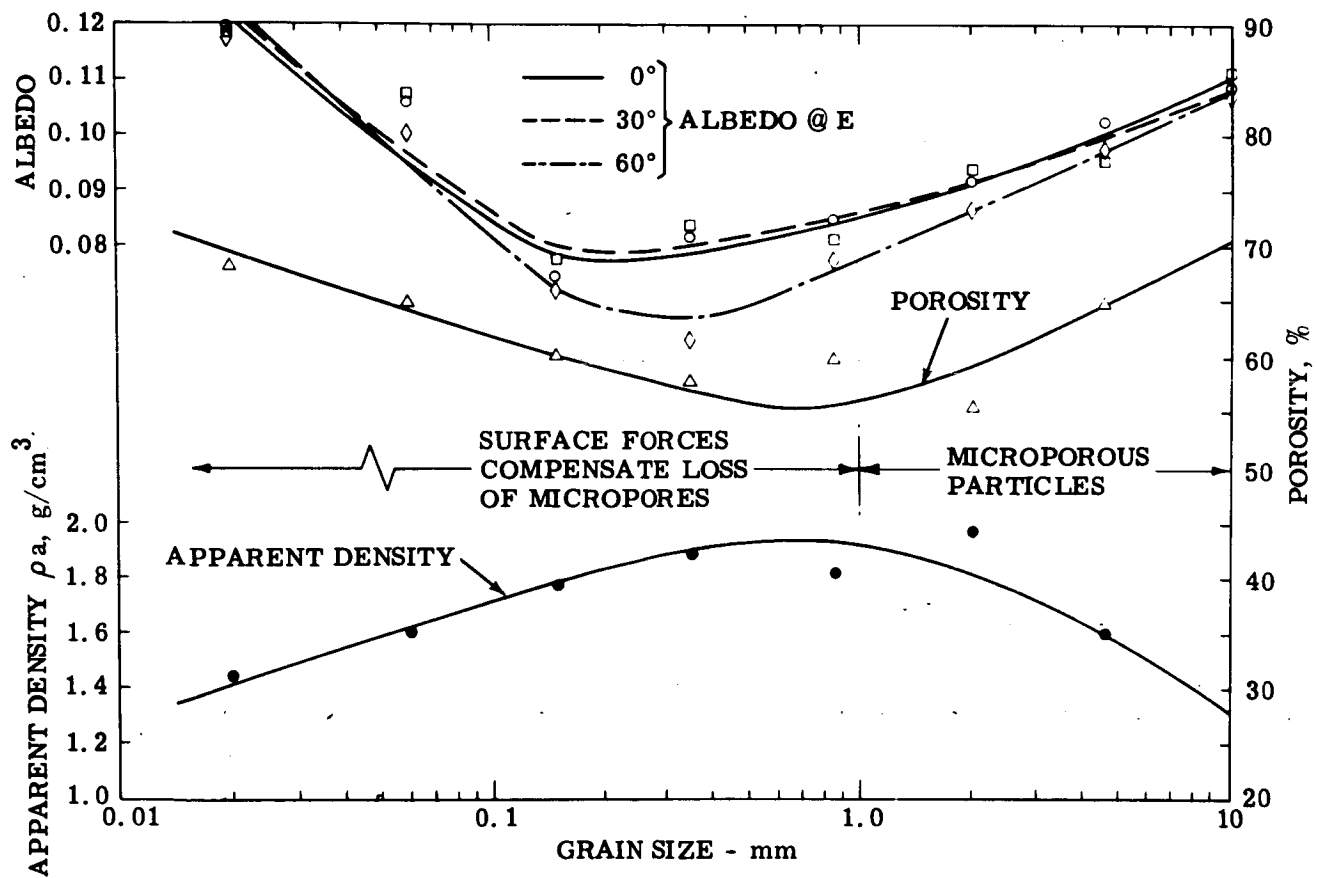


Figure 63. Albedo and Porosity of Furnace Slag No. 4 Powders vs Grain Size

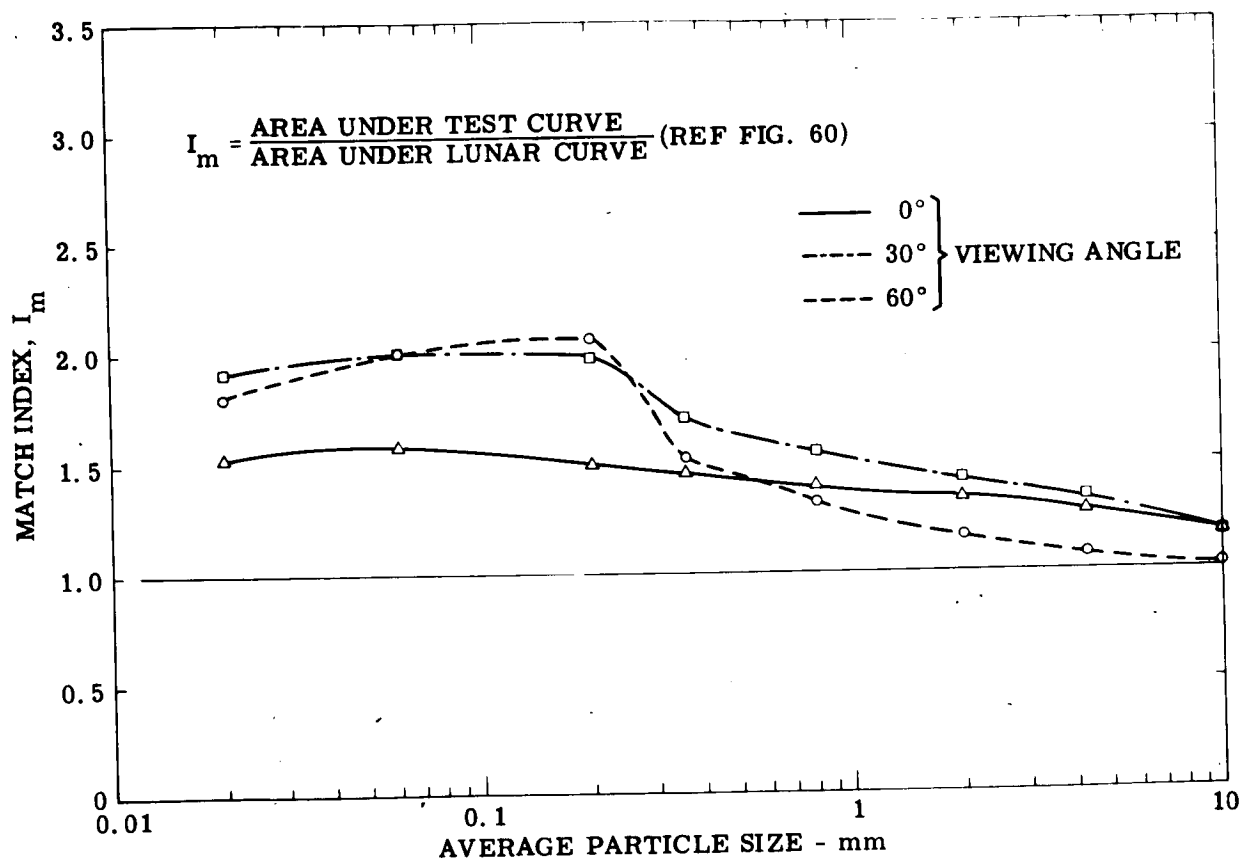


Figure 64. Photometric Match Index vs Grain Size of Furnace Slag No. 4

CONCLUSIONS

The following conclusions may be made at this time regarding the nature of the lunar surface; these conclusions are based on photometric experiments and analyses performed in three phases, dealing respectively with "natural," "artificial," and "controlled" models.

Phase I

The "natural" models include granular, vesicular, and dendritic specimens. Good agreement with the lunation curves of the moon at 0° , 30° , and 60° is obtained with very fine powders, coarse volcanic cinders and scoriae, furnace slags, sea corals, metallic meteorites, etc.

Some of the specimens exhibit a brightness surge near zero phase angle similar to lunar data recently reported in the literature. This peak exceeds by as much as 20 per cent the extrapolated peak of the Orlova-van Diggelen lunar standards used throughout this report as a basis of comparison.

It does not seem necessary to postulate a layer or veneer of fine dust on the moon in order to account for the lunar photometric data, since "macrorough," cohesive materials such as volcanic cinder or furnace slags, satisfy this data equally well when they are sufficiently dark and porous, and when they are examined by a large photometer. Most of the specimens that are photometrically analogous to the lunar surface exhibit, as reported by others, a low reflectivity and an "underdense" porous structure, but they differ widely from one another in composition, strength, consistency, depth, and grain size or roughness. It is apparent that the latter properties are not photometrically relevant, hence, it would be premature to infer them from the lunar photometric data to favor any given specimen as a lunar model on the basis of its photometric analogy to the lunar surface. It does seem possible, however, to determine the porosity of the outermost layer of the moon from its photometric properties and to use this information to help interpret the lunar radiothermal data which, in turn, could lead, under certain assumptions, to an estimate of the internal consistency and bearing strength of the lunar surface.

Additional advantage was taken of the large area-viewing capability of the Grumman photometric analyzer in investigating "macrorough" contrived models in an attempt to account for the photometric properties of the natural specimens, or the moon, in terms of their albedo, porosity, and grain size.

Phase II

"Artificial" models investigated in this phase included "composite" and "simple" models. "Composite" models consist of centimeter-size conventional geometric solids (such as prisms, pyramids, cusps, and domes, etc.) covered with a backscattering powder. These models fulfilled two useful purposes; they provided a means of evaluating the relative contribution of "first" and "second" order roughness to the photometric function, and they led to the discovery of unconventional, "simple" (i.e., dust-free) models which promise to offer an intuitive and mathematical basis for the study of the backscattering phenomenon in general and the reflection laws of the moon in particular.

In the study of the "composite" models, the dimensions, slopes, distribution, and orientation of the geometric solids were changed while keeping the microstructure and albedo of their surfaces the same. A useful analytical technique was developed to check and confirm the test results. It was found that the conventional geometric solids do contribute to the backscatter when they have steep slopes and sharp edges, and when they are oriented in a direction perpendicular to the intensity equator. However, they are unable to reproduce by themselves the lunation curves of the moon without a complex microstructure, which in these models is simulated by a veneer of CuO powder. If we assume that the geometric solids simulate relatively large lunar features such as craterlets, ridges, and rills, we may tentatively conclude that these features play a minor role in the over-all change of brightness of the lunar surface during a lunation, and that the lunar backscatter is predominantly due to the shadow casting characteristic of innumerable small surface irregularities. The well-known photometric similarity of the seemingly smooth maria and the obviously rugged highlands of the moon lend some weight to this view and suggest that the outermost layer of the moon, regardless of the origin and nature of the underlaying layer, is nearly uniformly covered by a dark, disrupted material to an unknown depth in which the shadow casting, solid elements are arranged in an "underdense" pattern separated by a complex array of cavities

which might be interconnected. Since for each photometric function there corresponds an infinite variety of geometric reliefs, it would seem difficult to give a more reliable description of this layer in terms of the actual dimension and spatial arrangement of its constituent elements. It is safe to state that the "first" order irregularities are below telescopic resolution and (judging from radar data and close-up photographs of the moon relayed by "Ranger") are likely to be no larger than a few millimeters or centimeters. As to the spatial arrangement of the small solid elements, some insight was gained into this important property of the lunar surface. Knowledge was gained of backscattering surfaces in general, when a successful attempt was made to simulate the microscopic complexity of "fairy castle" structures by means of dust-free, contrived models made up of centimeter-size elements arranged in such a manner as to present sharp vertical edges and overhanging horizontal members.

The "simple" models and their future derivatives have many advantages. They reveal the relevant photometric parameters, and help to establish, quantitatively, the proper value of these parameters. A preliminary model built by means of thumb tacks has shown that shadowing on and within such a porous structure, more than any other optical phenomenon, can be primarily responsible for the peculiar photometric properties of the lunar surface, and that both quasi-horizontal and quasi-vertical elements having a well-defined proportion and spacing appear to be necessary components of a lunar photometric model because neither set of members is sufficient by itself to account for the reflection of the moon at all viewing and phase angles. This preliminary conclusion is significant but must remain tentative until a number of "suspended geometries," devoid of vertical elements, are studied. Additional advantages of "simple" models of the "Thumb Tacks" variety include the convenient simulation and study of newly observed lunar phenomena such as the "opposition effect," "reddening with phase," etc. The technique could apply equally to the study of other reflecting celestial bodies whose photometric properties are known.

Phase III

Hawaiian volcanic cinder and furnace slag specimens, both photometrically analogous to the moon, have been ground and sorted into seven particle sizes, ranging from centimeters to microns and photometrically analyzed at 0° , 30° , and 60° viewing angles. As anticipated, the match of both specimens with the lunar data deteriorates as the particles get finer. The test results do

not necessarily imply that the photometric properties of the moon are incompatible with very fine particles; instead, they tend to confirm the conclusions of Phase I experiments regarding the apparent irrelevance of grain size as a key photometric property.

The effect of grain size on the photometric "match index" may be interpreted mainly in terms of changes in porosity and albedo. This interpretation is complicated, but not obscured by the apparently beneficial role played by micropores within individual particles at the coarse end of the particle size spectrum and by the "fluffing" action of surface forces at the fine end of the spectrum. The match index reaches its maximum deviation at around a grain size of 0.1 mm (at 1g) where the influence of these beneficial effects appears to be at its minimum.

Although the porosity of the original, uncomminuted specimens is restored at the fine end of the spectrum (micron range) due to the action of surface forces, the 30 per cent to 40 per cent increase of albedo and the consequent attenuation of the shadows due to multiple reflection and loss of opacity, appears to be sufficiently detrimental to offset the beneficial effect of rise in porosity and to prevent the match index from going back to 1.0.

Conflicting statements made in the literature regarding the presence and grain size of volcanic cinder on the moon, based on photometric experiments, may be resolved if the test results are primarily interpreted in terms of porosity and albedo rather than in terms of grain size and chemical composition. There is extensive lunar data and good agreement on albedos. As to the porosity of the lunar surface material, our experiments suggest a value of the order of 70 per cent. Additional experiments and analytical studies are possible and desirable to improve or confirm this estimate.

RECOMMENDATIONS

A number of useful areas for further investigation suggest themselves. Some of these areas are directly related to photometry, other areas involve the study of the less explored aspects of the lunar data.

A major recommendation in the photometric field is to utilize the recently observed data reported in the literature. It would be of interest to account for the "opposition effect" and the color change of the lunar surface with phase. Some of the natural specimens described in this report exhibit the "opposition effect" (recorded by means of a beam splitter specially provided for that purpose). But the implications of this interesting phenomenon in terms of the porosity and albedo of the specimens are not very clear; they could, however, be studied experimentally and/or analytically. It would be of interest to look for evidence of reddening at large phase angles among our natural specimens by measuring the change of the brightness of their surface at discrete wavelengths. Laboratory data on the wavelength dependence of the backscattering of surfaces may be of engineering interest as well as an additional clue in model matching experiments when the lunar counterpart of this data becomes available.

Contrived models of the "Thumb Tacks" variety promise a new departure in lunar surface research. Such models help the investigator to think of a particular aspect of the lunar data in terms of relevant properties rather than in terms of natural specimens which often confuse the issue and lead to unnecessary disagreements among the interpreters of these data. In the field of photometry, the preliminary models we have developed appear to promise further insight and quantitative data on the porosity, albedo and relative roughness of the lunar surface.

Specifically, the following studies are recommended:

- . Measurements of brightness versus phase relationship at discrete wavelengths ranging from far ultraviolet to near infrared of natural specimens that passed the photometric test under integrated light.
- . Measurements of brightness versus phase relationship under integrated and spectral light of "suspended" particulate models ranging in porosity from 50 to 99 per cent.

- . Measurements of brightness versus phase relationship of other artificial but "stable" models under uniform and nonuniform albedo conditions.
- . Derivation of empirical functions relating the photometric and geometric properties of backscattering tri-dimensional "surfaces" under uniform and nonuniform albedo conditions.

Similar investigations of the polarimetric, near infrared, thermal dielectric and other known properties of the moon should be coordinated with photometric studies in an attempt to verify and complement the limited amount of information that each one of these clues is capable of contributing to our understanding of the lunar surface.

ACKNOWLEDGMENTS

I am indebted to many people in and out of Grumman who have helped to bring this project to a successful culmination.

Among those at Grumman, I am particularly grateful to H. B. Hallock of Servo Engineering and his assistants J. Grusauskas, D. R. Lamberty, and D. Schlaijker for their resourcefulness, diligence, and care in building and operating the photometric analyzer and in making the measurements; also to Dr. S. N. Milford, Dr. W. G. Egan and Dr. G. C. McCoyd of the Geo-Astrophysics Section of the Research Department for their valuable suggestions throughout the performance of this work and in reading the manuscript; to K. Rillings of Quality Control for taking the microphotographs and to K. Ryback for editing. Special credit is due to Mr. Hallock for conceiving and setting up the "Thumb Tacks" photometric model.

I am equally grateful to: Dr. B. H. Mason of the American Museum of Natural History in New York City for lending the rare meteorite specimens; to Dr. W. R. Steiger of the University of Hawaii, Honolulu, for supplying the volcanic ash specimens and to R. L. Jones, W. W. Mendell, and J. E. Dornbach of the Lunar Technology Branch of NASA, Manned Spacecraft Center, Houston, Texas, for supplying the furnace slag specimens and giving their valuable advice and support.

REFERENCES

1. Barabashev, N.P., Astr. Nachr., 1922, pp. 217, 445; Astr. Nachr., 1927, pp. 229, 7.
2. Barabashev, N.P., and Chekirda, A.O., "A Study of the Rocks Most Closely Resembling the Surface Constituents of the Moon," Astron. Zhurnal, Vol. 36, No. 5, 1959, pp. 851-855.
3. Barabashev, N.P., and Garazhon, V.I., "The Microstructure of the Lunar Surface," Soviet Astronomy, Vol. VI, No. 2, September-October 1962.
4. Bennett, A.L., Astro. Jour., Vol. 88, No. 1, 1938.
5. Byrne, L.J., "Lunar Photographic Orbiter: Lighting and Viewing Conditions," Bellcomm Report TM6 3111 21, 1963.
6. Egan, W.C., "Polarization and the Lunar Surface," Grumman Research Department Memorandum RM-271 (1965).
7. Fedoretz, V.A., Pub. Karkov Obs., Vol. II, 1952; Vch. Zap. Karkov Univ., 1952, pp. 42, 49.
8. Fessenkov, V.C., "Photometry of the Moon," in Physics and Astronomy of the Moon (ed. by Kopal, Z.) New York, N.Y.: Academic Press, 1962.
9. Gehrels, T. Coffeen, T., and Owings, D., "Wavelength Dependence of Polarization of the Lunar Surface," Astronomical Journal, Vol. 69, No. 10, December 1964.
10. Gold, T., "Dust on the Moon," Vol. II, Vistas in Astronautics, Pergamon Press, pp. 261-266.
11. Halajian, J.D., "The Search for a Lunar Surface Model - Vol. I Photometry," (a proprietary preproposal study) Grumman Report, 1964. Also presented in part at the Meeting of the Committee of Extraterrestrial Resources, Golden, Colorado, as: "Old and New Lunar Photometric Models and What They Mean," 1964.
12. Halajian, J D., "The Case for a Cohesive Lunar Surface Model," Grumman Report ADR-04-04-62.2, presented at the N.Y. Academy of Sciences Meeting on "Geological Problems in Lunar Research," 1964.

13. Halajian, J.D., "Photometric Measurements of Simulated Lunar Surfaces," Grumman Research Department Memorandum RM-250, First Progress Report on NASA Contract No. NAS9-3182, November 1964.
14. Halajian, J.D., "Photometric Measurements of Simulated Lunar Surfaces," Grumman Research Department Memorandum RM-262, Second Progress Report on NASA Contract No. NAS9-3182, January 1965.
15. Hapke, B.W., and Van Horn, H., "Photometric Studies of Complex Surfaces with Applications to the Moon," Center for Radiophysics and Space Research Publication No. 127 (1962).
16. Hapke, B.W., "A Theoretical Photometric Function for the Lunar Surface," Center for Radiophysics and Space Research Publication No. 138 (1963).
17. Herschel, F.J.W., "Results of Astronomical Observations made at the Cape of Good Hope," London, 1847.
18. Lyot, B., Ann. Obs. Paris, Vol. VIII, Fasc. 1, 1929.
19. Markov, A.V., Astr. Nachr., 1924, pp. 65, 221.
20. Minnaert, M., "Planets and Satellites," Vol. III, The Solar System (ed. by G. P. Kiripec and B.M. Middlehurst) Univ. of Chicago Press, 1962, p. 235.
21. Öpik, E., Pub. Astr. Obs. Tartu., Vol. 26, No. 1, 1924.
22. Orlova, N.S., "Selected Articles on Light Scattering and Photometric Relief of the Lunar Surface," Astron. Zhurnal, Akad. Nauk, SSSR, Vol. 33, No. 1, NASA TTF-75, 1962.
23. Pearse, C.A., "Photometry and Polarimetry of the Moon and their Relationship to Physical Properties of the Lunar Surface," Washington, D.C.: Bellcom, Inc., August 1963.
24. Sharanov, V.V., The Moon," Report on Symposium No. 14 of the Inst. Astron. Union, Pulkova Obs. (1960) Academic Press, 1962, p. 385.
25. Steiger, W.R., Private Communication, Institute of Geophysics, University of Hawaii (1965).

26. Sytinskaya, N.N., "Probable Dimensions of Roughness of Lunar Microtopography," News of the Commission of Physics of Planets, No. 1, 1959, pp. 81-84.
27. Van de Hulst, H.C., "Light Scattering by Small Particles," New York, N.Y., Wiley Press, 1957.
28. Van Diggelen, L., "Photometric Properties of Lunar Crater Floors," Recherche Astronomique de l'Observatoire d'Utrecht, Vol. XIV, No. 2, 1959.
29. Wirtz, C., Astr. Nachr., 1915, pp. 201, 289.
30. Wislezinus (1895) reported in Wirtz, C., Astr. Nachr. (1915) pp. 201, 289.

APPENDIX

ANALYTICAL INVESTIGATION OF THE PHOTOMETRY OF CuO -COVERED PRISMS

by

H. B. Hallock

and

D. Lamberty

PART I

ANALYSIS OF THE PRISMS WHEN SUN MOVES PARALLEL TO PRISM RIDGES

The model and illuminations geometry is shown in Fig. A-1.

Let:

ϕ_f = photometric function of CuO on flat surface
at viewing angle α

ϕ_p = photometric function of sample viewed

α = phase angle

W_n = relative viewed area of surface S_n in Fig. A-1

Assume:

collimated incident light

homogeneous surface

viewing from large distance

reflection curve from flat surface of CuO is symmetric

$$\phi_f(\theta) \big|_{\alpha} = \phi_f(-\theta) \big|_{\alpha}$$

secondary reflection is negligible.

From geometry of Fig. A-2:

area of S_1 = area of S'_1 or $W_1 = W'_1$

area of S_n = area of S'_n or $W_n = W'_n$

and

$$\phi_f(\theta) \big|_{\alpha} = \phi_f(-\theta) \big|_{\alpha} \quad \text{or} \quad \phi_f(\alpha) \big|_{\theta} = \phi_f(\alpha) \big|_{-\theta}$$

$$\phi_p(\alpha) = \sum_{n=1}^{N/2} \phi_f(\alpha) \big|_{-\theta} W_{2n} + \sum_{n=1}^{N/2} \phi_f(\alpha) \big|_{\theta} W'_{2n-1}$$

$$\phi_p(\alpha) = \sum_{n=1}^{N/2} \phi_f(\alpha) |_{\theta} w'_{2n} + \sum_{n=1}^{N/2} \phi_f(\alpha) |_{\theta} w'_{2n-1}$$

$$= \sum_{n=1}^N \phi_f(\alpha) |_{\theta} w'_n$$

$$= \phi_f(\alpha) |_{\theta} \sum_{n=1}^N w'_n$$

$$\phi_p(\alpha) = k \phi_f(\alpha) |_{\theta} \quad \text{where } k = \text{constant} = \sum_{n=1}^N w'_n = 1$$

PART II

ANALYSIS OF THE PRISMS WHEN SUN MOVES PERPENDICULAR TO PRISM RIDGES

The elongated prisms are covered with copper oxide powder screened through 400 mesh screen. This material is known to have an excellent "backscatter" resembling the lunar signature. Except for possible irregularities in coverage of the geometric forms due to gravitational effects, the essential signature type is unchanged by sprinkling it on the geometric forms. However, the prism surfaces are now of two opposite slopes corresponding to two "viewing angles" for any one orientation of the whole base structure.

As an example, one-prism and three-prism geometries with 45° vertex angles, as illustrated in Fig. A-3b and 3c, are analyzed in Tables A-I and A-II in terms of the photometry of a CuO-covered flat plane as shown in Figs. A-3a and A-4. In the case of the three-prism geometry, the analysis takes also into consideration a secondary effect of noticeable proportion due to the shadowing of the "trough" areas by the prisms at very oblique incidence

(beyond 45°). Light incident from the direction toward the even surface inclination will not strike the odd surfaces until an angle of 45° incidence to base has been reached. Also beyond 45° the even surfaces with the exception of the end one (S_6) are shadowed partly.

The reflection of light from one prism to an adjacent prism face can be neglected since the reflectance is less than 10% and the double reflection could not possibly account for 10% x 10% or 1% of the total.

The geometries defined in Fig. 43 restrict the configurations to one with an "edge factor," in which surfaces 1 and 6 are not affected by adjacent structures beyond the base defined.

To analyze the whole structure, a single " 45° viewing angle" photometric curve is taken on copper oxide sprinkled on a flat. This curve, shown in Fig. A-4, is then used to provide the basic photometric values extracted in Table A-II, ϕ_f (photometric function of the flat plate).

Since a circular field of view is involved, a weighting factor for the area of each surface viewed is calculated and tabulated in Table A-II. Shadowing is treated as a per cent figure, shown in the tables as P (%). A product of ϕ_f and the two factors mentioned for each surface can be summed over the entire structure to yield an over-all photometric function ϕ_p (photometric function of prisms). Figures 45a and c show a comparison of the calculated ϕ_p and a measured ϕ_p for one and three prisms respectively. The analysis for the one-prism geometry is shown in Table A-I.

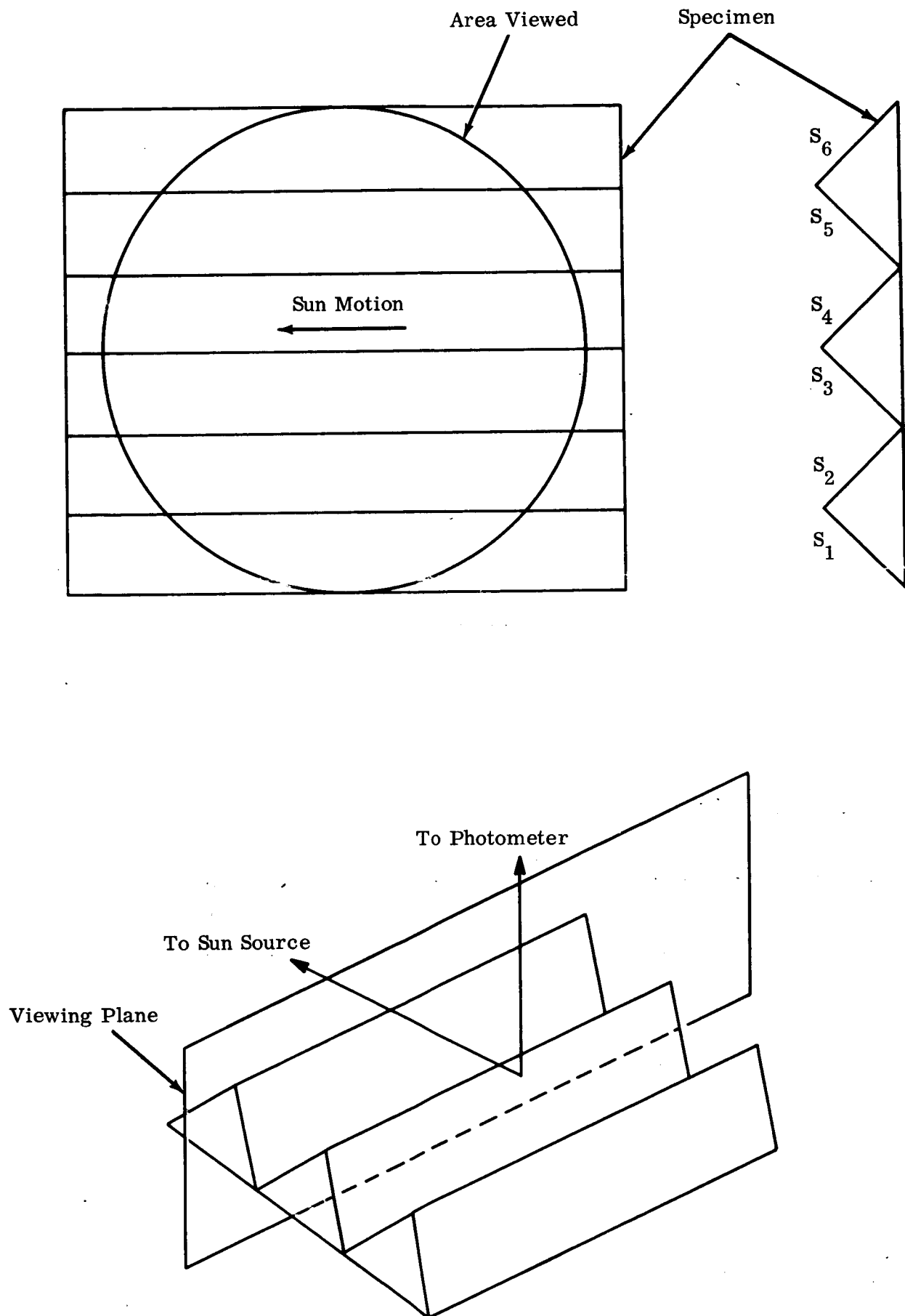


Figure A-1. Three-Prism and Illumination Geometry for Sun Motion Parallel to Prism Ridges

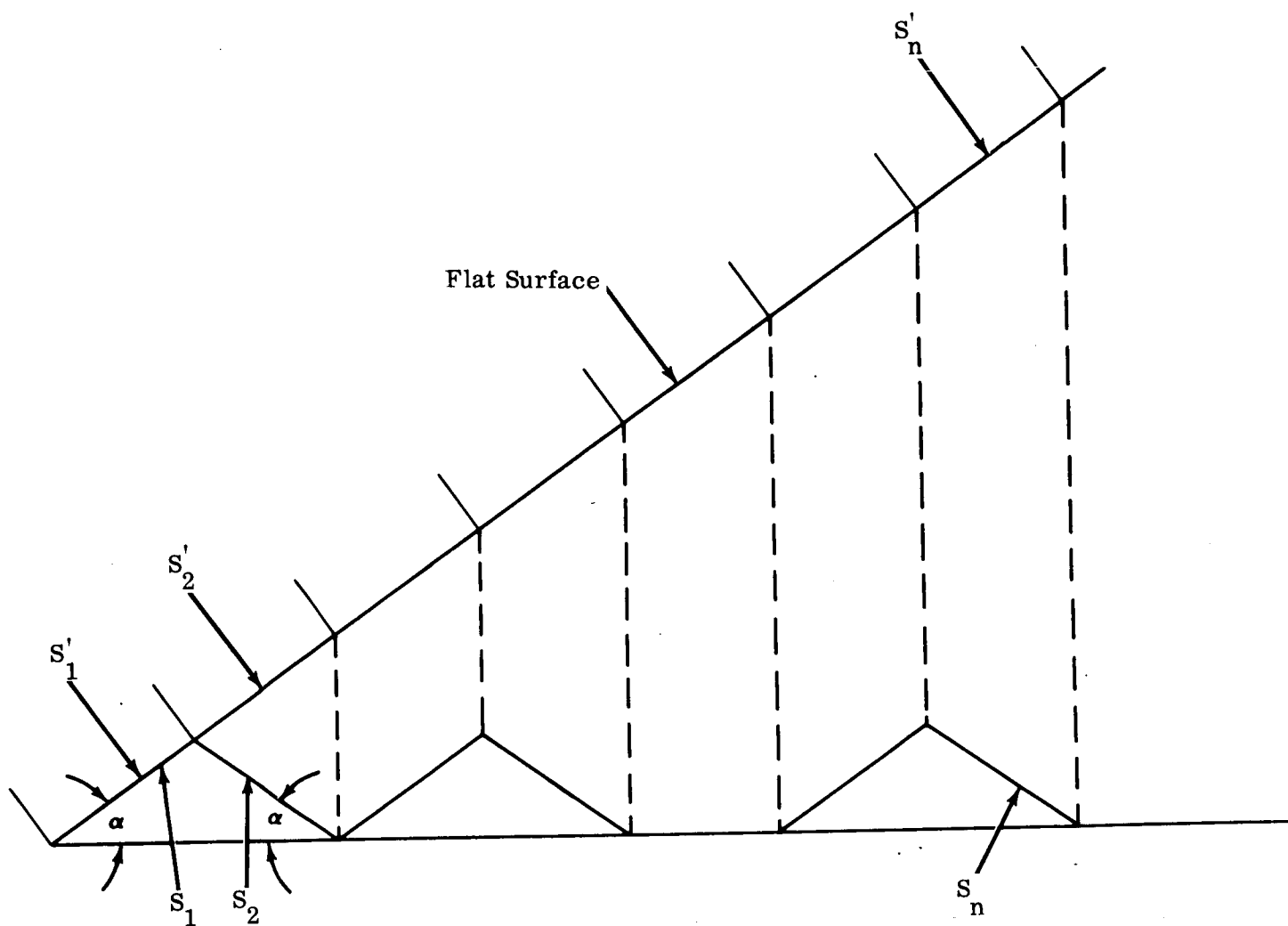
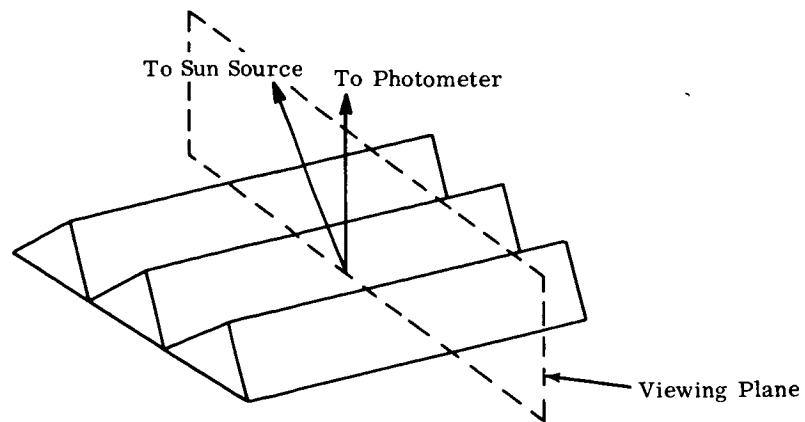
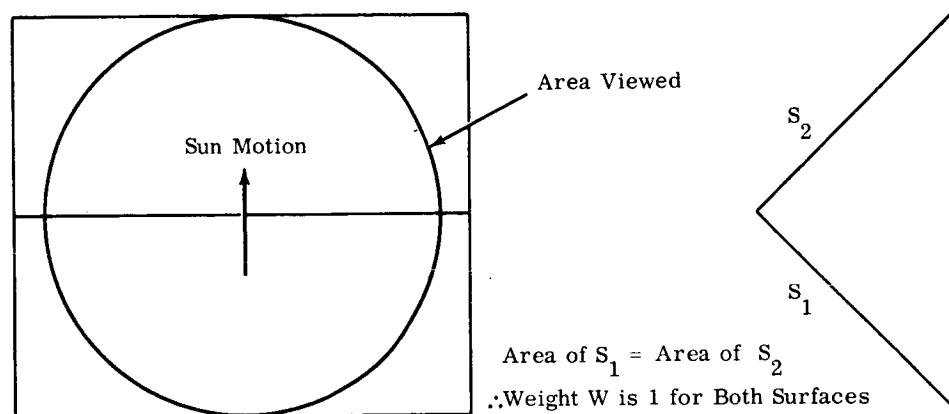


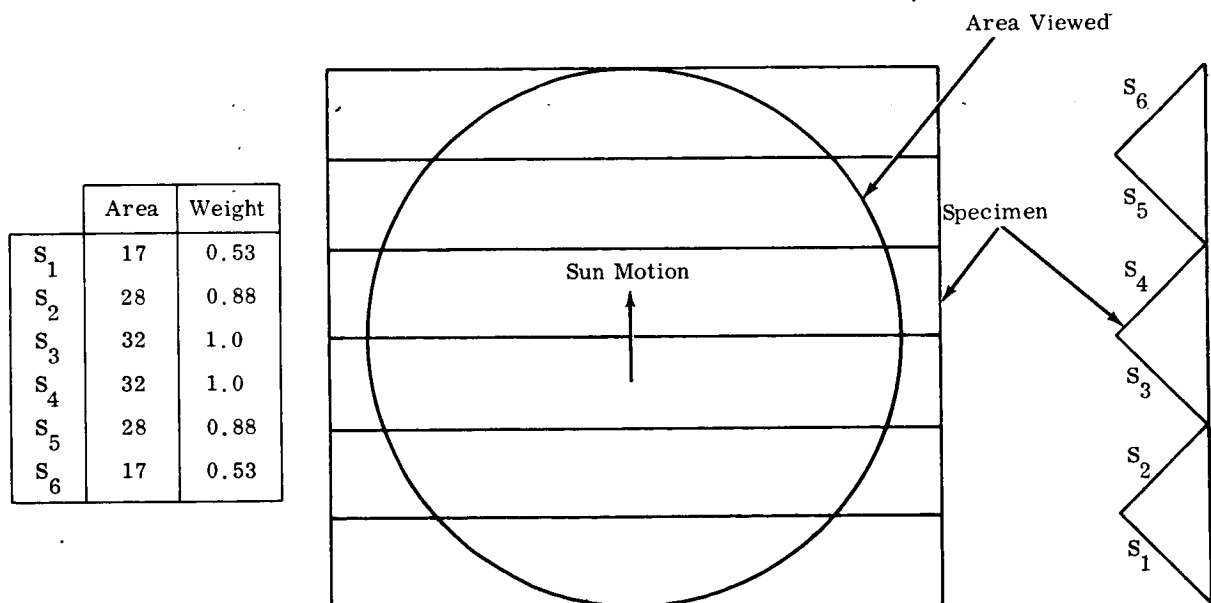
Figure A-2. Prisms and Equivalent Flat Surface



(a) Transverse Illumination
(Ref. Figures 45a to 45e and 48)



(b) One-Prism Geometry (Ref. Figure 45a and Table A-1)



(c) Three-Prism Geometry

Figure A-3. Prism and Illumination Geometry for Sun Motion Perpendicular to the Ridges

Table A-I.

ANALYSIS OF ONE-PRISM GEOMETRY FOR SUN MOTION PERPENDICULAR TO RIDGE
Ref. Figures A-3a and 3c

α	S_1					S_2						
	I	W	P (%)	ϕ_f	Prod.	I	W	P (%)	ϕ_f	Prod.	ϕ_p	$R \cdot \phi_p$
60	105	1	0	0	0	-15	1	1	33.5	33.5	33.5	16
50	95	1	0	0	0	-5	1	1	38.0	38.0	38.0	18
40	85	1	1	7.5	7.5	5	1	1	43.0	43.0	50.5	24
30	75	1	1	22.0	22.0	15	1	1	50.0	50.0	72.0	35
20	65	1	1	38.0	38.0	25	1	1	57.5	57.5	95.5	46
10	55	1	1	56.5	56.5	35	1	1	67.0	67.0	123.5	59
0	45	1	1			45	1	1				

$$\begin{aligned}
 R &= \frac{\phi_p \text{ of sample curve at } \alpha = 10^\circ}{\phi_p \text{ of calculated curve at } \alpha = 10^\circ} \\
 &= \frac{59}{123.5} \\
 &= 0.48
 \end{aligned}$$

Note: Data Taken from Figure A-4 and Plotted
on Graph in Figure 45a

Table A-II

ANALYSIS OF THREE-PRISM GEOMETRY FOR SUN MOTION PERPENDICULAR TO RIDGES

Ref. Figures A-3a and 3c

	S_1					$S_2 + S_4$				
α	I	W	P (%)	ϕ_f	Prod.	I	W	P (%)	ϕ_f	Prod.
60	105	.53	0	0	0	-15	1.88	73	33.5	46
50	95	.53	0	0	0	-5	1.88	92	38.0	66
40	85	.53	100	7.5	4	5	1.88	100	43.0	81
30	75	.53	100	22.0	12	15	1.88	100	50.0	94
20	65	.53	100	38.0	20	25	1.88	100	57.5	108
10	55	.53	100	56.5	30	35	1.88	100	67.0	126

	$S_3 + S_5$					S_6						
α	I	W	P (%)	ϕ_f	Prod.	I	W	P (%)	ϕ_f	Prod.	ϕ_p	R • ϕ_p
60	105	1.88	0	0	0	-15	.53	100	33.5	18	64	12.5
50	95	1.88	0	0	0	-5	.53	100	38.0	20	86	17.0
40	85	1.88	100	7.5	14	5	.53	100	43.0	23	122	24.0
30	75	1.88	100	22.0	41	15	.53	100	50.0	26	173	34.5
20	65	1.88	100	38.0	71	25	.53	100	57.5	30	229	45.5
10	55	1.88	100	56.5	106	35	.53	100	67.0	35	297	59.0

$$\begin{aligned}
 R &= \frac{\phi_p \text{ of sample curve at } \alpha = 10^\circ}{\phi_p \text{ of calculated curve at } \alpha = 10^\circ} \\
 &= \frac{59}{297} \\
 &= .199
 \end{aligned}$$

Note: Data Taken from Figure A-4 and Plotted on Graph in Figure 45c